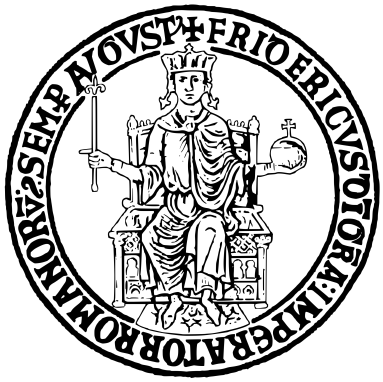

UNIVERSITÀ DEGLI STUDI DI NAPOLI "FEDERICO II"

DEPARTMENT OF PHYSICS "ETTORE PANCINI"

PH.D. IN **QUANTUM TECHNOLOGIES**

XXXIV CYCLE

COORDINATOR: PROF. FRANCESCO TAFURI

Modeling and design of novel van der Waals materials for the quantum simulation

---

SCIENTIFIC DISCIPLINARY SECTOR: FIS/03

Author:
Felice CONTE

Supervisor:
Prof. Giovanni CANTELE

2018-2021

"What we observe is not nature itself,
but nature exposed to our method of questioning."

Werner Karl Heisenberg

Contents

Chapter 1

Introduction

"A person who never made a mistake
never tried anything new."

Albert Einstein

This chapter is devoted to provide an extended introduction of the topics covered during the Ph.D. program, in order to sensitize the reader to the motivations and the ideas behind my research journey, in addition to allow a fluid reading of the thesis. At the end, the general structure of the latter will be outlined. The technical details will be left for the subsequent chapters.

1.1 Two-dimensional materials: successes and challenges

The two-dimensional (2D) materials field can be traced back to the successful isolation of single-layer graphene sheets exfoliated from (bulk) graphite in 2004 by the group of Andre K. Geim and Konstantin S. Novoselov [1]. This material showed its own novel physical phenomena distinctly different from graphite, being a transparent semimetal with massless Dirac electrons [2–4]. Since then, novel 2D materials have been studied and synthesized, becoming the focus of intense research. In general, a 2D material consists of a dangling-bond-free single or few-atom-thick layer, and can be synthesized from a bulk material with a layered structure, where the stack is kept together by van der Waals (vdW) interactions, which are very weak compared to the in-plane covalent bonds[1]. Since van der Waals interactions involve induced dipoles between the layers, they are referred to as London interactions, i.e., vdW interactions act as a "quantum glue"[2]. Nowadays, the 2D library includes hundreds of thermodynamically stable materials [8], including monolayers (MLs) of hexagonal boron-nitride (h-BN) [9], transition metal dichalcogenides (TMDs, e.g., MoS_2, $NbSe_2$, WSe_2) [10], metal nitrides/carbides (MXenes) [11], metal halides (e.g., PbI_2, $MgBr_2$) [12], transition metal halides (TMHs, e.g., CrX_3 [13] and Nb_3X_8 [14, 15], with X = Cl, Br, I), transition metal carbon/nitrogen compounds and elemental 2D materials, other than graphene, called Xenes (e.g., borophene [16], silicene [17], germanene [18], phosphorene [19], and bismuthene [20]). Among them, one can find a wide range of properties, passing through conductors (e.g., graphene and

[1]The vdW forces strength is $\sim$ 0.1-1 kJ mol^{-1} ($\sim$ 1-10 meV per bond), whereas the covalent or ionic bonds strength is $\sim$ 10^2-10^3 kJ mol^{-1} ($\sim$ 10^3-10^4 meV per bond).

[2]Van der Waals interactions between atoms or molecules can be of three types: Keesom (permanent dipoles), Debye (permanent-induced dipoles), London (induced dipoles) interactions. Although all of them could manifest as quantum effects, London interaction has a purely quantum origin, since its R^{-6} dispersion law, where R is the dipoles reciprocal distance, can be derived only by the second-order perturbation theory of quantum mechanics [5–7].

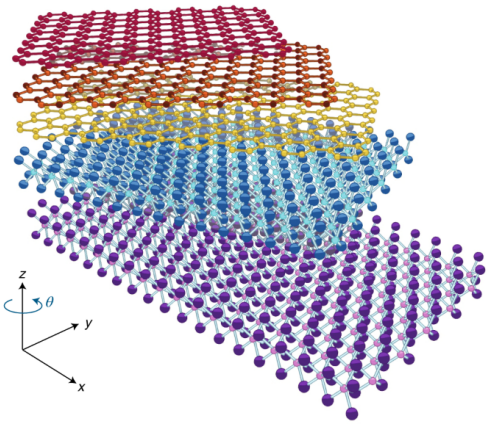

FIGURE 1.1: Van der Waals heterostructures built by piling different 2D materials. Each heterostructure brick is a dangling-bond-free single- or few-atom-thick layer with in-plane covalent bonds and out-of-plane van der Waals interactions. The latter allow to stack up 2D materials with different lattice parameters, geometries, atomic constituents, and a twist angle among consecutive layers. Adapted with permission from Ref. [22].

$NbSe_2$), semiconductors (e.g., MoS_2 and WSe_2), superconductors (e.g., $NbSe_2$), insulators (e.g., h-BN), Weyl semimetals (e.g., $PtCl_3$ [21]), and so on.

2D materials have revolutionized the way we think about materials for many reasons. First of all, nanoscale thin materials have opened up the possibilities of subnanometer engineering, in order to realize central processing units (CPUs) with hundreds of $\lesssim$ 1 nm thick transistors (see [23]). They are ideal platforms for the state-of-the-art electronics applications, such as flexible displays, due to their high space-efficiency and flexibility [24–26]. More importantly, 2D materials allow to construct a huge variety of novel layered structures, that are built much like "Lego" at an atomic-scale by vertically stacking the 2D blocks [27]. Indeed, due to the absence of dangling bonds and the weak intensity of the out-of-plane vdW interactions, it is possible to integrate highly different 2D materials without the constraints of crystal lattice matching, with a control on single layers relative orientation or *twist angle*, their order and number, as sketched in Fig. 1.1. The layered structures obtained by acting on such an unprecedented number of degrees of freedom (DOFs) are known as *van der Waals homostructures* (vdWHos) or *heterostructures* (vdWHes), depending on whether layers of the same material or of different materials are stacked together. All these DOFs directly affect the interactions characterizing such vdW structures, thus providing a unique way to understand and predict their novel physical properties and phenomena. Therefore, the vdW interaction between adjacent layers, named as *interlayer coupling*, is expected to have a key role in the switching on of the latter. This has recently been proven in several types of vdW systems, such as bilayer graphene (BG) and TMDs, acting in particular on the twist angle [28–35], which provides a direct response on the interlayer coupling through the steric effects[3] between the atoms of faced layers.

Besides the great structural advantages and the high degree of tunability of vdW materials, the interest of research and technological communities on such systems

[3] A steric effect is a nonbonding interaction affecting the spatial distribution and reactivity of atoms and molecules.

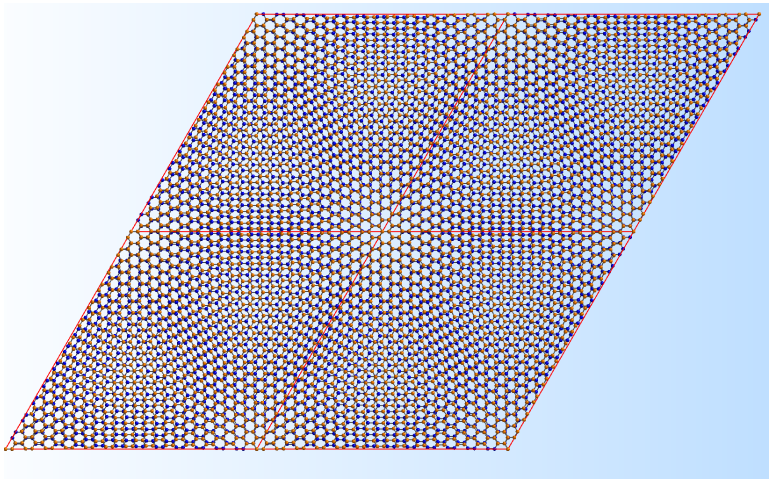

FIGURE 1.2: Repetition of the multiatomic supercell of TBG for the twist angle $\theta = 2.65°$. The supercell is defined by the red box reflecting the hexagonal symmetry, enclosing the top layer of red carbon atoms twisted with respect to the bottom layer of blue carbon atoms.

has exponentially increased due to their novel and remarkable properties, both experimentally observed and confirmed or predicted by more and more accurate theoretical predictions. Before to proceed, we will mention only some of the most striking outcomes of selected 2D families, i.e., twisted bilayer graphene (TBG), TMDs, and TMHs, that will play a central role in this thesis.

1.1.1 Twisted bilayer graphene

Theoretical predictions and experimental measurements on TBG, favored by the precise control of the twist angle through the recent tear-and-stack fabrication technique [36], unveiled coexistent phenomena and phases of intriguing and complex branches of condensed matter physics, such as Mott insulating behavior and unconventional superconductivity. This is enormously beneficial both for the chance to experimentally access tunable complex physics regimes in a easily realizable system and for providing new insights for topics that have been the object of intense research the last 30 years.

Since 1988, the moiré patterns on graphite surface formed by the misorientation θ between two faced layers with the same symmetries was observed in STM images [37–45], where the name refers to the induced visive moiré pattern effect. While the moiré pattern exists for any θ, there are particular twist angles, known as *commensurate angles*, that realize a superlattice, that is a strickly periodic repetition of some large multiatomic supercell, as shown in the example of Fig. 1.2. The existence of commensurate (twist) angles is a great advantage from a theoretical point of view, since it allows to study a twisted bilayer (BL) by using theories or methods, such as density functional theory (DFT) or tight-binding (TB) method, that take advantage from the periodicity induced by the repetition of a unit cell in the space (i.e., the Bravais lattice). In general, the resulting supercells in commensurate structures may contain contain hundreds or thousands of atoms. For instance, the number of carbon

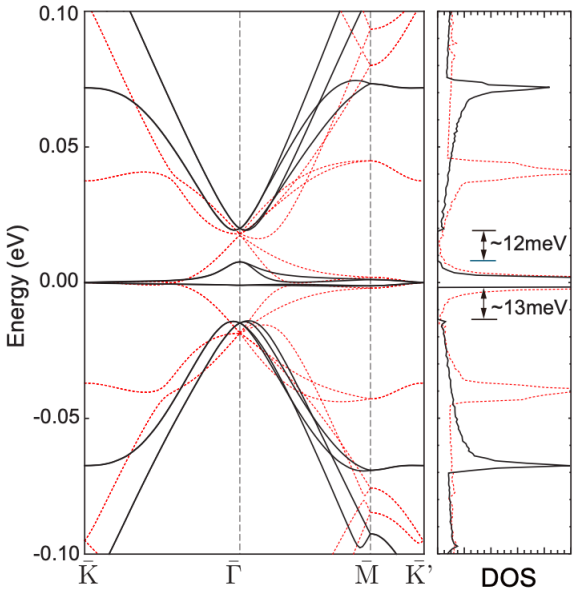

FIGURE 1.3: Band structure and DOS of TBG with $\theta = 1.05^\circ$ obtained by using a continuum model. Red dashed lines are the bands obtained by using the flat-layer assumption on the TBG, i.e., with unrelaxed structure, according to Ref. [46]. Black solid lines are the bands obtained by taking into account the in-plane relaxation of TBG. As shown in the DOS, the relaxation induces a band gap opening at the Γ point of the MBZ for both electron and hole sides with sizes of $\sim$ 12 meV and $\sim$ 13 meV, respectively. Adapted with permission from Ref. [28].

atoms in the TBG supercell, starting from the AA or AB stacking[4], increases with decreasing the angle of twist and reaches very large values, such as 11164 atoms for $\theta = 1.08^\circ$, as will be deeply explained in Sec. 3.1. Correspondingly, the periodicity of the honeycomb superlattice represents the new scale of periodicity of the system.

In 2007, Lopes dos Santos *et al.* carried out the first study on the TBG electronic structure by analyzing the electronic structure close around the Fermi energy, referred to as *low-energy spectrum*, in the continuum limit[5] for small commensurate angles smaller than 10°, in terms of massless Dirac fermions coupled by a slowly varying periodic interlayer hopping [47]. The low-energy electronic structure was quite different from the AB-stacked BG[6]. Indeed, Dirac cones were persistent, but the Fermi velocity v_F of the massless Dirac fermions was substantially reduced with respect to the MG. Moreover, unlike the AB-stacked BG, the particle-hole symmetry was absent and the external electric field did not open a gap in the electronic spectrum, but just gave a **k**-point dependent energy shift. Subsequently, the continuum model was improved by Bistritzer and MacDonald through a low-energy effective Hamiltonian valid for $\theta \lesssim 10^\circ$ [46], irrespective of whether or not the twist angle

[4]When putting two graphene layers on top of each other, two fundamental stacking geometries can be realized. In the first, an atom of the top layer is exactly superimposed to an atom of the bottom layer. In the second, an atom of the top layer is put on top of the center of a hexagon of the honeycomb lattice. These are referred to as AA and AB stackings, respectively. AB stacking is more stable and corresponds to the Bernal stacking observed in graphite.

[5]The continuum limit holds for long-wavelength electronic states and excitations. In graphene this implies the condition $|\mathbf{q}|a_0 \ll 1$, where $\mathbf{q}$ is the wave-vector separating an electronic state from the Dirac point and a_0 is the lattice parameter.

[6]The low-energy spectrum of BG is quadratic rather than linear as in ML, and the Fermi velocity is momentum dependent, unlike the ML [48, 49].

was commensurate, and by Lopes dos Santos *et al.* through the analytical calculation of the spatially modulated hopping amplitudes for any type of commensurate structures in the low twist-angle limit [50]. When the twist angle reached the values $\theta = 1.05^\circ, 0.5^\circ, 0.35^\circ, 0.24^\circ, 0.2^\circ$, referred to as *magic angles*, the Fermi velocity vanished and showed maxima between them. Then, this was confirmed through the TB method applied to TBG by Trambly de Laissardière *et al.* [51], also noting that the magic angles were defined by the series $\theta_n = 1.05^\circ/n$. Furthermore, close to the first theoretically predicted magic angle $\theta_1 = 1.05^\circ$, the interlayer hybridization induced four nearly flat low-energy bands around the charge neutrality point (CNP), that are known as *minibands*, well distinct from the others and having a bandwidth of the order of 10-20 meV, as shown in Fig. 1.3 (red dashed lines). They were predicted by both the continuum model [46] and the TB method [51], and then confirmed by the two symmetric van Hove singularities in the density of states (DOS) [50]. Furthermore, the local density of states (LDOS) associated to the flat minibands were highly peaked at the AA stacking regions of the moiré pattern, prohibiting the tunneling from the AA to the AB or BA regions.

The first experimental observations on TBG confirmed the Fermi velocity behavior and the flat minibands, but insulating gaps of the order of 10 meV at Γ point of the mini Brillouin Zone (MBZ) of the superlattice separated the latter from the other valence or conduction bands for $\theta = 1.8^\circ$ [52] and $\theta = 0.99^\circ$ [53]. This discrepancy between theory and experiments was associated to the flat-layer assumption adopted because of the inaccessible computational cost behind the lattice relaxation. This was confirmed in 2017 by Nam and Koshino [28], when the lattice relaxation in general TBGs was obtained by an effective continuum theory, although the out-of-plane components of the atomic displacement vectors were neglected for the sake of simplicity. Indeed, for $0.99^\circ < \theta < 1.20^\circ$, gaps opened up at Γ point, as shown in Fig. 1.3 (black solid lines) for $\theta = 1.05^\circ$, where there is a gap of $\sim$ 12 meV on the electron side and a gap of $\sim$ 13 meV on the hole side.

In 2018, Cao *et al.* unveiled the coexistence of Mott-like insulating [29] and unconventional superconductivity phases [30] in TBG by performing measurements of conductance of an electrostatically doped TBG and switching-on perpendicular magnetic fields. In Fig. 1.4(a), the conductance measured at the magic angle $\theta = 1.08^\circ$ and the temperature $T = 0.3$ K [29] shows that, in addition to the insulating states related to the gaps at the Γ point of the MBZ at the total filling $\pm n_s = \pm 2.7 \times 10^{12}$ cm^{-2} of the electron/hole flat minibands, another pair of insulating states occurs for a narrower density range near the half-filling charge doping $\pm n_s/2$ of the flat minibands. Furthermore, such half-filling insulating states exhibit a strong dependence on the temperature, since the system is a metal above 4 K, becomes an insulator at 4 K, and the conductance drops to zero from 4 K to 0.3 K. Since they were not expected in absence of interactions between the electrons and corresponded to localized electrons on AA-stacked regions, Cao *et al.* proposed a Mott-like insulating phase for explaining them. The first confirmation was obtained by verifying the condition $U/W > 1$, i.e., the quenching of the quantum kinetic energy, for an Hubbard model on a triangular lattice of sites as the AA-stacked localized regions, where U is the effective on-site Coulomb energy and W is the bandwidth of the $E > 0$ flat-miniband branch in TBG for $0.04^\circ < \theta < 2^\circ$. The suppression of the half-filling insulating states under a perpendicular magnetic field provided another proof of the Mott-like insulating phase. Indeed, the gap separating the electron flat minibands from the upper bands is reproduced only within a many-body picture of the DOS, i.e., by including the many-body interactions, and the application

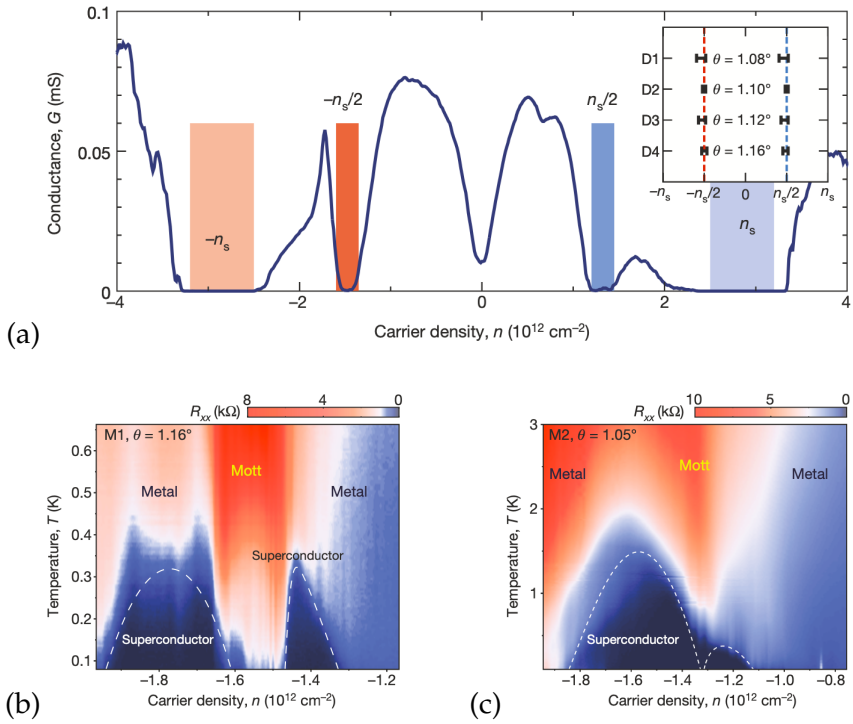

FIGURE 1.4: Mott-like insulating and unconventional superconductivity phases of TBG. (a) Measured conductance at the magic angle $\theta = 1.08°$ and the temperature $T = 0.3$ K. Adapted with permission from Ref. [29]. (b-c) Measured longitudinal resistance R_{xx} as a function of carrier density and temperature for $\theta = 1.16°$ and $\theta = 1.05°$. See text for details. Adapted with permission from Ref. [30].

of $B_\perp$ polarizes the excitations of the spectrum according to their spin, thus allowing charge conduction when the Zeeman energy exceeds the charge gap. As far as the superconductivity is concerned, the longitudinal resistance R_{xx} was measured for $\theta = 1.16°$ and $\theta = 1.05°$ as a function of carrier density and temperature, revealing two pronounced superconducting domes near half-filling of the lower flat minibands, that are similar to cuprates (copper oxides) temperature-carrier-density phase diagrams (see Figs. 1.4(b) and (c)) [30]. The superconducting phase was confirmed by the current-voltage curves, for $\theta = 1.05°$ TBG as an example, that become ohmic for $T \gtrsim 2$ K at $n = -1.44 \times 10^{12}$ cm^{-2}. Moreover, critical field values evidently depended on the doping density with two similar domes on each side of the half-filling state and a good agreement to the Ginzburg-Landau theory. In addition to the superconducting domes, the unconventional character of superconductivity is motivated by the ratio between the critical temperature and the Fermi temperature, since most conventional superconductors have a ratio of about 0.01-0.05, conventional superconductors have a ratio of order 0.001, and TBG exhibits values from 0.04 to 0.08. In other words, the measurements of Cao *et al.* strongly suggested that the magic-angle TBG superconductivity originates from electronic correlations instead of weak electron-phonon coupling.

The most recent works on TBG have been aimed to find a theoretical explanation of the observed phenomenology and to further investigate on the four minibands, whose role has proven to be certainly central. Therefore, many efforts have been made to focus only on the minibands, by finding the suitable set of real space Wannier orbitals and the corresponding centers to perform a TB calculation. Also this task has turned out to be not easy. For instance, the model proposed in Refs. [54]

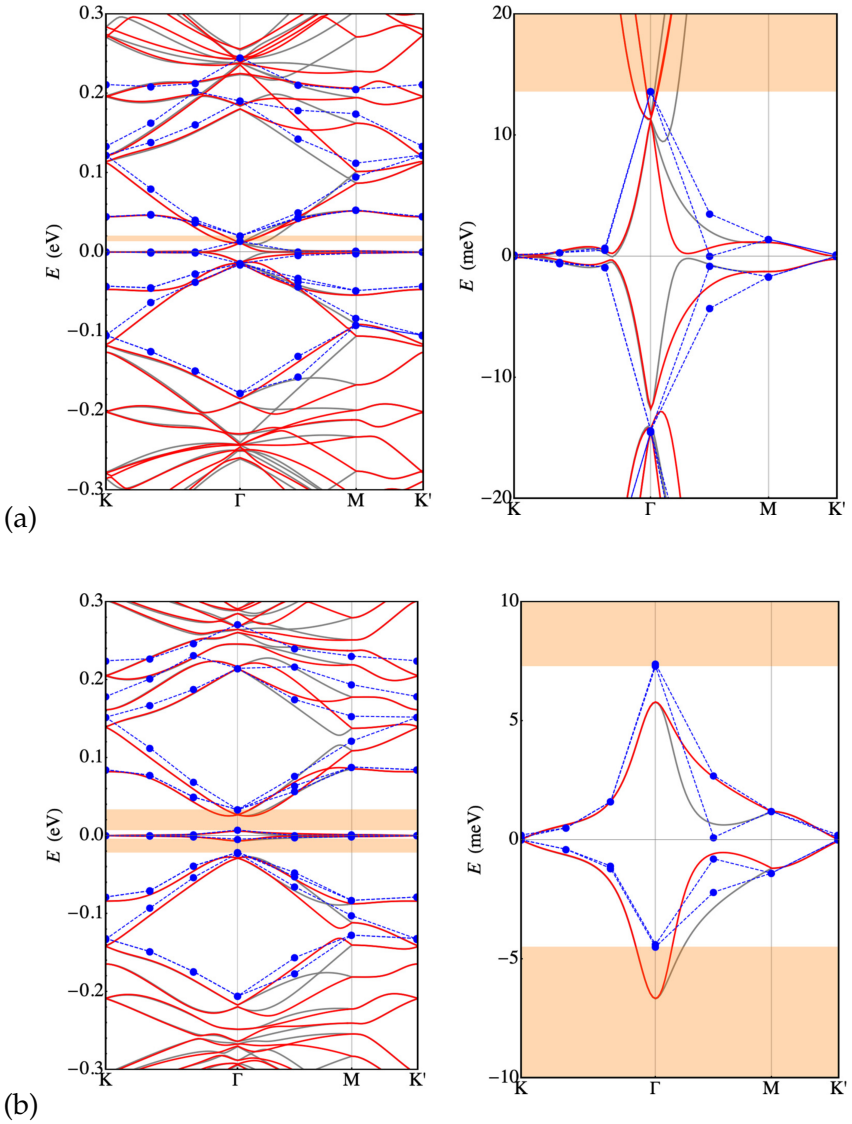

FIGURE 1.5: Comparison between the electronic structures calculated through a fully ab initio DFT calculation and a continuum model for TBG at $\theta = 1.08°$ along the along the K-Γ-M-K' line of the MBZ. (a) Unrelaxed structure. (b) Relaxed structure. The blue dots are the DFT eigenvalues, whereas the solid red and gray curves represent the continuum model bands deriving from the $\xi = 1$ and $\xi = -1$ valleys, respectively. Each right panels shows a zoom around the Fermi energy of its left panel, highlighting the nearly flat minibands. Zero energy corresponds to the Fermi level. The orange shaded regions correspond to the energy ranges of the DFT gaps. Adapted with permission from Ref. [31].

and [55], based on four Wannier orbitals, reproduces perfectly the four flat minibands near CNP, but not the correct symmetry properties. This is a crucial point, since it has been demostrated by Ref. [56] that the correct symmetries are needed in order to find the mechanisms that could explain the correlated physics and the opening of the insulating gaps. Under this guideline, Angeli *et al.* [57] performed an in-depth symmetry analysis of the TBG minibands at $\theta = 1.08°$, finding out an unexpected one-electron complexity. They performed a full, in- and out-of-plane, relaxation of the TBG atomic positions via classical molecular dynamics simulations, selecting a few commensurate structures for $1° < \theta < 1.5°$. The relaxation induced the insulating gaps at the Γ point of the MBZ, as expected from previous studies. Moreover, they established a minimum number of eight Wannier orbitals as necessary but not sufficient condition to describe the minibands, due to the emergent D_6 symmetry (despite the lack of any manifest point-group symmetry in the relaxed lattice), the valley charge conservation $U_v(1)$ symmetry, the C_{3z} invariance of the Bloch functions at the Γ point, and the even (odd) parity of the lower (upper) doublet under C_{2x}. For the first time, Lucignano *et al.* [31] have performed a fully ab initio DFT calculation of the band structure of TBG at $\theta = 1.08°$, by also comparing it to a continuum model generalizing the model proposed in Refs. [46, 47, 55, 58]. The results show a band structure consistent with that measured in Ref. [29], stating a first accurate single-particle description of $\theta = 1.08°$ TBG electronic structure, in order to guide a full many-body calculation taking into account the electronic correlations. Unlike the previous works, the relaxation has been carried out without approximations and the vdW dispersion between the graphene layers has been correctly modelled through one of the most recent and accurate methods. Out-of-plane displacements tend to increase (decrease) the interplane distance in correspondence to the AA (AB) stacking regions, seeming to be in agreement with the emergent D_6 symmetry described in Ref. [57]. The results on the band structure are shown in Fig. 1.5 for both the unrelaxed and the relaxed structure. The blue dots are the DFT eigenvalues obtained through an ab initio calculation, whereas the solid red and gray curves are obtained by diagonalizing the continuum model in the two valleys $\xi = 1$ and $\xi = -1$, respectively, referring to the valleys of the BZs of the MLs. First of all, the unrelaxed calculation does not reproduce the gaps separating the flat minibands from the other ones, that are responsible for the band insulating phases, as shown in Ref. [29]. Furthermore, the flat minibands show a dispersion of ~ 20 meV, that is almost twice the value $\lesssim 10$ meV measured in the experiment. However, the DFT eigenvalues are in good agreement with the continuum model, except for very fine details of the flat minibands. Instead, the relaxation proves indispensable to interpret experimental data, especially in ab initio calculations. Indeed, the flat minibands show a dispersion of ~ 12 meV around the Fermi energy and a gap of 26 meV (16 meV) separates the minibands branch from the highest occupied (lowest unoccupied) bands, according to the thermal activation gap of ~ 40 meV measured in experiments. Finally, this work has shown the major role played by the vdW interaction. Indeed, the DFT charge transfer analysis reveals an electronic charge depletion within each plane and a relevant charge redistribution in the interplane region.

1.1.2 Transition metal dichalcogenides

Transition metal dichalcogenides have MX_2 chemical formula, where M is a transition metal (Mo, W, Nb, etc.) and X is a chalcogen (S, Se, Te, etc.). Their MLs have been among the first intensively investigated 2D materials after graphene. In particular,

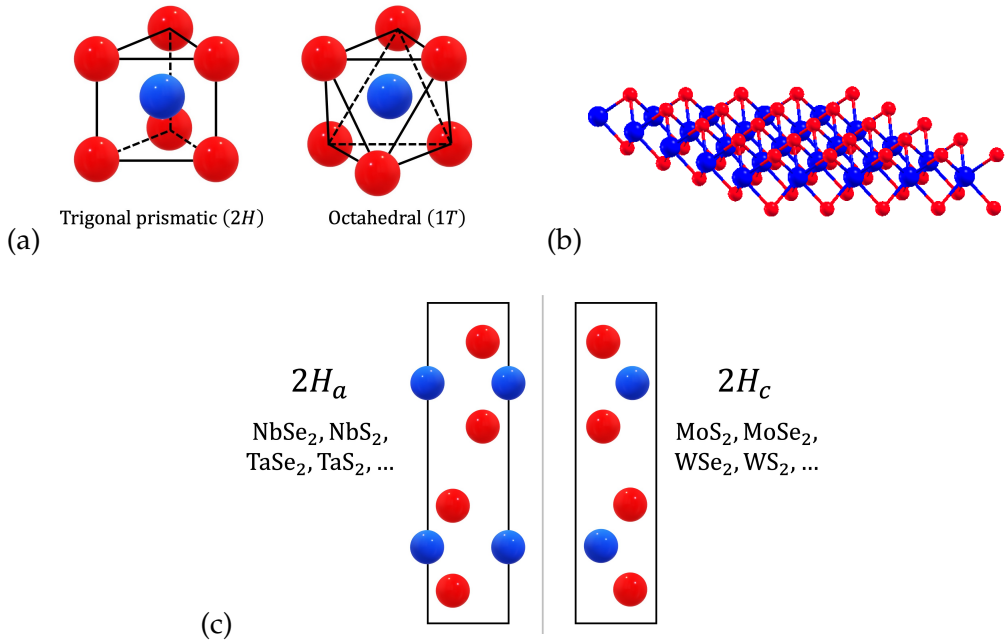

FIGURE 1.6: Transition metal dichalcogenides geometries. (a) Trigonal prismatic or octahedral bonding geometries of the six-fold coordinated metal atoms. (b) Sketch of a 2H single layer. (c) $2H_a$ and $2H_c$ polymorphs (side views), as the most common forms of the 2H polymorph. Blue and red spheres represent metal and chalcogen atoms, respectively.

the most interesting ones are group-VIB (e.g., MoS_2, $MoSe_2$, WSe_2, WS_2) and group-VB (e.g., $NbSe_2$, NbS_2, TaS_2, $TaSe_2$) TMDs[7], that are semiconductors and metals [59], respectively. Metal atoms within a single layer are six-fold coordinated and their bonding geometry can be either trigonal prismatic or octahedral, as shown in Fig. 1.6(a). The two chalcogenide planes forming a slab with a typical thickness of 6-7 Å are stacked directly above each other in the trigonal prismatic arrangement, whereas they stagger in the octahedral arrangement. The preferred phase adopted by TMDs depends predominantly on the *d*-electron count of the transition metals, although a certain dependence on the relative size of the atoms plays a role. Most of group-VB metals have octahedral structures, whereas some have trigonal prismatic structures. The reverse is true for the group-VI metals. In the bulk forms, the trigonal prismatic arrangement of MLs can give two distinct polymorphs, namely 2H and 3R, depending on the MLs stacking order, where the number counts the MLs in the unit cell and the letter indicates the symmetry (H-hexagonal and R-rhombohedral). Instead, the octahedral arrangement can just give the 1T (T-trigonal) polymorph. There exist less common polymorphs or subcategories. For instance, $2H_a$ and $2H_c$ are the two most common forms of the 2H polymorph, showing two layers with hexagonal symmetry (see Fig. 1.6(b)) with the AbA CbC and the CaC AcA stacking configurations, respectively, where different uppercase (lowercase) letters denote different positions of the chalcogen (transition metal) atoms (see Fig. 1.6(c)). The $2H_a$ polymorph is reported to occur in group-VB TMD crystals, even if the latter are also observed in 1T polymorph. Instead, the $2H_c$ polymorph occurs in group-VIB TMD crystals. TMDs exhibit the time-reversal symmetry $\mathcal{T}$ for an arbitrary number of layers and the inversion symmetry $\mathcal{I}$ for an even number of layers, where the inversion center lies between the layers of bulk form unit cell.

[7]The group name refers to the transition metal group.

a) Group-VIB 2D TMDs

The first effects of the group-VIB TMDs thickness reduction to the single-layer limit concern the electronic band gap and have been predicted by DFT calculations [60, 61]. In particular, the band gap increases by $\sim$ 1 eV up to $\sim$ 1.5-2 eV (visible range) and changes from indirect to direct, with a consequent influence on the measured photoluminescence (PL) spectra, in terms of blue-shifting and intensity increase of the PL peaks [62, 63]. Furthermore, the inversion symmetry breaking induces non-linear optical phenomena, such as second-harmonic generation, and an important selection rule about the optical interband transitions, referred to as a *valley polarization* [64–66]: the interband transitions are coupled exclusively with left-handed (right-handed) or counter-clockwise (clockwise) circularly polarized optical fields at the K (K') valley, that is the **k**-point of the hexagonal Brillouin Zone (BZ) where the direct band gap edges are located. Therefore, K and K' valleys of group-VIB TMDs MLs provide a pseudospin DOF for electrons and holes, making possible conceptual electronic applications known as *valleytronics*. The lacking of the inversion symmetry along with the presence of time-reversal symmetry endows Bloch electrons non-zero Berry curvature and orbital magnetic moment, assuming opposite values at K and K' points, so that valley-contrasting phenomena manifest themselves. The strong spin-orbit coupling (SOC) induced by the heavy transition metal atoms removes the spin-degeneracy, making the spin as a further DOF, enabling *spintronics* applications. The properties described so far are shown in Fig. 1.7. Starting from the first report of valley manipulation by optical pumping [67], several results on spin- and valley-tronics have been obtained on group-VIB TMD MLs, such as different methods for tuning the valley polarization [68–71], realization and control of the valley Hall effect (VHE) [72, 73], spin Hall effect (SHE) [74], and quantum spin Hall effect (QSHE) [75].

Group-VIB TMDs also revealed as optimal platforms to investigate 2D exciton[8] physics. Indeed, their BLs exhibit a large degree of valley polarization related to the non-negligible contribution of the excitons, despite the inversion symmetry. In general, the degree of valley polarization is inversely proportional to the exciton lifetimes and directly proportional to the intervalley scattering time (valley lifetime). The exciton binding energies of $\sim$-0.5 eV in these materials [76] are much larger than the values of the previously explored bulk materials (0.010 eV for Si and 0.0027 eV for Ge [77]). This is a peculiarity of 2D materials because the dielectric screening is obviously reduced and remarkably enhances the Coulomb interaction between electrons and holes, giving excitons and other many-particle excitations (e.g., trions and biexcitons) with larger binding energies. In 2017, Hall effect of excitons for MLs was reported for the first time by Onga *et al.* [78]. Moreover, at present, nonlinear excitonic spin Hall effect is demostrated [79] and the experimentally measured excitons show short lifetimes up to the order of magnitude of a nanosecond, giving a first important motivation for a non-negligible degree of valley polarization. As far as the valley lifetime contribution is concerned, this can be tuned by exploiting, for instance, electron-phonon interactions and charge-transfer processes [80, 81].

Following the intense efforts to explain the TBG physics, the research focus extended to the interplay between twist angle and electronic properties in gapped 2D

[8] As well known, an exciton is a neutral two-particle excitation of a semiconductor consisting of an electron-hole bound state arising from the poorly-screened long-range Coulomb force, strong enough to attract an electron to a hole and form a bound state with a binding energy E_b lying below the electronic band gap. The difference between the electronic band gap and the exciton binding energy E_b is the optical band gap, that is, de facto, the energy required to create an exciton starting from the semiconductor ground state.

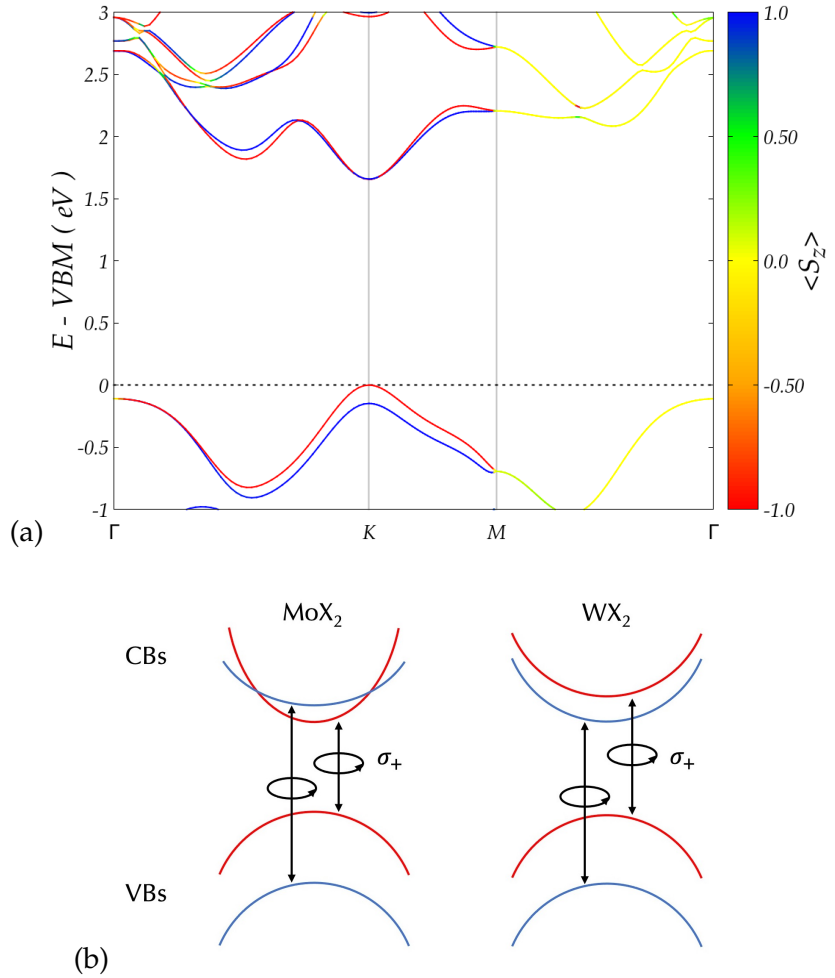

FIGURE 1.7: Spin- and valley-tronics of group-VIB TMD MLs. (a) Band structure of ML MoS_2, calculated with the PBE exchange-correlation functional within the DFT (see Chap. 2 for technical details). The averaged z-component of the spin is indicated by the color code on the band structure. Zero energy (highlighted by the dashed black line) corresponds to the valence band maximum (VBM) energy. (b) Schematic drawing of valley polarization at the K valley for MLs of MoX_2 and WX_2. Valence bands (VBs) and conduction bands (CBs) are coupled by left-handed circularly polarized optical fields for both spin-up (blue) and spin-down (red) bands. K' valleys may be visualized simply by time-reversal of the K valley scheme.

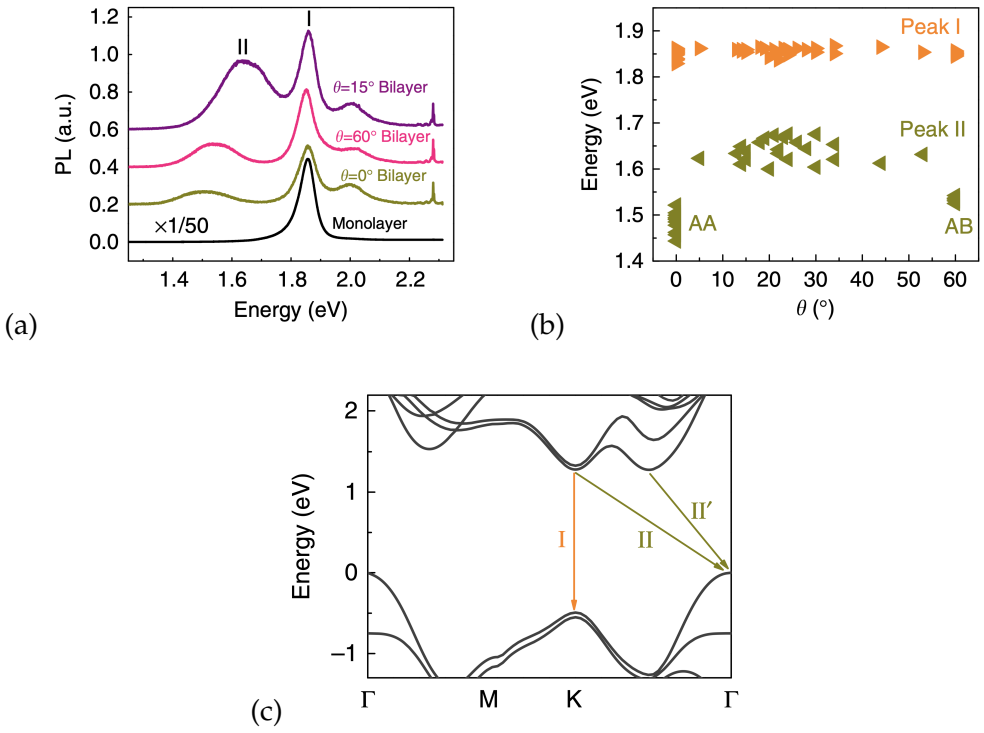

FIGURE 1.8: Effect of twisting on the PL spectra of AA-stacked BL MoS_2. (a) Comparison between PL spectra of ML, AA-stacked BL, and twisted BL MoS_2, for $\theta = 15°, 60°$. (b) Evolution of the PL peak energies as a function of the twist angle for 44 BLs with different twist angles. (c) DFT band structure of the untwisted AA-stacked BL MoS_2. The almost degenerate indirect bandgap transitions II and II′ may be related to the peak II in the PL spectra. Spin-orbit coupling is not included in calculations. Adapted with permission from Ref. [32].

materials, due to the wide range of technological applications of the latter. This allowed to perform a more clear and systematic analysis of the interlayer coupling depending on how twist angle acted on band gaps. Group-VIB TMD vdWHos and vdWHes were chosen as starting model systems, for which the exciton physics revealed to play a key role. In particular, BL MoS_2 had already shown significant effects of interlayer coupling on PL measurements in 2013 [82], since an external gate voltage could continuously tune circularly polarized PL from -15% to 15%. Therefore, in 2014, PL spectra of twisted BL MoS_2 samples were measured and compared to those ones of ML and AA-stacked BL MoS_2 by Liu *et al.* [32], for $\theta = 15°, 60°$, where the latter corresponds to the AB stacking. The twist angle induced a blueshift and a significant increase of the intensity of the secondary PL peak or peak II of BL MoS_2, that added to the primary peak or peak I related to the direct band gap transition (see Fig. 1.8(a)), i.e., the direct exciton transition at the *K*-valley. In particular, a systematic analysis performed on 44 BLs with different twist angles revealed that blueshift and intensity increase reached their maximum values far from 0° and 60° with almost constant values, as shown in Fig. 1.8(b). Based on DFT calculations at 0°, 60° and four intermediate commensurate angles (13.17°, 21.78°, 38.2°, 46.8°), peak II was related to the Γ-*K* indirect gap (indirect exciton Γ-*K* transition), due to the appreciable enhancement of the latter for the commensurate angles, thus providing a measurement of the reduced effective interlayer electronic coupling strength. Since the evolution of the indirect band gap as a function of the interlayer distance (defined by the averaged Mo-Mo distance) agrees with the values depending on the twist angles, the main role of the interlayer coupling is unveiled: the twisting induces an highly mismatched atomic alignment between the layers, followed by steric effects and, thus, variations of the interlayer distances. For twist angles far from 0° and 60°, the interlayer distance enhancement due to the interlayer coupling as steric effect increases the indirect band gap size. The inverse proportionality relating the interlayer distance and the Γ-*K* indirect band gap size was more precisely and deeply investigated in Ref. [33], where the interlayer coupling is entirely attributed to the inner S atoms of the two faced layers. Indeed, both p_z orbitals of S atoms and d_{z^2} orbitals of Mo atoms contribute to the VBM at Γ of BL MoS_2 (see Fig. 1.8(c)), whereas CBM only depends on the latter. Due to the antibonding nature of the S atoms p_z orbitals, the interlayer distance enhancement induced by the twisting lowers the VBM. Instead, CBM is relatively insensitive to such structural changes and, as a consequence, indirect band gap variations essentially follow VBM ones. Such an in-depth comprehension of the electronic properties supported by PL measurements to investigate exciton physics allowed to understand that vdWHes with one layer including tungsten as transition metal can be used as platform to study the recently unveiled many-body phenomenon known as *interlayer exciton*. Indeed, such vdW system shows a type-II band alignment, where VBM and CBM are located in different layers [83]. The interlayer excitons are the bound states of the such different layer electron and hole pairs, and have been observed in heterobilayers (HeBLs) of $MoSe_2/WSe_2$ [83], MoS_2/WS_2 [84], and MoS_2/WSe_2 [85]. In 2017, the effect of the twist angle on the interlayer excitons has been studied for the first time by Nayak *et al.* [86], and HeBL $MoSe_2/WSe_2$ has been chosen as model system (see Fig. 1.9). In the HeBL, an extra excitonic peak appears 200 meV below the two direct excitonic peaks of the $MoSe_2$ and WSe_2 layers, indicating the interlayer exciton. As a result of the twisting, all the peaks show an intensity decrease due to the interlayer coupling and, in particular, the interlayer excitonic peak intensity is significantly weakened. This is easily explained through the enhancement of the interlayer distance, that can be equivalently read as the interlayer coupling decrease. Hence,

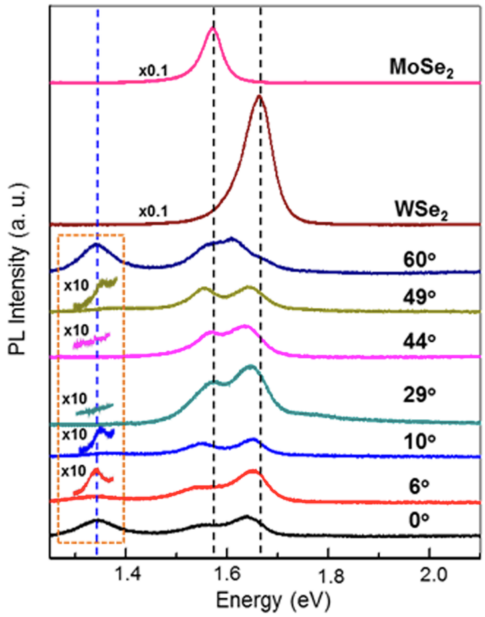

FIGURE 1.9: Twist-angle dependent room-temperature PL spectra of HeBL $MoSe_2/WSe_2$. Vertical black dashed lines indicate the direct excitonic peaks of the $MoSe_2$ and WSe_2, whereas the vertical blue dashed line indicates the interlayer excitonic peak. For twist angles different from 0° and 60°, high-magnification insets are required to visualize the latter. Adapted with permission from Ref. [86].

according to the previous findings, the twist-angle-induced interlayer coupling reduction quenches the PL of the interlayer excitons. Finally, the investigation on the effect of the twist angle on different group-VIB TMD vdWHes has gradually deepened. As an example, the work by Lu *et al.* [35] reports a DFT analysis of the band structure evolution with the twist angle for HeBLs of $CrSe_2/MoS_2$, $MoSe_2/MoS_2$, WSe_2/MoS_2, WS_2/MoS_2 and CrS_2/MoS_2, with $\theta = 0°, 13.17°, 21.78°, 27.8°, 32.20°, 38.2°, 46.8°, 60°$. Interlayer distance increases between 0° and 60° in all cases. The first two systems exhibit an indirect to direct band gap transition upon the twisting. As far as the inclusion of the SOC is concerned, the heavier the transition metal involved, the larger the variations on the band gaps. For instance, the direct band gap reduces by 70 meV for $CrSe_2/MoS_2$, by 130 meV for $MoSe_2/MoS_2$, and by 260 meV for WSe_2/MoS_2. In general, the SOC affects direct band gap more than the indirect one, due to the large SO splitting of VBM at the *K* point.

b) Group-VB 2D TMDs

Group-VB TMDs, such as NbX_2 and TaX_2 (X = Se, S), are metals known for their competiting charge-density wave (CDW)[9] and superconducting phases. For instance, theory or experiments predicted or demonstrated that $2H_a$-$NbSe_2$ undergoes a CDW transition at 33 K to an incommensurate structure very similar to a $3 \times 3 \times 1$ ordering [87, 88] before becoming a type-II superconductor at 7.2 K [89, 90], but the CDW phase shows an inexplicable instability and competes with superconductivity [91–98], leading to a phase diagram similar to the high-temperature superconductors [99, 100]. Inelastic X-ray experiments reveal that the CDW transition is second order [96]. However, the mechanism behind the CDW-superconductivity competition

[9] A charge-density wave is defined as a structural distortion of the crystal lattice inducing a modulation of the electronic density.

remains still mysterious [101–104]. Similar phenomena involve 1T-TaS_2, that, under pressure, melts a Mott phase into a CDW phase, within which superconductivity develops and survives to very high pressures, also when the CDW phase disappears [105]. As $2H_a$-$NbSe_2$, 1T-TaS_2 shows a typical type-II superconducting behavior [106]. Models and experimental results on CDW phase of 1T-TaS_2 and $2H_a$-$TaSe_2$ have been compared [107], but they still require an acceptable agreement. The tunability of group-VB TMDs phase diagrams has been extensively explored, by acting on pressure [105, 108, 109] and gate voltage [110]. For instance, the thickness of $2H_a$-$NbSe_2$ decreases, the superconducting transition temperature decreases and reaches a value of to $\sim$ 3.1 K in ML $NbSe_2$ [111]. CDW phase coexists along with the superconducting phase down to the ML limit, with the CDW transition temperature increasing from 33 K to 145 K. Furthermore, low-temperature scanning tunnelling microscopy/spectroscopy (STM/STS), angle-resolved photoemission spectroscopy (ARPES), and electrical transport measurements demonstrate that $3 \times 3 \times 1$ ordering of CDW is preserved in the ML limit [112]. In 2016, Xi *et al.* demonstrated the Ising pairing for ML $NbSe_2$, that is, Cooper pairs of the superconducting phase are K and K' electrons with spin locked to the two opposite out-of-plane directions[10] [116]. This feature makes ML $NbSe_2$ as the ideal platform for experiments in which superconductivity is required to survive at high in-plane magnetic fields. Fig. 1.10 reports the coexistent CDW and Ising superconducting phases of ML $NbSe_2$. More recent works on the competition between CDW and superconducting phases in the ML limit show that the CDW order enhancement derives from the rising energy gain and strengthened Fermi surface gapping, while the superconductivity weakening is motivated by the increasingly reduced Fermi energy density of states in the CDW state [117]. CDW phases have been also observed for ML NbS_2, unlike the bulk form, although this result seems substrate dependent [118, 119]. As far as TaX_2 (X = Se, S) systems are concerned, CDW phase disappears going from bulk to ML for TaS_2 [120], whereas it remains unchanged in the isolectronic and isostructural $TaSe_2$ [121]. It is important to mention that superconductivity has been also observed in some group-VIB TMD MLs, such as MoS_2 and WS_2. For the latter, the superconductivity is electrostatic field-induced at low carrier densities [122]. Instead, ML MoS_2 showed a field-induced superconductivity not following the Bardeen-Cooper-Schrieffer (BCS) theory [123, 124] and a proximity-induced *s*-wave BCS superconductivity on a Pb substrate [125].

1.1.3 Two-dimensional magnetism of transition metal halides

The realization of magnetism in two dimensions has long been sought because of the promising theoretical models and predictions of potentially innovative and breakthrough applications in the spintronics field. Indeed, different Hamiltonian models, such as the classical XY and Ising model or the quantum Heisenberg model, can be defined on a two-dimensional lattice of magnetic moments [126–131]. Moreover, from an experimental and technological perspective, magnetism is the most intuitive

[10] Ising and Cooper pairing differ for the superconductivity persistence and suppression, respectively, under sufficiently high values of in-plane magnetic fields. Indeed, for Cooper pairing, the superconductivity is destroyed by Pauli paramagnetism with the upper critical field $H_{c2}^{\parallel}$ given by the Pauli paramagnetic limit $H_p = (1.86\text{TK}^{-1})T_{c0}$ at $T = 0$ K [113, 114], where T_{c0} is the superconducting transition temperature. Instead, since the Dresselhaus SOC pins the electron spins to the out-of-plane direction in the Ising pairing, the pair-breaking effect of the in-plane field is reduced and superconductivity survives due to strongly enhanced in-plane critical field [64, 115]

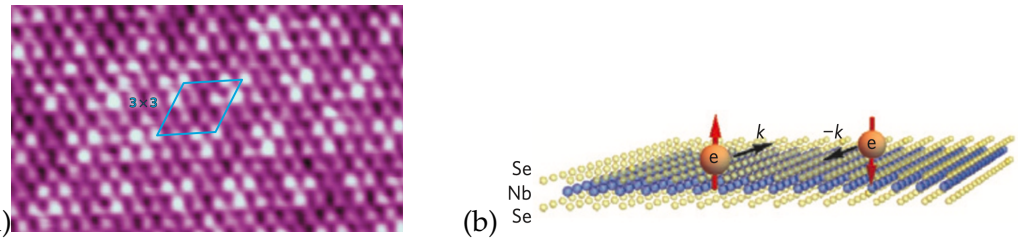

FIGURE 1.10: Coexistent CDW and Ising superconducting phases of ML $NbSe_2$. (a) Atomically resolved STM images at $T = 5$ K showing the 3×3 ordered CDW. Adapted with permission from Ref. [112]. (b) Schematics of Ising superconductivity. Adapted with permission from Ref. [116].

and direct way to manipulate the electron spin, as predicted by theory, thus adding to the countless DOFs of 2D materials.

Until 2017, most of the available pristine 2D materials were intrinsically non-magnetic (NM). Strain [132–134], doping [135–137], and defect engineering [138–140] were used to induce magnetism in those materials, but these techniques were still not easily controlled in experiments or, in the last two cases, strongly deteriorated the transport properties because of their tendency to form scattering centers. Measurements of magneto-optical Kerr effect (MOKE)[11] microscopy as a function of an applied magnetic field by Huang *et al.* produced the first evidence of intrinsic 2D magnetic ordering in ML CrI_3 [13]. Although magnetism has also been observed in other 2D materials, such as $Cr_2Ge_2Te_6$ [141], CrX_3 (X = Cl, Br, I) compounds have certainly shown the most intriguing properties and applications in the 2D magnetism landscape, as will be explained. For this reason, we will only focus on 2D CrX_3 and Nb_3I_8, where the latter is the TMH belonging to the materials investigated in this thesis work.

Bulk CrI_3 was known to be an insulator exhibiting ferromagnetism below the Curie temperature T_C of $\sim$ 61 K with an out-of-plane easy-axis orienting its spontaneous magnetization. However, the occurrence of magnetism in a 3D structure is not sufficient to ensure the magnetic ordering up to the ML limit, due to the *Mermin-Wagner-Hohenberg* (MWH) *theorem* [131, 142]. The latter, that is a rare example of an exact result in many-body physics, states that in an infinitely extended system having one and two spatial dimensions ($d \leq 2$), the continuous $O(3)$ symmetry of the (isotropic) Heisenberg model for three spin dimensions ($d_S = 3$) cannot be spontaneously broken at finite temperatures, i.e., the (isotropic) Heisenberg model for $d_S = 3$ does not admit any spontaneous magnetization at finite temperatures[12]. The same result holds for $d_S = 2$, that is the XY model with the $O(2)$ continuous symmetry. Instead, for $d_S = 1$, that is the Ising model, Onsager demonstrated that a spontaneous magnetization is possible for $d = 2$ [128], as the result of the spontaneous (discrete) $\mathbb{Z}_2$ symmetry breaking. Therefore, based upon the MWH theorem and the Onsager's result, it follows that the 2D magnetic ordering could be described only through the Ising model or anisotropic terms in the Heiseberg model, favoring a particular easy-axis direction and satisfying the constraint to recover the Ising model in the limit of an infinite anisotropy.

Hence, in general, searching for a long-range ferromagnetic (FM) ordering in a ML system means to measure the so-called *magnetocrystalline anisotropy*, which could

[11] The magneto-optic Kerr effect is the rotation of the light plane of polarization registered if the light is reflected by a material with a nonzero magnetization.

[12] In these cases the magnetization fluctuations would be strong enough to destroy the spontaneous $O(3)$ symmetry breaking.

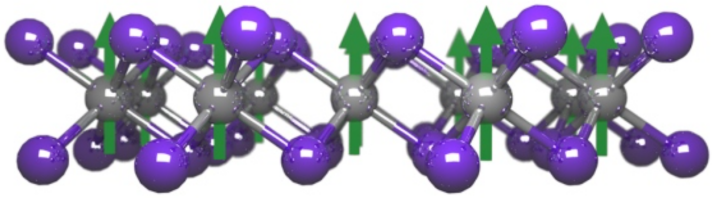

FIGURE 1.11: Ising ferromagnetism of ML CrI_3. Gray and purple spheres represent chromium and iodine atoms, respectively. Green arrows in the direction perpendicular to the plane of ML CrI_3 are the magnetic moments of chromium atoms, providing the Ising ferromagnetism. Adapted with permission from Ref. [144].

possibly lift the MWH restriction. In Ref. [13], Huang *et al.* detected the small Kerr rotations of reflected linearly polarized light from a ML CrI_3 sample under a perpendicular magnetic field, thus revealing an out-of-plane magnetization inherited from the bulk form, i.e., Ising ferromagnetism in a 2D system, as sketched in Fig. 1.11. Similar analysis extended to BL and trilayer (TL) CrI_3 revealed a layer-dependent magnetic ordering, since the BL is an out-of-plane antiferromagnet and the TL is an out-of-plane ferromagnet as ML and bulk. The measurements of T_C gave ~ 45 K for ML and ~ 61 K for TL, according to the bulk estimation, implying that the interlayer coupling has not a crucial role for the FM ordering persistence down to the ML limit. As far as the origin of the magnetic anisotropy is concerned, the DFT calculations by Lado and Fernández-Rossier unveiled the crucial role of the SOC effects [143], as the result of the interaction between the mean exchange spins field and the magnetic ions orbital angular momenta. Moreover, they found that the XXZ model[13] is the effective spin Hamiltonian suitably describing ML CrI_3 and the magnetic anisotropy induces a gap in the spectrum of spin-wave excitations.

The combination between ferromagnetism and insulating behavior holding for ML CrI_3 opened a new pathway to realize spintronic applications based on use of both charge and spin DOFs in electronic devices. This is one of the reasons why great efforts have been made to combine such a system to well-known but non-intrinsically magnetic 2D materials. As an example, the deposition of WSe_2 on CrI_3 to form the HeBL WSe_2/CrI_3 has proved to be a robust way to manipulate the valley pseudospin of the first [145], due to the tuning of the valley Zeeman splitting, induced by the magnetic exchange field[14], through the power of ultrafast laser pulses over a range of 20 T. Furthermore, to date, there exist several works, both theoretical and experimental, that highlight the tuning of few-layer CrI_3 magnetic properties by acting on the several 2D platforms DOFs. For instance, changing the direction of magnetic moments in ML significantly affects the band structure, inducing direct-to-indirect band gap transitions and modifications of the topological states [146]. Also, biaxial strain engineering and charge doping change the magnetic Hamiltonian regime, making antiferromagnetic (AFM) phases or in-plane magnetization phases as accessible on demand [147], due to the consequent variations of the magnetic anisotropy [148]. As far as BL and TL CrI_3 are concerned, the out-of-plane pressure and the electrostatic doping turned out to be efficient control knobs on the magnetic ground state. Electrostatic doping applied to BL CrI_3 significantly affects the interlayer exchange coupling, providing a phase transition (PT) from the layered AFM state of two FM layers with opposite spin directions to an FM state [137, 149].

[13] The XXZ model is the Heisenberg model having equal x- and y- direction magnetic couplings.

[14] The intrinsic 2D magnet induces a magnetic exchange field in the non-intrinsically magnetic 2D material through the magnetic proximity effect.

An out-of-plane pressure of 2.70 GPa on BL CrI_3 destroys the AFM state to favor an FM ordering [150, 151], whereas an out-of-plane pressure of 2.45 GPa on TL CrI_3 can create coexisting domains of three phases, one FM and two AFM, or can induce an FM ordering [151].

$CrBr_3$ is a more recent example of TMH ferromagnet in ML form. MOKE and magneto-photoluminescence measurements revealed a spontaneous magnetization below $T_C \sim 34$ K with an out-of-plane easy-axis [152]. Distinct from BL CrI_3, exhibiting AFM interlayer coupling in the ground state, BL $CrBr_3$ preserves ferromagnetism. 2D $CrCl_3$ has been recently fabricated [153–155], showing in-plane magnetic anisotropy. As a consequence, the XY model is the effective spin Hamiltonian simulating ML $CrCl_3$ that, as such, must exhibit a Berezinskii-Kosterlitz-Thouless (BKT) [130] PT separating a quasi-ordered[15] low-temperature state of bound vortex/anti-vortex pairs from a disordered high-temperature state of unbound vortex/anti-vortex pairs, both having a zero net magnetization due to the MWH theorem. The XY physics of ML $CrCl_3$ has been discussed in a recent experiment [156].

Despite CrX_3 compounds exhibit the most remarkable and intriguing properties as 2D magnetic systems, the research on the latter has been also based on needs related to specific applications. For instance, FM and biocompatible 2D materials are the ideal candidate platforms for biomedical applications, such as magnetic labeling and near infrared (IR) light induced hyperthermia treatment of tumors [158]. Unfortunately, Cr^{3+} ions constituting CrX_3 compounds are highly toxic and could cause permanent neurological damage [159], thus being not definitely recommended for such purposes. Instead, Nb ions of niobium halides Nb_3X_8 (X = Cl, Br, I) are non-toxic and biocompatible, besides to offer a large atomic magnetic moment due to the $4d^45s^1$ electronic configuration. These reasons encouraged Jiang *et al.* in 2017 [157] to perform the first DFT calculations on the structural, electronic, magnetic, and optical properties of a novel candidate as 2D magnet, that is ML Nb_3X_8, whose structure is reported in Fig. 1.12(a). While bulk Nb_3X_8 were first synthesized in 1993 [160], the 2D structures had not yet been exfoliated at the time. Therefore, Jiang et al firstly estimated the cleavage energies from bulk to MLs, obtaining values comparable to or smaller than that of graphite (0.37 J m^{-2} [161]), that give indication of an easy cleavage to the ML form. The analysis of the electronic and magnetic properties revealed the insulating and FM behavior of the ML Nb_3X_8, exactly as CrI_3, with an electronic band gap between 0 and $\sim$ 1 eV. In particular, the FM state was identified as the ground state among three additional AFM configurations. Moreover, the mean field approximation was used to estimate the Curie temperatures, obtaining the values of 31, 56, and 87 K. The calculated absorption coefficient for an incident light having the polarization vector parallel to the layers plane promoted, in particular, ML Nb_3I_8. Indeed, although all the three MLs showed a non-negligible absorption over the entire sunlight spectrum with isolated peaks in the IR, visible, and UV regions, the highest peaks were produced by ML Nb_3I_8, as shown in Fig. 1.12(b). Hence, Ref. [157] showed that 2D Nb_3X_8 TMHs are optimal candidates for both 2D spintronics and biomedical applications. The interest raised on Nb_3I_8 favored its synthesis and characterization as ML and multilayer (MuL) flakes [14]. In addition to confirm the layered structure of the bulk form, atomic force microscopy

[15]The quasi-ordering implies the power-law decay of spin correlations as a function of distance separating the magnetic moments, despite the net magnetization is zero. Thus, whereas in the full thermodynamic limit the long-range ordering is lost, the decay of the correlation is slow enough that the smaller the finite size of the system, more possible is some magnetic ordering. Furthermore, the first signature of BKT transition is a divergent magnetic susceptibility below T_{BKT}.

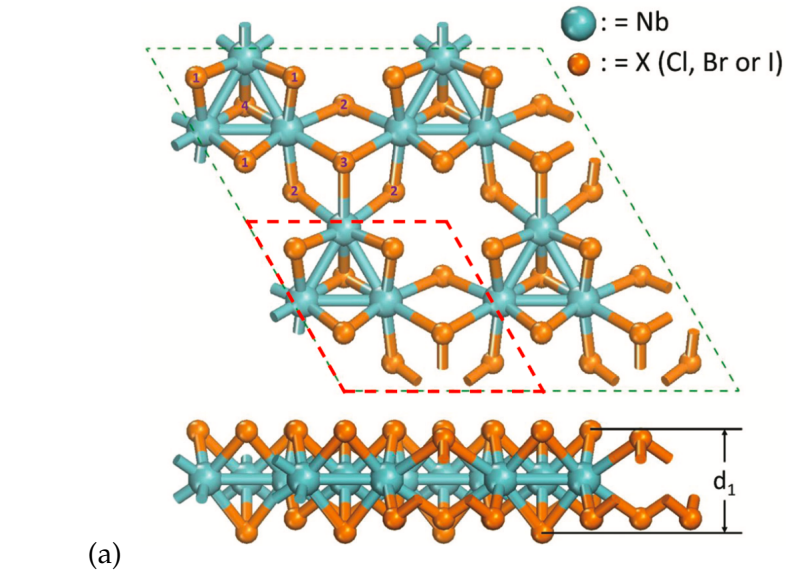

(a)

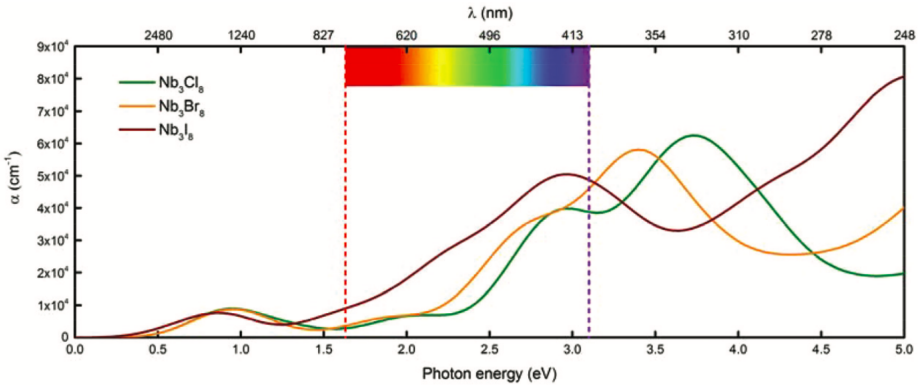

(b)

FIGURE 1.12: Properties of ML Nb_3X_8. (a) Top and side views of the optimized geometric structures. The top X atoms sheet and bottom X atoms sheets are not equivalent. On the top X atoms sheet, the X(1) and X(3) atoms are contained. The bottom X atoms sheet contain the X(2) and X(4) atoms. The thickness d_1 is 3.446 for X = Cl, 3.728 for X = Br, and 4.052 for X = I. The unit cell is limited by the red dashed line. (b) Optical absorption coefficient α (cm^{-1}). Adapted with permission from Ref. [157].

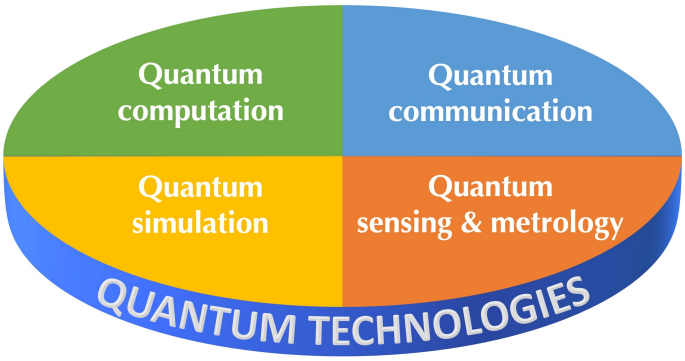

FIGURE 1.13: The four categories constituting the quantum technologies field, according to the final report of the 2017 High-Level Steering Committee on the European QT flagship initiative [167].

and scanning Kelvin probe microscopy (SKPM) measured a monotonically decreasing work function with decreasing thickness, from $\sim$ 5 eV for 20 nm thickness to $\sim$ 4.71 eV for 1 nm thickness, stating Nb_3I_8 as a tunable-performance metal electrode for the realization of future optoelectronic devices. The most recent experimental work provides the electrical and optical characterization of exfoliated ML and few-layer Nb_3I_8, rather than the flakes [15]. The choice of the latter among the Nb_3X_8 compounds relies on the solid state at room temperature and non-toxicity of iodine compared to Cl and Br. The increasing current flowing at the same applied voltage with increasing temperatures demonstrated the semiconducting behavior of bulk Nb_3I_8. The IR-visible light absorption analysis on the latter exhibited a distinct increase in absorption around 1200 nm, providing an electronic band gap value of $\sim$ 1 eV. Moreover, the synthesized Nb_3I_8 as a 2D material revealed to be a semiconductor with narrow band gap.

1.2 What is meant by quantum technologies?

In the last two decades, the quantum theory laws have been heavily used through novel technologies, the so-called *quantum technologies* (QTs) [162], to access the most counterintuitive and mysterious quantum properties of the physical world, such as the entanglement, and exploit them in order to achieve unprecedented performance levels compared to the classical devices. Such an approach has defined the *second quantum revolution* or *quantum 2.0*, overcoming the previous first quantum revolution or quantum 1.0, that simply underpinned the Information Age with new devices based on quantum laws (e.g., laser, transistor and other semiconductor devices), exactly as the classical theory laws underpinned the Industrial Revolution. These reasons motivated both governative research programmes, such as the European QT flagship initiative, the Chinese or US programs [163], and multinational companies, such as IBM [164] and Google [165, 166], to invest several billion Euros to boost the research and the technological advance. According to the final report of the 2017 High-Level Steering Committee on the European QT flagship initiative [167], Fig. 1.13 reports the four categories constituting the research field of QTs: quantum computation, quantum communication, quantum sensing and metrology, and quantum simulation.

Quantum computation is the computation based on the quantum theory laws and is performed by quantum computers. The idea of quantum computing was first

proposed by Manin [168] and Benioff [169] in 1980, with an explicit Schrödinger equation description of Turing machines, and then by Feynman in 1982 [170], with a basic model of a quantum computer, observing that a classical computer could not efficiently simulate the evolution of a quantum system. As a consequence, rather than to be a faster, bigger or smaller version of an ordinary computer, a quantum computer is a different kind of computer, able to control and use the quantum coherence for different applications. In a classical computer, the information is stored and processed in binary bits, admitting two classical states 0 and 1. Instead, the elementary brick of the quantum computation is the qubit, that is the normalized-to-1 quantum superposition of the two basis elements $|0\rangle$ and $|1\rangle$ of a two-dimensional Hilbert space, thus admitting infinite states in the latter. Also, similarly to the classical gates reading and processing the bits for the classical computation, the quantum computation works through quantum gates. The longer the quantum coherence of the qubits is preserved during the quantum gates operations, the more the performances of the computation results are benefited by the quantum theory laws. In other words, the most critical and universal aspect of quantum computers is the "closed box" requirement, that is the isolation from any kind of decoherence sources. In general, DiVincenzo established the necessary requirements for any experimental implementation of a quantum computer [171]:

1. physical scalability with well-characterized qubits;
2. ability to initialize the qubits states to a simple fiducial state;
3. long relevant decoherence times;
4. a "universal" set of quantum gates;
5. a qubit-specific measurement capability.

Nowadays, qubits and quantum computers count a wide range of physical implementations, coming from the fields of quantum optics (e.g., cavity QED, circuit QED, Linear optical quantum computing), ultracold atoms (e.g., optical lattice, trapped ions), spin control (e.g., nitrogen-vacancy center, nuclear magnetic resonance), and superconducting circuits (e.g., charge qubit, flux qubit, phase qubit, transmon), having different performances depending on the uses and purposes. At the end of 2020, the Chinese team composed by Zhong *et al.* declared the achievement of the quantum supremacy[16] by means of the Jiuzhang photonic quantum computer, since such a photonic peak 76-qubit system (43 average) performed calculations at $\sim 10^{14}$ times the speed of classical supercomputers [172].

Quantum communication bases on the generation and use of quantum states and resources to transmit information in an ultra-secure way by exploiting the quantum laws, at least in theory. Since the information is essentially encoded in qubits, two additional DiVincenzo's criteria indicate the necessary requirements to implement the quantum communication:

1. ability to interconvert stationary and mobile (or flying) qubits;
2. ability to faithfully transmit mobile (or flying) qubits between specified locations.

[16]The quantum supremacy is the demonstration that a programmable quantum device can solve a problem that no classical computer can solve in any feasible amount of time.

Hence, quantum cryptography methods, such as the quantum key distribution (QKD) protocols (e.g., BB84, E91), govern the quantum communication protocols, that are employed to securely transmit highly sensitive data with the purpose to realize a secure quantum network, similar to the current internet.

Quantum sensing and metrology deal with the measurement of physical parameters of a system by using a quantum probe interacting with the latter in a non-destructive way. In particular, depending on how the prepared state of the probe has changed, a properly designed measurement is able to catch a certain number of properties or parameters of the system under examination. Obviously, a quantum probe paves the way for a higher precision regime compared to the classical one, due to the wider choice of phenomena displayed by the quantum theory, such as entanglement and squeezing. As an example, the squeezed light has a central role in the Advanced LIGO (Laser Interferometer Gravitational-Wave Observatory) project [173], since the injection of 3 dB of squeezed light significantly increased the detection rate of gravitational wave candidates [174, 175]. However, the higher precision regimes achievable by quantum sensors instead of classical sensors are intrinsically justified by the classical-quantum crossover, since the best classical sensors exhibit a precision scaling proportionally to the square root of the number of particles N in the probe (known as the *standard quantum limit*, SQL), whereas the best quantum sensors can, in principle, attain a precision scaling as N (known as the *Heisenberg limit*) [176, 177].

The concept of quantum simulation has been formulated by Feynman in 1982 [170], in order to conceptually turn the problem of the quantum systems simulation upside down. In general, the classical simulation of a quantum system requires exponentially large resources because of the exponential scaling of the system Hilbert space with the size. Feynman suggested that interacting quantum systems could be efficiently simulated employing other precisely controllable quantum systems, showing that his hypothetical universal quantum computer would be able to simulate needed quantum effects, unlike a classical Turing machine. A working definition of a quantum simulator can be given as follows: it is an easily realizable experimental quantum system or an easily implementable quantum model allowing to simulate an unexplained quantum phenomenon or unsolvable quantum model in a controlled way. The latter comprises the initial state preparation, a high level of coherence over large time scales, a good access to measurements, in addition to different precise control knobs for tuning the system phenomenology basing upon a detailed miscroscopic knowledge. To date, different experimental platforms work as quantum simulators, including optical lattices, trapped ions, photonic systems, Rydberg atom arrays, and superconducting quantum circuits. Among them, the optical lattices are the most performing quantum simulators, due to the huge number (from thousands to tens of millions) of bosonic or fermionic quantum elements of their ultracold neutral atoms, their high geometrical flexibility, degree of isolation, and spin and interaction control, that allowed to implement several models, including the Bose-Hubbard [178] and Fermi-Hubbard [179] models, quantum spin liquids (QSLs) [180], and fractional quantum Hall physics [181]. Nevertheless, Hamiltonian engineering with tunable long-range interactions and preparation of strongly correlated quantum many-body states at low temperatures are not still easy tasks [182]. Indeed, engineered bath techniques, optimizing initial state-preparation protocols, and cooling techniques have been implemented against the interactions with the environment. Trapped ions and Rydberg atom arrays also realize unexplored condensed matter models, especially providing remarkable results on quantum PTs in exotic quantum spin models [183, 184], but they often suffer from cross-talk or

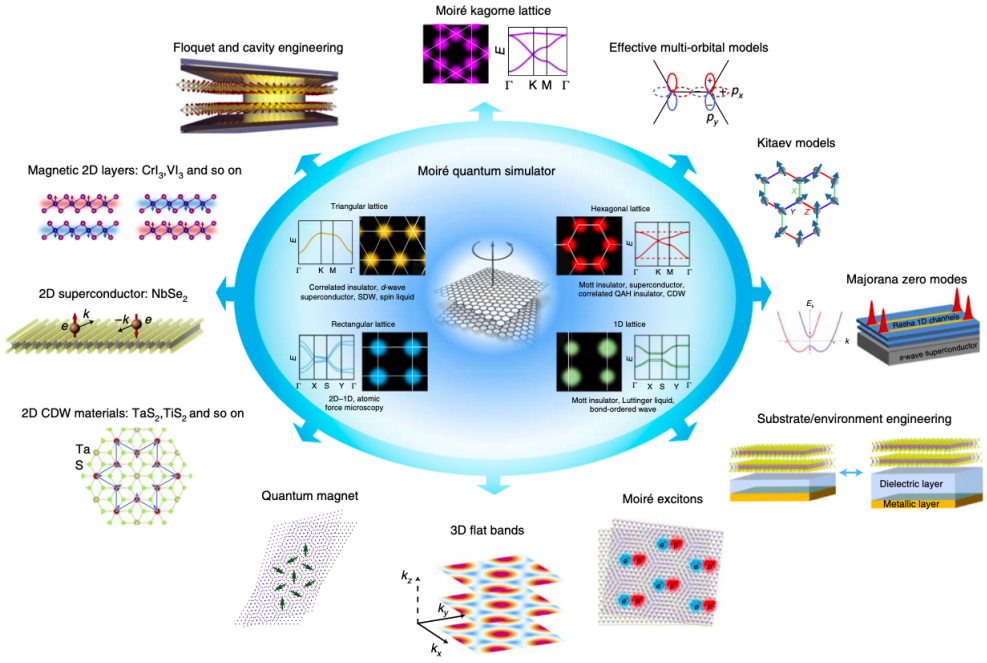

FIGURE 1.14: Schematics of moiré quantum simulators, based on the remarkable quantum properties of different 2D materials. Adapted with permission from Ref. [189].

unwanted interactions or, particularly in the second case, require engineered bath methods. Other models are implemented with superconducting quantum circuits (e.g., frustrated spin systems, PTs beyond mean-field theory, Mott insulating phase in the Bose-Hubbard model) [185], despite the limit of variability, that is the different performances of nominally identical design quantum devices induced by nearby environments or defects, in addition to the needed engineered bath methods.

1.3 Two-dimensional condensed-matter quantum simulators

The unprecedented number of DOFs of 2D materials and the more easily reachable low temperatures make them a valid and cheap alternative to the optical lattices as quantum simulators. For instance, ML $NbSe_2$ and ML CrI_3 are ideal platforms to explore Ising superconductivity and quantum magnetism, respectively, and how such correlated phases could be affected by the variations in lattice spacing (interactions tunability), the presence of a substrate, magnetic fields and other easily available external actions or effects. Indeed, as far as the quantum magnetism is concerned, several studies have analyzed the change in magnetic anisotropy as a function of strain [148], establishing a controlled way to pass from Ising-like models [186, 187] to XY models or nontrivial topological spin states [188].

The quantum simulation idea applied on 2D materials can reach its full realization if one takes into account the van der Waals heterostructures and the additional DOFs as interlayer coupling, twist angle, order and number of layers. Such a high tunability enormously expands the range of possible physical systems and, consequently, the same occurs to the target quantum models or phenomena of the quantum simulation. In the recent years, many striking examples have already been observed. As an example, the realization of the $NbSe_2$/graphene heterostructure allowed to investigate the proximity-induced Ising superconductivity by avoiding inter-mixing, issues related to lattice mismatch, and chemical modifications of the

interface through strong chemical bonds, thus giving novel information for future and controlled studies of Majorana wires and lattices [190–192]. In the van der Waals material CrI_3, quantum magnetic properties can be realized and depend on the number of layers and relative stacking order [193]. However, the twist angle has proven to be the most suitable DOF for the quantum simulation through van der Waals systems, realizing the so-called *moiré quantum simulators* [189], schematically grouped in Fig. 1.14. TBG opened up the way for the latter, since particular values of twist angle induce very complex correlated phases in the simplest BL system ever. The experimental observation of the Mott insulating phase and the unconventional superconductivity in TBG has certainly boosted the tuning-on-demand paradigm of the 2D materials world, giving an eventual shortcut to explore the collective quantum phases. Indeed, next studies showed new orbitally magnetized phases with a quantized Hall effect, as signature of topological phases [194, 195]. Twist angle unveiled hidden collective quantum phases also in twisted BL BN, that exhibited both spin-density wave (SDW) and *d*-wave superconductivity phases [196]. The proximity-induced Ising superconductivity of HeBL $NbSe_2$/graphene has been theoretically investigated as a function of the twist angle, in order to assess the robustness to external in-plane magnetic fields [197]. The variations of twist angle and the three-dimensional dielectric environment have been identified as ideal knobs for tuning hopping and interaction strength parameters of the triangular-lattice Hubbard model on HeBL WSe_2/WS_2 [198, 199], in order to simulate the model phase diagram for a dimensionality larger than one. The large availability of experimental measurement techniques, the easier cooling, and the huge number of DOFs characterizing van der Waals systems trace a very promising path for the quantum simulation of emergent physics which has been still experimentally elusive so far.

1.4 Purposes and structure of the thesis

The vision of van der Waals systems as condensed-matter quantum simulators motivated the choice of the three distinct materials considered in this thesis work, i.e., TBG, twisted HeBL $MoS_2/NbSe_2$, ML and MuL Nb_3I_8. The interest on TBG has been focused on the fundamental role played by the atomic relaxation in the electronic band structure [200], especially regarding the origin of the electron/hole flat minibands, for small commensurate angles down to the first magic angle $\theta \sim 1.08^\circ$. As far as the twisted HeBL $MoS_2/NbSe_2$ is concerned, previous reports on twisted TMD metal-semiconductor HeBLs are not present in literature, although the electronic properties of the untwisted vdWHe $MoS_2/NbSe_2$ have been explored through DFT first-principles calculations [201] and the untwisted vdWHe $WSe_2/NbSe_2$ has been fabricated and tested as electrode-channel contact of a field-effect transistor (FET) [202]. Moreover, the discovery of ML $NbSe_2$ Ising superconductivity has addressed the interest in exploring how it would be affected in or would affect such a twisted HeBL [203]. Therefore, the analysis on twisted HeBL $MoS_2/NbSe_2$ is original and proposes as starting point to explore the twist-angle-dependent 2D superconductivity. Finally, several electronic and magnetic analyzes have been performed on ML and MuL Nb_3I_8 [204, 205], that is a novel vdW magnet whose collective phase derives form the Nb atoms magnetic moments. Since the latter form an irregular kagome lattice, this material and its twisted homostructures could be used as quantum simulators of highly exotic correlated phases, such as Z_2 QSL, $U(1)$ QSL, quantum chiral spin liquid, and valence bond crystal [189].

The thesis is organized as follows:

- in Chap. 2 we present the DFT, its computational implementation, and the involved approximations;
- in Chap. 3 we examine in depth the twisting and magnetism theoretical frameworks in two-dimensional systems, providing the geometrical description of twisted HeBLs, the energy mapping between DFT and magnetic Hamiltonians, and presenting the *Metropolis algorithm* of Monte Carlo simulation used for analyzing the magnetic Hamiltonian models on 2D lattices;
- in Chap. 4 we present, discuss, and analyze the results for each investigated system.

Chapter 2

Density functional theory: basics and implementation

"I have also testified repeatedly and published some articles in favor of Small Science."

Philip Warren Anderson

Over the time, modeling and design of materials is performed by means of ever more accurate and efficient advances in theory, algorithms, and hardware. In order to investigate on a specific property, first-principles calculations enormously accelerate the typical times required for the experiments by allowing a more systematic analysis on a larger set of systems, especially if guided by tools from computer science. Simulations failures are more and more slight and specific compared to the expected predictions, thus stimulating further progress in methods.

Nowadays, DFT is the widely used theory to efficiently and often accurately compute the ground-state properties of condensed-matter systems. It developed driven by the experimental observations, reaching a high accuracy level also in the detection of eventual prediction errors [206–208].

This chapter is aimed to present the DFT, both in the non-relativistic and relativistic formulations, and its computational implementation used in this thesis.

2.1 Non-relativistic theory

In the framework of non-relativistic quantum mechanics, the dynamics of the microsopic costituents of matter is described by the Schrödinger equation [209], that neglects spin and relativistic effects. Such an equation is exactly solvable only for the hydrogen atom, and the larger the number of the system particles, the more difficult it is to find an approximate solution. Different theories and approximations were formulated in order to determine the ground state of a many-particles system, mostly based on the Ritz variational method [210], for which a trial wavefunction will always give an expectation value larger than or equal to the ground-state energy. Among them, the Hartree-Fock (HF) method [211, 212] was used for many-electrons problems, giving even now good results for systems where the exchange effects are more important than the correlation effects, since it exactly takes into account the former and completely neglects the correlations[1]. The density functional

[1]The exchange effects of the Coulomb interaction between identical fermions are purely quantum effects arising from the Pauli exclusion principle [213] and, thus, occurring as the repulsion of parallel-spin fermions. Instead, the correlation effects simply manifest as the repulsion of fermions with the same charge sign, regardless of their spins, but having both classical and quantum aspects, due to their local and non-local components.

theory is an ab initio and ground-state theory introduced in the mid 60s by Pierre Hohenberg, Walter Kohn, and Lu Jeu Sham [214, 215] to determine the approximate ground state of a many-body system also including the correlation effects, in a more efficient way compared to all the post-HF methods.

In this section, the quantum many-body problem will be formally introduced, pointing out the difficulties rising from the Schrödinger equation application and the main ideas and steps of the DFT to face them.

2.1.1 The quantum many-body problem

Atoms, molecules or, in general, solids can be schematized as systems composed of ions (nuclei and their respective core electrons that are tightly bound to them) and valence electrons (outer shell electrons that can participate in the formation of a chemical bond). The time-independent Schrödinger equation of a solid with N electrons (of coordinates $\mathbf{r}_i$, moments $\mathbf{p}_i$, mass m[2], and charge $-e$) and M ions (of coordinates $\mathbf{R}_\alpha$, moments $\mathbf{P}_\alpha$, mass M_α, and charge $Z_\alpha e$) with mutual Coulomb interactions reads [216–218]

$$\hat{H}(\{\mathbf{r}_i\},\{\mathbf{R}_\alpha\})\Psi(\{\mathbf{r}_i\},\{\mathbf{R}_\alpha\}) = E\Psi(\{\mathbf{r}_i\},\{\mathbf{R}_\alpha\}), \tag{2.1}$$

where $\{\mathbf{r}_i\} = (\mathbf{r}_1,...,\mathbf{r}_N)$ is the set of electronic coordinates, $\{\mathbf{R}_\alpha\} = (\mathbf{R}_1,...,\mathbf{R}_M)$ is the set of ionic coordinates, $\Psi(\{\mathbf{r}_i\},\{\mathbf{R}_\alpha\})$ is the total many-body wavefunction of the system, and E is the total energy of the system, that is eigenvalue of the Hamiltonian

$$\begin{aligned}\hat{H}(\{\mathbf{r}_i\},\{\mathbf{R}_\alpha\}) = &\overbrace{-\frac{\hbar^2}{2m}\sum_{i=1}^{N}\nabla_i^2}^{\hat{T}_e(\{\mathbf{r}_i\})} \overbrace{-\sum_{\alpha=1}^{M}\frac{\hbar^2}{2M_\alpha}\nabla_\alpha^2}^{\hat{T}_i(\{\mathbf{R}_\alpha\})} + \overbrace{\frac{1}{2}\sum_{\substack{i,j=1\\ i\neq j}}^{N}\frac{e^2}{|\mathbf{r}_i-\mathbf{r}_j|}}^{\hat{V}_{e-e}(\{\mathbf{r}_i\})} \\ &+ \underbrace{\frac{1}{2}\sum_{\substack{\alpha,\beta=1\\ \alpha\neq\beta}}^{M}\frac{Z_\alpha Z_\beta e^2}{|\mathbf{R}_\alpha-\mathbf{R}_\beta|}}_{\hat{V}_{i-i}(\{\mathbf{R}_\alpha\})} \underbrace{-\sum_{i=1}^{N}\sum_{\alpha=1}^{M}\frac{Z_\alpha e^2}{|\mathbf{r}_i-\mathbf{R}_\alpha|}}_{\hat{V}_{e-i}(\{\mathbf{r}_i\},\{\mathbf{R}_\alpha\})}.\end{aligned} \tag{2.2}$$

The first term at the right-hand side is the kinetic energy operator $\hat{T}_e$ of the electrons, the second term is the kinetic energy operator $\hat{T}_i$ of the ions, the third term is the electron-electron Coulomb repulsion energy operator $\hat{V}_{e-e}$, the fourth term is the ion-ion Coulomb repulsion energy operator $\hat{V}_{i-i}$, and the last term is the electron-ion Coulomb attraction energy operator $\hat{V}_{e-i}$.

Eq. (2.1) refers to a many-body problem because both the number of electrons N and the number of ions M are of the order of the Avogadro constant $N_A \simeq 6.022 \times 10^{23}$. Moreover, all the components strongly interact with each other and, thus, exactly solving the Eq. (2.1) is impossible in practice. For this reason, it is convenient to introduce some approximations.

2.1.2 Born-Oppenheimer approximation

The *Born-Oppenheimer* (BO) or *adiabatic approximation* [219] allows to decouple the electronic and the ionic dynamics in order to solve the Eq. (2.1) more efficiently,

[2] Typically, electron mass is denoted by m_e in literature. Here, the notation m will be adopted for the sake of simplicity.

based on the fact that the nuclei are much heavier than the electrons. Indeed, the *adiabaticity ratio* m/M_α typically is at least of the order of 10^{-4} (it is enough to think that a proton has a mass about 1836 times greater than that of an electron)[3]. Such an assumption allows, in a first step, to set $\hat{T}_i(\{\mathbf{R}_\alpha\}) = 0$, i.e., to assume infinite masses for the ions. As a result, the ionic coordinates $\{\mathbf{R}_\alpha\}$ become constant parameters identifying the positions of the nuclei clamped in space (*clamped-nuclei approximation*), the operator $\hat{V}_{i-i}(\{\mathbf{R}_\alpha\})$ is a constant contribution for each assigned set $\{\mathbf{R}_\alpha\}$, and $\hat{V}_{e-i}(\{\mathbf{r}_i\},\{\mathbf{R}_\alpha\})$ is the operator describing moving electrons that "feel" the Coulomb potential of the clamped nuclei. Hence, under the BO approximation, the Eq. (2.1) can be solved first passing through the Schrödinger equation

$$\hat{H}_e(\{\mathbf{r}_i\},\{\mathbf{R}_\alpha\})\Psi_e(\{\mathbf{r}_i\},\{\mathbf{R}_\alpha\}) = E_e(\{\mathbf{R}_\alpha\})\Psi_e(\{\mathbf{r}_i\},\{\mathbf{R}_\alpha\}), \tag{2.3}$$

governed by the electronic Hamiltonian

$$\hat{H}_e(\{\mathbf{r}_i\},\{\mathbf{R}_\alpha\}) = \hat{T}_e(\{\mathbf{r}_i\}) + \hat{V}_{e-e}(\{\mathbf{r}_i\}) + \hat{V}_{e-i}(\{\mathbf{r}_i\},\{\mathbf{R}_\alpha\}). \tag{2.4}$$

Once the ground state of the electronic problem has been determined[4], the ionic dynamics must be someway included to solve the Eq. (2.1). Indeed, nuclei can be assumed as fixed in space with respect to the electrons, but not with respect to each other. Therefore, the second step of the BO approximation consists in treating $\hat{T}_i$ as a perturbation in the total Hamiltonian $\hat{H} = \hat{H}_e + \hat{T}_i + \hat{V}_{i-i}$. If such a perturbation induces only negligible transitions between different electronic states, that are eigenstates of the electronic Hamiltonian in Eq. (2.4), then the total many-body wavefunction of the system can be written in the factorized form

$$\Psi(\{\mathbf{r}_i\},\{\mathbf{R}_\alpha\}) \simeq \Psi_i(\{\mathbf{R}_\alpha\})\Psi_e(\{\mathbf{r}_i\},\{\mathbf{R}_\alpha\}). \tag{2.5}$$

Here, the ionic part $\Psi_i(\{\mathbf{R}_\alpha\})$ is intended as the ground state of the Schrödinger-like equation

$$[E_e(\{\mathbf{R}_\alpha\}) + \hat{T}_i(\{\mathbf{R}_\alpha\}) + \hat{V}_{i-i}(\{\mathbf{R}_\alpha\})]\Psi_i(\{\mathbf{R}_\alpha\}) = E\Psi_i(\{\mathbf{R}_\alpha\}), \tag{2.6}$$

stating that the ions move on the Born-Oppenheimer potential energy surface (PES)

$$\Phi^{BO}(\{\mathbf{R}_\alpha\}) \equiv E_e(\{\mathbf{R}_\alpha\}) + \hat{V}_{i-i}(\{\mathbf{R}_\alpha\}). \tag{2.7}$$

2.1.3 The ideas behind the density functional theory

The electronic problem described by Eq. (2.3) appears easier solvable than the whole electronic and ionic problem of Eq. (2.1). Notwithstanding, the interaction term $\hat{V}_{e-e}$ requires further discussion and analysis. Interacting-electron models aim to determine the ground state of an Hamiltonian

$$\hat{H}_e = \hat{T} + \hat{U} + \hat{V}, \tag{2.8}$$

[3]There are cases in which the BO approximation loses validity and, thus, one must invoke other approximations, but this is then often used as a starting point for more refined methods.

[4]This problem can be faced by using the HF method or, more efficiently and accurately, the DFT, as will be described afterwards.

where $\hat{T}$ is the kinetic energy operator, $\hat{U}$ is the Coulombian repulsion (two-body) potential and

$$\hat{V}(\mathbf{r}_1, ..., \mathbf{r}_N) = \sum_{i=1}^{N} v(\mathbf{r}_i) \tag{2.9}$$

is an external (one-body) potential. Prior to the DFT formulation, several approaches have been proposed for studying the interacting systems: the HF method, exactly taking into account the exchange energy of the Coulomb interaction but completely neglecting the correlation energy; the configuration interaction (CI) approach [220], used as a post-HF method to take into account correlation effects, that consisted in constructing accurate approximations of the ground state from linear combinations of the Slater determinants. $K > N/2$ single-particle spatial states resulting from the HF iterative procedure are typically used and an acceptable accuracy corresponds to $K \sim 10^9$, thus introducing a remarkable computational complexity.

The DFT is an ab initio and ground-state theory that overcomes this problem by entirely reformulating the Ritz variational method in an extremely efficient way both from a computational and a conceptual point of view, so much to earn Kohn the Nobel Prize in Chemistry in 1998. In his Nobel Lecture [221], Kohn clarified such an advance by first defining the "exponential computational wall" that one encounters trying to solve the Eq. (2.3) for $N \gtrsim 10$. If p is the number of parameters for each independent variable of the electronic wavefunction $\Psi_e(\{\mathbf{r}_i\})$[5] that are needed to obtain a certain accuracy and the symmetries are neglected, then the Ritz functional

$$\epsilon[\Psi_e] = \frac{\langle \Psi_e | \hat{H} | \Psi_e \rangle}{\langle \Psi_e | \Psi_e \rangle} \tag{2.10}$$

must be minimized in an hyperspace of p^{3N} parameters. Assuming that $p = 3$ and $p^{3N} \lesssim 10^9$, the maximum number of electrons is $N \simeq 6$, that is rather small compared to the minimum acceptable value of 20 electrons, although the energy in Eq. (2.10) is minimized in a huge parameter space. The exponential computational wall is further manifest when one considers that the number of parameters for $p = 3$ and $N = 100$ is $3^{300} \simeq 10^{150}$. As far as the DFT conceptual innovation is concerned, the Ritz functional is reformulated by expressing the energy as a functional of the ground-state electronic density

$$n(\mathbf{r}_1) = N \int |\Psi_e(\{\mathbf{r}_i\})|^2 d^3r_2 ... d^3r_N \tag{2.11}$$

rather than the electronic wavefunction $\Psi_e(\{\mathbf{r}_i\})$, thus requiring trial functions of only 3 instead of $3N$ variables. Therefore, regardless of the value of N, the ground-state electronic density has the main role and the exponential computational wall is torn down[6]. As expected, the ground-state electronic density defined in Eq. (2.11) satisfies the condition

$$\int n(\mathbf{r}) d^3r = N. \tag{2.12}$$

[5] In the following, the dependence on the ionic coordinates will be neglected for the sake of simplicity, due to the clamped-nuclei approximation.

[6] In 1927, Llewellyn Hilleth Thomas and Enrico Fermi formulated the first theory based on the ground-state electronic density [222, 223], but the kinetic term could not be expressed, unless to introduce substantial approximations, as a functional of $n(\mathbf{r})$. As a consequence, despite good results for some many-electron atoms, Thomas-Fermi (TF) theory underestimated the binding energies, did not provide good predictions for properties depending on valence electrons, and did not predict the chemical bond.

The mathematical structure of the DFT is based on two fundamental theorems proved by Hohenberg and Kohn (HK) [214], and the derivation of a set of equations by Kohn and Sham (KS) [215], mapping the many-body problem of interacting electrons onto a fictitious single-particle problem of non-interacting electrons in an effective local potential.

2.1.4 The theorems of Hohenberg and Kohn

First theorem

Given an electronic density $n(\boldsymbol{r})$, if exists at least one potential $v(\boldsymbol{r})$ such that $n(\boldsymbol{r})$ is the electronic density of the ground state of $\hat{H}_e$, then the potential $v(\boldsymbol{r})$ is unique less than a constant.

Second theorem

The ground state energy corresponds to the minimum of the functional

$$E_v[n] = \langle \Psi_e | \hat{H}_e | \Psi_e \rangle = \langle \Psi_e | (\hat{T} + \hat{U}) | \Psi_e \rangle + \langle \Psi_e | \hat{V} | \Psi_e \rangle = F[n] + \int v(\mathbf{r}) n(\mathbf{r}) d^3r \tag{2.13}$$

with respect to the electronic density.

The first theorem states that the external potential $v(\mathbf{r})$ can be uniquely determined from the ground-state electronic density $n(\mathbf{r})$ (i.e., $n(\mathbf{r}) \rightarrow v(\mathbf{r})$), in contrast to the opposite statement of the typical Schrödinger approach (i.e., $v(\mathbf{r}) \rightarrow n(\mathbf{r})$), that is, there exists a one-to-one correspondence between the ground-state electronic density and the external potential. It is worthwhile noticing that at a fixed number of electrons, the operators $\hat{T}$ and $\hat{U}$ are universal (and so is the functional $F[n]$ defined in Eq. (2.13)), i.e., they are independent on the particular kind of many-electron system, and the operator $\hat{V}$ (or, in ultimate analysis, the potential $v(\mathbf{r})$) uniquely specifies the Hamiltonian. An immediate consequence of the correspondence $n(\mathbf{r}) \rightarrow v(\mathbf{r})$ is that the ground-state expectation value of any observable $\hat{A}$ is a unique functional of the exact ground-state electronic density, i.e.,

$$n(\mathbf{r}) \rightarrow v(\mathbf{r}) \Rightarrow \langle \Psi_e[n] | \hat{A} | \Psi_e[n] \rangle = \hat{A}[n]. \tag{2.14}$$

The second theorem defines the reformulation of the Ritz variational method of the Schrödinger approach in terms of the electron density, also giving an operative form of the concept of density functional.

2.1.5 The Kohn-Sham equations

The *Kohn-Sham equations* are a set of exact Hartree-like equations [224–226] that allow to self-consistently determine the ground-state electronic density, as an alternative to minimize the functional of Eq. (2.13). They can be derived by considering an auxiliary non-interacting system with the same ground-state electronic density as the original interacting system. Indeed, for a general electronic density $n'(\mathbf{r})$, it is always possible to find a unique non-interacting system of electrons with single-particle states $\varphi_i'(\mathbf{r})$, electronic density

$$n'(\mathbf{r}) = \sum_i^{occ} |\varphi_i'(\mathbf{r})|^2, \tag{2.15}$$

and kinetic energy functional

$$T_s[n'] = -\frac{\hbar^2}{2m}\sum_i^{occ}\int \varphi_i'^*(\mathbf{r})\nabla^2\varphi_i'(\mathbf{r})d^3r, \tag{2.16}$$

where the sums run over the subset of the occupied states. Once this non-interacting electron system has been defined, the universal functional of Eq. (2.13) can be recasted as

$$F[n'] = T_s[n'] + \frac{e^2}{2}\int \frac{n'(\mathbf{r})n'(\mathbf{r}')}{|\mathbf{r}-\mathbf{r}'|}d^3rd^3r' + E_{xc}[n']. \tag{2.17}$$

The second term at the right-hand side is the Hartree energy functional $E_H[n']$ or the classical electrostatic energy of the electronic density $n'(\mathbf{r})$ interacting with the electrostatic potential generated by itself. In other words, whereas the general form of $F[n']$ is unknown, it is possible to single out terms that are easily handled in the common Hartree-like approach. In particular, the kinetic energy of the unique non-interacting system with the same electron density and the Hartree energy are explicited in Eq. (2.17). Therefore, the last term, named as *exchange-correlation energy functional*, contains the quantum contributions of the Coulomb interaction (exchange and quantum correlation effects) and the kinetic energy of the interacting system of electrons lacking the non-interacting system contribution. According to the variational method, the ground-state electronic density minimizes the HK-reformulated Ritz functional of Eq. (2.13), under the constraint of Eq. (2.12). Introducing a Lagrange multiplier μ, this is equivalent to impose the equation[7]

$$\delta\left[E_v[n'] - \mu\left(\int n(\mathbf{r})d^3r - N\right)\right] = 0. \tag{2.19}$$

Since $T_s[n']$ is explicitly expressed as a functional of the non-interacting system single-particle states in Eq. (2.16), but all other terms in Eq. (2.13) are functionals of the electronic density, one can exploit the chain rule of the functional derivatives and vary the single-particle states $\varphi_i'^*(\mathbf{r})$[8]. Furthermore, the condition of Eq. (2.12) is included in the orthonormality condition of the states $\varphi_i'(\mathbf{r})$. Therefore, the minimization condition becomes

$$\begin{aligned}\Bigg[&\frac{\delta T_s}{\delta\varphi_i'^*(\mathbf{r})} + \frac{\delta E_H}{\delta n'(\mathbf{r})}\frac{\delta n'(\mathbf{r})}{\delta\varphi_i'^*(\mathbf{r})} + \frac{\delta E_{xc}}{\delta n'(\mathbf{r})}\frac{\delta n'(\mathbf{r})}{\delta\varphi_i'^*(\mathbf{r})}\\ &+ \int v(\mathbf{r})\frac{\delta n'(\mathbf{r})}{\delta\varphi_i'^*(\mathbf{r})}d^3r - \sum_{i,j}^{occ}\mu_{ij}(\langle\varphi_i|\varphi_j\rangle - \delta_{ij})\Bigg] = 0.\end{aligned} \tag{2.20}$$

[7]The variation of a functional $\mathcal{F}[f(x)]$ is

$$\delta\mathcal{F}[f(x)] = \int \frac{\delta\mathcal{F}}{\delta f(y)}\delta f(y)dy \tag{2.18}$$

and $\delta\mathcal{F}/\delta f(y)$ is the functional derivative of $\mathcal{F}$ with respect to its argument.

[8]In principle, one should simultaneously vary both $\varphi_i'(\mathbf{r})$ and $\varphi_i'^*(\mathbf{r})$, but one case is the complex conjugate of the other one and, thus, it is enough to vary only the latter in order to obtain the final result.

Since

$$\frac{\delta T_s}{\delta \varphi_i'^*(\mathbf{r})} = -\frac{\hbar^2}{2m}\sum_i^{occ}\nabla^2\varphi_i'(\mathbf{r}), \quad \frac{\delta E_H}{\delta n'(\mathbf{r})} = e^2\int\frac{n'(\mathbf{r}')}{|\mathbf{r}-\mathbf{r}'|}d^3r' = v_H(\mathbf{r}), \quad \frac{\delta n'(\mathbf{r})}{\delta \varphi_i'^*(\mathbf{r})} = \varphi_i'(\mathbf{r}) \tag{2.21}$$

and if

$$v_{xc}(\mathbf{r}) \equiv \frac{\delta E_{xc}[n']}{\delta n'}, \quad v_{KS}(\mathbf{r}) \equiv v_H(\mathbf{r}) + v_{xc}(\mathbf{r}) + v(\mathbf{r}), \tag{2.22}$$

then Eq. (2.20) gives for each solution $\varphi_i(\mathbf{r})$ the Hartree-like single-particle equation[9]

$$\left[-\frac{\hbar^2}{2m}\nabla^2 + v_{KS}(\mathbf{r})\right]\varphi_i(\mathbf{r}) = \epsilon_i\varphi_i(\mathbf{r}). \tag{2.23}$$

Eqs. (2.23) and (2.15) are the so-called *Kohn-Sham self-consistent equations*, that are formally identical to the equations of a non-interacting system of electrons in which the *Kohn-Sham potential* $v_{KS}(\mathbf{r})$ is the only external (fictitious) potential giving the same ground-state electronic density of the interacting system. It must be pointed out that the total energy is not the sum of the Kohn-Sham eigenvalues ϵ_i's. Indeed, the latter is

$$\sum_i^{occ}\epsilon_i = \sum_i^{occ}\int\varphi_i'^*(\mathbf{r})\left[-\frac{\hbar^2}{2m}\nabla^2 + v_{KS}(\mathbf{r})\right]\varphi_i'(\mathbf{r})d^3r = T_s[n] + \int v_{KS}(\mathbf{r})n(\mathbf{r})d^3r \tag{2.24}$$

and, thus, the total energy is

$$\begin{aligned} E =& T_s[n] + E_H[n] + E_{xc}[n] + \int v(\mathbf{r})n(\mathbf{r})d^3r \\ =& \sum_i^{occ}\epsilon_i - \frac{e^2}{2}\int\frac{n(\mathbf{r})n(\mathbf{r}')}{|\mathbf{r}-\mathbf{r}'|}d^3rd^3r' + E_{xc}[n] - \int v_{xc}(\mathbf{r})n(\mathbf{r})d^3r. \end{aligned} \tag{2.25}$$

The KS equations can be iteratively and self-consistently solved once $E_{xc}[n]$ is known. In practice, only approximations of the latter can be provided, as it will be detailed later. In general, nor the KS eigenvalues nor the KS eigenstates have proved physical meanings. The only physically meaningful quantity is the ground-state electronic density $n(\mathbf{r})$.

2.1.6 Spin-polarized density functional theory

The spin extension of the density functional theory allows to calculate the magnetic ground state, metastable states, and magnetic orders of magnetic materials by explicitly including the magnetization or spin density in the formalism. In the framework of non-relativistic quantum mechanics, the spin was first introduced by Wolfgang Ernst Pauli, that derived a Schrödinger equation for a charged spin-½ particle interacting with an electromagnetic field [227]. In particular, the Pauli Hamiltonian for an electron is

$$\hat{H}_{Pauli} = \left[\frac{1}{2m}\sum_{i=x,y,z}\left(-i\hbar\partial_{x_i} + \frac{e}{c}A_i\right)^2 - e\phi\right]\hat{\mathbb{I}}_2 + \mu_B\hat{\boldsymbol{\sigma}}\cdot\mathbf{B}, \tag{2.26}$$

[9] It can be demonstrated that the Lagrange multipliers matrix is hermitian and, therefore, admits an unitary transformation into a diagonal matrix of diagonal elements ϵ_i's.

where $\mathbf{A}(\mathbf{r})$ is the vector potential, $\phi(\mathbf{r})$ is the scalar potential, $\mu_{\mathcal{B}}$ is the Bohr magneton, $\mathbf{B}(\mathbf{r}) = \boldsymbol{\nabla} \times \mathbf{A}(\mathbf{r})$ is the magnetic field, and $\hat{\sigma} = (\hat{\sigma}_x, \hat{\sigma}_y, \hat{\sigma}_z)$ is the vector operator of the Pauli matrices. The external potential $v(\mathbf{r}) = \mu_{\mathcal{B}} \sigma \cdot \mathbf{B}$ of Eq. (2.26), coupling spin and magnetic field, induces the single-particle states to be two-component spinors

$$\varphi_i(\mathbf{r}) = \begin{pmatrix} \varphi_{i,\uparrow}(\mathbf{r}) \\ \varphi_{i,\downarrow}(\mathbf{r}) \end{pmatrix}. \tag{2.27}$$

As a consequence, the Pauli Hamiltonian or, in general, an Hamiltonian with a spin-½-dependent external potential $v_{\alpha\beta}(\mathbf{r})$ applied to a system of N particles induces single-particle states having components $\varphi_{i,\alpha}(\mathbf{r})$ with $\alpha = \uparrow, \downarrow$. In addition to the electronic density $n(\mathbf{r})$, the basic variable of the spin-polarized DFT is the magnetization density

$$\mathbf{m}(\mathbf{r}) = \sum_i^N \langle \varphi_i | \, \hat{\boldsymbol{\mu}} \, | \varphi_i \rangle, \tag{2.28}$$

where

$$\hat{\boldsymbol{\mu}} = -\frac{g_s \mu_{\mathcal{B}}}{\hbar} \hat{\mathbf{S}} \tag{2.29}$$

is the spin magnetic moment containing the spin-½ matrices vector $\hat{\mathbf{S}} = (\hbar/2)\hat{\sigma}$. In particular, if the electron spin g-factor g_s is set to 2, then the magnetization density of Eq. (2.28) reduces to

$$\mathbf{m}(\mathbf{r}) = -\mu_{\mathcal{B}} \sum_i^N \langle \varphi_i | \, \hat{\sigma} \, | \varphi_i \rangle \tag{2.30}$$

The magnetization $\mathbf{M}$ of the unit cell with volume Ω describing the material Bravais lattice can be obtained by integrating the magnetization density over it:

$$\mathbf{M} = \int_\Omega \mathbf{m}(\mathbf{r}) d^3 r. \tag{2.31}$$

Electronic density and magnetization density can be grouped in the hermitian matrix [228–230]

$$\tilde{N}(\mathbf{r}) = \frac{1}{2} \left[n(\mathbf{r}) \mathbb{I}_2 + \frac{1}{\mu_{\mathcal{B}}} \mathbf{m}(\mathbf{r}) \cdot \hat{\sigma} \right], \tag{2.32}$$

where

$$n(\mathbf{r}) = tr\tilde{N}(\mathbf{r}), \quad \mathbf{m}(\mathbf{r}) = \mu_{\mathcal{B}} tr(\sigma \tilde{N}(\mathbf{r})). \tag{2.33}$$

Hence, based upon the definitions

$$\tilde{N}'_{\alpha\beta}(\mathbf{r}) \equiv \sum_i^{occ} \psi'^*_{i,\beta}(\mathbf{r}) \psi'_{i,\alpha}(\mathbf{r}), \quad T_s[\tilde{N}'_{\alpha\beta}] \equiv -\frac{\hbar}{2m} \sum_i^{occ} \sum_\alpha \int \psi'^*_{i,\alpha}(\mathbf{r}) \nabla^2 \psi'_{i,\alpha}(\mathbf{r}) d^3 r, \tag{2.34}$$

the spin-polarized energy functional is

$$E_{v,sp}[\tilde{N}'_{\alpha\beta}] = T_s[\tilde{N}'_{\alpha\beta}] + E_H[n'] + E_{xc}[\tilde{N}'_{\alpha\beta}] + \sum_{\alpha,\beta} \int v_{\alpha\beta}(\mathbf{r}) \tilde{N}'_{\alpha\beta}(\mathbf{r}) d^3 r \tag{2.35}$$

and the spin-polarized KS equations are

$$\left\{ -\frac{\hbar^2}{2m} \nabla^2 + \sum_\beta [v_H(\mathbf{r}) \delta_{\alpha\beta} + v_{xc,\alpha\beta}(\mathbf{r}) + v_{\alpha\beta}(\mathbf{r})] \right\} \psi_{i,\alpha}(\mathbf{r}) = \eta_i \psi_{i,\alpha}(\mathbf{r}), \tag{2.36}$$

where

$$v_{xc,\alpha\beta}(\mathbf{r}) = \frac{\delta E_{xc}[\tilde{N}_{\alpha\beta}]}{\delta \tilde{N}_{\alpha\beta}} \tag{2.37}$$

is the *spin-dependent exchange-correlation potential* and the η_i's are the Lagrange multipliers in the diagonal basis related to the constraint

$$\sum_{\alpha} \langle \psi_{i,\alpha} | \psi_{j,\alpha} \rangle = \delta_{ij}. \tag{2.38}$$

Writing the spin-dependent exchange-correlation potential as

$$v_{xc,\alpha\beta}(\mathbf{r}) = v_{xc}(\mathbf{r})\delta_{\alpha\beta} + \mu_{\mathcal{B}}(\boldsymbol{\sigma} \cdot \mathbf{B}_{xc}(\mathbf{r}))_{\alpha\beta}, \tag{2.39}$$

it turns out that the presence of many electrons generates an effective magnetic field $\mathbf{B}_{xc}(\mathbf{r})$, named as *exchange-correlation magnetic field*. The general non-diagonal form of the matrix $\tilde{N}$ implies that there is not a unique quantization axis, i.e., the formalism developed so far can describe noncollinear magnetism.

The formalism for collinear magnetism can be obtained by exploiting the hermiticity of $\tilde{N}(\mathbf{r})$. Indeed, due to such a property, there exist (unitary) spin-½ rotation matrices transforming the latter into a diagonal matrix in the σ_z basis, that is $\tilde{n}_{\alpha\beta} = n_\alpha \delta_{\alpha\beta}$ with

$$n_\alpha = \sum_{i}^{occ} |\varphi_{i,\alpha}(\mathbf{r})|^2, \quad \alpha = \uparrow, \downarrow . \tag{2.40}$$

Therefore, the spin-polarized KS equations become

$$\left[-\frac{\hbar^2}{2m}\nabla^2 + v_H(\mathbf{r}) + v_{xc,\alpha}(\mathbf{r}) + v_\alpha(\mathbf{r}) \right] \varphi_{i,\alpha}(\mathbf{r}) = \epsilon_{i,\alpha}\varphi_{i,\alpha}(\mathbf{r}), \tag{2.41}$$

where

$$v_{xc,\alpha}(\mathbf{r}) = \frac{\delta E_{xc}[n_\uparrow, n_\downarrow]}{\delta n_\alpha} = v_{xc}(\mathbf{r}) + \mu_{\mathcal{B}}\sigma_z B_{xc,z}(\mathbf{r}). \tag{2.42}$$

The electronic density and the magnetization density are respectively

$$n(\mathbf{r}) = n_\uparrow(\mathbf{r}) + n_\downarrow(\mathbf{r}), \quad m_z(\mathbf{r}) = -\mu_{\mathcal{B}}[n_\uparrow(\mathbf{r}) - n_\downarrow(\mathbf{r})]. \tag{2.43}$$

2.1.7 Basic approximations for the exchange-correlation functional

In both spin-unpolarized and spin-polarized formulations of DFT, all the steps performed in order to obtain the KS equations are exact, since no approximation has been introduced. Nevertheless, the explicit definition of the exchange-correlation energy functional is unknown and the final success of the theory depends on how accurately it is approximated. The first classification of the exchange-correlation energy functional approximations was given by John Perdew *et al.* [231], reporting the five main rungs of a *Jacob's ladder* to move from the Hartree world of unrealistically weak or missing chemical bonding in solids to the heaven of chemical accuracy. In general, the exchange-correlation energy functional is written as

$$E_{xc}[n] = \int e_{xc}(\mathbf{r}, [n]) n(\mathbf{r}) d^3r \tag{2.44}$$

and the approximations affect the exchange-correlation energy per particle $e_{xc}(\mathbf{r}, [n])$.

In this paragraph, I will only describe the first two rungs of the Jacob's ladder, that are needed to introduce the advanced approximations presented in the next paragraph and used for the results reported in the Chap. 4 of the thesis.

a) The local-density approximation

The simplest approximation of the Eq. (2.44) is the *local-density approximation* (LDA) [215], assuming that $e_{xc}(\mathbf{r}, [n])$ is such a slowly-variable function around each point $\mathbf{r}$ in space that it could be that of an homogeneous electron gas. Formally, this implies that the dependences on the entire function $n(\mathbf{r})$ and the point $\mathbf{r}$ are lost and, therefore, the exchange-correlation energy functional is

$$E_{xc}^{LDA}[n] = \int e_{xc}^{hom}(n(\mathbf{r}))n(\mathbf{r})d^3r. \tag{2.45}$$

The electronic density of an homogeneous electron gas is $n = (3/4\pi)(r_s a_0)^{-3}$, where r_s is the average radius in units of the Bohr radius a_0 of the electrons forming the homogeneous gas and schematized as adjacent spheres. The HF method exactly computes the exchange energy per particle as

$$e_x^{hom}(n) = -\frac{0.9163}{r_s}\frac{e^2}{2a_0}. \tag{2.46}$$

As a consequence, it is possible to separately treat the exchange and correlation contributions by writing

$$e_{xc}^{hom}(n(\mathbf{r})) = e_x^{hom}(n) + e_c^{hom}(n(\mathbf{r})). \tag{2.47}$$

The correlation energy per particle $e_c^{hom}(n(\mathbf{r}))$ has been obtained numerically for a sample of densities by fitting previous quantum Monte Carlo results with an interpolation function satisfying the known high-density ($r_s \to 0$) and low-density ($r_s \to \infty$) expansions [232].

LDA is exact in the limit of uniform densities. It is often considered satisfactory for solids, but much less for atomic and molecular physics, for which highly accurate experimental data are available. Indeed, the chemical bondings of atoms and molecules are highly inhomogeneous regions, where the LDA has not a suitable application, and have a crucial role in the properties of these systems. As a consequence, LDA usually underestimates bond lengths and badly overestimates ($\gtrsim 20\%$) the cohesive energies and bond strengths [233].

In the spin-polarized DFT, the LDA is specifically referred to as the *local-spin-density approximation* (LSDA) [229] and assumes an exchange-correlation energy functional

$$E_{xc}^{LSDA}[n_\uparrow, n_\downarrow] = \int e_{xc}^{hom}(n_\uparrow(\mathbf{r}), n_\downarrow(\mathbf{r}))[n_\uparrow(\mathbf{r}) + n_\downarrow(\mathbf{r})]d^3r. \tag{2.48}$$

The exchange energy per particle is given by the Eq. (2.46) multiplied by a spin-scaling function $\phi_2(\zeta)$, where $\zeta \equiv (n_\uparrow - n_\downarrow)/n$. Instead, as for the unpolarized case, the correlation energy per particle requires parametrizations, among which Vosko, Wilk, and Nusair (VWN) [234] and Perdew and Wang (PW92) [235] are the most used ones. In addition to the problems of the spin-unpolarized case, LSDA adds the exponential decay of the exchange potential

$$v_x^{LSDA}(\mathbf{r}) = \frac{\delta E_x^{LSDA}[n]}{\delta n(\mathbf{r})} \tag{2.49}$$

at infinity for finite molecular systems versus the expected r^{-1} asymptotic behavior [236].

b) The generalized-gradient approximation

In the 1980s, Langreth and other authors [237–243] took into account the information about the spatial variation of the electronic density to improve the results of L(S)DA in applications to atoms, molecules, and solids. The so-obtained *generalized-gradient approximation* (GGA) has the general form[10]

$$E_{xc}^{GGA}[n_\uparrow, n_\downarrow] = \int e_{xc}^{GGA}(n_\uparrow(\mathbf{r}), n_\downarrow(\mathbf{r}), \boldsymbol{\nabla} n_\uparrow(\mathbf{r}), \boldsymbol{\nabla} n_\downarrow(\mathbf{r}))[n_\uparrow(\mathbf{r}) + n_\downarrow(\mathbf{r})]d^3r. \quad (2.50)$$

The GGA is often named as semilocal (SL) approximation, since the gradients of the spin-polarized electronic densities give an additional "semilocal information" to their local values. The different ways to include the electronic density gradients in the GGA functional provide a wide variety of GGA functionals. They generally give a remarkable improvement over LDA for molecular systems at a modest additional computational cost, despite the overestimation of the bond lengths. The most widely used GGA functionals in calculations for solids are the Perdew-Wang functional (PW91) [235] and the Perdew-Burke-Ernzerhof functional (PBE) [244]. In both cases, the exchange energy per particle is obtained by multiplying Eq. (2.46) by an enhancement factor $F_x(s)$, that is function of the reduced density gradient $s(\mathbf{r}) \equiv |\boldsymbol{\nabla} n(\mathbf{r})|/2k_F n(\mathbf{r})$, where k_F is the Fermi wave vector. Instead, the correlation energy per particle is $n(\mathbf{r})e_c^{hom}(n_\uparrow(\mathbf{r}), n_\downarrow(\mathbf{r}))$ added to a function of $n_\uparrow(\mathbf{r})$, $n_\downarrow(\mathbf{r})$ and another reduced density gradient t depending on the spin-scaling function $\phi_2(\zeta)$. PBE functional has the advantage to be a simplified version of PW91 without fitted parameters, but with empirical parameters. It improves over PW91 providing an accurate description of the linear response of the uniform electron gas and correct behavior under uniform coordinate scaling. There are also extensions of PBE. For instance, revPBE by Zhang and Yang [245] is a revised version of the PBE exchange part, obtained by fitting to only the exchange atomic energies of He and Ar, thus giving more accurate total atomic energies and molecular atomization energies.

2.1.8 Advanced approximations for the exchange-correlation functional

Although LDA and GGA have been successful in predicting ground-state properties of several systems, they suffer from two main sources of error that limit the application of DFT to a still too restricted range of materials: *self-interaction error* (SIE) and absence of the nonlocal component of the interactions.

The self-interaction is the interaction of an electron with the Coulomb field it generates. As known, the HF method contains a self-interaction term in the direct potential that cancels exactly with an opposite term in the exchange potential. However, the approximations of the exchange-correlation functional $E_{xc}[n]$ in DFT do not completely cancel the self-interaction, leaving a residual SIE [246, 247]. There is a large number of problems in basic approximations of $E_{xc}[n]$ coming from the SIE. Among them, the most common ones are the *band gap problem* and the incorrect prediction of localized states occupancy in the strongly correlated electron materials. The band gap problem is the underestimation of insulators band gaps on the order of 40% [248] arising from the unphysical LDA and GGA curvatures of the total energy as a function of the number of electrons. Indeed, it can be demonstrated that

[10] In literature, the spin-polarized version of GGA is also denoted as σ-GGA.

the band gap of an insulating N-particle system, obtained by the KS eigenvalues as

$$E_g^{KS} = \epsilon_{H+1}(N) - \epsilon_H(N), \tag{2.51}$$

where $\epsilon_H(N)$ is the highest-occupied KS level and $\epsilon_{H+1}(N)$ is the next one, differs from that of the true interacting system by a quantity equal to the discontinuity of the functional derivative of the exchange-correlation functional[11]:

$$E_g^{real} = E_g^{KS} + \left.\frac{\delta E_{xc}[n]}{\delta n(\mathbf{r})}\right|_{N+\delta} - \left.\frac{\delta E_{xc}[n]}{\delta n(\mathbf{r})}\right|_{N-\delta}, \quad \delta \to 0. \tag{2.52}$$

As a consequence, the total energy must be a piecewise linear function of the number of electrons. Instead, the SIE introduced by LDA and GGA gives a nonlinear contribution to the total energy for fractional numbers of electrons with mainly a quadratic term coming from the Hartree energy not canceled properly in the exchange-correlation energy. As far as the strongly correlated electron materials are concerned, they are materials in which the electrons behavior cannot be described in terms of effective non-interacting elements because the scale of the electronic quantum correlations is comparable to or larger than the typical system energies, such as the hopping integral t. Among them there are the materials with partially filled d- or f-shells. The SIE acts on these systems by predicting localized d or f atomic-like electronic states with fractional instead of integer occupations.

The other main deficiency of LDA and GGA is the absence of the nonlocal component of the interactions, since they are based on local density and its local derivatives. In principle, the exchange-correlation potential obtained as the functional derivative of the exchange-correlation energy functional is nonlocal, as the Hartree potential or the exchange potential of the HF method. As a consequence, the long-range and nonlocal correlations characterizing the van der Waals interactions cannot be described.

The third rung of the Jacob's ladder is occupied by the meta-GGA functionals [249], that are complicated extensions of the GGA ones almost completely eliminating the SIE in the correlation part but still heavily suffering from it in the exchange part. For these reasons, they have not been used as much and are not as well tested as next rungs functionals. The fourth rung of the Jacob's ladder is occupied by the self-interaction correction (SIC) functionals [246], the hybrid functionals (e.g., B3LYP [250], PBE0 [251, 252], HSE06 [253]), and the DFT+U method [254–256], that have been the first ones to sensibly correct the SIE. SIC functionals were proposed as early as in 1981 by Perdew and Zunger, but they are not widely used. Hybrid functionals mix a fraction of the exact (Fock) exchange energy of the HF method, referred to as *mixing parameter* α, with GGA functionals. Unfortunately, in general, they are semiempirical methods, since the value of α depends on the hybrid functional [236] and could also depend on the material for a selected functional, as shown for HSE06 [257]. Moreover, they suffer from extremely demanding computational costs, limiting wider applications, and issues about the calculations of solid screening parameters controlling the exact exchange amount. Nevertheless, hybrid functionals almost completely eliminate the SIE. The DFT+U method is an alternative to them, depending on self-consistently calculated rather than semiempirical parameters [258] and showing a more affordable computational cost [259]. It consists into adding an on-site Hubbard-like interaction functional to the standard DFT

[11] The demonstration relies on the fact that the external potential and the Hartree potential are both continuous functionals of the electronic density.

(LDA/GGA) functional, in order to provide a piecewise linearity to the total energy as a function of the number of electrons. Such a method corrects SIEs for systems with localized d- and f-type electrons, even if mostly for ions with the latter, unlike the hybrid functionals. Recently, the DFT+U approach has also been extended to take into account inter-site Hubbard interactions [260], succeeding in describing materials with strong inter-site electronic hybridizations [261, 262]. The fifth rung of the Jacob's ladder is occupied by van der Waals functionals, that were proposed as both semiempirical dispersion corrections and nonlocal functionals starting from 2000s.

In this paragraph, I will describe DFT+U and nonlocal van der Waals (NL-vdW) functionals, that have been of utmost importance to describe the NM and magnetic van der Waals systems considered in this thesis work.

a) The DFT+U method

The DFT+U method is based on an additive correction to the standard DFT (LDA or GGA) energy functional based on the Hubbard model. The latter is the model Hamiltonian representing the natural theoretical framework to describe strongly correlated materials with partially filled d- or f-shells, such as transition metal, rare-earth, and actinide compounds. Indeed, by adding an on-site Coulomb repulsive energy U to the tight-binding model Hamiltonian, the Hubbard model takes into account the behaviors of both the ordinary band model and the atomic model related to the d- or f-type electrons [263], correctly predicting, for instance, the Mott insulating phases of materials with strongly repulsive electrons that should be conductors by band theory because of the odd number of electrons per unit cell. The simplest Hubbard model for a monoatomic basis lattice and only one kind of atomic orbital is described by the single-orbital Hubbard model Hamiltonian

$$\hat{H}_{so,Hub} = -\sum_{I\neq J,\sigma} t_{IJ}\hat{c}^{\dagger}_{I\sigma}\hat{c}_{J\sigma} + U\sum_{I}\hat{n}_{I\uparrow}\hat{n}_{I\downarrow}, \tag{2.53}$$

where t_{IJ} is the hopping integral between the I and J atomic sites, σ is the spin index, U is the screened on-site Coulomb electron-electron repulsive energy, and $\hat{c}^{\dagger}_{I\sigma}$ ($\hat{c}_{I\sigma}$) is the electron creation (annihilation) operator in the site I and with spin σ. In more complex systems, other parameters compose the Hubbard model Hamiltonian in addition to t_{IJ} and U. For instance, a just more complicated model is the multi-orbital Hubbard model Hamiltonian, that for d orbitals in a cubic lattice [264] is

$$\begin{aligned}\hat{H}_{mo-d,Hub} = &-\sum_{I\neq J,m,m',\sigma} t^{mm'}_{IJ}\hat{c}^{\dagger}_{Im\sigma}\hat{c}_{Jm'\sigma} + U\sum_{I,m}\hat{n}_{Im\uparrow}\hat{n}_{Im\downarrow} \\ &+\frac{1}{2}\sum_{I,m\neq m',\sigma}[(U-2J)\hat{n}_{Im\sigma}\hat{n}_{Im'-\sigma} + (U-3J)\hat{n}_{Im\sigma}\hat{n}_{Im'\sigma}] \\ &+\frac{1}{2}J\sum_{I,m\neq m',\sigma}(\hat{c}^{\dagger}_{Im\sigma}\hat{c}^{\dagger}_{Im'-\sigma}\hat{c}_{Im-\sigma}\hat{c}_{Im'\sigma} + \hat{c}^{\dagger}_{Im\sigma}\hat{c}^{\dagger}_{Im-\sigma}\hat{c}_{Im'-\sigma}\hat{c}_{Im'\sigma}),\end{aligned} \tag{2.54}$$

where m and m' are projections of the orbital momentum ($m, m' = -2, -1, ..., 2$ in the case of d-electrons), and the Hund's exchange parameter J appears to describe the exchange interaction. In Eq. (2.54), the terms containing U alone describe intra-orbital Coulomb interactions, while the terms also containing J describe inter-orbital Coulomb interactions, where the last sum has a spin-flip term and a pair-hopping term, describing two-electron transfers from an orbital to other orbitals.

The energy functional of the DFT+U method [254–256] reads

$$E_{DFT+U} = E_{DFT} + E_U. \tag{2.55}$$

Here, E_{DFT} represents the approximate LSDA or σ-GGA DFT energy, and E_U contains the additional Hubbard term. Eq. (2.54) suggests that the latter depends on both U and J, that, in general, should depend on the atomic species. In the simplified rotationally invariant formulation by Sergei L. Dudarev *et al.* [265], the Hubbard term is

$$E_U = \frac{1}{2} \sum_{I,\sigma,m,m'} U^I_{eff} (\delta_{mm'} - n^{I\sigma}_{mm'}) n^{I\sigma}_{m'm}, \tag{2.56}$$

where $U^I_{eff} = U^I - J^I$ is the effective screened on-site Coulomb repulsive energy and

$$n^{I\sigma}_{mm'} = \sum_{\mathbf{k}}^{N_\mathbf{k}} \sum_{v} f_{v,\mathbf{k},\sigma} \left\langle \varphi_{v,\mathbf{k},\sigma} \middle| \psi^J_{m'} \right\rangle \left\langle \psi^I_m \middle| \varphi_{v,\mathbf{k},\sigma} \right\rangle \tag{2.57}$$

is the element of an atomic occupation matrix, where $\mathbf{k}$ is a point in the first BZ, $N_\mathbf{k}$ is the number of $\mathbf{k}$-points in the first BZ, $f_{v,\mathbf{k},\sigma}$ is the occupation of the KS state $\varphi_{v,\mathbf{k},\sigma}$[12] (it is fractional to account for metals), and $\psi^I_m(\mathbf{r}) \equiv \psi^{\gamma(I)}_m(\mathbf{r} - \mathbf{R}_I)$ is a localized orbital centered on the Ith atom of type $\gamma(I)$ ath the position $\mathbf{R}_I$. Essentially, the matrix elements $n^{I\sigma}_{mm'}$'s are based on a generalized projection of the KS states on localized orbitals of neighbor atoms. The Hubbard manifold $\{\psi^I_m\}$ can be constructed from the nonorthogonalized atomic orbitals (which are provided with the pseudopotentials defined in Sec. 2.3.2 and which are orthonormal within each atom) or from the orthogonalized atomic orbitals (which are obtained by orthogonalizing the atomic orbitals from different sites). The term corresponding to the functional derivative of the energy functional of Eq. (2.55) with respect to the complex conjugate of the KS state is

$$v^\sigma_{Hub} = \sum_{I,m,m'} U^I_{eff} \left(\frac{\delta_{mm'}}{2} - n^{I\sigma}_{mm'} \right) \left| \psi^J_{m'} \right\rangle \left\langle \psi^I_m \right|. \tag{2.58}$$

Hence, the DFT+U method by Dudarev *et al.* provides a set of Kohn-Sham self-consistent equations depending on the effective screened on-site Coulomb repulsive energies U^I_{eff}'s as the only new parameters compared to the standard DFT approximations.

The final success of the DFT+U method relies on the calculation of the parameters U^I_{eff}'s. This can be done either by fitting the theoretical predictions to some experimental data or by means of a self-consistent procedure. Since the effective screened on-site Coulomb repulsive energies reflect intrinsic properties of the strongly correlated material, the fitting approach should be considered just when a very stringent agreement with the experimental data is required, since it is neither predictive nor fully ab initio. Hence, a calculation from first-principles is the best way to proceed. In the framework of the linear-response constrained DFT (LR-cDFT), Matteo Cococcioni *et al.* [266] formulated a definition of U^I_{eff} restoring the desired piecewise linearity of the total energy. By adding a perturbation $\hat{V}^J_{pert} = \alpha_J \sum_m \left| \psi^J_m \right\rangle \left\langle \psi^J_m \right|$ on the Jth atom to the KS equations, the initial total energy of the system E^0_{DFT+U} changes up to E_{DFT+U} because of the self-consistent system readjustment to optimally screen

[12] The quantum numbers of the KS orbital identify it as a Bloch state of the crystal, as it will be explained in Sec. 2.3.1.

the localized perturbation, and the desired definition is

$$U^I_{eff} = \frac{d^2 E_{DFT+U}}{d(n^I)^2} - \frac{d^2 E^0_{DFT+U}}{d(n^I)^2}. \tag{2.59}$$

Since the linear-response (LR) theory relates the total energies to the susceptibility matrices as

$$\frac{d^2 E_{DFT+U}}{d(n^I)^2} = -\frac{d\alpha^I}{dn^I} = -(\chi^{-1})_{II}, \quad -\frac{d^2 E^0_{DFT+U}}{d(n^I)^2} = -\frac{d\alpha^I}{dn^I} = -(\chi_0^{-1})_{II}, \tag{2.60}$$

Eq. (2.59) becomes

$$U^I_{eff} = (\chi_0^{-1} - \chi^{-1})_{II}. \tag{2.61}$$

According to a many-body complementary view, Eq. (2.61) can be read as the solution of the Dyson equation for the self-consistent susceptibility χ, where U^I_{eff} acts as the interaction kernel[13]. Ref. [266] considers a perturbation acting on a supercell, to avoid the spurious interactions, and finite differences for computing the response quantities in Eq. (2.60). Instead, the recent work by Iurii Timrov *et al.* [269] recasts the LR-cDFT via *density functional perturbation theory* (DFPT) to treat the isolated perturbation in the supercell as a sum of monochromatic perturbations in a primitive cell of reciprocal **q**-space, besides not to need finite differences. Therefore, even if a **q**-point grid is added to the **k**-point grid, the absence of a supercell reduces the computational cost, in addition to a linear scaling with respect to the number of **q** points. Also, DFPT approach makes such a calculation robust, automatic, and user-friendly. Nevertheless, DFPT and LR-cDFT approaches have the shared limitation that they are applicable only to open-shell systems.

b) The nonlocal van der Waals exchange-correlation functionals

The scheme to include van der Waals interactions as London dispersion forces has been recently introduced by Dion *et al.* [270]. The exchange-correlation functional is written as sum of a SL or hybrid exchange-correlation functional and a long-range and nonlocal correlation functional [271, 272], i.e.,

$$E_{xc} = E_{xc}^{SL/hybrid} + E_{c,disp}^{NL}, \tag{2.62}$$

where the latter has the expression

$$E_{c,disp}^{NL} = \frac{1}{2} \int d^3r \int d^3r' n(\mathbf{r}) \Phi(\mathbf{r}, \mathbf{r}') n(\mathbf{r}') \tag{2.63}$$

and describes the London dispersion through the kernel $\Phi(\mathbf{r}, \mathbf{r}')$. Formally, the functional $E_{c,disp}^{NL}$ contributes to the binding energy between two systems A and B even when the contribution of $E_{xc}^{SL/hybrid}$ is negligible ($n_A(\mathbf{r}) n_B(\mathbf{r}) = 0 \; \forall \mathbf{r}$). As an example, in the particular case of the vdW-DF functional by Dion *et al.*, the first term of Eq. (2.62) is the sum of the LDA correlation functional and the revPBE exchange functional:

$$E_{xc}^{vdW-DF} = E_c^{LDA} + E_x^{revPBE} + E_{c,disp}^{NL}. \tag{2.64}$$

[13] This is exactly the expression of reciprocal-space susceptibility within the well-known random-phase approximation (RPA) [267, 268] of the LR theory, where the bare Coulomb interaction acts as the interaction kernel.

Nowadays, the solid-state community can count on five different analytical expressions of the kernel Φ, characterizing the vdW-DF [270], VV09 [273], VV10 [274], rVV10 [275], PBEsol+rVV10s [276] functionals. Moreover, there are several reoptimizations of the parameters in Φ [277–281]. Nevertheless, the so-called *chemical accuracy* of 1 kcal/mol is not systematically reached [282, 283]. In general, the kernel Φ depends on $n(\mathbf{r})$, $\boldsymbol{\nabla} n(\mathbf{r})$, and $|\mathbf{r} - \mathbf{r}'|$.

The DFT analysis of the materials explored in this thesis has been carried out through different nonlocal vdW exchange-correlation functionals, depending on the needs. Here, we only summarize their features, motivating their choices only in Chap. 4. The structural and electronic properties of TBG have been analyzed by using the vdW-DF2 functional by Kyuho Lee *et al.* [279], the latter being the second version of vdW-DF by Dion *et al.*. It was introduced to reduce the interatomic distances overastimated by the vdW-DF functional. In particular, the PW86 exchange functional replaces the revPBE one, since the latter is too repulsive near the equilibrium distances, and a large-N asymptote gradient correction [284] is used to compute the vdW kernel, in order to take better into account the contributions of the exponentially decaying atomic tails in molecular systems to the vdW attraction. As a result, it improved the description of polarizability for highly inhomogeneous low-density region, the accuracy for molecular dimers, and, in general, the attractive vdW interactions near the equilibrium over the original vdW-DF, also predicting reasonable values of binding energies compared to the experiments. Nevertheless, the residual overestimation issues required the development of novel exchange-correlation functionals. Calculations for the twisted HeBL $MoS_2/NbSe_2$ work [203] were carried out by using the vdW-DF2-C09 exchange-correlation functional by Ikutaro Hamada [285], that adds the C09 exchange functional ($C09_x$) by Valentino R. Cooper [286] to the vdW-DF2 correlation functional. Such a functional was chosen due to the satisfactory agreement with both the experimental data on the graphene adsorption on (111) metal surfaces, such as Ni, Cu, Pd, Ag, Au, and Pt [285, 287, 288], the experimental binding energies and structural properties of semiconducting SnS_2 stacked nanosheets [289], and, more properly for a metal-semiconductor HeBL as $MoS_2/NbSe_2$, the experimental structural corrugation of h-BN on a Ir(111) metal surface [290]. Furthermore, the vdW-DF2-C09 functional has been preferred to the vdW dispersion correction DFT-D [291] used for the previous report on untwisted HeBL $MoS_2/NbSe_2$, since the latter is a semiempirical method. For the first work on ML and MuL Nb_3I_8, the performances of the most recent rev-vdW-DF2 or vdW-DF2-B86R exchange-correlation functional by Hamada [292] was tested compared to vdW-DF2-C09, providing better results in the cases of interest. Further confirmations are reported in literature, since rev-vdW-DF2 provides accurate values of lattice constant and cohesive energy of rare-gas solids (Ne, Ar, Kr, and Xe), reasonably small errors for intralayer and interlayer lattice constants and interlayer binding energy of hexagonal layered solids (graphite, h-BN, TiS_2, $TiSe_2$, MoS_2, $MoSe_2$, $MoTe_2$, $HfTe_2$, WS_2, WSe_2), and the smallest errors for the lattice constant and cohesive energy of molecular solids (NH_3, CO_2, $C_6H_{12}N_4$) [293]. As a consequence, the rev-vdW-DF2 functional has been finally employed for the second work on ML and MuL Nb_3I_8. Since it is one of the most accurate vdW functionals available today, I will only describe it in detail below.

The rev-vdW-DF2 exchange-correlation functional proposed by Hamada adds a revised version of the GGA exchange functional proposed by Becke (B86b) [294], named as B86R, to the nonlocal vdW-DF2 correlation functional:

$$E_{xc}^{rev-vdW-DF2} = E_x^{SL,B86R} + E_c^{NL,vdW-DF2}. \tag{2.65}$$

The B86R exchange functional has been designed to satisfy two properties:

- second-order gradient expansion approximation (GEA) [215] at the slowly varying density limit, i.e., $F_x(s) = 1 + \mu_{GEA} s^2$, where $\mu_{GEA} = 10/81$ [295];
- $s^{2/5}$ dependence of $F_x(s)$ at the inhomogeneous limit (large gradient limit).

The first requirement allows to predict accurate equilibrium geometries, in particular, for solids and surfaces [296], and was already used in other exchange functionals for vdW-DF, such as C09$_x$ [286] and optB88-vdW [282, 297]. The second requirement is needed to reproduce the Hartree-Fock exchange interaction curves beyond binding separations and, thus, to avoid the spurious binding from exchange only, and was already fulfilled by PW86 [241] and B86b [294] exchange functionals [298]. The enhancement factor of B86R functional is

$$F_x(s) = 1 + \frac{\mu s^2}{(1 + \mu s^2/\kappa)^{4/5}}, \quad \mu = \mu_{GEA}, \quad \kappa = 0.7114. \tag{2.66}$$

2.2 Relativistic theory

The non-relativistic formulation of the density functional theory, presented in Sec. 2.1, does not include spin and relativistic effects. However, a wide variety of properties of materials crucially depends on the latter, thus requiring a more complete theoretical framework. For instance, relativistic effects are essential in heavy atoms, where core electrons exhibit velocities being appreciable fractions of the speed of light. Moreover, the spin-orbit interaction splits bands that would be otherwise degenerate, and the particular form of this splitting depends on the system.

In this section, I will give an introduction to the relativistic formalism of the many-body electronic problemby presenting a relativistic generalization of the density functional theory.

2.2.1 The Dirac-Hohenberg-Kohn formulation of the Relativistic Density Functional Theory

A few years after the formulation of DFT, a relativistic extension, including both non-magnetic and magnetic systems, was proposed [299, 300]. The basic variables of the relativistic DFT are the charge and the vector-current densities. Rajagopal and Callaway showed [300] that the HK theorems could be generalized by including the relativistic effects. This led to the so-called Dirac-Hohenberg-Kohn (DHK) theorems. Exactly as in the non-relativistic version of DFT, the energy is seen as a density functional, named as the *Dirac-Hohenberg-Kohn energy functional*. Moreover, as in the spin-polarized non-relativistic DFT, the latter can be writtenas a functional dependent on the electronic density $n(\mathbf{r})$ and the magnetization density $\mathbf{m}(\mathbf{r})$, i.e., $E_{DHK} = E_{DHK}[n(\mathbf{r}), \mathbf{m}(\mathbf{r})]$. One can prove that the ground-state energy is a unique functional of the ground-state electronic density and magnetization density, provided that the system is not subject to an external magnetic field, as shown in Ref. [301]. This means that the system can be completely described by its electronic density and magnetization density.

2.2.2 The Dirac-Kohn-Sham equations

Similarly to spin-polarized DFT formulation, electronic density and magnetization density can be grouped in the hermitian matrix $\tilde{N}(\mathbf{r})$ [302] with elements

$$\tilde{N}'_{\eta_1\eta_2}(\mathbf{r}) = \sum_i^{occ} \psi'^{*}_{i,\eta_2}(\mathbf{r})\psi'_{i,\eta_1}(\mathbf{r}), \tag{2.67}$$

where

$$n'(\mathbf{r}) = tr\tilde{N}'(\mathbf{r}), \quad \mathbf{m}'(\mathbf{r}) = \mu_{\mathcal{B}} tr(\beta\boldsymbol{\Sigma}\tilde{N}'(\mathbf{r})). \tag{2.68}$$

In particular, β is a matrix of the set of the standard-representation Dirac matrices

$$\alpha_i = \begin{pmatrix} \mathbb{O}_2 & \sigma_i \\ \sigma_i & \mathbb{O}_2 \end{pmatrix} = \sigma_1 \otimes \sigma_i, \quad \beta = \begin{pmatrix} \mathbb{I}_2 & \mathbb{O}_2 \\ \mathbb{O}_2 & -\mathbb{I}_2 \end{pmatrix} = \sigma_3 \otimes \mathbb{I}_2, \tag{2.69}$$

whereas

$$\boldsymbol{\Sigma} = \begin{pmatrix} \boldsymbol{\sigma} & \mathbb{O}_2 \\ \mathbb{O}_2 & \boldsymbol{\sigma} \end{pmatrix} = \boldsymbol{\sigma} \otimes \mathbb{I}_2 \tag{2.70}$$

is the matrix defining the spin $\mathbf{S} = (\hbar/2)\boldsymbol{\Sigma}$ in the Dirac equation formalism. The occupied states i in the sum of Eq. (2.67) are positive-energy states only. The kinetic energy functional of the auxiliary relativistic system of non-interacting electrons is

$$T_s[\tilde{N}'_{\eta_1\eta_2}] = \sum_i^{occ} \sum_{\eta_1,\eta_2} \left\langle \psi'_{i,\eta_1} \middle| \hat{T}_D \middle| \psi'_{i,\eta_2} \right\rangle, \tag{2.71}$$

with the Dirac kinetic energy operator

$$\hat{T}_D = c(\boldsymbol{\alpha} \cdot \hat{\mathbf{p}}) + (\beta - \mathbb{I}_4)mc^2\hat{\mathbb{I}}_4. \tag{2.72}$$

The DHK energy functional is

$$E_{DHK}[\tilde{N}'_{\eta_1\eta_2}] = T_s[\tilde{N}'_{\eta_1\eta_2}] + E_H[n'] + E_{xc}[\tilde{N}'_{\eta_1\eta_2}] + \int v(\mathbf{r})n'(\mathbf{r})d^3r \tag{2.73}$$

and the DKS equations are

$$\sum_{\eta_2} \{[T_{D,\eta_1\eta_2}(\mathbf{r}) + v_{DKS}(\mathbf{r})\delta_{\eta_1\eta_2} - \mu_{\mathcal{B}}(\beta\boldsymbol{\Sigma})_{\eta_1\eta_2} \cdot \mathbf{B}_{xc}(\mathbf{r})]\psi_{i,\eta_2}(\mathbf{r})\} = \epsilon_i\psi_{i,\eta_1}(\mathbf{r}), \tag{2.74}$$

where

$$v_{DKS}(\mathbf{r}) = v_H(\mathbf{r}) + v_{xc}(\mathbf{r}) + v(\mathbf{r}), \quad \frac{\delta E_{xc}[\tilde{N}_{\eta_1\eta_2}]}{\delta n(\mathbf{r})}. \tag{2.75}$$

In addition to the many-particle exchange and correlation effects of the non-relativistic formalism, the exchange-correlation functional $E_{xc}[\tilde{N}'_{\eta_1\eta_2}]$ of Eq. (2.73) takes also into account the relativistic effects, such as the retarded Liénard-Wiechert potentials and the coupling between electron magnetic dipole moments. The DKS eigenvalues ϵ_i's are the Lagrange multipliers related to the constraint

$$\sum_{\eta} \langle \psi_{i,\eta} | \psi_{j,\eta} \rangle = \delta_{ij}. \tag{2.76}$$

Finally, the exchange-correlation magnetic field

$$\mathbf{B}_{xc}(\mathbf{r}) = -\frac{\delta E_{xc}[\tilde{N}_{\eta_1\eta_2}]}{\delta \mathbf{m}(\mathbf{r})} \tag{2.77}$$

naturally arises from the minimization of the DHF energy functional of Eq. (2.73).

2.2.3 Approximations for the exchange-correlation functional

As in the non-relativistic case, the exchange-correlation functional $E_{xc}[\tilde{N}_{\eta_1\eta_2}]$ requires an approximation to calculate the electronic density, the magnetization density, and the ground-state energy through the relativistic DFT. The relativistic extension of the exchange-correlation functional approximations is still matter of research [303–305], with a more solid formalism only on the exchange contribution to the relativistic extension of LDA (RLDA) [299, 300] and GGA (RGGA) [306]. Practice shows that the non-relativistic versions of the exchange-correlation functionals can be reliably used for relativistic calculations due to the small differences with respect to the relativistic versions. This has been demonstrated on both single atoms [307] and solids [308, 309].

2.3 Computational implementation of the theory

The practical resolution of the KS equations, in both non-relativistic and relativistic formulations, requires a suitable basis set to expand the KS wavefunctions. Since this thesis focuses on the description of solids, the plane-wave basis set is the recommended choice, since it takes the periodicity of the electron wavefunctions, despite some computational disadvantages. Among the latter, there is the large number of plane waves (PWs) required to describe the rapid oscillations of the electron wavefunctions near the atomic nuclei, even if this problem is easily overcome by using the pseudopotential (PP) approximation. I will describe all these concepts in Secs. 2.3.2 and 2.3.3, taking the non-relativistic case for the sake of simplicity. In this thesis, unless differently specified, the simulations were carried out in a first-principles calculations framework by means of the Quantum-ESPRESSO (QE) package [310–312], that is an integrated software suite for electronic structure atomistic simulations based on PPs to represent the atomic cores and PWs to represent the KS states and the electronic density. In Secs. 2.3.4, 2.3.5, and 2.3.6, I will describe the implementation of the iterative and self-consistent resolution of the KS equations in QE and similar packages.

2.3.1 Plane-wave basis set

The atomic arrangement in perfect crystals is described by a periodically repeated unit cell. In the following, I will assume that the crystalline system is characterized by a Bravais or direct lattice of vectors $\mathbf{R}$, that connect different unit cells defined by the Bravais lattice basis vectors $\mathbf{a}_1$, $\mathbf{a}_2$, $\mathbf{a}_3$ and are expressed as linear combinations $\mathbf{R} = n_1\mathbf{a}_1 + n_2\mathbf{a}_2 + n_3\mathbf{a}_3$ through the integer numbers n_i's. Moreover, the reciprocal lattice, only related to the symmetries of the Bravais lattice, has vectors $\mathbf{G}$, that can be expressed as linear combinations $\mathbf{G} = m_1\mathbf{b}_1 + m_2\mathbf{b}_2 + m_3\mathbf{b}_3$ of the reciprocal lattice basis vectors

$$\mathbf{b}_1 = \frac{2\pi}{\Omega}\mathbf{a}_2 \times \mathbf{a}_3, \quad \mathbf{b}_2 = \frac{2\pi}{\Omega}\mathbf{a}_3 \times \mathbf{a}_1, \quad \mathbf{b}_3 = \frac{2\pi}{\Omega}\mathbf{a}_1 \times \mathbf{a}_2, \tag{2.78}$$

with the unit cell volume $\Omega = \mathbf{a}_1 \cdot (\mathbf{a}_2 \times \mathbf{a}_3)$, through the integers m_i's. Hence, the crystal potential $v(\mathbf{r})$ is a periodic function with periodicity $\mathbf{R}$, i.e., $v(\mathbf{r}+\mathbf{R}) = v(\mathbf{r})$, that is the same as that of the crystal. According to the *Bloch theorem*[14] [313], an electron moving in the periodic potential $v(\mathbf{r})$ can be described by a wavefunction of the form

$$\varphi_{n,\mathbf{k}}(\mathbf{r}) = e^{i\mathbf{k}\cdot\mathbf{r}} u_{n,\mathbf{k}}(\mathbf{r}), \tag{2.79}$$

where n is the band index, $\mathbf{k}$ is the point in the BZ, $e^{i\mathbf{k}\cdot\mathbf{r}}$ is a plane wave, and $u_{n,\mathbf{k}}(\mathbf{r})$ is a function having the periodicity of the crystal, i.e., $u_{n,\mathbf{k}}(\mathbf{r}) = u_{n,\mathbf{k}}(\mathbf{r}+\mathbf{R})$. The theorem implies that all the important properties of the crystal can be studied within the unit cell. Each solid is described by a specific set of KS equations (see Eq. (2.23)) with a specific periodic KS potential $v_{KS}(\mathbf{r})$. The PW basis set is the recommended choice to expand the KS equations for the Bloch electrons, where the index i collectively indicates the pair $(n, \mathbf{k})$. Indeed, since $\mathbf{R}\cdot\mathbf{G} = 2\pi l$ for each integer l, the periodicity of $u_{n,\mathbf{k}}(\mathbf{r})$ allows to write

$$u_{n,\mathbf{k}}(\mathbf{r}) = \sum_{\mathbf{G}} c_{n,\mathbf{k}+\mathbf{G}} e^{i\mathbf{G}\cdot\mathbf{r}}, \tag{2.80}$$

where the summation runs over all the possible values of the integers m_i's defining $\mathbf{G}$, and $c_{n,\mathbf{k}+\mathbf{G}}$ are the expansion coefficients. Therefore, the electron wavefunction becomes

$$\varphi_{n,\mathbf{k}}(\mathbf{r}) = \sum_{\mathbf{G}} c_{n,\mathbf{k}+\mathbf{G}} e^{i(\mathbf{k}+\mathbf{G})\cdot\mathbf{r}}. \tag{2.81}$$

and the related KS equation reads

$$\sum_{\mathbf{G}} c_{n,\mathbf{k}+\mathbf{G}} \left[\frac{\hbar^2}{2m} |\mathbf{k}+\mathbf{G}|^2 \delta_{\mathbf{G}',\mathbf{G}} + v_{KS}(\mathbf{G}-\mathbf{G}') \right] = \epsilon_{n,\mathbf{k}} c_{n,\mathbf{k}+\mathbf{G}'}, \tag{2.82}$$

where the KS potential has been Fourier-transformed. In principle, the resolution of Eq. (2.82) at each $\mathbf{k}$-point requires an infinite number of possible values of $\mathbf{G}$. In practice, the infinite sum over $\mathbf{G}$ is usually truncated, in order to include PWs with kinetic energy values less than some kinetic-energy cutoff E_{cut}:

$$\frac{\hbar^2}{2m} |\mathbf{k}+\mathbf{G}|^2 < E_{cut}, \quad \frac{\hbar^2}{2m} G_{cut}^2 = E_{cut}. \tag{2.83}$$

This procedure provides a simple control over the convergence of the meaningful physical quantities, which is simply based on the increase of the kinetic-energy cutoff. Hence, the solutions of Eq. (2.82) can be found by diagonalizing the Hamiltonian matrix, whose elements are enclosed in the square brackets and have a very simple form. The dimension of the matrix depends upon the kinetic-energy cutoff.

Despite these huge computational advantages with respect to other basis sets (e.g., localized basis sets as Gaussian-type orbitals), PW basis sets has also some disadvantages. Indeed, the extended character of PWs makes it very difficult to accurately reproduce localized functions, such as the charge density around a nucleus. In general, the number of PWs required to get a satisfactory convergence of the important quantities can quickly become prohibitive for most of the systems of interest. This difficulty is actually overcome by using the *pseudopotential approximation*.

[14] It is a direct consequence of the translational symmetry of the crystal.

2.3.2 Pseudopotential approximation

The pseudopotential approximation eliminates the core electrons and the strong oscillations of the valence-electron wavefunctions within the core region of core radius r_c by replacing the all-electron potential, i.e., the nuclear Coulomb potential felt by all the electrons outside the core region, with an effective and smoother potential of a suitable pseudo-ion, i.e., a suitable pseudopotential [314].

The first step of the pseudopotential approximation is the *frozen core approximation*, based on the fact that many physical and chemical properties of materials are determined by the valence electrons much more than by the core electrons. Indeed, valence electrons play a crucial role both in the formation of chemical bonds and in determination of the properties of materials, such as optical and transport effects. Conversely, core electrons do not contribute to these properties, since they are largely unaffected by the environment. Therefore, one can reliably assume that the core electrons and the corresponding density are independent of the chemical environment and any external perturbation of the atom, i.e., the core KS wavefunctions can be taken identical to the atomic core states. As a consequence, the core electrons are considered together with the nuclei as rigid non-polarizable ion cores, and KS equations have to be solved only for the valence electrons. Obviously, avoiding to calculate the core KS wavefunctions is a great computational advantage, since the sharply peaked behavior of core-electron states close to nuclei requires a huge number of PWs to be properly reproduced.

The second step is the effective removal of the core electrons and the strong oscillations of the valence-electron wavefunctions within the core region, that is needed in order to further reduce the required number of PWs. Despite the screening effect of the core electrons on the nuclear charge, the ionic potential still has a Coulomb singularity at the nucleus position due to the nuclear Coulomb potential $-Ze^2/|\mathbf{r}-\mathbf{R}|$ (see Fig. 2.1). As a consequence, the valence-electron wavefunctions strongly oscillate in the core region with several nodes related to the orthogonality to core wavefunctions, thus requiring an extremely large number of PWs to be reproduced. Therefore, the nuclear Coulomb potential is replaced by a pseudopotential including all the effects induced by the core electrons (potential of the nucleus, the screening and repulsion by these electrons), reproducing the true scattering potential outside the core region, and being a slowly variable function inside the latter resulting from the cancellation effect of the intense crystalline potential. This cancellation effect is equivalent to the elimination of core states. The valence-electron wavefunctions calculated by solving the KS equations including the pseudopotential, i.e., the valence-electron pseudo-wavefunctions, are smooth functions, as shown in Fig. 2.1.

The first introduced PP was the norm-conserving (NC) kind by Hamann *et al.* [315]. NC-PPs fulfill the following conditions:

- KS eigenvalues of the all-electron wavefunctions (both valence and core ones) and pseudo-wavefunctions must be the same;
- all-electron wavefunctions and pseudo-wavefunctions must be identical outside the core region, whose radius r_c is usually located around the outermost maximum of the atomic wavefunction;
- the true electronic density and the pseudo-density must be identical within the core region;
- they must have the same scattering properties (or phase shifts) of the true potential.

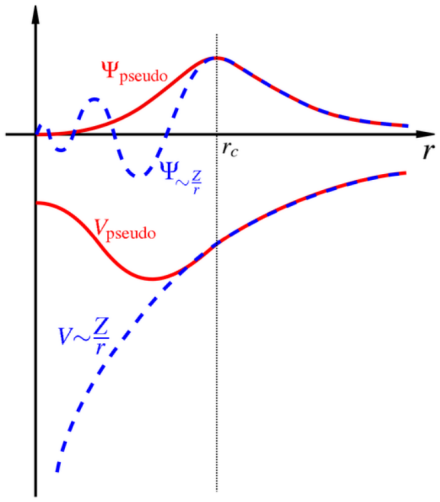

FIGURE 2.1: Schematic illustration of the replacement of the true potential $V(r) \sim Z/r$ and true valence-electron wavefunction $\Psi_{\sim Z/r}$ by a fictitious pseudopotential $V_{pseudo}(r)$ and valence-electron pseudo-wavefunction Ψ_{pseudo}, respectively. For $r > r_c$, PPs and wavefunctions become identical.

The norm-conservation of such PPs refers to the third condition, since the latter holds if the norm of each pseudo-wavefunction is identical to its corresponding all-electron wavefunction for $r < r_c$. NC-PPs are transferable, i.e., they reproduce the scattering properties of the true potential in a wide range of energy, and relatively smooth. Nevertheless, they are still hard, i.e., they still require a large basis-set size. The ultrasoft (US) PPs were formulated by Vanderbilt to overcome such problem [316]. They are based on a generalized eigenvalue problem arising from the non-zero differences in norms (relaxation of the norm-conservation condition), leading to kinetic-energy cutoffs appreciably smaller than the NC-PPs ones. Afterwards, Blöchl introduced the projector augmented-wave (PAW) method [317], that was later adapted for plane-wave calculations by Kresse and Joubert [318]. NC- and US-PPs result as approximations of the PAW method [319]. Of all the works on which this thesis is based, only the calculations of the work on twisted HeBL $MoS_2/NbSe_2$ [203] were carried out by using US-PPs, then choosing PAW-PPs for all the next works. The reason is that the Wannier90 (W90) package [320] was employed in that case, that allows to calculate maximally localized Wannier functions (MLWFs) in combination with electronic codes based on PWs and PPs, such as QE, by using only NC- and US-PPs. However, it has been demonstrated that solid-state US- and PAW-PPs give essentially identical results in many cases [321, 322], which are also in good agreement with all-electron calculations. Therefore, I will briefly discuss only the principles of the PAW method.

a) Projector augmented-wave method

The PAW method provides the pseudo KS equations to calculate the (numerically convenient) auxiliary smooth valence-electron pseudo-wavefunctions, starting from the definition of a particular linear transformation connecting the latter to the true all-electron KS single-particle wavefunctions. Formally, if $|\Psi\rangle$ is a true all-electron KS state and $|\tilde{\Psi}\rangle$ is an auxiliary smooth pseudo-state, the linear transformation $\hat{T}$ is defined as

$$|\Psi\rangle = \hat{T}\,|\tilde{\Psi}\rangle\,. \tag{2.84}$$

Since $|\Psi\rangle$ is solution of the KS equation $\hat{H}_{KS}|\Psi\rangle = \epsilon_{KS}|\Psi\rangle$, the pseudo KS equation is

$$\hat{T}^{\dagger}\hat{H}_{KS}\hat{T}\left|\tilde{\Psi}\right\rangle = \epsilon_{KS}\hat{T}^{\dagger}\hat{T}\left|\tilde{\Psi}\right\rangle. \tag{2.85}$$

The transformation $\hat{T}$ should only modify the auxiliary states in Eq. (2.84) only within the core region because the true valence-electron states are already smooth outside. Therefore, it can be defined as

$$\hat{T} = \hat{\mathbb{1}} + \sum_{\mathbf{R}} \hat{T}_{\mathbf{R}}, \tag{2.86}$$

where $\hat{T}_{\mathbf{R}}$ is non-zero only within some spherical augmentation region $\Omega_{\mathbf{R}}$ with radius $r_c^{\mathbf{R}}$ and the atom at $\mathbf{R}$ as center. The radii must be chosen such that there is no overlap of the augmentation spheres. The formal definition in Eq. (2.86) can be conveniently turned in a more practical expression. Inside the augmentation spheres, the true state $|\Psi\rangle$ can be expanded in the partial waves $|\phi_i\rangle$, and for each of these partial waves, it is possible to define a corresponding auxiliary smooth pseudo-partial wave $|\tilde{\phi}_i\rangle$ to expand the auxiliary smooth pseudo-state $\left|\tilde{\Psi}\right\rangle$:

$$|\Psi\rangle = \sum_i c_i |\phi_i\rangle, \quad \left|\tilde{\Psi}\right\rangle = \sum_i c_i |\tilde{\phi}_i\rangle, \quad \mathbf{r} \in \Omega_{\mathbf{R}}. \tag{2.87}$$

The linear nature of the transformation $\hat{T}$ requires that the coefficients c_i are linear functionals of the pseudo-states. Hence, the coefficients are scalar products

$$c_i = \left\langle \tilde{p}_i \middle| \tilde{\Psi} \right\rangle \tag{2.88}$$

of the pseudo-state with some fixed state $|\tilde{p}_i\rangle$, that is named as projector state. The latter must fulfill the condition

$$\sum_i |\tilde{\phi}_i\rangle \langle \tilde{p}_i| = 1, \quad \mathbf{r} \in \Omega_{\mathbf{R}}, \tag{2.89}$$

so that the expansion $\sum_i |\tilde{\phi}_i\rangle \left\langle \tilde{p}_i \middle| \tilde{\Psi} \right\rangle$ is identical to $\left|\tilde{\Psi}\right\rangle$. This implies that

$$\left\langle \tilde{p}_i \middle| \tilde{\phi}_j \right\rangle = \delta_{ij}. \tag{2.90}$$

Starting from the Eqs. (2.84) and (2.87), one has

$$\hat{T}\left|\tilde{\Psi}\right\rangle = \sum_i c_i |\phi_i\rangle, \tag{2.91}$$

from which the addition and removal of $\left|\tilde{\Psi}\right\rangle$ gives

$$\hat{T} = \hat{\mathbb{1}} + \sum_i \left(|\phi_i\rangle - |\tilde{\phi}_i\rangle\right) \langle \tilde{p}_i|. \tag{2.92}$$

Hence, the transformation $\hat{T}$ is expressed in terms of three "external functions": the partial waves, the pseudo-partial waves, and the projector states. If the latter are known, then Eq. (2.85) can be solved to find the auxiliary smooth valence-electron pseudo-wavefunctions. Obviously, different implementations of the PAW method rely on the very large degree of freedom when choosing such functions, even if the latter should always be finite and ensure fast and reliable convergence. The partial waves can be chosen as the eigenstates of the KS Schrödinger equation for the isolated spin-saturated atoms. In particular, by considering a spherical KS potential,

they would read

$$\phi_i(\mathbf{r}) = R_{nl}(r)Y_l^m(\theta,\varphi), \tag{2.93}$$

where $R_{nl}(r)$ are the eigenstates of the radial KS Schrödinger equation and $Y_l^m(\theta,\varphi)$ are the spherical harmonics, i.e., eigenstates of the Laplacian. As far as the pseudo-partial waves are concerned, they must be chosen identical to the partial waves outside the augmentation spheres and can be any computationally convenient smooth continuation inside. Finally, the projector states can be chosen as a finite set of states satisfying the orthonormality condition of Eq. (2.90).

2.3.3 The supercell method

Bloch theorem is not applicable if the perfect periodicity is absent, though the system is either approximately periodic or periodic in one or two directions or periodic except for a small part. As an example, 2D materials, that are the systems studied in this thesis, break the three dimensional translational symmetry, both as single-layer and multilayer structures. The breaking of perfect periodicity makes PWs as unsuitable basis functions, since the discontinuity in the perpendicular direction to the 2D material would require an infinite number of PWs to be properly treated.

The solution of the problem of broken periodicity is to simulate the system with a periodically repeated larger cell, named as supercell, where the periodicity is artificially restored and the 2D materials are far apart. Form and size of the supercell depend on the physical system being studied. For 2D materials, one uses a crystal slab alternated with a slab of empty space (see Fig. 2.2), both large enough to ensure that the bulk behavior is recovered inside the crystal slab and that the 2D behavior is unaffected by the presence of the periodic replica of the crystal slab. The great advantage of supercell calculations is that the periodic boundary conditions allow the utilization of the many efficient techniques derived for the quantum physics of periodic systems. The wavevectors of the BZ in the reciprocal space of the supercell are good quantum numbers, and the standard "band-structure methods" of periodic solids can be applied in full force. The size of the unit cell, intended as the number of atoms and the volume, is of utmost importance. Indeed, together with the type of the atoms, it determines the computational cost of the calculation: large unit cells mean large calculations. Unfortunately, many interesting physical systems are described, exactly or approximately, by large unit cells.

2.3.4 Brillouin-Zone and Fermi surface sampling

According to Eq. (2.15), the electronic density $n(\mathbf{r})$ in a periodic system can be calculated by carrying out a sum of the Bloch states over the N occupied bands and the discrete mesh of $\mathbf{k}$-points[15] in the BZ:

$$n(\mathbf{r}) = \sum_{i=1}^{N} \sum_{\mathbf{k}\in BZ} |\varphi_{i,\mathbf{k}}(\mathbf{r})|^2. \tag{2.94}$$

In the thermodynamic limit of an infinite crystal, the discrete sum over $\mathbf{k}$ becomes an integral over the BZ:

$$n(\mathbf{r}) = \frac{V}{(2\pi)^3} \sum_{n=1}^{N} \int_{BZ} |\varphi_{n,\mathbf{k}}(\mathbf{r})|^2 d^3k, \tag{2.95}$$

[15]The discretization of the wavevectors is allowed by the Born-von Karman periodic boundary conditions applied to the periodic crystal.

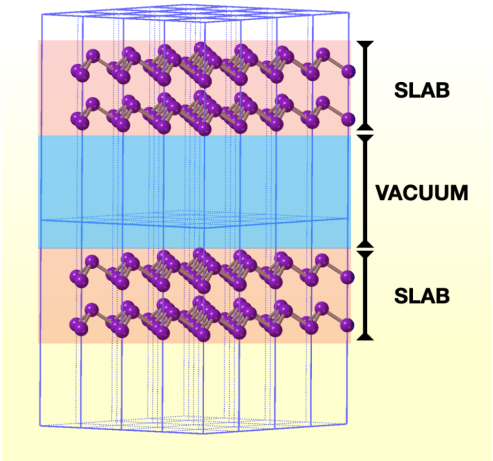

FIGURE 2.2: The supercell method applied to a BL system. The latter is represented by a periodic sequence of slabs separated by vacuum along the direction perpendicular to the 2D system.

where V is the true crystal volume. In practice, the integrals over the BZ are approximated with finite sums over some appropriately chosen **k**-points grids, such as the Monkhorst-Pack (MP) grid of uniformly distributed points [323] and the Baldereschi grid made of a single point [324]. Each lattice type has a specific grid geometry, and the denser the grid, the more accurate and heavy the calculation. The computational cost of the latter can be reduced by using the symmetries, when present: only one **k**-point is left for the calculation to represent each star (i.e., the set of **k**-points that are equivalent by symmetry) with a weight ω_i that is proportional to the number of **k**-points in the star. Hence, once the **k**-points grid has been chosen, the electronic density is calculated by replacing the infinite sum over the BZ with a discrete sum over a set of points $\mathbf{k}_i$ and weights ω_i, and symmetrizing the resulting sum.

In general, the electronic density in Eq. (2.94) can be written in terms of both occupied and unoccupied bands by means of their occupation numbers $f_{i,\mathbf{k}}$'s:

$$n(\mathbf{r}) = \sum_i \sum_{\mathbf{k}\in BZ} f_{i,\mathbf{k}} |\varphi_{n,\mathbf{k}}(\mathbf{r})|^2. \tag{2.96}$$

Similarly, the KS total energy can be expressed as a sum over the BZ and the bands, each one weighted by its occupation number. In principle, the latter is the Fermi-Dirac (FD) distribution [218]. This integration technique provides excellent accuracy in estimating total energy and electronic density, except for the metals. Indeed, since at $T = 0\ K$ the FD distribution is an integral of the Dirac delta functions $\delta(\epsilon - \epsilon^{KS}_{i,\mathbf{k}})$, the integration requires very fine meshes. This problem can be solved by formulating a finite (electronic) temperature description equivalent to the absolute zero one because the finite-temperature FD distribution is an integral of broaded delta functions and there is not the discontinuity at the Fermi energy. Since the delta functions broadening or "smearing" is uniquely associated to the electronic temperature, i.e., it has a real physical meaning. The equivalence holds if the zero-temperature total-energy functional is replaced by the Helmholtz free-energy functional $F = E - TS$, where S is the system entropy[16]. However, using the FD distribution has strong limitations: **k**-point sampling can really improved only at thousands of degrees (~ 0.1

[16]Indeed, in this way, the temperature increasing could compensate the energy increasing and the comparison to the zero-temperature total energy is ensured.

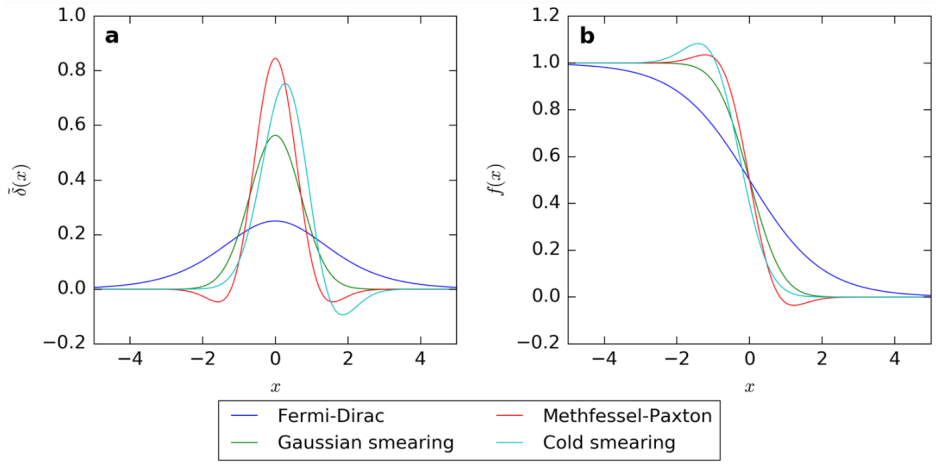

FIGURE 2.3: Plots of the different smeared delta functions $\tilde{\delta}(x)$, and their corresponding occupation functions $f(x)$, shown as functions of $x = (\epsilon - \mu)/k_B T$. [325]

eV), and without removing the problem of calculating a relatively large number of states slowly decaying to zero occupation, due to the long tails of the distribution. Thus, one needs a fictitious occupation function having sufficiently short tails, with the cost that the smearing has not any physical meaning[17] (see Fig. 2.3). The first choice was an occupation function defined as integral of Gaussian functions with an a priori defined broadening, due to Fu and Ho [326]. Although the Gaussian smearing required a less amount of **k**-points, it introduced very persistent systematic errors on free energies and forces. Furthermore, entropy and the free energy could not be written in terms of the occupancies. For this reason, Methfessel and Paxton generalized the idea of Gaussian smearing by introducing an Hermite polynomial expansion of Dirac delta functions, that keeping a reasonably smooth occupation function but significantly reducing the systematic error[18] [327]. In practice, a second-order Hermite polynomial (the common choice nowadays) has an occupation function that is still very smooth, but provides a free-energy functional that is much closer, at a given temperature, to the original zero-temperature total-energy functional (and much easier to determine accurately, since much fewer **k**-points are needed). This occurs because the order-2 Methfessel-Paxton (MP) free-energy functional induced by the smearing depends only quartically on the temperature, whereas the Gaussian free-energy functional is quadratic in temperature. Despite the improvements given by the MP scheme, the latter shows negative or larger than 1 partial occupancies. In particular, for negative occupancies the electronic charge density is not anymore guaranteed to be positive definite, and the same could occur for the density of states. Even if semiconducting or insulating materials should not be sensitive to the smearing, MP scheme is particularly incorrect for them[19], leading, for example, to errors on phonon frequencies exceeding 20%. Thus, MP scheme is certainly not suitable for semiconducting or insulating materials. The most efficient smearing scheme was formulated by Marzari and Vanderbilt and is known as *cold smearing* scheme, that has two strenghts: the occupations are forced to be always positive and it shares with order-2 MP the quadratic non-dependence on temperature, even if it is cubic.

[17] The meaning of the broadening is exactly controlled in terms of electronic temperature only in the FD distribution.

[18] Obviously, the larger the broadening, the closer the Gaussian and Methfessel-Paxton errors.

[19] One could be forced to consider a smearing scheme in a metal-semiconductor junction system.

In this thesis, all the calculations were carried out by considering the cold-smearing scheme by Marzari and Vanderbilt.

2.3.5 Relaxation of the atomic positions

In the previous sections, I described the theory and some practical approximations to solve the electron Hamiltonian defined by the Eq. (2.3). This is accomplished by an iterative and self-consistent procedure which is inserted into the searching for the ionic configuration of the ground state. Indeed, one has to solve the eigenvalue problem for the ions given by Eq. (2.6), where the ions move on the BO-PES of Eq. (2.7). The ground state geometry of the system is obtained by minimizing the forces acting on the ions, i.e., by searching for the minimum of the PES. The forces acting on each ion can be calculated as the energy gradient with respect to the ionic positions. Then, the Hellman-Feynman theorem [328, 329] can be used to construct an algorithm that finds the ground state geometry.

Theorem of Hellman-Feynman

Let $\hat{H}_\eta$ be an Hamiltonian dependent on a certain parameter η. Assuming that in a certain range of values of η it is possible to solve the Schrödinger equation associated with $\hat{H}_\eta$ providing a complete set of eigenstates $|\Psi_\eta\rangle$ and eigenvalues E_η, the following relation holds:

$$\frac{\partial E_\eta}{\partial \eta} = \langle \Psi_\eta | \frac{\partial \hat{H}_\eta}{\partial \eta} | \Psi_\eta \rangle . \tag{2.97}$$

In the DFT framework, the parameter η represents the set of ionic positions $\{\mathbf{R}_\alpha\}$ of a given system. Different techniques have been implemented to actually find the minimum energy geometry of the systems, all based on the Hellman-Feynman theorem. The QE package, used in this thesis, implements the Broyden-Fletcher-Goldfarb-Shanno (BFGS) procedure, which is a quasi-Newton method based on the calculation of an approximate Hessian matrix. In this algorithm, the total energy is considered as a function of the coordinates of the released atoms $E_{tot} = E_{tot}(\{\mathbf{R}_\alpha\})$. An expansion of E_{tot} around the minimum energy configuration $\{\mathbf{R}_\alpha\}_{min}$ yields

$$\begin{aligned} E_{tot}(\{\mathbf{R}_\alpha\}) \simeq\ & E_{tot}(\{\mathbf{R}_\alpha\}_{min}) + \nabla_{\{\mathbf{R}_\alpha\}} E_{tot} \cdot (\{\mathbf{R}_\alpha\} - \{\mathbf{R}_\alpha\}_{min}) \\ & + \frac{1}{2} \sum_{i,j} (\{\mathbf{R}_\alpha\} - \{\mathbf{R}_\alpha\}_{min})_i H_{i,j} (\{\mathbf{R}_\alpha\} - \{\mathbf{R}_\alpha\}_{min})_j, \end{aligned} \tag{2.98}$$

where

$$H_{i,j} = \frac{\partial^2 E}{\partial \{\mathbf{R}_\alpha\}_i \partial \{\mathbf{R}_\alpha\}_j} \tag{2.99}$$

is the (i,j) element of Hessian matrix. The gradient of the total energy at the minimum is zero, so that the first order term vanishes. The gradient of the Eq. (2.98) gives the forces as function of the coordinates. From the determination of the total energy values it is possible to derive the forces acting on the atoms and, by inversion, the ionic configurations. The procedure stops when the forces are smaller than a certain threshold.

2.3.6 Self-consistency

In Fig. 2.4, the scheme of the entire calculation is reported, summarizing the fundamental steps of the self-consistent approach in solving the total Hamiltonian and its

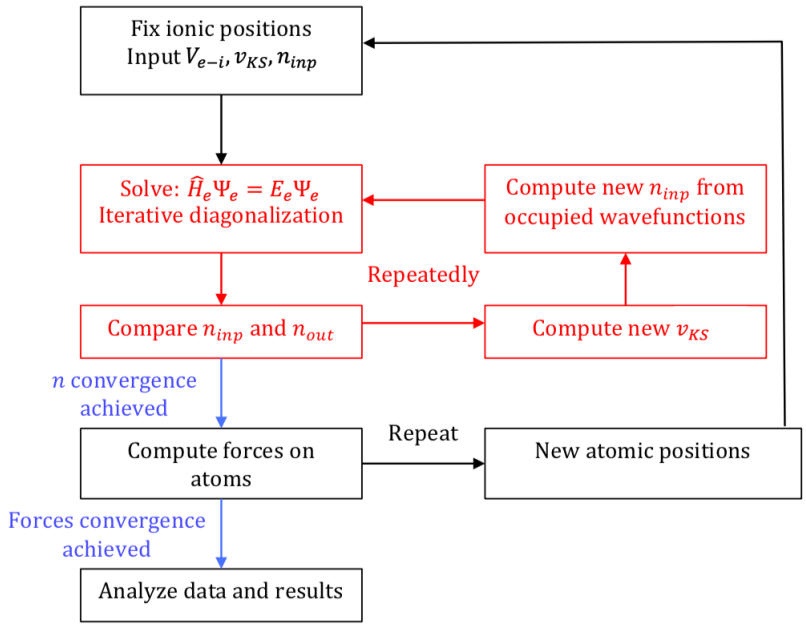

FIGURE 2.4: The electronic Hamiltonian is self-consistently solved and a new electronic density is computed until convergence (red scheme). The structural optimization is achieved through the calculation of the forces acting on atoms. The latter are moved until the total force is less than the required threshold (black scheme) representation.

electron and ionic parts. Starting from a given set of atomic positions in the unit cell and an initial guess of the electronic density (generally obtained by a superposition of atomic orbitals), the electronic Hamiltonian is self-consistently solved due to the dependence of the KS potential on the density. The convergence of the electronic Hamiltonian is reached when the electronic density difference between two consecutive steps is less than a given threshold. At this point, the ionic Hamiltonian is solved and the forces acting on atoms are computed. If these forces are higher than a given threshold, then the ions are moved and a new set of coordinates determines the input ionic potential for a further electronic self-consistent calculation. When the forces acting on atoms are below a desired threshold, the computational process comes to end, so that it is possible to extract the physical quantities of interest. Unless differently stated, as convergence criterion for this thesis, we considered 10^{-4} Ry as threshold of the total energy difference between consecutive structural optimization steps and 10^{-4} Ry/bohr as threshold of all the components of the forces acting on the atoms.

Chapter 3

Twisting and magnetism in two-dimensional systems

"Before I came here I was confused about this subject.
Having listened to your lecture, I am still confused,
but on a higher level."

Enrico Fermi

This chapter is dedicated to present the theoretical tools and concepts used in addition to the DFT to investigate the properties of the materials explored in this thesis work. First of all, commensurate twist angles will be defined in Sec. 3.1, in order to quantitatively show both the great advantage of the superlattices and the computationally increasing limits at increasingly small angles for twisted BL systems. In Sec. 3.2, the theory of 2D magnetism will be outlined, starting from the 3D case for a full comprehension of the main quantities and concepts involved. Sec. 3.3 will be devoted to explain how a specific magnetic Hamiltonian could be implemented on a crystal structure, first extracting the Hamiltonian parameters from the DFT calculations, and then calculating the equilibrium temperature dependence of the main thermodynamic functions characterizing the magnetic PT via Monte Carlo (MC) methods.

3.1 Geometry of twisted bilayer structures

A twisted BL structure can be obtained starting from an untwisted BL structure of two layers separated by a certain interlayer distance d_{inter} and by rotating one layer with respect to the other one by an angle θ. Since the twisted BL materials explored in this thesis, i.e., graphene and TMDs, derive from untwisted geometries having honeycomb lattices, here we will focus on the latter.

As known, the honeycomb lattice is a two-atom basis hexagonal lattice and, thus, can be described as the interpenetration of two hexagonal sublattices A and B shifted between each other by a vector δ (see Fig. 3.1(a)). For MG, both the sublattices consist of carbon atoms. Instead, as far as the ML TMDs are concerned, one sublattice is formed by the transition-metal atoms and the other one from two overlapped planes of chalcogen atoms, above and below the transition-metal atoms plane, as previously explained in Sec. 1.1.2. Unless differently specified, the Bravais lattice basis vectors

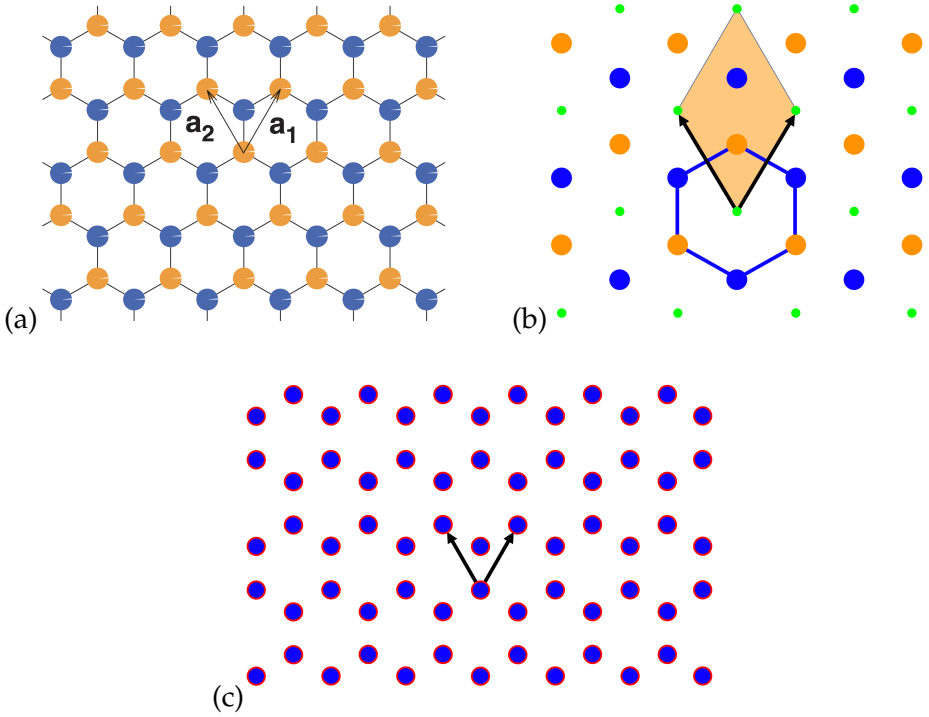

FIGURE 3.1: Honeycomb lattice. (a) Bravais lattice basis vectors of the honeycomb lattice $\mathbf{a}_1$ and $\mathbf{a}_2$. The sublattice A is the hexagonal lattice made of the orange circles, whereas the sublattice B is the hexagonal lattice made of the blue circles. Adapted with permission from Ref. [50]. (b) A different choice of the origin of the hexagonal Bravais lattice describing the structure. (c) Overlapped honeycomb lattices of the two layers constituting the an untwisted BL. Red (blue) circles represent the bottom (top) layer.

of the honeycomb lattice are [1]

$$\mathbf{a}_1 = (1, 0, 0)\, a, \quad \mathbf{a}_2 = \left(-\frac{1}{2}, \frac{\sqrt{3}}{2}, 0\right) a, \tag{3.1}$$

where $a = |\mathbf{a}_1| = |\mathbf{a}_2|$ is the lattice parameter. They can be chosen, as shown in Fig. 3.1(a), with the origin placed on an atom of the sublattice A, such that the basis vectors identifying the sublattices are

$$\mathbf{d}_1 = 0, \quad \mathbf{d}_2 = \delta. \tag{3.2}$$

As a consequence, the graphene unit cell contains two carbon atoms: one at the origin of the Bravais lattice and the other one located at δ. Instead, if the transition-metal atom occupies the origin of the ML TMDs Bravais lattice, then the unit cell contains three atoms: the transition-metal atom at the origin and the two overlapped chalcogen atoms located at δ_1 and δ_2, where the latter differ only by the out-of-plane coordinate. Alternatively, the honeycomb lattice can be described as in Fig. 3.1(b), i.e., by choosing the origin of the Bravais lattice as the centers of the hexagons, that are represented by the green dots in figure. In this case, the basis vectors are

$$\mathbf{d}_1 = \delta, \quad \mathbf{d}_2 = 2\delta. \tag{3.3}$$

Obviously, the description of the system does not depend on the choice of the basis

[1] This is the definition implemented in QE package.

vectors. Referring to Sec. 2.3.3, an isolated ML or BL can be described by defining the 2D unit cell in a 3D supercell, whose height c includes the layer thicknesses, the interlayer distance, and the vacuum, and is defined by the third basis vector

$$\mathbf{a}_3 = (0, 0, c). \tag{3.4}$$

For the sake of simplicity, we will consider the untwisted BL as composed by two layers with aligned Bravais lattices (see Fig. 3.1(c)). Therefore, the period of the untwisted structure is that of the Bravais lattices of the two layers. The basis sets of the two layers can be denoted by $\{\mathbf{a}_1^{(l)}, \mathbf{a}_2^{(l)}\}$, with $l = 1, 2$ (bottom and top layer, respectively). Assuming that the rotation axis passes through two overlapped atoms each belonging to the sublattice A of its layer, the twist angle θ is formally defined as the angle between $\mathbf{a}_1^{(1)}$ and $\mathbf{a}_1^{(2)}$ or, equivalently, between $\mathbf{a}_2^{(1)}$ and $\mathbf{a}_2^{(2)}$. As anticipated in Sec. 1.1.1, the twist angle realizes two types of moiré patterns: commensurate ones, for which the translational symmetry is preserved, and incommensurate ones, for which the twisting breaks the translational symmetry. In particular, a commensurate twisted structure or superlattice is obtained if it is possible to identify two in-plane vectors connecting the pair of atoms defining the rotation axis direction to two equivalent pairs. The smallest of such vectors can be denoted by $\mathbf{L}_1$ and $\mathbf{L}_2$, and they are the basis vectors of the superlattice [330, 331], as shown in the example of Fig. 3.2(a). Formally, this means that the first superlattice basis vector satisfies the relation

$$\mathbf{L}_1 = n\mathbf{a}_1^{(1)} + m\mathbf{a}_2^{(1)} = n'\mathbf{a}_1^{(2)} + m'\mathbf{a}_2^{(2)} \tag{3.5}$$

where n, m, n', m' are integer numbers, whereas, in our case of hexagonal symmetry, $\mathbf{L}_2$ can be simply obtained by rotating $\mathbf{L}_1$ by $\pi/3$. It is worthwhile noticing that the starting alignment of the two layers imposes that their lattice parameters must be equal. As a consequence, as far as the twisted HeBLs are concerned, the calculations on the latter include a certain lattice mismatch obtained by adapting the size of one layer unit cell to the other one. By an appropriate choice of Bravais lattice basis vectors $\mathbf{a}_i^{(l)}$, the pair (n', m') can be made equal to (n, m), and, thus, the twisted structure is specified by a single pair (n, m). It turns out that the commensurate twist angle θ and the superlattice parameter $L = |\mathbf{L}_1| = |\mathbf{L}_2|$ are related to (n, m), respectively, through the relations

$$\cos\theta = \frac{1}{2}\frac{n^2 + m^2 + 4nm}{n^2 + m^2 + nm}, \tag{3.6a}$$

$$L = a\sqrt{n^2 + m^2 + nm} = \frac{|n - m|}{2\sin\theta/2}a. \tag{3.6b}$$

By choosing different values of n and m, one can obtain all the twist angles describing commensurate rotations through the Eq. (3.6a) and the corresponding superlattice parameter through Eq. (3.6b). Obviously, the larger the superlattice parameter, the heavier the computational cost required to compute physical quantities by means of DFT or TB method, since the number of atoms contained in the superlattice unit cell increases correspondingly. Fig. 3.2(b) reports the number of lattice sites as a function of the twist angle, from which the actual number of atoms of the superlattice unit cell can be obtained by multiplying it by the number of atoms of untwisted BL unit cell. The area of the superlattice unit cell is $S = |\mathbf{L}_1 \times \mathbf{L}_2| = (\sqrt{3}/2)L^2$. The BZ related to the supercell, often referred to as the MBZ due to its smaller spatial extent with respect to that of the untwisted BL, can be generated by

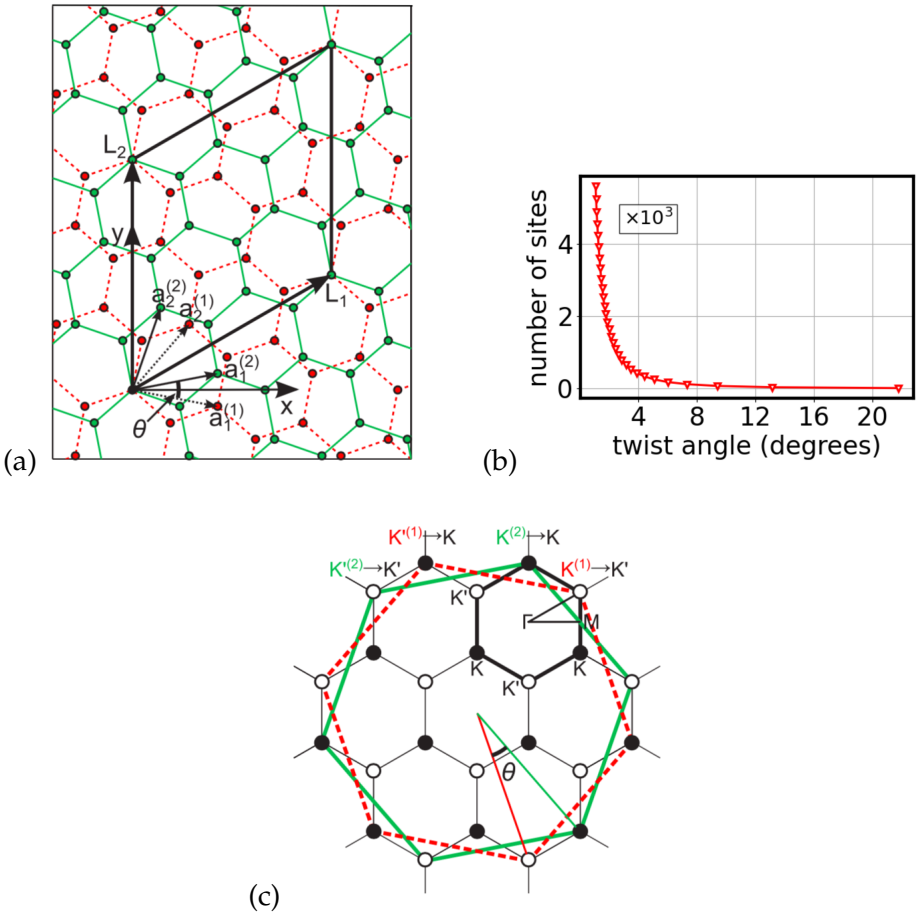

FIGURE 3.2: Commensurate rotation for hexagonal symmetry. (a) Superlattice obtained at the twist angle $\theta = 21.78°$. Dashed (red) and solid (green) lines represent the lattices of layers 1 and 2, respectively. (b) Number of lattice sites as a function of the (commensurate) twist angle. The number of atoms contained in the superlattice unit cell is obtained by multiplying the number of lattice sites by the number of atoms in the basis of the untwisted BL (e.g., 4 in the case of BG). (c) Definition of the mini Brillouin zone. Dashed (red) and solid (green) large hexagons correspond to the BZ of layers 1 and 2, respectively, and thick small hexagon to the MBZ. Open and filled circles are two inequivalent K and K' points. Adapted with permission from Ref. [331].

considering the BZ of the rotated layers. As shown in Fig. 3.2(c), the two hexagonal BZs of the layers can be superimposed with a relative rotation. The line connecting the closest two original $K^{(1)}$ and $K^{(2)}$ points forms one edge of the MBZ, and they are transformed into the inequivalent K' and K points of the latter, respectively. From this, the Γ and M points of the MBZ can be obtained.

In general, the untwisted BL structure may show a stacking configuration with non-aligned lattices, as the Bernal stacking of BG. In these cases, the commensurate twisted structure can be described by first performing a translation of one layer to reach the alignment, by identifying the pair (n, m) corresponding to the target twist angle (or the nearest one, if absent), and finally by performing the inverse of the starting translation. Obviously, the choice of (n, m) giving the desired twist angle could correspond to a huge computational cost for the reasons previously explained. Therefore, although the commensurate rotations allow to apply the Bloch theorem and use DFT or TB method, their use rapidly becomes computationally prohibitive below $\theta \sim 3^\circ$.

3.2 Two-dimensional magnetism

Two-dimensional magnetism is an intriguing branch of magnetism for both theoretical and experimental reasons. Although the 2D materials era was inaugurated through the graphene synthesis in 2004, the first native 2D magnetism was observed only in 2017, as explained in Sec. 1.1.3. The search for 2D magnetic materials is based on different criteria compared to the 3D case. In order to understand the motivations behind these differences, a brief reminder about the main concepts of 3D magnetism is required.

It is well-known that many paramagnetic materials, below the Curie temperature T_C, present a magnetic ordering even in the absence of applied magnetic fields, that is known as *spontaneous ordering* for this reason. As a consequence, this phenomenon cannot rise from a coupling between the magnetic moments $\boldsymbol{\mu}_\alpha$ and the magnetic field, where $\boldsymbol{\mu}_\alpha$ is the magnetic moment of the material atom at the position $\mathbf{R}_\alpha$. To date, there exist two mechanisms that predict a spontaneous magnetic ordering: reciprocal interactions between the magnetic moments and strong screened on-site Coulomb interaction. The former describes materials where some or all magnetic moments are localized, that are metals[2] or insulators, respectively. The latter, mainly based on the Hubbard model, describes only the materials with delocalized magnetic moments, that are metals[3]. The 2D magnet investigated in this thesis is Nb_3I_8, that is predicted and observed as an insulator. Therefore, the focus will be placed only on the first class of spontaneous magnetic ordering mechanism for insulators. In particular, since the localized magnetic moments are related to nuclei and core electrons, the interactions involve the ions instead the whole atoms.

In 1928, Heisenberg realized that the Coulomb repulsion between electrons was the responsible interaction between the magnetic moments [332]. Indeed, following the Heitler-London method [333] to analyze the (core) electrons in a H_2 molecule, he derived that the exchange matrix elements of the electron–electron Coulomb interaction between couples of ions, evaluated by means of the first-order perturbation theory, provide an effective coupling between spin-vector operators. Therefore, Heisenberg postulated such an interaction for each couple of ions close enough that

[2] In this case, the so-called *localized magnetism* occurs, that arises from the interaction between localized magnetic moments and the delocalized ones of the conduction electrons.

[3] This is known as *band magnetism*.

the exchange matrix elements do not vanish, that was described by the Hamiltonian

$$\hat{H}_{\mathcal{H}} = -\frac{1}{2}\sum_{\alpha,\beta} J_{\alpha\beta}\hat{\mathbf{S}}_{\alpha}\cdot\hat{\mathbf{S}}_{\beta}, \tag{3.7}$$

where $J_{\alpha\beta}$ is the exchange integral. The latter is spatially isotropic[4], satisfies the relations

$$J_{\alpha\beta} = J_{\beta\alpha}, \quad J_{\alpha\alpha} = 0, \tag{3.8}$$

and the $1/2$ factor avoids double counting of the interactions between the spin-vector operators. The spatially isotropic behavior guarantees the full spherical symmetry $O(3)$ for the Heisenberg Hamiltonian, in addition to the time-reversal symmetry $\mathcal{T}$ related to the scalar products. If the localized moments are related to the total angular momentum rather than the spin, then $\hat{\mathbf{S}}_{\alpha}$ must be replaced by $(g_{\mathcal{L}}-1)\hat{\mathbf{J}}_{\alpha}$ [334], where $g_{\mathcal{L}}(L_{\alpha}, S_{\alpha}, J_{\alpha})$ is the Landé g-factor. Typically, the orbital angular momentum is quenched in transition-metal ions and iron-group ions, whereas it must be taken into account in rare-earth ions due to the significant energy contributions of the SOC.

By definition, the magnetism described through the Heisenberg model could be caught also by reducing the summation only to the first- or next-nearest neighbors. In this way, the Hamiltonian of Eq. (3.7) can describe different kinds of magnetic orders, such as ferromagnetism, antiferromagnetism, ferrimagnetism, helimagnetism, and other more complex structures [334], depending on the sign of nearest neighbor couplings, the presence of competing second-neighbor or higher-order interactions, the additional effect of external fields, and the on-site interactions. By using the spin-vector operators (or, in general, the total angular momentum operators) commutation rules, it is easy to demonstrate the commutation relation

$$[\hat{\mathbf{S}}_{tot}, \hat{H}_{\mathcal{H}}] = 0 \tag{3.9}$$

involving the total spin $\hat{\mathbf{S}}_{tot} = \sum_{\alpha}\hat{\mathbf{S}}_{\alpha}$. As a consequence, the Heisenberg Hamiltonian possesses the $SU(2)$ symmetry, i.e., it describes a system invariant under any rotation of the total spin or, equivalently, of the system spins, and $\hat{\mathbf{S}}_{tot}$ is a conserved quantity.

The simplest ground state of $\hat{H}_{\mathcal{H}}$ can be written for a ferromagnetic system. If the latter consists of N_S ions having spins with values S, then the states

$$|\Psi_{\pm}\rangle = |S_1 = S, m_{S_1} = \pm S\rangle \ldots \left|S_{N_S} = S, m_{S_{N_S}} = \pm S\right\rangle \tag{3.10}$$

are the degenerate ground states of the Heisenberg Hamiltonian with the eigenvalue

$$E_0 = -\frac{\hbar^2}{2}\sum_{\alpha,\beta=1}^{N_S} J_{\alpha\beta}S^2. \tag{3.11}$$

Referring to $|\Psi_+\rangle$ as ground state $|\Psi_0\rangle$ by convention, the $SU(2)$ symmetry of $\hat{H}_{\mathcal{H}}$ provides $2S_{tot}+1$ degenerate ground states, where $S_{tot} = N_S S$. Since the spontaneous magnetization $\mathbf{M}_s$ of a 3D ferromagnet below T_C is observed with the spins pointing in a specific direction, a spontaneous $O(3)$ symmetry breaking occurs for the Hamiltonian and the system remains invariant only under $SO(2)$ rotations around the spontaneous magnetization direction. The latter is known as *easy-axis* of the

[4]This is the reason why the model is commonly named as *isotropic Heisenberg model*.

magnet, denoted by the unit vector $\hat{\mathbf{e}}$, being, in general, the direction inside the crystal along which small applied magnetic fields are sufficient to reach the saturation magnetization. By the contrary, the hard-plane is the plane inside a crystal where large applied magnetic fields are needed to reach the saturation magnetization. Formally, the Curie temperature is the critical temperature describing the second-order PT from the paramagnetic regime ($T > T_C$) to the ferromagnetic ($T < T_C$) regime, where the all spins are perfectly parallel to $\mathbf{M}_s$ only at $T = 0$ K [335]. Spontaneous magnetization is the order parameter of such a PT, showing divergent magnetic susceptibility $\chi(T)$ and heat capacity $C_V(T)$ at $T = T_C$. As far as the antiferromagnets are concerned, they can be schematized as spin patterns that, below the Neél temperature T_N, consist of different FM sublattices ordered in such a way that the net total spontaneous magnetization is zero.

As anticipated in Sec. 1.1.3, the values of the spatial dimensionality d and the spin dimensionality d_S are crucial in order to have magnetism. Indeed, MWH theorem [131, 142] of 1966 states that "in one and two dimensions ($d \leq 2$), the isotropic Heisenberg model ($d_S = 3$) does not admit any spontaneous magnetization or spontaneous continuous symmetry breaking for $T > 0$", i.e.,

$$M_s(T) = 0, \quad d \leq 2, \quad T > 0. \tag{3.12}$$

In other words, in these cases the magnetization fluctuations are strong enough to destroy the $O(3)$ spontaneous symmetry breaking[5]. Nevertheless, in 1944 Lars Onsager had demonstrated that a spontaneous magnetization is possible for the Ising model applied to 2D systems ($d_S = 1$ and $d = 2$) [128], as the result of the spontaneous (discrete) $\mathbb{Z}_2$ symmetry breaking. Therefore, based upon the MWH theorem and the Onsager's result, it follows that the magnetic ordering in 2D materials could be described only through the Ising model or anisotropic terms in the Heiseberg model, favoring a particular easy-axis direction and satisfying the constraint to recover the Ising model in the limit of an infinite anisotropy. For $d_S = 2$, the spins on a 2D lattice are essentially 2D vectors and the material is well described by the XY model, showing a PT below the BKT temperature T_{BKT} [130], where a divergent magnetic susceptibility shows up[6]. All these possibilities for 2D magnetism are schematically shown in Fig. 3.3 and can be modeled, in the simplest cases, through the generalized Heisenberg spin Hamiltonian [336]

$$\hat{H}^{2D}_{\mathcal{H}} = -\frac{1}{2}\sum_{\alpha,\beta}\left(J_{\alpha\beta}\hat{\mathbf{S}}_\alpha \cdot \hat{\mathbf{S}}_\beta + \Lambda_{\alpha\beta}\hat{S}_{\alpha,z}\hat{S}_{\beta,z}\right) - \sum_\alpha A_\alpha(\hat{S}_{\alpha,z})^2, \tag{3.13}$$

assuming that the 2D material lies on the xy plane. Here, A_α and Λ_α are the single-ion magnetic anisotropy and the inter-site or exchange magnetic anisotropy, respectively. For $A_\alpha, \Lambda_\alpha \simeq 0$, the Hamiltonian in Eq. (3.13) reduces to the isotropic Heisenberg model. For $A_\alpha \to \infty$, the limit of strong easy-axis (parallel to the z axis) anisotropy holds and the Ising model

$$\hat{H}_{\mathcal{I}} = -\frac{1}{2}\sum_{\alpha,\beta} J_{\alpha\beta}\hat{S}_{\alpha,z}\hat{S}_{\beta,z}, \tag{3.14}$$

[5]The proof is valid only for $T > 0$ and not for $T = 0$.

[6]In the quasi-ordered state ($T < T_{BKT}$) the fundamental low-energy excitations are bound spin vortex/anti-vortex pairs, where the energy of a single vortex diverges and the bound vortex/anti-vortex pair has a finite energy. At the critical temperature T_{BKT} the vortex/anti-vortex pairs unbind and the system becomes disordered. The "quasi-ordering" refers to spin correlations decaying behavior, that shows a power law dependence on the distance between the magnetic moments.

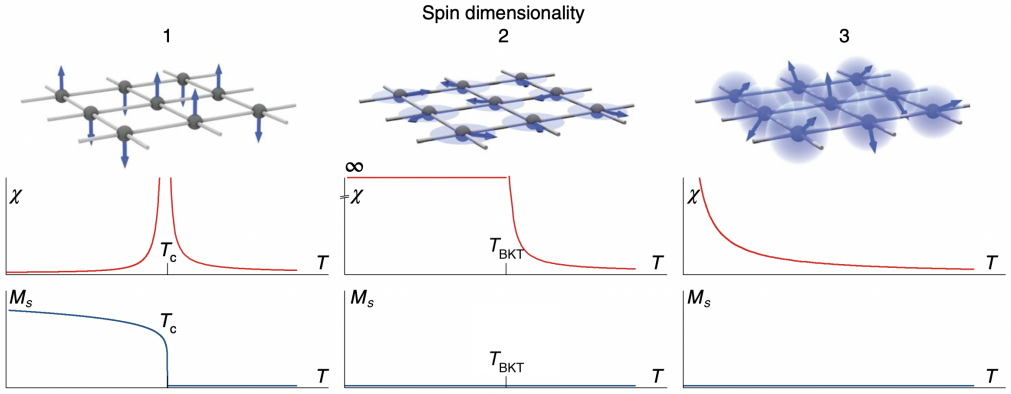

FIGURE 3.3: Magnetism on a 2D lattice for different spin dimensionalities d_S. For $d_S = 1$ (Ising model), a nonzero spontaneous magnetization can be measured below T_C and the susceptibility diverges at T_C, as predicted by Onsager. For $d_S = 2$ (XY model), no spontaneous magnetization can be measured and the susceptibility diverges below T_{BKT}, where spin vortex/anti-vortex pairs bind. For $d_S = 3$, no PTs can be observed on a 2D lattice. Adapted with permission from Ref. [336].

is recovered. Finally, for $A_\alpha \to -\infty$, the limit of strong easy-plane (perpendicular to the z axis) anisotropy holds and the XY model

$$\hat{H}_{\mathcal{XY}} = -\frac{1}{2}\sum_{\alpha,\beta} J_{\alpha\beta}(\hat{S}_{\alpha,x}\hat{S}_{\beta,x} + \hat{S}_{\alpha,y}\hat{S}_{\beta,y}), \tag{3.15}$$

is recovered.

In some complicated cases, other magnetic coupling terms must be added to the Hamiltonian of Eq. (3.13), such as Dzyaloshinsky–Moriya (DM) [337, 338], Kitaev [127, 339], and higher-order (e.g., biquadratic) interactions [340]. DM interaction, also known as antisymmetric exchange, is induced by the strong atomic SOC of the magnetic ions and a lack of inversion symmetry of the compound, and is formally related to the off-diagonals terms of the tensor-like Heisenberg model

$$\hat{H}^{tensor}_{\mathcal{H}} = -\frac{1}{2}\sum_{\alpha,\beta,i,j} \hat{S}_{\alpha,i} J^{ij}_{\alpha\beta} \hat{S}_{\beta,j}. \tag{3.16}$$

It is described by the Hamiltonian term $\hat{\mathcal{H}}^{DM}_{\alpha\beta} = -\mathbf{D}_{\alpha\beta} \cdot (\hat{\mathbf{S}}_\alpha \times \hat{\mathbf{S}}_\beta)$ for each magnetic ion pair (α, β), where magnitude and direction of the vector $\mathbf{D}_{\alpha\beta}$ (DM vector) depend on the symmetries of neighboring magnetic ions. In particular, exactly as for CrI_3 [143], this term can be neglected for Nb_3I_8 because for each couple of magnetic Nb ions there exist two iodine contributes with the same magnitude and opposite signs. Kitaev interaction also derives from the off-diagonal terms of Eq. (3.16) [341], providing a term $-(1/2)\hat{S}_{\alpha,n}\hat{S}_{\beta,n}$, where $\{l, m, n\}$ is the label set of the basis diagonalizing the $J^{ij}_{\alpha\beta}$ tensor. Finally, higher-order interactions provide terms as powers of $\hat{\mathbf{S}}_\alpha \cdot \hat{\mathbf{S}}_\beta$ and are typical for systems for which the magnetic ion can exist in two different valence states. However, Kitaev and higher-order interactions are taken into account to investigate specific and complex magnetic properties, such as QSLs [341] and spin topological spin excitations [340], respectively. Therefore, the remaining simpler contributions are sufficient to perform an initial investigation on the magnetism of a 2D material.

In this thesis, the main case of interest is the 2D ferromagnetism. Therefore, a practical way to determine the easy-axis direction by means of first-principles calculations requires to be defined. The energy contribution of the magnetic anisotropy described in Sec. 1.1.3, named as *magnetic-anisotropy energy* (MAE), is the energy required to rotate the spontaneous magnetization at $T = 0$ K from the easy-axis direction to a direction contained in the hard-plane. As a consequence, MAE is defined as the difference between the system energies with $\mathbf{M}_s \perp \hat{\mathbf{z}}$ and $\mathbf{M}_s \parallel \hat{\mathbf{z}}$, where $\hat{\mathbf{z}}$ is the z-axis unit vector. A positive (negative) value of MAE indicates an out-of-plane (in-plane) easy-axis. Usually [143, 342–344], the direction perpendicular to z axis is taken as the x-direction and the MAE is evaluated in μeV per magnetic ion (the common order of magnitude is $\sim 10^{1\div 2}$ μeV/ion). Therefore, the MAE is defined as

$$\mathrm{MAE} = E_{\mathbf{M}_s \parallel \hat{\mathbf{x}}} - E_{\mathbf{M}_s \parallel \hat{\mathbf{z}}} \tag{3.17}$$

and can be computed through the DFT, once the suitable approximation for the exchange-correlation functional has been chosen (see Secs. 2.1.7 and 2.1.8).

3.3 Model magnetic Hamiltonians on crystal structures

A complete magnetic simulation of a crystal structure is not limited to reveal if there exists at least one magnetic state whose energy is lower than that of the NM state and to determine its easy-axis direction. These tasks can be performed by all the softwares implementing DFT, such as QE. Indeed, once a magnetic stable or metastable phase has been identified, the next steps are to select a magnetic Hamiltonian that could suitably describe the magnetic state. For this purpose, the Hamiltonian parameters must someway extracted from the DFT calculations, in order to perform a spin dynamics simulation, that allows to compute the equilibrium temperature dependence of the main thermodynamic functions characterizing the magnetic PT, such as the average single-ion magnetic moment $\langle \boldsymbol{\mu}(T) \rangle$ and $\chi(T)$, investigate topological spin properties, and so on [186, 188].

The Hamiltonian parameters can be extracted from the DFT calculations by means of the energy-mapping analysis [345], that is nowadays widely used [186, 187, 346]. As shown in Sec. 3.2, the most general magnetic Hamiltonian is an operator

$$\hat{H}_{mag} = \hat{H}_{mag}(\hat{J}_{\alpha,i}, g_{\mathcal{L}}, \{P^{(n)}_{\alpha\beta}\}, \{Q_\alpha\}), \tag{3.18}$$

where $P^{(n)}_{\alpha\beta}$ is a parameter involving the nth nearest neighbor magnetic ion pair (α, β) and Q_α is a parameter related to the single magnetic ion α. The simplest form of the energy-mapping analysis considers the same value of the Hamiltonian parameters for each pair (α, β) and magnetic ion α, at a specific order of neighbors. Furthermore, since magnetism of Nb_3I_8 derives from the magnetic moments of Nb ions as transition-metal ions, the orbital angular momentum quenching is ensured. Therefore, the magnetic Hamiltonians describing materials as Nb_3I_8 and CrI_3 appear in the simplified form

$$\hat{H}'_{mag} = \hat{H}'_{mag}(\hat{S}_{\alpha,i}, \{P^{(n)}\}, \{Q\}). \tag{3.19}$$

The choice of $\hat{H}'_{mag}$ fixes the number $\mathcal{N}$ of parameters to compute. If different specific magnetic configurations are simulated on the crystal structure by means of the DFT, then the mapping of their computed total energies to the selected $\hat{H}'_{mag}$ gives a set of algebraic equations defined unless an undefined fixed energy E_0 and differing for the magnetic configuration energy contributions, where the magnetic parameters

are unknown and the spins have been calculated from first principles. Therefore, by choosing $\mathcal{N}+1$ different magnetic configurations, the undefined energy E_0 can be removed and the magnetic parameters can be uniquely calculated. A specific case will be shown in Chap. 4, where the energy-mapping analysis will be performed on ML Nb_3I_8 mapped onto the Ising model. It is worthwhile noticing that such a method does not require the knowledge of the $\hat{H}'_{mag}$ exchange mechanism, since the latter exists in different forms obtained in the framework of second-order perturbation theory and all giving an Heisenberg-like term, such as the Rudermann-Kittel-Kasuya-Yosida (RKKY) interaction and the superexchange [334]. Rather, the accuracy of the energy-mapping analysis relies only on the quality of the applied approximation of the exchange-correlation functional. However, the magnetic parameters are so calculated at $T = 0$ K and, thus, their next use is based on the assumption that they slightly change with temperature.

Once the Hamiltonian parameters have been computed, one can generate the crystal structure by means of a programming language and implement the Hamiltonian on it in order to simulate the spin dynamics. For the simplest and most common structures, the first task can be performed by using suitable open-source software packages, such as Vampire [347]. Instead, for complex lattice structures as ML Nb_3I_8, the implementation of dedicated programs is required, generating a finite sample of $N_x \times N_y$ unit cells in the xy plane of the 2D material. As far as the spin dynamics task is concerned, the simulation is always based on the Metropolis algorithm as MC method, that can be briefly explained in the particular case of spin systems governed by magnetic Hamiltonians [348]. The purpose of the Metropolis algorithm is to generate a collection of random variables according to a desired probability distribution. Here, the random variables are the N_S system spins $\mathbf{S}_i$, which must sample the (equilibrium) canonical distribution

$$\pi(T, N_S, \mathbf{S}_1, ..., \mathbf{S}_{N_S}, \{P^{(n)}\}, \{Q\}) = \frac{e^{-\beta H'_{mag}(\mathbf{S}_1,...,\mathbf{S}_{N_S},\{P^{(n)}\},\{Q\})}}{Z(T, N_S, \{P^{(n)}\}, \{Q\})}, \tag{3.20}$$

at the last step for each temperature T, where $\beta = 1/k_B T$ and

$$Z(T, N_S, \{P^{(n)}\}, \{Q\}) = \sum_{\{\mathbf{S}_i\}} e^{-\beta H'_{mag}(\mathbf{S}_1,...,\mathbf{S}_{N_S},\{P^{(n)}\},\{Q\})} \tag{3.21}$$

is the canonical partition function. Spins are treated as classical quantities, since they are three-dimensional vectors in the spin space. The steps of the algorithm are listed below:

1. an arbitrary initial spin configuration $\{\mathbf{S}_i\}_0$ is chosen;
2. one spin is rotated in 3D space and the initial configuration becomes the trial configuration $\{\mathbf{S}_i\}_{trial}$;
3. by defining the quantity

$$w = \frac{\pi(T, N_S, \{\mathbf{S}_i\}_{trial}, \{P^{(n)}\}, \{Q\})}{\pi(T, N_S, \{\mathbf{S}_i\}_0, \{P^{(n)}\}, \{Q\})}, \tag{3.22}$$

   the trial move is accepted and $\{\mathbf{S}_i\}_1 = \{\mathbf{S}_i\}_{trial}$ only if a uniformly generated random number $r \in (0, 1)$ satisfies the condition $r \leq w$;
4. the new configuration is used as initial configuration and the procedure iterates for N_{MC} steps.

The canonical distribution is exactly reproduced for $N_{MC} \to \infty$, but, typically, a good convergence[7] is reached for $N_{MC} \gtrsim 10^5$. This result derives from the *Metropolis theorem* satisfied by the Markov chain generated through the algorithm, since each spin configuration only depends on the previous one. Typically, the initial spin configuration is chosen with all the spin aligned to the easy-axis direction. Depending on the d_S value, the second step of the algorithm changes, being a 2D rotation for $d_S = 2$ (XY model) and a spin flip $S_i \to -S_i$ for $d_S = 1$ (Ising model). When the algorithm concludes, the values of the main thermodynamic (equilibrium) functions characterizing the magnetic PT, such as $\langle \boldsymbol{\mu}(T) \rangle$, $\chi(T)$, $\langle E(T) \rangle$, $C_V(T)$, can be calculated at the temperature T, and their temperature dependence can be obtained by iterating the algorithm on a dense set of T values. As far as the implementation of this thesis is concerned, for each T the algorithm is executed for N_{trans} steps, with $N_{trans} \sim N_{MC}$, to first achieve the desired equilibrium distribution, and then it executes N_{MC} cycles of N_S steps each to obtain N_{MC} contributions to the final averages. In particular, if $\boldsymbol{\mu}_\alpha(T)$ is a normalized-to-1 single-ion magnetic moment, for each T the algorithm calculates

$$\langle \boldsymbol{\mu}(T) \rangle = \frac{1}{N_{MC} N_S} \sum_{i=1}^{N_{MC}} \left(\sum_{\alpha=1}^{N_S} \boldsymbol{\mu}_\alpha(T) \right)_i, \quad \langle E(T) \rangle = \frac{1}{N_{MC}} \sum_{i=1}^{N_{MC}} E_i \tag{3.23}$$

and, similarly proceeding for $\langle \mu^2(T) \rangle$ and $\langle E^2(T) \rangle$, it also computes

$$\chi(T) = \frac{\langle \mu^2(T) \rangle - \langle \boldsymbol{\mu}(T) \rangle^2}{k_B T}, \quad C_V(T) = \frac{\langle E^2(T) \rangle - \langle E(T) \rangle^2}{k_B T^2}, \tag{3.24}$$

as stated from the canonical ensemble fluctuation-dissipation relations (FDRs) [335]. Periodic boundary conditions are implemented, meaning that after each change of the spin configuration, the unit cells defining the borders of the finite lattice have the same spins of the unit cells on the opposite border on the same direction. The computation of the temperature dependence of the quantities calculated by means of Eqs. (3.23) and (3.24) allows to estimate the Curie temperature T_C for the ferromagnets, as an example, as the temperature at which $\langle \boldsymbol{\mu}(T) \rangle$ vanishes for $T \to T_C^-$ and $\chi(T)$ or $C_V(T)$ show a maximum. Due to the variables of the equilibrium distribution of Eq. (3.20), the value of T_C depends on N_S, $\{P^{(n)}\}$ and $\{Q\}$ as well. Therefore, convergence tests for different values of N_x, with $N_x = N_y$ for the sake of simplicity, are required in order to determine the sample size needed to provide a sufficiently accurate estimation of T_C for a given set of parameters $\{P^{(n)}\}$ and $\{Q\}$.

[7] Obviously, the spin rotation must be performed at least for a number of times larger than the number of spins. Therefore, the condition $N_{MC} \gg N_S$ is a good starting point for the convergence.

Chapter 4

Insights on novel van der Waals materials: ab initio simulations

"It doesn't matter how beautiful your theory is,
it doesn't matter how smart you are.
If it doesn't agree with experiment, it's wrong."

Richard Phillips Feynman

In this chapter, I will present the analysis on the vdW materials explored in this thesis, whose remarkable properties and applications have been summarized in Sec. 1.1. The ab initio simulations will be described in detail, in order to ensure the correct interpetration of the results, that are in line with the purposes outlined in Sec. 1.4 and have been obtained through the theoretical concepts and tools reported in Chaps. 2 and 3.

4.1 Relaxation effects on low-energy spectrum of twisted bilayer graphene

Here, we present a systematic analysis of the relaxation of TBG and its effects on the low-energy spectrum, at the four commensurate angles $\theta = 1.08°$, $1.61°$, $2.65°$, and $3.89°$ [200]. The electronic properties have been computed through both DFT and TB approaches, by choosing the relaxed atomic positions for the latter as those obtained through the relaxation procedure within the DFT scheme explained in Sec. 2.3.5. As a consequence, the full and correct description of the relaxation mechanism has allowed to better elucidate its role in the TBG electronic properties, without semi-classical [28, 57, 349, 350], multiscale [351, 352], or continuum relaxation [353] techniques. Indeed, this study is also based on a direct comparison with the available experimental data, pushing up to an unexplored computational cost until now. Distinct analyzes on the effects of only in-plane and only out-of-plane relaxations have been performed, for both an investigation of the ground-state stability against the temperature and the low-energy spectrum. Also, the comparison between DFT and TB electronic properties has allowed to extract an estimation of the electron-electron interaction in TBG. The relaxation has been confirmed as crucial for the gap opening at Γ point of the MBZ, mostly due to the out-of-plane contributions and less to the in-plane ones. Finally, the continuum model of Ref. [31] has been tested to approximate the DFT results, demonstrating that it is a powerful tool to explore small twist angles, for which the computational cost would become prohibitive. This is a remarkable result, since it gives a starting point for a minimal single-particle description within

n	m	θ (°)	L (Å)	N_{at}
31	30	1.08	129.75	11164
21	20	1.61	87.21	5044
13	12	2.65	53.19	1876
9	8	3.89	36.18	868

TABLE 4.1: The commensurate angles considered to investigate the properties of TBG. N_{at} is the number of atoms in the unit cell, L is lattice parameter of the superlattice, n and m identify the TBG unit cell according to Sec. 3.1.

more complex many-body approaches to study the superconductivity and the Mott insulating phases of TBG.

4.1.1 Geometry and first-principles calculations details

The geometrical description of TBG follows Sec. 3.1, except for the convention used to describe the 2D Bravais lattice of each graphene layer, whose basis vectors are here

$$\mathbf{a}_1 = (1,0)\,a, \quad \mathbf{a}_2 = \left(\frac{1}{2}, \frac{\sqrt{3}}{2}\right) a, \tag{4.1}$$

where $a = 2.456$ Å is the MG lattice parameter. The corresponding reciprocal lattice basis vectors are

$$\mathbf{b}_1 = \frac{2\pi}{a}\left(1, -\frac{1}{\sqrt{3}}\right), \quad \mathbf{b}_2 = \frac{2\pi}{a}\left(0, \frac{2}{\sqrt{3}}\right). \tag{4.2}$$

Since the rotation axis is chosen as passing through a pair of AA-stacked C atoms, each belonging to one of the layers, then a twist angle θ corresponds to rotate the first and second layers by $-\theta/2$ and $\theta/2$, respectively. As a consequence, the 2D Bravais lattice basis vectors of the graphene layers after the rotation are $\mathbf{a}_i^{(l)} = R(\mp\theta/2)\mathbf{a}_i$ and the corresponding reciprocal lattice basis vectors are $\mathbf{b}_i^{(l)} = R(\mp\theta/2)\mathbf{b}_i$, where $R(\theta)$ is the 2×2 matrix describing the rotation by θ. As anticipated, the commensurate angles $\theta = 1.08°$, $1.61°$, $2.65°$, and $3.89°$ have been considered to investigate the structural and electronic properties of TBG. In particular, based upon the notation introduced in Sec. 3.1, Table 4.1 resumes the features of the considered commensurate angles, along with the lattice parameter and the number of atoms in the superlattice unit cell for each case. The last two columns justify the huge computational cost required to face such a study.

DFT calculations have been carried out using the Vienna Ab initio Simulation Package (VASP) [354], since the latter required a smaller computational cost for TBG with respect to QE at the same performance level. A PAW-PP [317, 318] has been employed for carbon with the $2p$ orbitals in valence and the $1s$ orbitals frozen in the core [355]. In order to properly take into account the long-range interactions taking place between atoms belonging to different graphene layers, the vdW-DF2 exchange-correlation functional [279] has been adopted within the DFT framework. In general, as described in Sec. 2.1.8.b, it reduces the interatomic distances overastimated by the vdW-DF functional by Dion *et al.* [270], also predicting reasonable values of binding energies compared to the experiments. Furthermore, vdW-DF2 has been recently tested for graphene and h-BN by using the VASP package, both in the form of bulk and BL, revealing as a good choice for structural and vibrational

properties [356]. The PW basis used to sample the reciprocal space has been set up with a kinetic-energy cutoff of 400 eV for the wavefunctions. The MBZ sampling for the self-consistent calculations has been restricted at the Γ point for all four systems, since no significant changes have been observed for larger sampling sizes. DFT eigenvalues at the other points in the MBZ were obtained by non-SCF calculations. For the smallest angle, i.e., the magic angle $\theta = 1.08^\circ$, the size of the simulation cell limited the computation to one $\mathbf{k}$ point at a time, so that the reported DFT eigenvalues are referred to the Fermi energy E_F computed in the self-consistent calculations. The vacuum has been set at $\sim$ 6.5 Å. Full relaxation of the atomic positions was carried out until the residual forces were smaller than 0.002 eV/Å. Additional calculations were repeated using supercells with z axis of 12 and 14 Å. A small residual (maximum) relaxation of less than 0.002 Å was observed as the z axis was increased to 12 Å, but no further relaxation was detectable with the largest 14-Å vacuum space. All symmetries were turned off.

The tight-binding calculations are based on the Slater-Koster parametrization for p_z carbon atoms, in which the transfer integral is

$$t(\mathbf{R}) = -V_{pp\pi}\left[1 - \left(\frac{\mathbf{R}\cdot\hat{\mathbf{z}}}{R}\right)^2\right] - V_{pp\sigma}\left(\frac{\mathbf{R}\cdot\hat{\mathbf{z}}}{R}\right)^2, \tag{4.3}$$

where

$$V_{pp\pi} = V^0_{pp\pi}e^{(R-a_0)/r_0}, \quad V_{pp\sigma} = V^0_{pp\sigma}e^{(R-d_0)/r_0}, \tag{4.4}$$

$r_0 = 0.184a$, $a_0 = a/\sqrt{3}$ is the first-neighbor distance in MG, and $d_0 = 3.35$ Å is the intralayer distance, chosen in agreement with that of graphite. $V^0_{pp\pi} = -2.7$ eV and $V^0_{pp\sigma} = 0.48$ eV are the in-plane and out-of plane nearest-neighbor hopping energies, as from Ref. [58].

4.1.2 Effective continuum model

Here, we will briefly present the effective continuum model used to approximate the DFT calculations and generalizing the model proposed in Refs. [46, 47, 55, 58]. As shown in Sec. 3.1, the MBZ related to the commensurate structure is a hexagon whose inequivalent K and K' points are the two Dirac points $K^{(1)}$ and $K^{(2)}$ of the two graphene layers after the rotation. Therefore, if $\xi = \pm 1$ denotes the valley index of MG, then such Dirac points can be denoted by $K^{(1)}_\xi$ and $K^{(2)}_\xi$. According to the previously described TBG geometry, it turns out that the Dirac points of each layer are $\mathbf{K}^{(l)}_\xi = -\xi(2\mathbf{b}^{(l)}_1 + \mathbf{b}^{(l)}_2)/3$. As known, the MG spectrum is linear close enough to these points, and the Hamiltonian of each layer takes the expression [31]

$$\hat{H}^{(l)}_\xi(\mathbf{k}) = -\hbar v_F\{R((-1)^{l+1}\theta/2)(\mathbf{k} - \mathbf{K}^{(l)}_\xi)\}\cdot(\xi\sigma_x, \sigma_y), \tag{4.5}$$

where $\hbar v_F/a = 2.1354$ eV. If the graphene layers of the TBG interact with each other, then the system is described by the matrix Hamiltonian

$$H_\xi(\mathbf{k}) = \begin{pmatrix} H^{(1)}_\xi(\mathbf{k}) & U^\dagger_\xi \\ U_\xi & H^{(2)}_\xi(\mathbf{k}) \end{pmatrix}, \tag{4.6}$$

where the interlayer Hamiltonian is

$$U_\xi = \begin{pmatrix} u & u' \\ u' & u \end{pmatrix} + \begin{pmatrix} u & u'\omega^{-\xi} \\ u'\omega^{\xi} & u \end{pmatrix} e^{i\mathbf{G}_1\cdot\mathbf{r}} + \begin{pmatrix} u & u'\omega^{\xi} \\ u'\omega^{-\xi} & u \end{pmatrix} e^{i(\mathbf{G}_1+\mathbf{G}_2)\cdot\mathbf{r}}, \tag{4.7}$$

with $\omega = e^{i2\pi/3}$. Reciprocal vectors $\mathbf{G}_1$ and $\mathbf{G}_2$ express the coupling between each $\mathbf{k}$ point of the first layer and each $\mathbf{k}'$ point of the second layer according to the selection rules $\mathbf{k} = \mathbf{k}', \mathbf{k}+\mathbf{G}_1, \mathbf{k}+\mathbf{G}_1+\mathbf{G}_2$. Finally, based upon the work of Koshino *et al.* [55], u and u' are $\mathbf{k}$-dependent functions expressed in terms of the tight-binding transfer integral $t(\mathbf{R})$ between two sites at distance $\mathbf{R}$:

$$u(\mathbf{k}) = -\frac{1}{S_0}\int t(\mathbf{R}+d(\mathbf{R})\hat{\mathbf{z}})e^{i\mathbf{k}\cdot\mathbf{R}}d^2R, \quad u'(\mathbf{k}) = -\frac{1}{S_0}\int t(\mathbf{R}+d(\mathbf{R}-\boldsymbol{\tau}_1)\hat{\mathbf{z}})e^{i\mathbf{k}\cdot\mathbf{R}}d^2R, \tag{4.8}$$

where $S_0 = \sqrt{3}a^2/2$ is the area of the superlattice unit cell and $\boldsymbol{\tau}_1 = (2\mathbf{a}_2 - \mathbf{a}_1)/3$. The particular case $u = u'$ refers to the unrelaxed BG. However, $u(\mathbf{k})$ and $u'(\mathbf{k})$ have not been calculated, but they have been used only as fitting parameters, since the continuum model has been aimed to give a minimal description of the low-energy properties of the ab initio band structure. It will be demonstrated that their values are almost independent on the twist angle. The solutions have the general form

$$\begin{pmatrix} \psi^{A_1}_{n,\mathbf{k}}(\mathbf{r}) \\ \psi^{B_1}_{n,\mathbf{k}}(\mathbf{r}) \\ \psi^{A_2}_{n,\mathbf{k}}(\mathbf{r}) \\ \psi^{B_2}_{n,\mathbf{k}}(\mathbf{r}) \end{pmatrix} = \sum_{\mathbf{G}} \begin{pmatrix} c^{A_1}_{n,\mathbf{k}}(\mathbf{G}) \\ c^{B_1}_{n,\mathbf{k}}(\mathbf{G}) \\ c^{A_2}_{n,\mathbf{k}}(\mathbf{G}) \\ c^{B_2}_{n,\mathbf{k}}(\mathbf{G}) \end{pmatrix} e^{i(\mathbf{k}+\mathbf{G})\cdot\mathbf{r}}, \tag{4.9}$$

where A_i and B_i are the A and B sublattices of the i-th MG, respectively. In principle, the $\mathbf{G}$ point expansion should extend over the full (infinite) set of $\mathbf{G}$ vectors. However, for numerical purposes, this set has to be truncated. We choose a cutoff radius $\mathbf{G}_{cut}$ large enough to ensure the convergence of the obtained results and keep only the $\mathbf{G}$ vectors inside the sphere of radius $\mathbf{G}_{cut}$.

4.1.3 Geometric relaxation

As demonstrated in Ref. [31], an accurate description of the TBG at the magic angle $\theta = 1.08^\circ$ in terms of the out-of-plane relaxation and the vdW interaction between the graphene layers is of utmost importance to reproduce the experimental measurements by Cao *et al.* [29] at a single-particle level. Therefore, the analysis of the out-of-plane atomic displacements required two complementary representations. The first one is the color/relief map of the out-of-plane displacements in TBG at the considered twist angles with respect to the unrelaxed structure and is shown in Fig. 4.1. The second representation reports the behavior of the out-of-plane displacements of each graphene layer as a function of the point on the unit-cell long and short diagonals with respect to the average z coordinate z_{avg} in that layer for the four twist angles and is shown in Fig. 4.2. Hills and valleys of Fig. 4.1 are the results of the steric effects involving the p_z orbitals, when the AA-stacked BG is rotated. Indeed, the atoms of a layer moving toward the less repulsive regions, such as the hexagon centers (AB stacking), tend to reduce their distance from the other layer. As a consequence, the repulsion between the AA-stacked atoms through which the rotation axis passes is enhanced and the same occurs for their reciprocal distance. Hence, the rotation induces an increase of the out-of-plane displacement around the

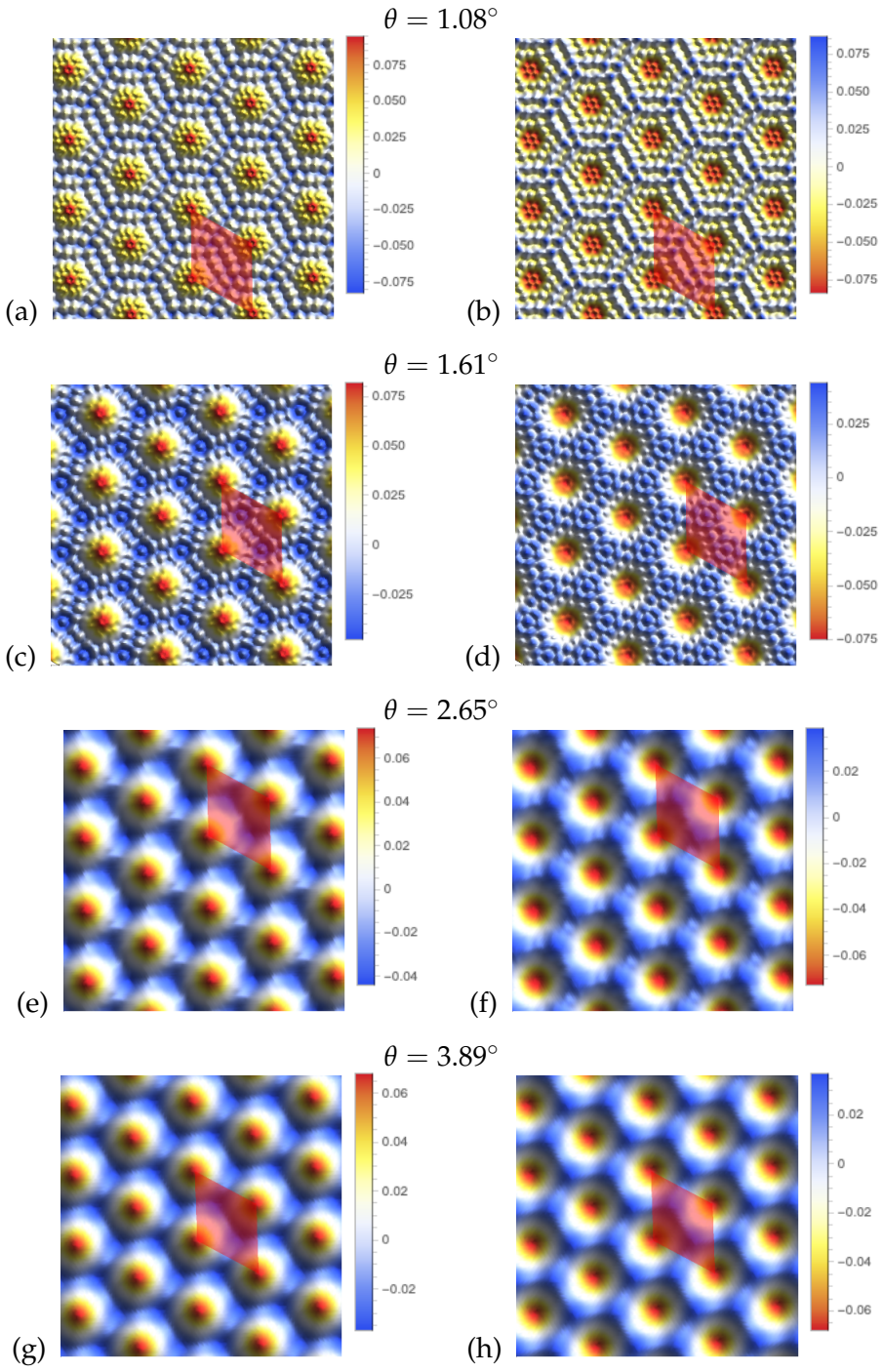

FIGURE 4.1: The color/relief map of the out-of-plane displacements in TBG at different twist angles: (a, b) 1.08°, (c, d) 1.61°, (e, f) 2.65°, (g, h) 3.89°. (a), (c), (e), and (g) refer to the top plane, whereas (b), (d), (f), and (h) to the bottom one. The color bar reports, in each plane, the measure of the z coordinate referred to its mean value in that plane (in Å units). In each map, the unit cell is highlighted in red.

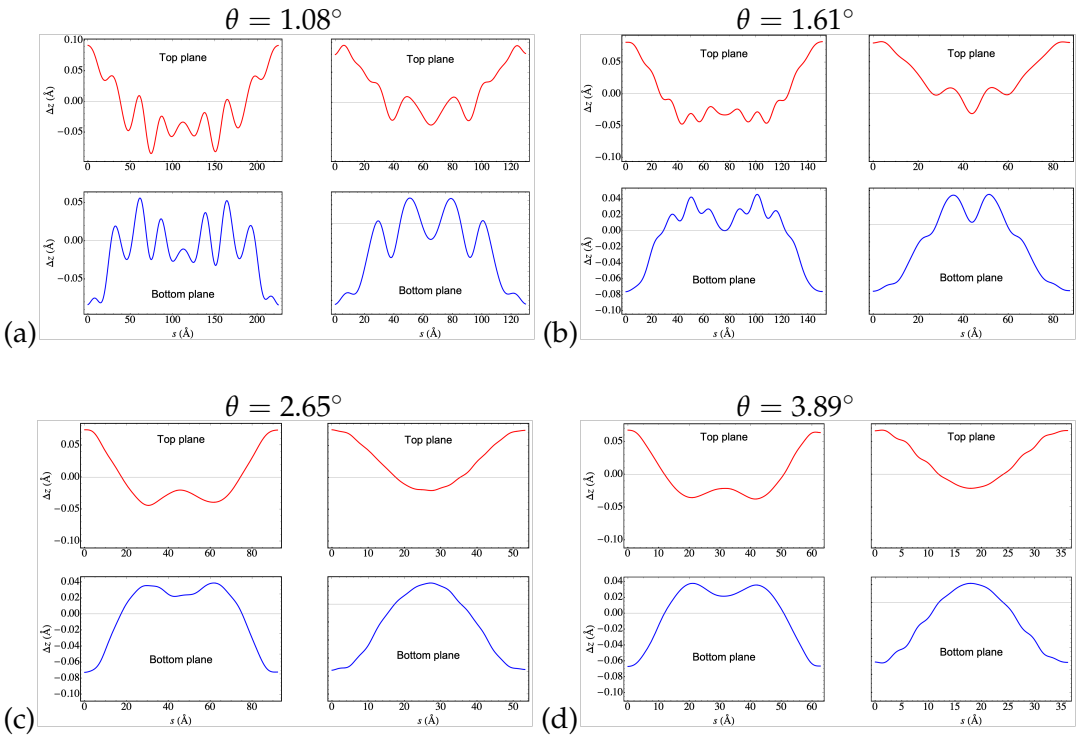

FIGURE 4.2: The out-of-plane displacements of each graphene plane along the unit-cell long and short diagonal for the four twist angles: $\theta = 1.08°$ (a), $\theta = 1.61°$ (b), $\theta = 2.65°$ (c), $\theta = 3.89°$ (d). The displacements are measured as the difference $\Delta z = z - z_{avg}$ of the z coordinate of each atom in a given plane and the average z coordinate z_{avg} in that plane ($\Delta z = 0$ for all atoms in the initial, twisted but unrelaxed configuration). In each box the higher (lower) panels correspond to the top (bottom) plane, whereas the left (right) panels correspond to the supercell long (short) diagonal (notice the different scale on the horizontal axis). The variable s represents the coordinate along the two diagonals, with $s = 0$ corresponding in both cases to the unit-cell origin (or a lattice equivalent site), where the AA stacking is preserved. To draw this plot, the atoms whose projections in the x-y plane lie onto or are closest to the unit-cell diagonals were considered.

AA-stacked atoms with the maximum on them and a decrease in the interstitial regions up to induce AB-stacked regions. As shown in Fig. 4.1, this naive prediction is strictly verified for the larger angles. For the smaller twist angles, an additional complicated atomic corrugation pattern of the unit cell, associated to the enormously increasing number of atoms, shows up. Fig. 4.2 confirms these observations, guiding the eye along specific paths in the unit cell. The larger the twist angle, the more predictable the out-of-plane displacement behavior in terms of AA- and AB-stacked regions, with a symmetry with respect to the path center because of the AA stacking before the twisting. It is worthwhile noticing that top and bottom layer relaxations should definitely not be the same, since the middle plane between the two graphene layers is not a reflection symmetry plane. Indeed, except for the corner sites of the unit cell, where there is a perfect AA stacking both in the unrelaxed and the relaxed structure, at a fixed point in the xy plane one can find an atom in the top plane whereas no one in the bottom and vice versa.

Full comprehension of the TBG relaxation is only achieved if also the in-plane displacements are considered. In particular, the C atoms create a vortexlike displacement field in each layer, with the vorticity (intended as the curl of the displacement field) changing sign when moving from the top to the bottom plane. This is shown in Fig. 4.3 only for $\theta = 1.08°$, since the patterns look quite similar at different twist

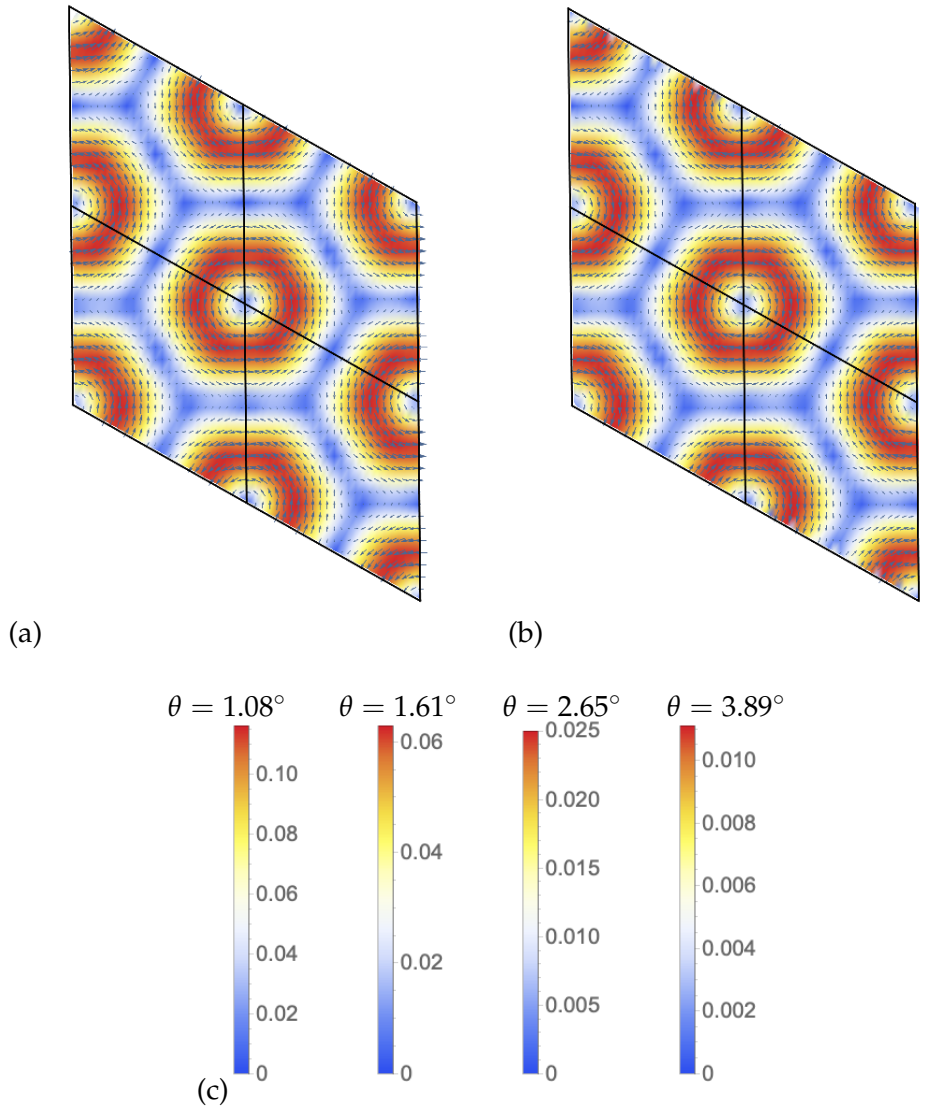

FIGURE 4.3: The color map and vector field of the in-plane displacements in TBG for the top (a) and bottom (b) plane. Each vector points in the displacement direction, and its magnitude is proportional to the displacement norm. The latter is also highlighted by the color. Since the patterns look quite similar at different twist angles, only the result for 1.08° is shown. (c) The color bars report the measure of the displacement in the x-y plane with respect to the unrelaxed structure (in Å units).

angles, except for the magnitude of the displacements, that decreases by an order of magnitude when moving from the smallest to the largest twist angle (the maximum displacement being of the order of $\sim$ 0.1 Å and $\sim$ 0.01 Å in the two cases, respectively). Here, the color map and the vector lengths are proportional to the displacement with respect to the unrelaxed TBG. Such a behavior originates from the total energy minimization toward the AB regions. Indeed, whereas AA- and AB-stacked atoms are not displaced, the displacement magnitude increase toward the unit-cell corners, thus for the atoms that mostly feel the repulsion due to a stacking that is quite close to AA (with the only exception of the pair of AA-stacked atoms in the unrelaxed structure, which show no displacement in the xy plane).

The investigation on the relaxation of TBG has allowed to establish a striking

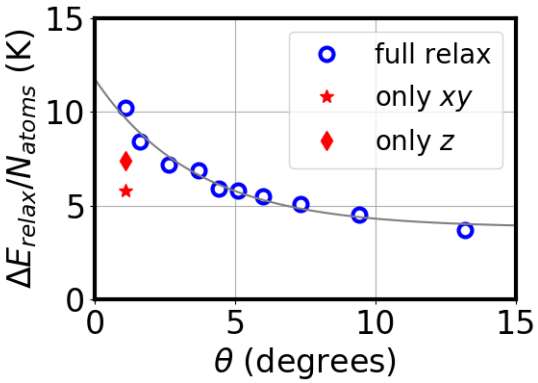

FIGURE 4.4: Per-atom relaxation energy as a function of the twist angle (blue circles). The red star (diamond) refers to $\theta = 1.08°$ and shows the relaxation energy when only the x-y (z) coordinates are allowed to relax. Dataset has been extended by considering the additional angles 4.41°, 5.09°, 6.01°, 7.34°, 9.43°, and 13.17°, corresponding to $(n,m) = (8,7), (7,6), (6,5), (5,4), (4,3), (3,2)$, respectively.

result about the ground-state stability against the temperature. In Fig. 4.4, the per-atom relaxation energy is reported in kelvin, with the relaxation energy defined as the energy gained by the structure when it is allowed to relax with respect to the unrelaxed configuration. Dataset has been extended by considering the additional angles 4.41°, 5.09°, 6.01°, 7.34°, 9.43°, and 13.17°, corresponding to $(n,m) = (8,7)$, $(7,6)$, $(6,5)$, $(5,4)$, $(4,3)$, $(3,2)$, respectively. Such a relaxation energy normalized to the number of atoms in the unit cell allows a comparison between different twist angles. Moreover, it can be also read as the upper bound of the thermal energy $k_B T$ that in a real experiment would induce thermal fluctuations of the atomic positions that in turn would destroy the ground-state geometry pattern shown in Figs. 4.1 and 4.3. The per-atom relaxation energy indicates that the smaller the twist angle, the more stable (with respect to the unrelaxed structure) the ground-state geometry pattern. This is explained by considering that in the case of large unit cells the atoms have more freedom to relax to a lower total energy. Indeed, in the particular case of $\theta = 1.08°$, the reduction of such a freedom by neglecting in-plane or out-of-plane relaxations gives a smaller per-atom relaxation energy, as shown in Fig. 4.4 (red diamond and star, respectively).

4.1.4 Low-energy spectrum for different twist angles

Once the analysis of the effects of relaxation on the structural properties has been carried out, an in-depth investigation of the low-energy spectrum for the four considered twist angles can be performed. The electronic structures calculated by using both the TB approach and the DFT, with and without including relaxation mechanisms, are reported in Fig. 4.5. The blue points are the DFT eigenvalues and are connected by the dashed blue in order to give a guide for the DFT bands shape. The red (full) lines are the TB bands, where, however, the atomic positions for the relaxed structures are the ones optimized within the DFT approach. The comparison between the two methods is a powerful tool to directly extract information on the electron-electron interactions characterizing the TBG, since these are not considered in the TB approach, whereas they are taken into account in the DFT exchange-correlation functional even though in an approximated manner. The most evident effect of the relaxation consists in opening the gaps separating the bands around E_F from the other bands, at both the electron and hole sides. In particular, a gap of 26

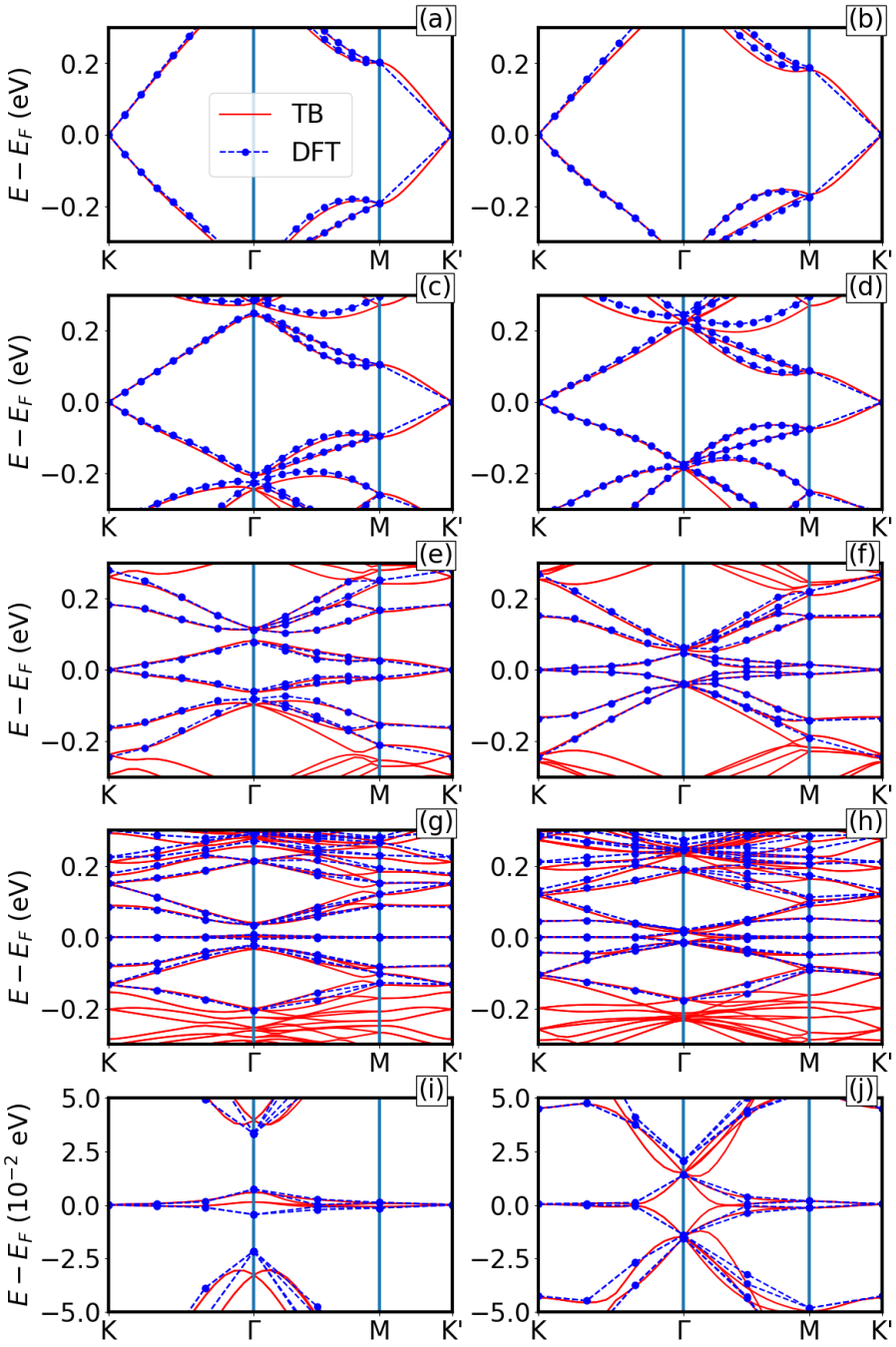

FIGURE 4.5: Low-energy spectrum of TBG along the K-Γ-M-K' path at different twist angles: (a, b) $\theta = 3.89°$, (c, d) $\theta = 2.65°$, (e, f) $\theta = 1.61°$, (g, h) $\theta = 1.08°$, (i, j) $\theta = 1.08°$ zoomed around the Fermi energy (notice the different scale on the y axis). The (a), (c), (e), (g), (i) panels correspond to the relaxed structure and the (b), (d), (f), (h), (j) ones to the initial, unrelaxed geometry. Blue dashed lines and filled dots correspond to the DFT calculation, red solid lines to the TB approach. Zero energy corresponds to the Fermi energy.

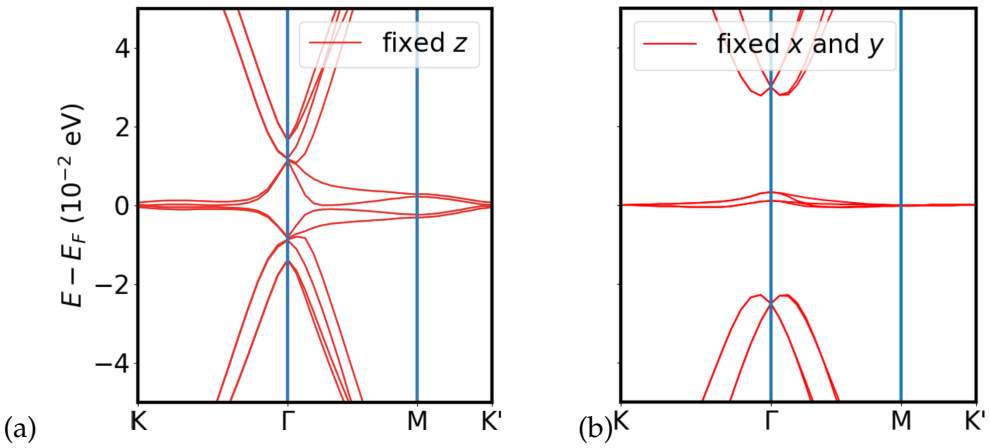

FIGURE 4.6: Tight-binding electronic band structure of TBG along the K-Γ-M-K' path at $\theta = 1.08°$, zoomed around the Fermi energy. The band structures corresponding to the geometry as obtained by allowing only (a) in-plane and (b) out-of-plane relaxations in the DFT calculation are shown.

meV (16 meV) separates the flat minibands of $\theta = 1.08°$ TBG from the highest occupied (lowest unoccupied) bands, consistent with the experiments [29, 30, 357–361]. The full bandwidth is $\sim$ 20 meV, according to that measured in the experiment of Ref. [29]. Overall, the TB bands agree with the DFT eigenvalues, except for small regions around the Γ point of the MBZ. The estimation of the electron-electron interaction provides quite small values, in particular being $\lesssim$ 10 meV for $\theta = 1.08°$ in the zoom of Fig. 4.5(i).

Similarly to the study of the structural properties, the effects of the relaxation when only the x-y (z) coordinates are allowed to relax have been evaluated on the low-energy spectrum, only for $\theta = 1.08°$ and by using the TB approach. The results are shown in Fig. 4.6, that can be directly compared to the fully relaxed and the unrelaxed cases of Figs. 4.5(i) and (j), respectively. When only the x-y coordinates are allowed to relax (see Fig. 4.6(a)), some variations in the flat minibands behavior occur around the Γ point, but there is not any gap opening. On the contrary, when only the z coordinates are allowed to relax (see Fig. 4.6(b)), the gaps open reaching values that are similar to the fully relaxed case, in addition to the almost identical shape of the flat minibands. Such a comparison has also been performed through DFT calculations only on the gaps, confirming the TB results. In the former case, the two gaps turn out to both be zero. In the latter case, we obtained gaps of $\sim$ 2 and $\sim$ 14 meV, which underestimates these values in the fully relaxed system, especially in the hole side. Hence, while the in-plane relaxation does not substantially modify the band structure with respect to the unrelaxed system, the out-of-plane relaxation is mainly responsible for the gap opening.

The effective continuum model described in Sec. 4.1.2 can be adopted to approximate the DFT calculations. It turns out that the number N_G of vectors to converge the lowest-energy states is rather small. The low-energy continuum Hamiltonian matrix has the dimension $D = 4N_G$, and $N_G = 19$ allows for good convergence in an energy shell of few hundred meV around the Fermi energy, whereas full convergence, i.e., band energies converged within less than 1 meV, is achieved with $N_G = 37$. The parameters u and u' result as independent on the twist angle and, within a reasonable error, can be approximated as $u = u' = 0.107 \pm 0.004$ in the unrelaxed case and $u = 0.078 \pm 0.002$, $u' = 0.098 \pm 0.004$ for relaxed structures. The independence on the twist angle addresses the use of the continuum model to smaller angles, where

the unit cell would become impractically large to employ atomistic approaches. As a consequence, the continuum model can be adopted as a minimal single-particle description within more complex many-body [55, 359] approaches, in order to study the superconductivity and the Mott insulating state of this system.

4.2 Electronic properties of twisted heterobilayer $MoS_2/NbSe_2$

In this section, an in-depth DFT analysis of the electronic properties of twisted HeBL $MoS_2/NbSe_2$ is presented [203]. Starting from the energetics of different stacking configurations through a proper and systematic inclusion of the vdW interaction, the untwisted geometries along with the commensurate structures at the twist angles $\theta = 9.43°$, $13.17°$, $21.78°$, $32.20°$, $42.10°$ allow to understand the role of each ML, the interplay between interlayer coupling and chosen materials, and the effect of the twisting operation on the HeBL electronic properties. Since the most significant effects are observed close to the Fermi energy and are related to ML $NbSe_2$, twisted HeBL $MoS_2/NbSe_2$ candidates as ideal platform to explore the twist-angle-dependent Ising superconductivity that could probably be induced by proximity effect by the latter, as subsequently predicted for HeBL $NbSe_2$/graphene [197].

4.2.1 Structural properties and energetics

Previous reports on untwisted TMD HeBLs had widely investigated the dependence of the electronic structure on the stacking [362, 363]. The explored stackings are referred to as AA, T, C27, and C7 and are schematically shown in Fig. 4.7. In the AA stacking, the metal (chalcogen) atoms of the first layer are on top of metal (chalcogen) atoms of the other layer. The C27 stacking is obtained from the AA one by rotating one layer with respect to the other by 180° around the axis that crosses a pair of overlapped metallic atoms of the two layers. The T stacking is obtained from the AA one by a translation such that the metals of a layer are on top of the hexagons centers of the other layer. The C7 stacking is obtained from the T one by rotating one layer with respect to the other by 60° around the axis that crosses a pair of overlapped metallic and chalcogen atoms of the two layers (in this way the metal atoms are on top of chalcogen atoms and chalcogen atoms are on top of metal atoms). Therefore, C7 stacking is $2H_c$ polymorph of bulk MoS_2, for instance. In both Refs. [362] and [363], the electronic structures obtained through DFT first-principles calculations negligibly change with the stacking, with the T and C7 stackings being the most stable ones. In particular, Ref. [362] analyzes HeBL MoS_2/WS_2 without including vdW interaction between the layers. Ref. [363] considers other semiconductor-semiconductor HeBLs and also metal-semiconductor HeBLs, the latter being FeS_2/MoS_2, VS_2/MoS_2, and VSe_2/MoS_2, by including the vdW dispersion through the optB88-vdW functional [282, 297]. The interlayer binding energy can be defined as $E_b = E_{HeBL} - E_{ML,1} - E_{ML,2}$, where E_{HeBL} is the total energy of the HeBL and $E_{ML,i}$ is the energy of the i-th isolated ML ($i = 1, 2$). Interlayer binding energies E_b for the metal-semiconductor HeBLs range from -160 meV to -310 meV, increasing in module with the transition-metal group and chalcogen period of the periodic table. Due to their stability, Ref. [35] chooses the T stacking and the C7 stacking as the initial ($\theta = 0°$) and final ($\theta = 60°$) configurations, respectively, in order to study the dependence of the electronic structure of only semiconducting TMD HeBLs on the twist angle, as anticipated in Sec. 1.1.2.b. In particular, by using the optB88-vdW

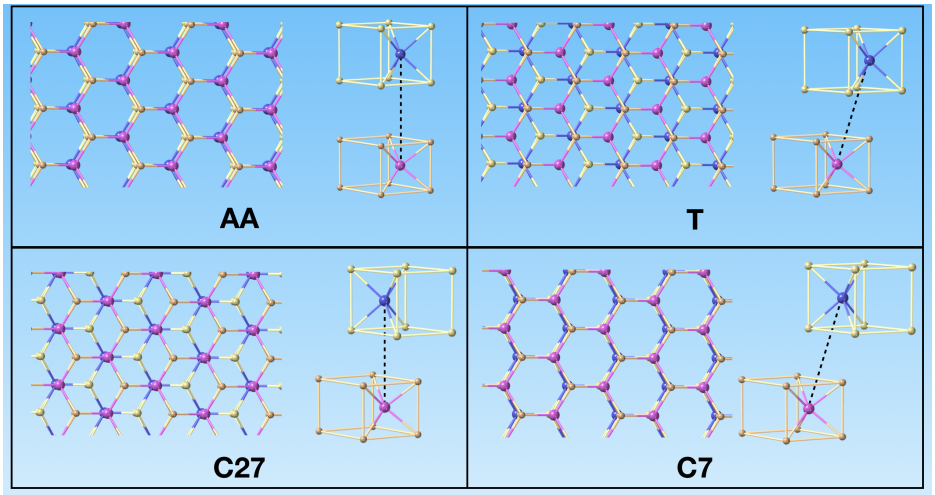

FIGURE 4.7: Schematic views of AA, T, C27, C7 stacking configurations. Each stacking is obtained from the fundamental AA stacking, where there is perfect overlap along the stacking direction of the two MLs, after a translation and/or a rotation of the MLs with respect to each other. Purple and blue spheres represent transition-metal atoms, whereas orange and yellow spheres represent chalcogen atoms.

functional, the authors compute binding energies over -230 meV, maybe suggesting that smaller values are related to the metal-semiconductor HeBLs.

In our work on the metal-semiconductor HeBL $MoS_2/NbSe_2$, we have considered the stacking configurations schematized in Fig. 4.7. The calculations have been performed by using US-PPs [364] based on the PBE exchange-correlation functional to represent the atomic cores [365]. The PW basis used to sample the reciprocal space has been set up with a kinetic-energy cutoff of 50 Ry for the wavefunctions, while a 300 Ry cutoff energy has been used to represent the charge density. The effect of the vdW interaction has been taken into account. In particular, at the stage of the calculations on structural properties and energetics of the untwisted geometries, we have tested and compared different functionals, i.e., vdW-DF [270], vdW-obk8 [282], vdW-DF-C09 [286], vdW-DF2 [279], vdW-DF2-C09 [285], and vdW-DF-cx [366]. Such a comparative analysis has been performed in order to compute the interlayer binding energy E_b of the HeBL $MoS_2/NbSe_2$ also as a function of the stacking. We have chosen a vacuum space of $\simeq$ 20 Å to define the supercell and sampled the BZ by a $8\times8\times1$ MP **k**-point grid for the untwisted geometries.

The full relaxation of the isolated MLs of MoS_2 and $NbSe_2$ provided the in-plane lattice parameters $a_{ML,MoS_2} = 3.15$ Å and $a_{ML,NbSe_2} = 3.44$ Å, in fair agreement with previous theoretical estimations $a^{th}_{ML,MoS_2} = 3.24$ Å [367] and $a^{th}_{ML,NbSe_2} = 3.39$ Å [368], in addition to the experimental estimation $a^{exp}_{ML,MoS_2} = 3.24$ Å [369]. Therefore, the HeBL had a slight lattice mismatch of $\simeq$ 9%. For all the stacking configurations, the HeBL optimized in-plane lattice parameter was $a = 3.29$ Å, which is intermediate between the MLs in-plane lattice parameters, and almost independent on the exchange-correlation functional.

As anticipated, the calculation of the binding energy and the equilibrium interlayer distance has been tested against different vdW functionals, in order to show whether and to what extent the calculated properties depend on the functional. As examples, the binding energy curves are reported for the T and AA stacking configurations in Fig. 4.8. Due to the lacking of experimental data on HeBL $MoS_2/NbSe_2$,

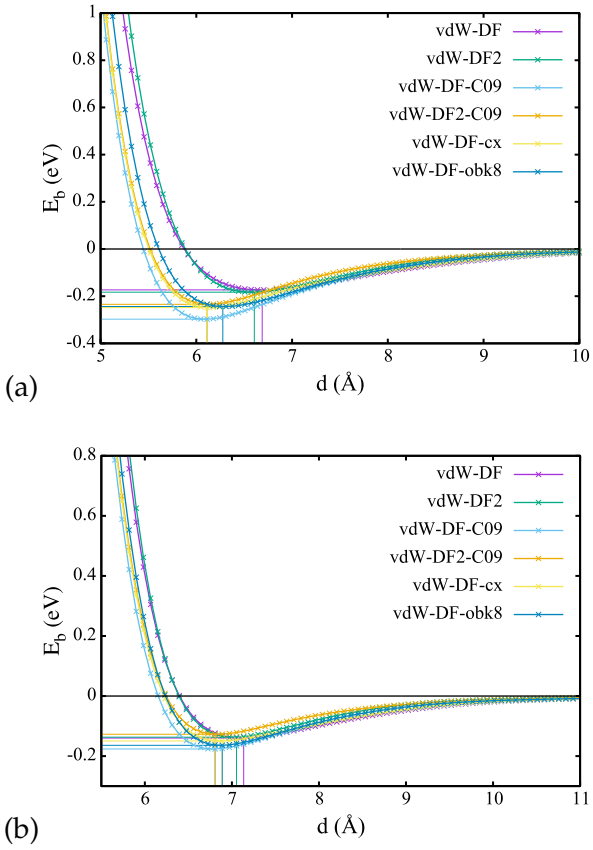

FIGURE 4.8: Interlayer binding energy E_b of HeBL $MoS_2/NbSe_2$ in the T (a) and AA (b) stacking configurations as a function of the interlayer distance d for different vdW functionals. Zero energy corresponds to the E_b at $d \simeq 15$ Å.

it is expected that the curves must be at least in agreement with the issues and performances of the functionals reported in literature for layered solids [370]. Typically, vdW-DF overestimates interatomic distances but predicts reasonable binding energies. Instead, vdW-DF2 reduces the interatomic distances by retaining accurate binding energies. The vdW-DF-C09 functional, obtained by including $C09_x$ in vdW-DF (see Sec. 2.1.8.b), provides smaller interlayer separations but overestimated binding energies. By using the vdW-DF2 correlation energy along with $C09_x$ (i.e., vdW-DF2-C09), the binding energy overestimation should be reduced, resulting in a value comparable with the vdW-DF2 one. Finally, vdW-obk8 and vdW-DF-cx provide good values of binding energies, but the former overestimates the interlayer distance. Therefore, it is expected that vdW-DF2-C09 and vdW-DF-cx give similar performances, and this is observed in Fig. 4.8, especially for the T stacking. The equilibrium interlayer distances range from 6.11 Å to 6.27 Å for the T stacking (from 6.80 Å to 6.88 Å for the AA stacking) and binding energies at the equilibrium distances from -297 eV to -235 eV for the T stacking (from -176 eV to -127 for the AA stacking). Since the T stacking is the most stable one, the choice of the vdW exchange-correlation functional for the electronic properties calculation can be inferred from its curves. All the functionals provide the expected behaviors. Following the literature reports cited in Sec. 2.1.8.b, we have chosen vdW-DF2-C09. It should be pointed out that all the mentioned functionals are self consistent and account for the electronic charge density at each step of the self consistency loop. This has to be contrasted with semiempirical vdW dispersion correction DFT-D [291], used for the

Stacking	E_b (meV)	d_{opt} (Å)	Interpenetration (eV)
AA	-125.46	6.97	0.23
C7	-220.46	6.23	0.15
C27	-233.51	6.08	0.22
T	-236.54	6.11	0.09

TABLE 4.2: Interlayer binding energies E_b, optimized interlayer distances d_{opt}, and interpenetration in the band structure of the untwisted stacking configurations of Fig. 4.7, computed through the vdW-DF2-C09 exchange-correlation functional. The rows are ordered from the less to the most stable stacking configuration. The interpenetration is defined as the energy range where an overlap close to the K point of the band that crosses the Fermi energy and the next upper band shows up (see Figs. 4.9(a) and 4.9(c) as examples).

previous report on untwisted HeBL $MoS_2/NbSe_2$ [201].

Table 4.2 shows the interlayer binding energies and the optimized interlayer distances d_{opt} for each stacking configuration, measured as the distance between Mo and Nb planes, computed through the vdW-DF2-C09 exchange-correlation functional. Although T and C7 stackings resulted as the the lowest-energy stackings for TMD HeBLs in the previous works, in our case the T stacking is the most stable, followed by the C27 stacking. The AA stacking shows the highest value of E_b, that is also quite different from the binding energies of the metal-semiconductor HeBLs of Ref. [363]. Therefore, although this stacking is the easiest to investigate under theoretical studies, its experimental implementation is probably complicated to keep stable and the atomic structure of the system easily turns into other lower energy stackings. Instead, C7, C27, and T stackings report binding energies in agreement with the previous work, even if the energy differences are sufficient to establish the T stacking as the most stable stacking at low temperatures. The relative stability of the different stackings is reflected in the values of d_{opt}. Indeed, the lower the binding energy, the smaller the optimized interlayer distance. This is an expected result because the repulsion in the interlayer space is stronger in the AA and C7 stackings compared to the T and C27 stackings due to the perfect overlap of the hexagons of the two layers in the first two cases. Finally, for the electronic properties, we have restricted our analysis only to the AA stacking, that is the most intuitive stacking configuration, and the T stacking, that is the most stable stacking configuration.

4.2.2 Electronic properties of untwisted HeBL $MoS_2/NbSe_2$

As observed in Refs. [362] and [363], the electronic structure of TMD HeBLs are quite insensitive to the stacking. In Fig. 4.9, the electronic properties of untwisted HeBL $MoS_2/NbSe_2$ in the T and AA stackings are reported through their band structures and DOSs. First, the HeBL is metallic, due to the band crossing at the Fermi energy. This behavior is certainly induced by the ML $NbSe_2$, that is a metal and totally contributes to the DOS at the Fermi energy. The band structures of the T and AA stackings differ by the interpenetration involving the band crossing the Fermi energy and the next higher energy band at the K point of the BZ. Further calculations show that all stackings exhibit such an interpenetration, with the values reported in Table 4.2. Our results are in agreement with those reported in Ref. [201] for both the band interpenetration and the PDOS, where AA, T, C27, and C7 stackings correspond to A, AB1, AB2, and B stackings, respectively. An in-depth PDOS analysis was performed

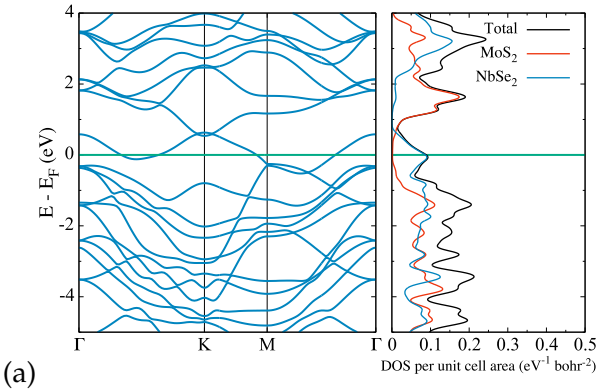

(a)

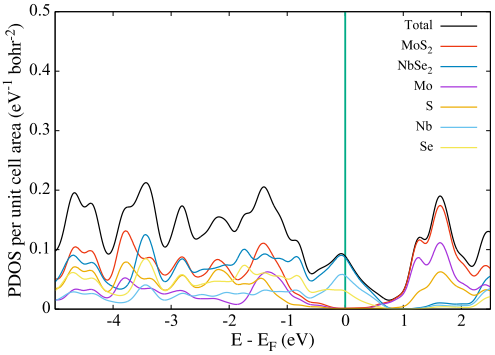

(b)

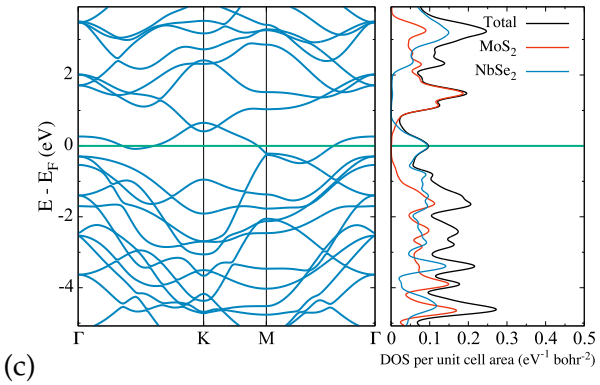

(c)

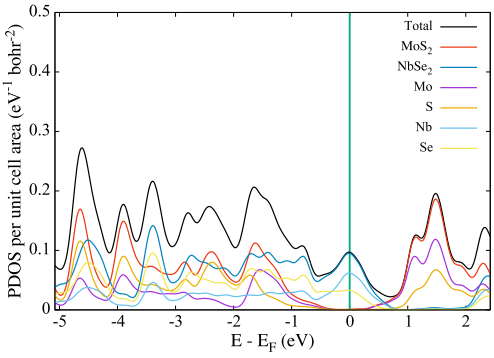

(d)

FIGURE 4.9: Band structure and DOS of $MoS_2/NbSe_2$ heterobilayer in the T stacking (a) and AA stacking (c), with respective (b) and (d) PDOS analysis for the individual atoms contributions. Zero energy (highlighted with green line) corresponds to the Fermi energy.

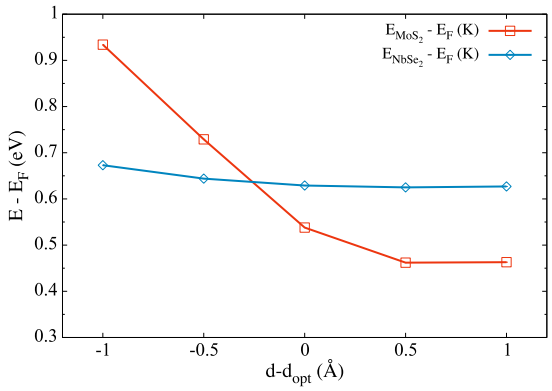

FIGURE 4.10: Dependence of the band edges of the MoS_2- and $NbSe_2$-related bands that form the interpenetration at the K point in the T stacking (see Fig. 4.9(a)) as a function of interlayer distance d, that is changed up to ± 1 Å with respect to the equilibrium distance d_{opt}.

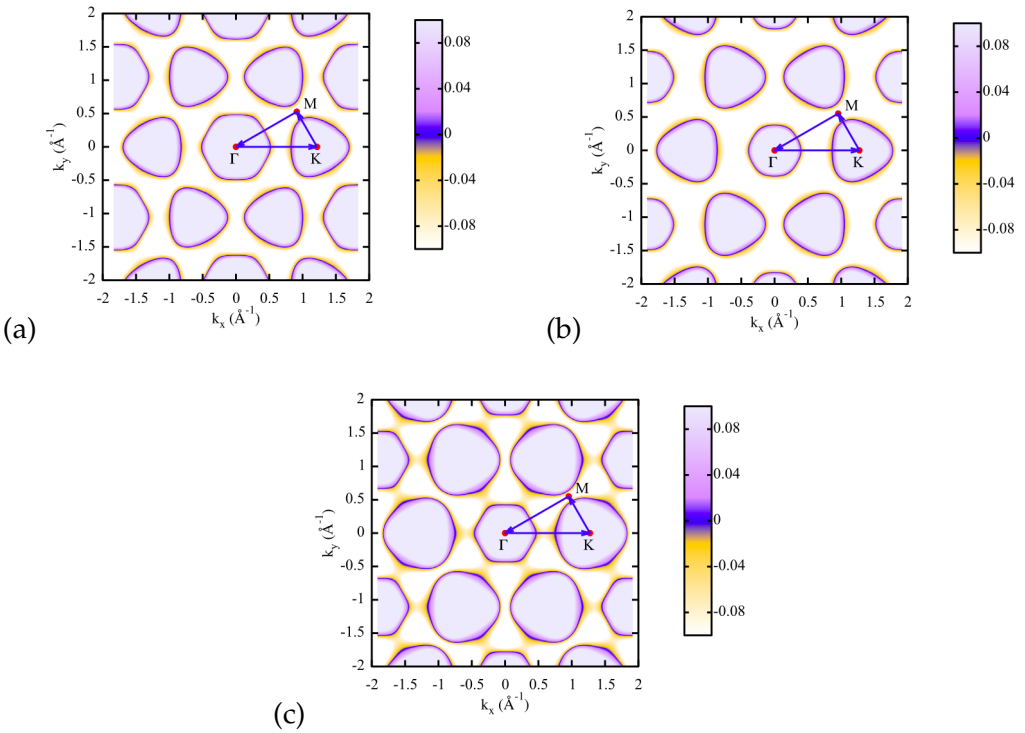

FIGURE 4.11: Representation of the 2D Fermi surface of ML $NbSe_2$ (a) and of the untwisted HeBL $MoS_2/NbSe_2$ in the T (b) and AA (c) stacking configurations. The shown DFT eigenvalues are included in a symmetrical range of amplitude 0.2 eV centered on the Fermi energy, that corresponds to zero energy. The energy scale on the color bars is in eV.

to distinguish, in addition to the individual layer contributions to the DFT eigenvalues, the individual atom contributions of each layer (see Figs. 4.9(b) and 4.9(d)). In both ML MoS_2 and ML $NbSe_2$, both the metallic and the chalcogen atoms contribute, with the predominance of the first ones. Due to the interpenetration at the K point of the band structures, it is difficult to distinguish the stacking just at the level of DOSs and PDOSs, with an essentially similar contribution from each atomic constituent.

The interpenetration is strictly related to the interlayer distance and, thus, the interlayer coupling. This is demostrated in Fig. 4.10, where, in the case of the T stacking, the band edges giving rise to the interpenetration at the K point are calculated as a function of the interlayer distance, with the latter changing up to $\pm$ 1 Å with respect to the optimized interlayer distance of Table 4.2. It turns out that the closer the MLs, the smaller the interpenetration, until the latter vanishes for $d \simeq$5.85 Å and a (direct) band gap opens up between the two bands. On the other hand, we checked that the interpenetration can be increased up to 0.16 eV by increasing d_{opt} by 1 Å. As a consequence, the interlayer distance tuning by a compressive or tensile external pressure on the HeBL directly changes the bands derived from different atomic orbitals (MoS_2- and $NbSe_2$-related orbitals in this case).

The predominance of the ML $NbSe_2$ contribution at E_F, as revealed by the PDOS analysis in Fig. 4.9, is also reflected on the Fermi surface (FS). Fig. 4.11 compares the FSs of the ML $NbSe_2$ to those of the untwisted geometries in the T and AA stackings. As known, the former consists of a hexagonal pocket around the Γ point and triangular pockets around the K and K' points. The slight differences between the band structures of T- and AA-stacked untwisted HeBL $MoS_2/NbSe_2$ are quite visible through the FS analysis, since the latter includes DFT eigenvalues in a symmetrical range of an amplitude of 0.2 eV centered on E_F. Therefore, the different contribution of ML MoS_2 and, thus, the above described interpenetration have crucial roles. Indeed, from Fig. 4.9(a) it is expected that FS does not differ too much from the ML $NbSe_2$ FS in the T stacking. Instead, in the AA stacking, the interpenetration is larger than the previous case and the interlayer coupling affects the shape of the ML $NbSe_2$ single band crossing E_F (see Fig. 4.9(c)), thus suggesting modifications in the FS. This is exactly what can be observed in Fig. 4.11. In the T stacking, the FS presents similar shape and extension of the ML $NbSe_2$ FS. Instead, in the AA stacking, the triangular shape of the pockets around the K and K' points is lost, as result of the larger interpenetration at these points. The ML $NbSe_2$ FS features are directly responsible for the Ising superconductivity [371]. In a recent study [197], the twist-angle-dependent proximity-induced Ising superconductivity has been predicted for HeBL $NbSe_2$/graphene, resulting from the hybridization around the Fermi energy of the ML $NbSe_2$ and graphene bands. Therefore, the Fermi energy physics of the ML $NbSe_2$ inherited by the HeBL $MoS_2/NbSe_2$ opens up to use the latter as platform to investigate 2D superconductivity, by studying how its DOFs, as stacking, interlayer distance, and twist angle, could be exploited to modify the interpenetration and the interlayer coupling. This would allow to understand the roles of the latter in the hybridization amount around E_F in order to favor the proximity effect and induce a superconducting gap.

4.2.3 Effects of twisting

The analysis carried out so far has been used as support to understand the intriguing effects of the twist angle on the electronic properties of the HeBL $MoS_2/NbSe_2$. As anticipated, we have considered the commensurate angles $\theta = 9.43^\circ, 13.17^\circ, 21.78^\circ,$

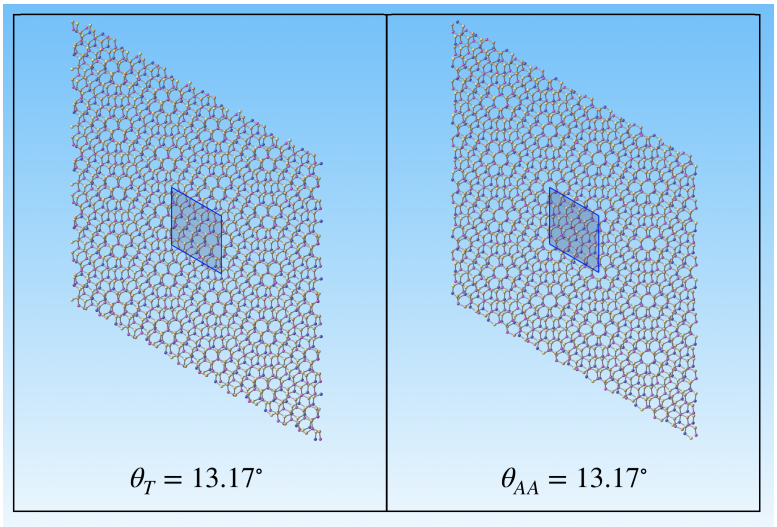

FIGURE 4.12: Two examples of commensurate moiré patterns investigated in this work. We denote with θ_T and θ_{AA} the twisted configurations obtained starting from the T and AA stackings, respectively.

n	m	θ (°)	L (Å)	N_{at}	d_T (Å)	d_{AA} (Å)
4	3	9.43	20.01	222	6.40	6.54
3	2	13.17	14.34	114	6.41	6.49
2	1	21.78	8.70	42	6.52	6.48
3	1	32.20	11.86	78	6.45	6.43
5	1	42.10	18.32	186	6.50	6.50

TABLE 4.3: The studied commensurate moiré patterns. We denote with d_T and d_{AA} the average optimized interlayer distances of the twisted configurations obtained from the T and AA stacking geometries, respectively, calculated as the differences between the average z coordinates of the Nb and Mo atoms planes. N_{at} is the number of atoms in the unit cell and L is lattice parameter of the superlattice.

32.20°, 42.10°. Such a choice relies on two reasons. First, the commensurate angles taken into account require the smallest computational cost in terms of sizes and number of atoms contained in the superlattice unit cell. Second, the selected angles give a representative sampling of the entire range from $\theta = 0^\circ$ to $\theta = 60^\circ$, that is relevant for hexagonal symmetries, thus providing preliminary information for further in-depth analysis. In Fig. 4.12, the commensurate moiré pattern for $\theta = 13.17^\circ$ is reported for both T and AA stackings, as an example. In particular, Table 4.3 shows the features of the selected commensurate angles, including the lattice parameter and the number of atoms in the superlattice unit cell, in addition to the optimized interlayer distances d_T and d_{AA} of the twisted configurations obtained from the T and AA stackings, respectively. For the AA stacking, results are in agreement with a priori qualitative predictions. Indeed, the comparison between Tables 4.2 and 4.3 shows that the optimized interlayer distance reduces far from $\theta = 0^\circ$ and $\theta = 60^\circ$, according to the fact that the atoms of a layer move towards the hexagon centers of the other layer and, thus, the consequent steric effects move closer the layers to represent the reduced interlayer coupling. The opposite occurs for the T stacking, since the rotation induces a displacement of the atoms of a layer with respect to the hexagon centers of the other layer and, thus, the interlayer distance enhances.

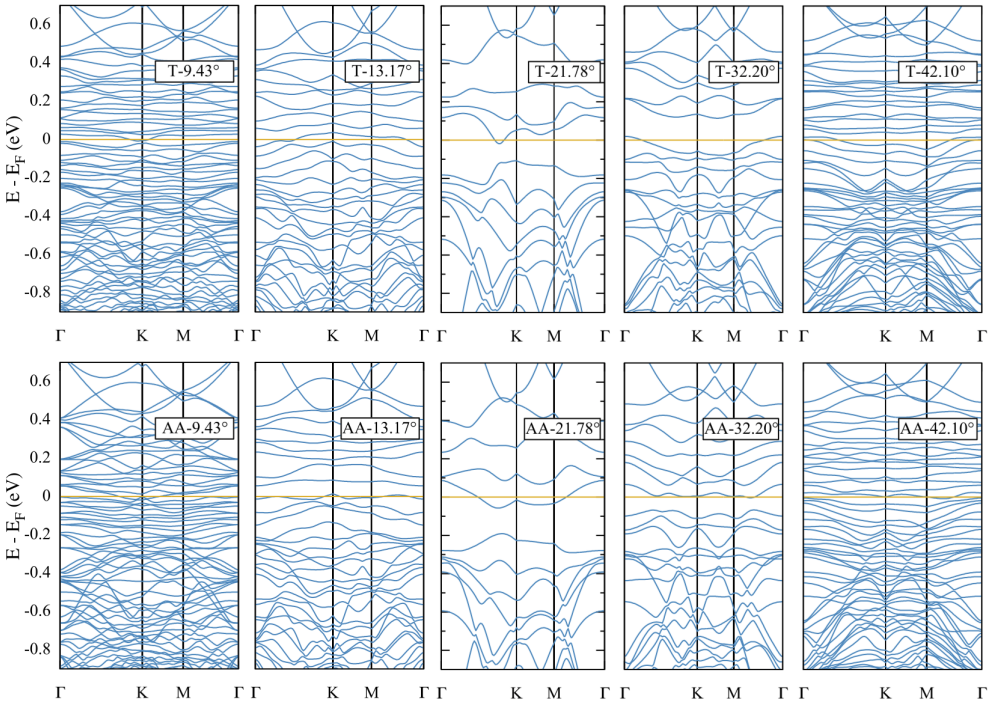

FIGURE 4.13: Computed band structures of the HeBL $MoS_2/NbSe_2$ in the twisted configurations obtained starting from T (top) and AA (bottom) stacking. Zero energy (highlighted with a yellow line) corresponds to the Fermi energy E_F.

As expected, the band structures of the twisted geometries have non-trivial behaviors, due to the complicated interactions and the atomic distribution in the superlattice unit cell. Therefore, we have only focused on a $\sim$ 1.5 eV-wide region around the Fermi energy, that is dominated by the ML $NbSe_2$ bands. The band structures for the examined twisted configurations are shown in Fig. 4.13. First, the twisted configurations corresponding to a larger number of atoms in the unit cell have a denser band structure due to the folding. The structures for the most far angles from $\theta = 0°$ and $\theta = 60°$, i.e., $\theta = 13.17°, 21.78°, 32.20°$, show an interesting common feature: an electronic gap opens up between the band crossing the Fermi energy and the previous or next one. The value of the gap reaches its maximum near $\theta \simeq 30°$. This is a remarkable result, since an external gate voltage could be used to move the Fermi energy and induce a metal-to-semiconductor transition with a low energetic cost, being of the order of 10 meV. The most close angles to $\theta = 0°$ and $\theta = 60°$, i.e., $\theta = 9.43°, 13.17°, 42.10°$, show extremely complex band structures due to the number of atoms in the unit cells and the folding, but a general band flattening occurs for them. We have performed an in-depth analysis for the most evident case, that is $\theta = 13.17°$. Indeed, for both $\theta_T = 13.17°$ and $\theta_{AA} = 13.17°$ the band above that crossing the Fermi energy undergoes a flattening, more evident for $\theta_{AA} = 13.17°$. This implies that another important effect of the twisting is to induce a band localization, since the band flattening certainly implies a low conductivity of the metallic HeBL and could also be linked to the presence of localized states. We have verified such a conclusion by calculating the square modulus of the Bloch states related to the above-mentioned bands at Γ, having observed that the results did not depend on the high-symmetry points Γ, K, and M of the MBZ. In order to interpolate the electronic bands around the Fermi energy, the localization analysis has been performed by calculating MLWFs through the W90 package [320]. The results are reported in

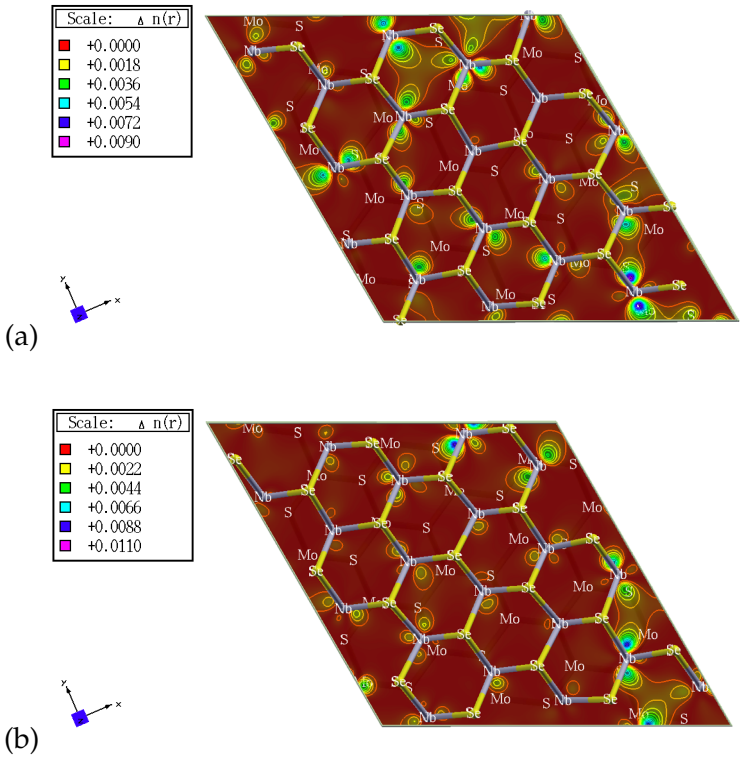

FIGURE 4.14: Squared modulus of the Bloch states related to the almost-flat bands for $\theta_T = 13.17°$ (a) and $\theta_{AA} = 13.17°$ (b) at the Γ point of the MBZ. This plot has been obtained by the XCrySDen (X-Window Crystalline Structures and Densities) software [372].

Fig. 4.14 for both $\theta_T = 13.17°$ and $\theta_{AA} = 13.17°$. According to the band structures, the localization is more pronounced in the AA case because of the lower overlap between orbitals belonging to nearest neighbors Nb atoms. The atomic orbitals that mostly contribute to the examined wavefunctions are the d_{z^2}, $d_{x^2-y^2}$ and d_{xy} orbitals of the Nb atoms.

4.3 Exploration of a novel van der Waals magnet: Nb_3I_8

In this final section, we present the systematic analysis of the structural, electronic, and magnetic properties of Nb_3I_8 in ML, BL, and TL forms, which will be referred to as Nb_3I_8-1L, Nb_3I_8-2L, and Nb_3I_8-3L, respectively [204, 205]. Nb_3I_8-1L has been predicted as a novel 2D ferromagnet by a recent DFT work [157], and experimental observations [15] have confirmed its semiconducting behavior. Nevertheless, experimental reports on its magnetism are not available yet. Therefore, we have performed a more accurate DFT study of this material in the ML and the above mentioned MuL forms, providing a precise and in-depth electronic characterization. Furthermore, we have focused on the Nb_3I_8-1L ferromagnetism by calculating its Curie temperature by means of MC simulations starting from a suitable model magnetic Hamiltonian [204]. We predict a ferromagnetism with a Curie temperature close to the room temperature, in addition to a good agreement with the experimental work functions measuread for Nb_3I_8 multilayered flakes [14] when the magnetism is properly taken into account. This allowed us to identify the best DFT setting to describe Nb_3I_8 in terms of the most recent vdW exchange-correlation functionals. The layer number

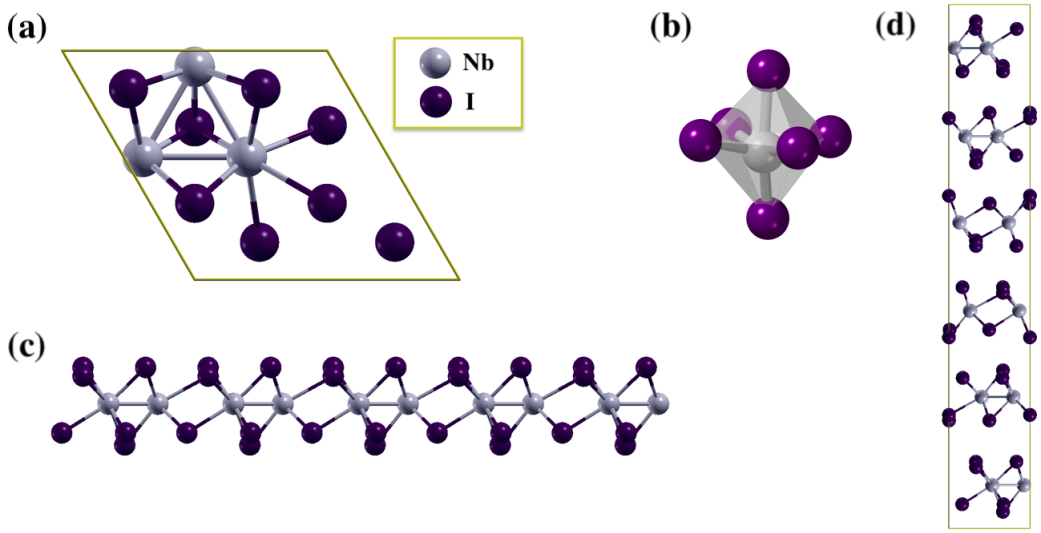

FIGURE 4.15: Nb_3I_8 structure. (a) Top view of the Nb_3I_8-1L unit cell. (b) Distorted octahedral environment of X atoms around each Nb atom. (c) Side view of a Nb_3I_8-1L sheet. (d) Side view of the bulk crystal unit cell (containing six MLs of Nb_3I_8).

directly influences the ground-state magnetism, i.e., a layer-dependent magnetism shows up, indicating the possibility of using the thickness as a parameter to control the magnetic response of the material. Then, inspired from the experimental observations on the layer-dependent ferromagnetism of CrI_3, we have improved the ground-state analysis of MuLs by considering new magnetic configurations and the role of the stacking. Furthermore, due to the remarkable effects of the strain engineering on different vdW systems [134, 373–375], we have examined how the strain could affect the electronic and magnetic properties of Nb_3I_8 [205]. The resulting interplay between film thickness, stacking geometry, and strain gave us a comprehensive view of this novel and promising vdW magnet.

4.3.1 Structure and DFT calculations details

Nb_3I_8 is a layered TMH belonging to the family of Nb_3X_8 (X = Cl, Br, I) crystals. The number of Nb_3X_8 layers per unit cell depends on the X atom, since Nb_3Cl_8 crystal structure has two layers and is termed α-Nb_3Cl_8 (space group $D^3_{3d} - P\bar{3}m1$, No. 164)[376], whereas Nb_3X_8 with X = Br, I crystal structure has six layers and is termed β-Nb_3X_8 (space group $D^5_{3d} - R\bar{3}m$, No. 166) [376]. In ML Nb_3X_8 (X = Cl, Br, I), the Nb atoms form triangular Nb_3 clusters and each Nb atom is under a distorted octahedral environment of X atoms, as shown in Figs. 4.15(a) and (b) for Nb_3I_8, respectively. In particular, the unit cell contains three Nb atoms and eight X atoms. Furthermore, the ML side view in Fig. 4.15(c) shows that a sheet of Nb atoms is sandwiched between two sheets of X atoms. The two sheets of X atoms, each having four atoms in the unit cell, are not equivalent, resulting in an essentially flat (top) and a corrugated (bottom) I sheet. Indeed, in a sheet three X atoms have almost the same z coordinate and the remaining one is between Nb sheet and three previous X atoms, whereas in the other sheet a X atom is outside of the other three X atoms sheet.

Bulk Nb_3I_8 was first synthesized by Magonov *et al.* in 1993 [160] and very recently cleaved to ML and MuL flakes [14, 15]. In the first case, single-crystal X-Ray Diffraction (XRD), Atomic Force Microscopy, and Scanning Tunneling Microscopy

System	Method	a (Å)	c (Å)	Ref.
Bulk	XRD	7.600	41.715	[160]
	Atomic Force Microscopy	7.73±0.31	-	[160]
	STM	7.76±0.43	-	[160]
ML	DFT-D	7.675	-	[157]

TABLE 4.4: Lattice parameters a and c for bulk Nb_3I_8 and Nb_3I_8-1L. Both experimental (XRD, Atomic Force Microscopy, and STM) and first-principles theoretical results are reported.

(STM) techniques was employed to explore the structure and measure the in-plane a and out-of-plane c lattice parameters, that are reported in Table 4.4. The stacking configuration assumed by the layered structure in the bulk Nb_3I_8, i.e., the bulk stacking, is shown in Fig. 4.15(d). Each layer is obtained by particular transformations of the first one. For example, the second layer results from the inversion operation of the first one with respect to a triangular Nb_3 cluster center (inversion center), whereas the third layer is shifted with respect to the first one of a certain quantity. Instead, first-principles calculations for the FM ML based on the vdW dispersion correction DFT-D [157] predict a lattice parameter $a = 7.675$ Å.

As anticipated in Sec. 2.1.8.b, in the first of the two works on ML and MuL Nb_3I_8, we have compared the performances of the vdW-DF2-C09 and rev-vdW-DF2 exchange-correlation functionals, demonstrating that the latter correctly describes the system properties, also according to the experimental observations. Therefore, also in this case, we have preferred nonlocal vdW functionals to the semiempirical ones. Furthermore, since larger cutoffs and **k**-point grids than the common ones are typically needed to ensure the DFT calculations convergence for magnetic systems, we have performed different and accurate convergence tests in a detailed discussion reported in the appendix of Ref. [204]. As result, we have considered a kinetic-energy cutoff of 50 Ry for the PWs, 300 Ry to represent the charge density, a $8\times8\times1$ MP **k**-point grid for the BZ sampling. Instead, in the next work on strain effects on ML and MuL Nb_3I_8, we have started with more accurate calculations by choosing a kinetic-energy cutoff of 60 Ry and a charge density cutoff of 480 Ry. Moreover, the calculations have been performed by employing PAW-PPs [377] and a vacuum space of $\simeq$ 20 Å. Based on the previous DFT report on Nb_3I_8-1L [157], the on-site Coulomb repulsion of Nb $4d$ electrons is taken into account by means of the DFT+U method described in Sec. 2.1.8.a. The lattice parameters have been optimized using spin-unpolarized (-polarized) calculations for NM (magnetic) states. Finally, the calculation of work function (W) and ionization potential (IP) has been carried out starting from the planar average of the electrostatic potential. Let $V_{system}(\mathbf{r})$ be the total electrostatic potential of a given system and S the area of its unit cell, assumed to be in the xy plane. The planar average of $V_{system}(\mathbf{r})$ on the unit cell area is

$$\langle V_{system}\rangle(z) = \frac{1}{S}\iint_S V_{system}(\mathbf{r})dx\,dy\,. \tag{4.10}$$

The constant value of the $\langle V_{system}\rangle(z)$ in the vacuum sufficiently far from the system is defined as the vacuum level energy E_{vac}. From E_{vac}, the work function of a metallic system is easily calculated as $W = E_{vac} - E_F$. Similarly, the ionization potential of a semiconducting system can be obtained as IP $= E_{vac} -$ VBM.

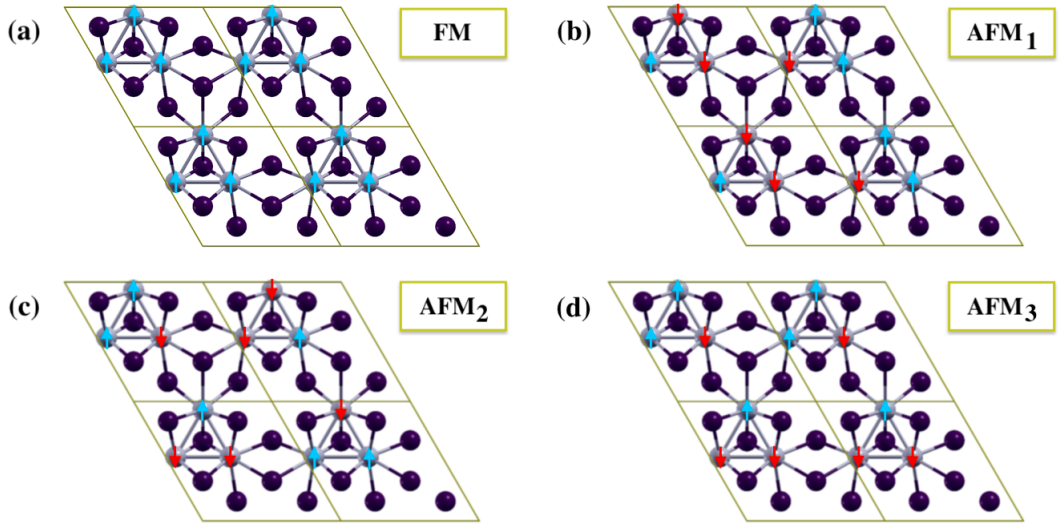

FIGURE 4.16: Schematic top views of FM (a), AFM_1 (b), AFM_2 (c), and AFM_3 (d) magnetic configurations for Nb_3I_8-1L. A 2×2 supercell has been adopted to build up the AFM states. Spin up (spin down) Nb sites are schematically depicted with upwards blue (downwards red) arrows.

4.3.2 Electronic and magnetic properties of the monolayer

Nb_3I_8-1L has been predicted as a FM semiconductor in the ground state by Jiang *et al.* [157], with an electronic band gap of 0.459 eV with the vdW dispersion correction DFT-D and 0.758 eV with the HSE06 hybrid functional. Moreover, the recent experimental work by Oh *et al.* [15] has confirmed its semiconducting behavior, measuring an electronic band gap value of $\sim$ 1 eV. These reasons have stimulated our interest in the search for a stable magnetic and semiconducting ground state with more accurate methods compared to Ref. [157], which could better match the experimental findings. To this aim, we have considered the NM state along with the FM and three different AFM states, referred to as AFM_1, AFM_2 and AFM_3, which are the magnetic states with the out-of-plane easy-axis (i.e., $\mathbf{M}_s \parallel \hat{\mathbf{z}}$) schematically drawn in Fig. 4.16.

First of all, the structural relaxation of the FM state gives a lattice parameter of 7.566 Å and 7.619 Å for the vdW-DF2-C09 and rev-vdW-DF2 exchange-correlation functionals, respectively. The lattice parameters of the other states under examination have proven to be essentially the same. The FM state has the lowest total energy for both the considered exchange-correlation functionals and the relative energies of the other states are reported in Table 4.5 per Nb_3I_8 formula unit (f.u.), in order to allow a straightforward comparison between 1×1 and 2×2 supercells. The ground state is separated from the NM state by an excitation energy of the order of $\sim$ 100 meV/f.u., that protects the magnetic ground state against thermal fluctuations even at high temperatures. Instead, the other magnetic states are at an energy of $\sim$ 10 meV/f.u. higher than the FM ground state. This is an interesting point because, despite the FM state is definitely stable over a wide range of temperatures, PTs between different magnetic states could easily occur under suitable conditions (e.g., applied magnetic fields). Moreover, DFT calculations predict a magnetic moment of 1 μ_B per unit cell. Most of the magnetic moment is carried by the Nb atoms with the same amount, as revealed by the Lowdin analysis for the per atom magnetizations, whereas the adjacent I atoms do not show any significant spin polarization

Magnetic state	ΔE (meV/f.u.)	
	vdW-DF2-C09	rev-vdW-DF2
NM	82.73	95.87
AFM_1	9.68	9.06
AFM_2	9.47	9.05
AFM_3	9.47	9.06

TABLE 4.5: Relative stability for different magnetic states of Nb_3I_8-1L for both vdW-DF2-C09 and rev-vdW-DF2 exchange-correlation functionals. ΔE is the energy difference per Nb_3I_8 formula unit with respect to the lowest-energy state, that in both cases corresponds to the FM state.

(as also reported in Ref. [157]). Therefore, Nb_3I_8-1L has a FM ground state with the magnetic moments of 1 μ_B delocalized on the Nb_3 clusters, resulting from the seven electrons shared by the Nb atoms, i.e., Nb_3I_8-1L is an intrinsic *2D cluster ferromagnet*. The ground-state analysis confirms the predictions by Jiang *et al.* obtained by using the DFT-D approach, also for the order of magnitude of the relative energies. It is worthwhile noticing that the larger cutoffs chosen for the second work on ML and MuL Nb_3I_8 provide slight differences in the ML lattice parameter related to the rev-vdW-DF2 functional, being 7.621 Å, and in the AFM_i relative energies, but the NM relative energy reaches a value of 174 meV. However, this value is not related to the Nb_3I_8-1L magnetism, being only a more accurate estimation due to better convergence parameters.

The band structure of the FM ground state is shown in Fig. 4.17(a). A semiconducting behavior is observed for both the spin-up and spin-down channels, in agreement with the less accurate theoretical predictions of Ref. [157] and the experimental results of Ref. [15]. In particular, the spin-up channel band gap $E_{g,\uparrow}$ is 0.542 eV for both functionals, whereas the spin-down channel band gap $E_{g,\downarrow}$ is 1.248 eV for vdW-DF2-C09 and 1.282 eV for rev-vdW-DF2. Therefore, the band structure is almost independent on the vdW exchange-correlation functional, as expected for the lack of vdW interlayer interactions. In order to complete the analysis of the electronic properties, we have computed the PDOS for the spin-up and spin-down channels, thus reporting the results in Figs. 4.17(b) and (c), respectively. Such a plot reveals that the highest valence bands and the lowest conduction bands are mostly dominated by hybridized Nb(d) and I(p) orbitals, with the larger contribution coming from the former. In particular, d_{z^2} orbitals of Nb atoms give the largest contributions, followed by all the orbitals involving the out-of-plane interactions, i.e., d_{zx}, d_{zy}, p_z, and the $d_{x^2-y^2}$ orbital.

It is worthwhile noticing that the choice of the magnetic states has been restricted to the cases with an out-of-plane easy-axis. As explained in Sec. 3.2, the easy-axis analysis requires the inclusion of the SOC in the first-principles calculations. We have performed further calculations comparing the band structures with and without the SOC along the BZ path of interest, i.e., Γ-K-M-Γ (as in Ref. [157]), demonstrating that the SOC provides a negligible contribution to the electronic properties of ML and MuL Nb_3I_8. Nevertheless, if the SOC were taken into account to perform the easy-axis analysis, then the resulting MAE would be $\simeq$ 0.5 meV, that is, Nb_3I_8-1L is an easy-plane magnet in the ground state. As observed by Peng *et al.* in Ref. [378], such a small value of MAE allows to easily manipulate the Nb magnetic moments by a magnetic field and use Nb_3I_8-1L as an out-of-plane easy-axis ferromagnet in the ground state. Furthermore, such a work confirms the negligible SOC contribution

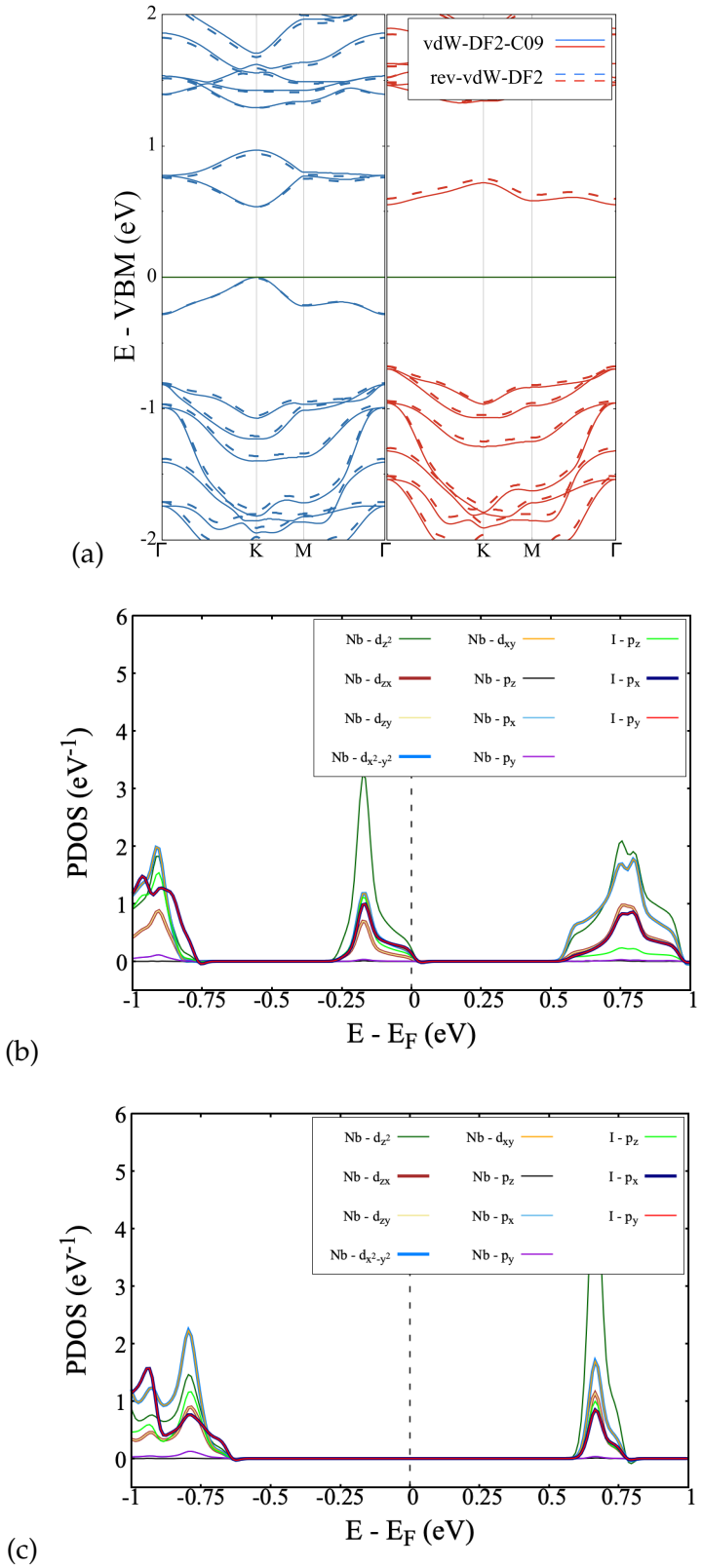

FIGURE 4.17: Electronic properties of Nb_3I_8-1L as a function of the vdW exchange-correlation functional. (a) Band structure for the spin-up channel (blue bands) and the spin-down channel (red bands). Zero energy is highlighted with a dark green line and corresponds to the VBM of the semiconducting system. PDOS for the spin-up channel (b) and spin-down channel (c) are shown. The *s*-orbital contributions for both Nb and I have not been reported because negligible if compared with the other contributions.

along the BZ path indicated above, instead pointing out an intrinsic valley polarization of 107 meV between K and K'. In other words, the anomalous valley Hall (AVH) effect shows up without external tunings. The simultaneous presence of ferromagnetism and valley polarization makes Nb_3I_8-1L as a *ferrovalley* material, that is an ideal candidate for spintronics and valleytronics applications.

4.3.3 Simulation of the monolayer model magnetic Hamiltonian

The FM ordering of the Nb_3I_8-1L ground state guarantees the existence of a second-order PT at a Curie temperature T_C, separating the FM regime ($T < T_C$) from the NM regime ($T > T_C$). As explained in Sec. 3.3, the spin dynamics simulation ranging from $T = 0$ K to temperatures larger than T_C allows to follows the temperature-dependent alignment of the Nb atom magnetic moments and compute the main thermodynamic functions characterizing the magnetic PT, such as the spontaneous magnetization and the magnetic susceptibility, for each temperature. In practice, this is done by applying MC methods, as the Metropolis algorithm in our case, to the suitable model magnetic Hamiltonian to describe the system. We have considered the 2D Ising model to simulate the spin dynamics of Nb_3I_8-1L, by including up to the third-nearest-neighbor magnetic exchange couplings. The nearest-, next-nearest- and third-nearest neighbors of a Nb atom are shown in Fig. 4.18. From the latter, we can easily calculate the coordination numbers $q^{(1)} = q^{(2)} = 2$ and $q^{(3)} = 4$ of each Nb atom up to the third-nearest neighbors. The model Hamiltonian is

$$H_{Nb_3I_8-1L} = -J^{(1)} \sum_{\langle \alpha,\beta \rangle_1} s_\alpha s_\beta - J^{(2)} \sum_{\langle \alpha,\beta \rangle_2} s_\alpha s_\beta - J^{(3)} \sum_{\langle \alpha,\beta \rangle_3} s_\alpha s_\beta, \tag{4.11}$$

where $\langle \alpha, \beta \rangle_n$ denotes the pair of nth nearest neighbors α and β Nb ions included only once in the sum, $J^{(n)}$ is the related magnetic exchange coupling measured in meV and chosen as independent on the magnetic-ion pair, and s_α is the z component of the αth Nb ion dimensionless spin. Since the QE package computes the magnetic moment of the unit cell, that is equal to the Nb_3 cluster magnetic moment, and sets the electron spin g-factor g_s to 2, then s_α can be obtained through the relation $\mu_\alpha = g_s \mu_B s_\alpha$ by setting $\mu_\alpha = 1\mu_B/3$ from the results of the Lowdin analysis. Therefore, it turns out that $s_\alpha = 1/6$, we can drop the subscript α and use the symbol s in the following, and the Nb_3 cluster carries a total spin $1/2$. The Hamiltonian of Eq. (4.11) has $\mathcal{N} = 3$ parameters to compute through the energy-mapping analysis. Therefore, based upon the Sec. 3.3, $\mathcal{N} + 1$ different magnetic configurations are needed for this purpose. By employing $H_{Nb_3I_8-1L}$ on the FM and AFM_i states of Fig. 4.16 in the 2×2 supercell, their total energies satisfy the equations

$$E_{FM} = E_0 - (12J^{(1)} + 5J^{(2)} + 10J^{(3)})s^2, \tag{4.12a}$$

$$E_{AFM_1} = E_0 - (-4J^{(1)} + 5J^{(2)} - 4J^{(3)})s^2, \tag{4.12b}$$

$$E_{AFM_2} = E_0 - (-4J^{(1)} - 3J^{(2)} + 6J^{(3)})s^2, \tag{4.12c}$$

$$E_{AFM_3} = E_0 - (-4J^{(1)} - J^{(2)})s^2, \tag{4.12d}$$

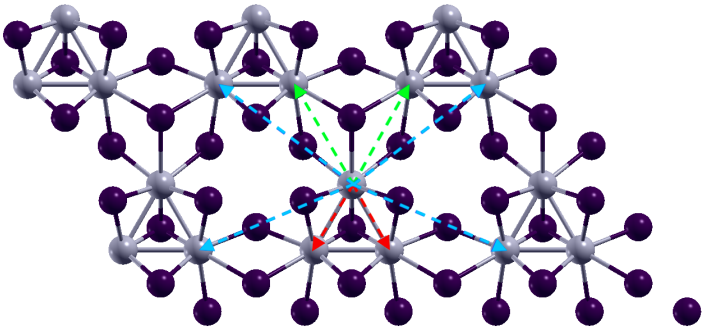

FIGURE 4.18: 3×2 supercell top view of Nb_3I_8 to identify nearest- (red arrows), next-nearest- (green arrows), and third-nearest neighbors (cyan arrows). The coordination numbers are $q^{(1)} = q^{(2)} = 2$ and $q^{(3)} = 4$, respectively.

Magnetic exchange coupling	vdW-DF2-C09	rev-vdW-DF2
$J^{(1)}$ (meV)	89.08	81.48
$J^{(2)}$ (meV)	-6.48	-0.06
$J^{(3)}$ (meV)	-2.19	0.15

TABLE 4.6: Magnetic exchange couplings of the third-nearest-neighbor Ising model described in Eq. (4.11), extrapolated from the energy-mapping analysis for the considered vdW exchange-correlation functionals.

where E_0 is an undefined reference energy. The energy differences with respect to the FM state energy provide the linear equations system

$$\Delta_{AFM_1} = (16J^{(1)} + 14J^{(3)})s^2, \tag{4.13a}$$

$$\Delta_{AFM_2} = (16J^{(1)} + 8J^{(2)} + 4J^{(3)})s^2, \tag{4.13b}$$

$$\Delta_{AFM_3} = (16J^{(1)} + 6J^{(2)} + 10J^{(3)})s^2, \tag{4.13c}$$

where $\Delta_{AFM_i} = E_{AFM_i} - E_{FM}$. The resulting magnetic exchange couplings $J^{(1)}$, $J^{(2)}$, and $J^{(3)}$ are reported in Table 4.6. The sign of $J^{(1)}$ and its magnitude with respect to $J^{(2)}$ and $J^{(3)}$ confirm the FM ordering of the ground state.

The calculated magnetic exchange couplings can be used as input of the Metropolis algorithm to determine the temperature dependence of the main thermodynamic functions characterizing the magnetic PT of Nb_3I_8-1L. Following Sec. 3.3, we have considered $N_{trans} = 10^4$ and $N_{MC} = 10^5$. The results are quite independent on the vdW exchange-correlation functional. As an example, in Fig. 4.19, the average single-ion spontaneous magnetic moment $\langle \mu(T) \rangle$, as defined in Eq. (3.23), and the magnetic susceptibility $\chi(T)$ are shown for the rev-vdW-DF2 functional. Both the functionals show the sought magnetic PT at $T_{C,MC} = 307.5$ K. This result, which predicts a FM state at the room temperature, certainly improves previous literature results from the mean-field theory (MFT) [157], since we have accurately taken into account both the lattice type and the number of neighbors of each Nb atom. It must be pointed out that, as shown in the appendix of our work [204], $J^{(2)}$ and $J^{(3)}$ couplings have a remarkable effect on the Curie temperature, in that including the second and third nearest neighbor interaction produces an approximately 50 K decrease of $T_{C,MC}$ with respect to the first-neighbor approximation, regardless of the vdW functional. Finally, the ab initio computational error in the calculation of $T_{C,MC}$ by increasing the charge-density cutoff up to 100 Ry and by doubling the **k**-point

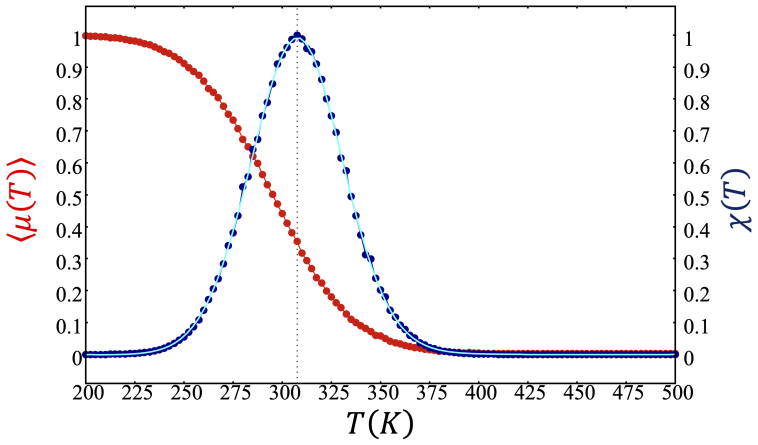

FIGURE 4.19: Average single-ion spontaneous magnetic moment $\langle \mu(T) \rangle$ and magnetic susceptibility $\chi(T)$ (normalized to 1) for Nb_3I_8-1L as results of Monte Carlo simulations. Data refer to the rev-vdW-DF2 functional, as an example. The vertical line highlights the Curie temperature, whereas the cyan line is a magnetic susceptibility fit and a guide for eyes.

(a) Nb_3I_8-2L

Magnetic state	ΔE (meV/f.u.)	
	vdW-DF2-C09	rev-vdW-DF2
NM	42.70	71.98
FM	40.89	33.69
AFM_1	39.69	54.20
AFM_2	0.45	0.96

(b) Nb_3I_8-3L

Magnetic state	ΔE (meV/f.u.)	
	vdW-DF2-C09	rev-vdW-DF2
NM	111.88	152.24
FM	31.14	29.31
AFM_2	0.27	0.26
AFM_3	0.28	5.30

TABLE 4.7: Relative stability for different magnetic states of Nb_3I_8-2L (a) and -3L (b) for both vdW-DF2-C09 and rev-vdW-DF2 exchange-correlation functionals. ΔE is the energy difference per Nb_3I_8 formula unit with respect to the lowest-energy state, that is the AFM_3 ordering for Nb_3I_8-2L and the AFM_1 ordering for Nb_3I_8-3L.

grid is at most ~ 20 K.

We have also estimated the Curie temperature within the MFT. By taking into account only up to the first-order spin fluctuations and imposing the condition of zero spontaneous magnetization in absence of an external magnetic field, the MFT Curie temperature related to the Hamiltonian of Eq. (4.11) for a system in thermal equilibrium with a heat bath at temperature T is

$$T_{C,MFT} = \frac{S(S+1)}{3k_B} \sum_{n=1}^{3} J^{(n)} q^{(n)}, \tag{4.14}$$

where S is the total spin of the unit cell. Since we have $S = 1/2$, the estimations are $\simeq 453$ K for vdW-DF2-C09 and $\simeq 470$ K for rev-vdW-DF2, changing to $\simeq 479$ K and $\simeq 472$ K, respectively, by neglecting the third-nearest neighbor couplings. Therefore, the MFT results are very different from the previous literature value 87 K by Jiang *et al.* [157], also by neglecting $J^{(3)}$ to consider the same accuracy of the latter, and, as expected, overestimate the Curie temperature. However, the scantiness of MFT with

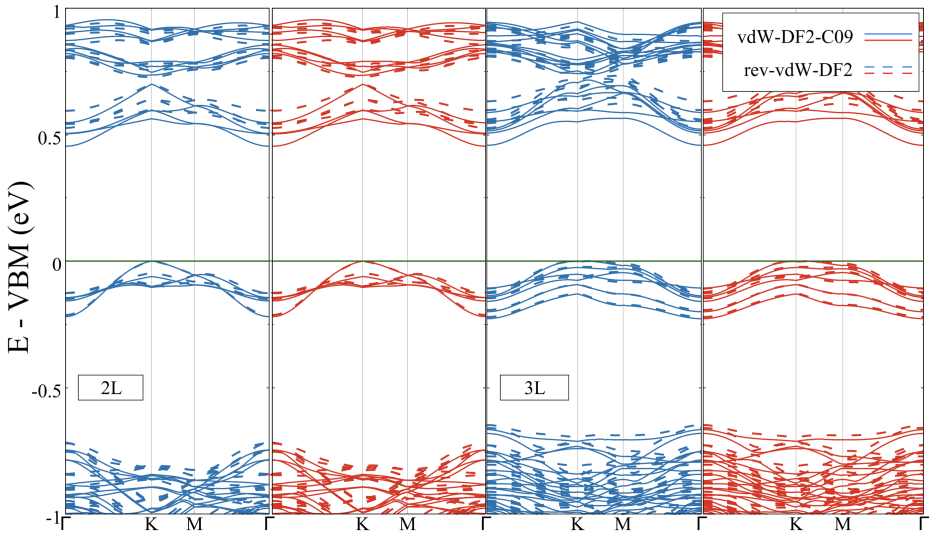

FIGURE 4.20: Band structure for the spin-up channel (blue bands) and the spin-down channel (red bands) of Nb_3I_8-2L in the AFM_3 state (left panel) and Nb_3I_8-3L in the AFM_1 state (right panel). Zero energy is highlighted with a dark green line and corresponds to the VBM of the semiconducting system.

respect to the MC simulation appears evident.

4.3.4 Layer-dependent magnetism of Nb_3I_8

In both works on ML and MuL Nb_3I_8, we have extended the ground-state analysis performed on Nb_3I_8-1L also to Nb_3I_8-2L and -3L. In the first work [204], we have compared the total energies of NM, FM, and the AFM_i states of the MuLs obtained from the AFM configurations of Nb_3I_8-1L shown in Fig. 4.16 by considering the symmetry constraints relating the atoms of different layers in the bulk stacking described in Sec. 4.3.1. Therefore, for instance, the second layer magnetic configuration is obtained by inversion operation of the first one with respect to a triangular Nb_3 cluster center. Table 4.7 reports the results on the ground-state analysis for both the vdW functionals. The ab initio calculations reveal that the considered MuLs have an AFM ground state, with the AFM_3 ordering for Nb_3I_8-2L and the AFM_1 ordering for Nb_3I_8-3L. This result is of utmost importance: Nb_3I_8 shows a layer-dependent magnetism, being FM in ML form and switching on the antiferromagnetism by adding one or two layers. The layer-dependent magnetism demonstrates how the number of layers is a very decisive DOF also for vdWHos, in that also different compounds of the TMH class, such as Nb_3I_8 and CrI_3, may show a significant dependence of their properties on the stacking of the single layers. Moreover, although the energy difference between different AFM states in Table 4.7 is also small in some cases, NM and FM are well separated from them and the results slightly depend on the vdW exchange-correlation functional. As far as the structural properties are concerned, the lattice parameters are 7.569 Å (7.619 Å) for Nb_3I_8-2L and 7.573 Å (7.623 Å) for Nb_3I_8-3L when the vdW-DF2-C09 (rev-vdW-DF2) functional is considered. Therefore, vdW-DF2-C09 tends to predict shorter interatomic distances with respect to rev-vdW-DF2 and the experimental values measured for bulk and reported in Table 4.4. The Nb_3I_8-2L and Nb_3I_8-3L band structures shown in Fig. 4.20 in the AFM_3 and AFM_1 states, respectively, show semiconducting behaviors, obviously independent on the spin channel. The band gaps are indirect (K-Γ), having values of 0.453 eV

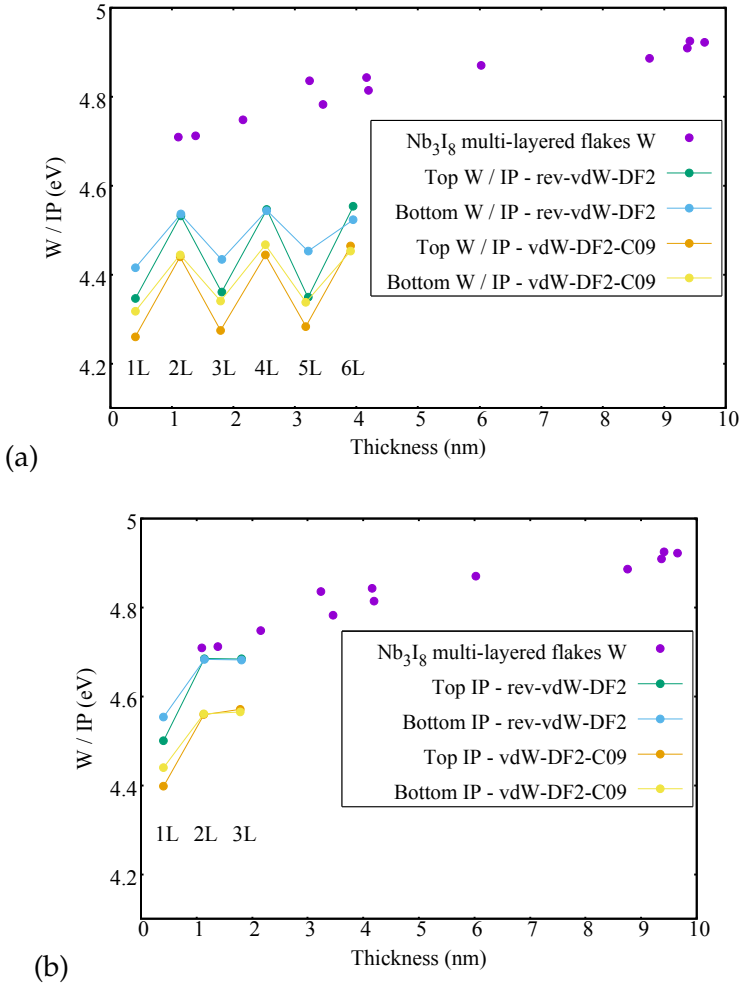

FIGURE 4.21: Comparison between experimental measurements of the work function (W) in Nb_3I_8 multilayered flakes and our theoretical estimations of the work function, W (ionization potential, IP) of NM MLs of Nb_3I_8 with odd (even) number of layers. The results obtained for both the NM (a) and the lowest-energy magnetic (b) ground state are shown.

(0.526 eV) for Nb_3I_8-2L and 0.458 eV (0.526 eV) for Nb_3I_8-3L, when the vdW-DF2-C09 (rev-vdW-DF2) functional is considered.

Although the experiments on Nb_3I_8 performed so far have not focused on the magnetic properties, the magnetism of ML and MuL Nb_3I_8 ground states predicted by first principles turns out to be in agreement with the available experimental observations. Indeed, if the first-principles calculations of Nb_3I_8-1L were not spin polarized, then the band structure would describe a metallic system against the recent measurements of band gaps by Oh *et al.* [15], as shown in our first work [204]. As a further demonstration that the inclusion of magnetism is needed to correctly describe MLs and MuLs of Nb_3I_8, we have calculated work functions and ionization potentials for both spin-unpolarized and spin-polarized calculations to compare them to the experimental data on Nb_3I_8 multilayered flakes by Kim *et al.* [14]. The results are shown in Fig. 4.21, as a function of the vdW functional and with additional MuLs for the NM states, by calculating these quantities for both the top and the bottom sides of the selected systems. In Fig. 4.21(a), theoretical data on NM MuLs show odd-even oscillations due to the semiconducting (metallic) behaviour of the systems composed by an even (odd) number of layers, as shown in detail in

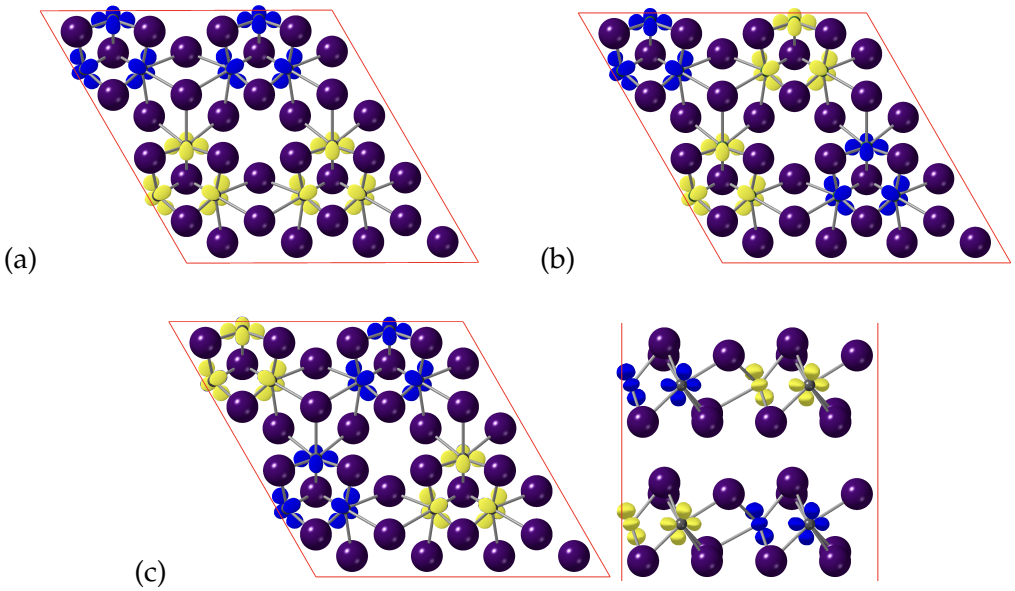

FIGURE 4.22: AFM_{xy} states considered for Nb_3I_8-2L. 2×2 supercells contain the spin densities around the magnetic Nb atoms for each AFM_{xy} state, where yellow (blue) isosurfaces correspond to positive (negative) spin densities. We can easily distinguish: (a) alternating rows with opposite spins in the stripy-2L state; (b) alternating clusters with opposite spins along both $\mathbf{a}_1$ and $\mathbf{a}_2$ directions in the Néel-2L state; (c) same pattern as in the Néel-2L state for the reverted-Néel-2L state, but the spins are reverted in the bottom plane. In (c), both the top (left) and side (right) views are shown because top and bottom planes have not the same magnetic ordering as (a) and (b).

our work [204]. Top and bottom work functions differ by $\sim$ 60-70 meV regardless of the vdW functional, whereas the top and bottom ionization potentials are almost identical. When the spin polarization is taken into account in the first-principles calculations, the discrepancy between our results and experimental data is evidently reduced, producing a much better agreement. Indeed, as far as Nb_3I_8-2L and -3L are concerned, the difference with the experimental data reduces from about 100 meV (200 meV) to about 30 meV (60 meV) for the rev-vdW-DF2 (vdW-DF2-C09) exchange-correlation functional. This analysis also provides a good benchmark to identify the most suitable vdW functional to use in order to properly reproduce the Nb_3I_8 properties among vdW-DF2-C09 and rev-vdW-DF2. Indeed, the latter definitely gives the best agreement with the experimental data. For this reason, we have selected the rev-vdW-DF2 exchange-correlation functional for the next work on Nb_3I_8.

The observation of BL CrI_3 as antiferromagnet with FM layers having opposite spins [13] has stimulated us to perform a new ground-state analysis of Nb_3I_8-2L and Nb_3I_8-3L in Ref. [205] by adding such "layered AFM" states to the previous ones. First of all, regardless of the magnetic configurations, we have extended the previous analysis by also taking into account the effect of the stacking geometry on the electronic and magnetic properties of ML and MuL Nb_3I_8. Indeed, we have compared the bulk stacking, that is the natural order of the layers as they would be arranged in the bulk form, to the A^n stacking, that is constructed by piling n layers with the same planar coordinates. As far as the magnetic configurations are concerned, since Nb_3I_8-1L has a FM magnetic coupling, we have assumed that its minimum-energy magnetic configurations consist at least of Nb_3 clusters having parallel spins rather

Magnetic state	ΔE (meV/f.u.)	
	A^2 stacking	bulk stacking
NM	292.1	103.0
$\uparrow\uparrow$	5.6	76.7
AFM$_{xy}$-Néel-2L	21.2	96.2
AFM$_{xy}$-reverted-Néel-2L	15.6	13.7
AFM$_{xy}$-stripy-2L	21.2	96.2

TABLE 4.8: Relative stability for different magnetic states of Nb_3I_8-2L for both bulk and A^2 stacking.

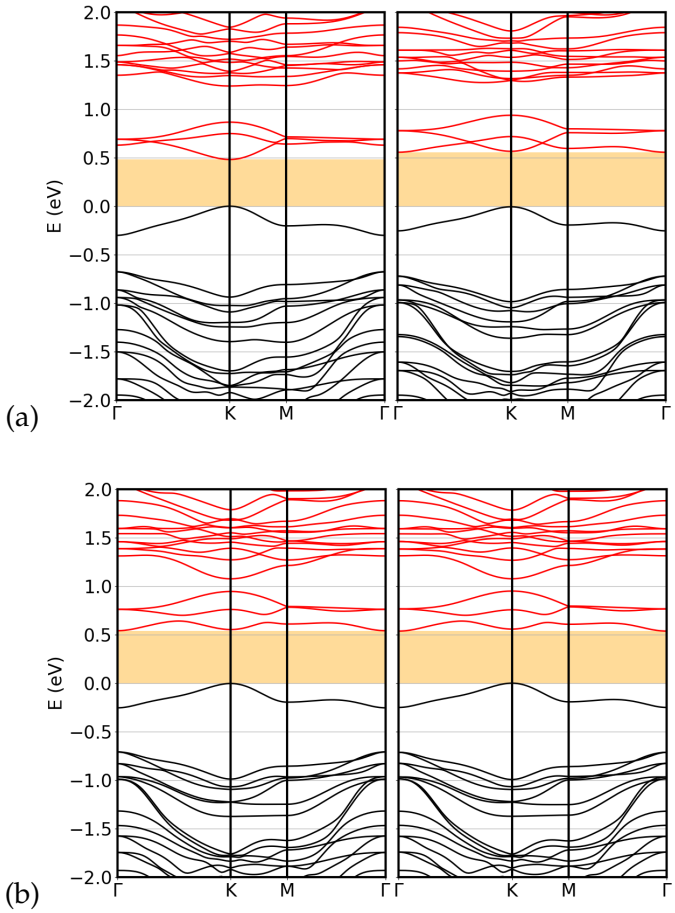

FIGURE 4.23: Spin-up (left panels) and spin-down (right panels) band structure along the Γ-*K*-*M*-Γ path of Nb_3I_8-2L in the AFM$_z$ state for (a) A^2 and (b) bulk stacking. Zero energy corresponds to the VBM and each shaded orange region highlights the spin-channel band gap.

than the complicated configurations schematized in Fig. 4.16. Therefore, we expected to find magnetic states at lower energies than the latter ones.

Let us start our analysis from Nb_3I_8-2L. Based on the above assumption, in addition to the NM and FM states, we have considered the AFM$_z$ state, that is the layered AFM state found for BL CrI_3, and different AFM$_{xy}$ states, which consist of a 2×2 supercell having two out of the four Nb_3 clusters in each plane carrying a spin up and the other two carrying a spin down, with a resulting zero net magnetization for each

plane[1]. In particular, the spin patterns chosen for the latter have been referred to as "stripy-2L", "Néel-2L", and "reverted-Néel-2L" states, and are shown in Fig. 4.22 through their spin densities, each one obtained as difference between spin-up and spin-down electron charge density. The stripy-2L state shows the spin distributed, in each plane, according to alternating rows parallel to a unit cell side, and the same pattern is identically repeated on the two layers. In the Néel-2L state, the in-plane pattern is such that the Nb_3 clusters along a supercell diagonal carry the same spin, the two diagonals correspond to opposite spins, and the same pattern is identically repeated on the two layers. Finally, the reverted-Néel-2L state is obtained by reverting the spins of the Néel-2L state in the second layer, such that to a spin-up cluster in the top layer corresponds a spin-down cluster in the bottom layer and similarly for spin down. FM and AFM_z will also be referred to as $\uparrow\uparrow$ and $\uparrow\downarrow$ in the following, respectively, to better highlight the relative spin orientation between the two layers.

The ground-state analysis is reported in Table 4.8. It turns out that the AFM_z state is the lowest-energy spin pattern for both the A^2 and bulk stackings, exactly as for BL CrI_3. This improves the results of our previous work [204], revealing that faced layers prefer opposite spins distributed with a FM ordering on each layer. The optimized lattice parameters are 7.620 Å and 7.624 Å for bulk and A^2 stacking, respectively. The FM state energy is $\sim$77 meV/f.u. and $\sim$6 meV/f.u. higher than the ground AFM_z state in the bulk and the A^2 stacking, respectively. The same calculated energies of the NM state are much larger, $\sim$103 and $\sim$292 meV/f.u., respectively. As far as AFM_{xy} states are concerned, for A^2 stacking they are separated from the AFM_z state by 10-20 meV, and for bulk stacking they all lay at quite high energies (comparable with that of the NM state), but AFM_{xy}-reverted-Néel-2L is situated about 10 meV above the AFM_z state. All these results reveal a fundamental role played by the deposition steps in the experimental fabrication of real samples, since the A^2 stacking tends to stabilize magnetism versus NM solutions compared to the bulk stacking, and the opposite concerns the stability of AFM_z versus other magnetic patterns. As such, the magnetic phase diagram and its dependence on the temperature can be modified by effect of the stacking geometry.

The effect of the stacking geometry also emerges from the analysis of the band structure. In Fig. 4.23, the band structure for both A^2 and bulk stacking is shown for the lowest-energy AFM_z state. It can be clearly inferred that for bulk stacking spin-up and spin-down channels provide almost identical band structures (see Fig. 4.23(b)), with a very tiny difference between the corresponding gaps, that are $E_{g,\uparrow} = 0.544$ eV and $E_{g,\uparrow} = 0.537$ eV. This can be ascribed to the inversion symmetry operation of the bulk stacking described in Sec. 4.3.1. On the other hand, for A^2 stacking, although the overall band structures look similar, the breaking of the inversion symmetry results in a **k**-point dependent spin splitting, yielding the band gaps $E_{g,\uparrow} = 0.481$ eV and $E_{g,\downarrow} = 0.562$ eV (see Fig. 4.23(a)).

The results obtained for Nb_3I_8-2L on the magnetic ground state along with the FM ground state of Nb_3I_8-1L suggest to exclude the AFM_{xy} states from the ground-state analysis of Nb_3I_8-3L, which, however, are computationally expensive. Therefore, for Nb_3I_8-3L we have considered the FM state ($\uparrow\uparrow\uparrow$) and the remaining possible AFM_z states, that are $\uparrow\downarrow\uparrow$, where neighbor layers carry opposite spin and obtained from FM by flipping the central layer spins, and $\uparrow\uparrow\downarrow$, obtained from FM by flipping the spin of one of the outermost layers. The optimized lattice parameters are 7.627 Å for the bulk stacking and 7.622 for the A^3 stacking. Again, the ground state is an

[1]The subscripts xy and z of the AFM configurations indicate that the net magnetization is zero in a single layer and in couples of faced layers with antiparallel spins, respectively.

Magnetic state	ΔE (meV/f.u.)	
	A^3 stacking	bulk stacking
NM	422.7	276.7
↑↑↑	11.9	79.5
↑↑↓	5.9	78.0

TABLE 4.9: Relative stability for different magnetic states of Nb_3I_8-3L for both bulk and A^3 stacking.

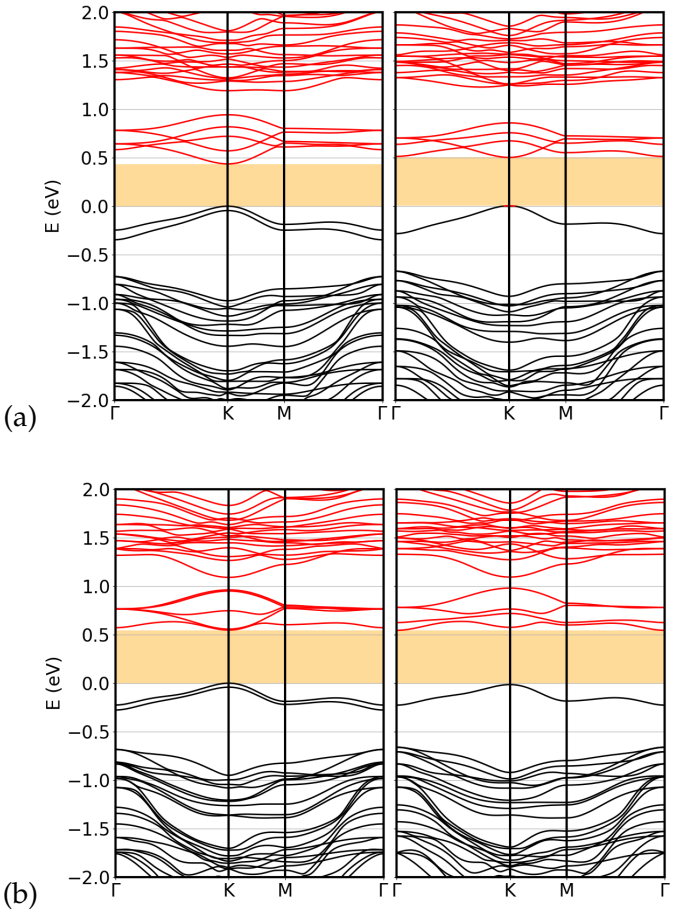

FIGURE 4.24: Spin-up (left panels) and spin-down (right panels) band structure along the Γ-*K*-*M*-Γ path of Nb_3I_8-3L in the ↑↓↑ state for (a) A^3 and (b) bulk stacking. Zero energy corresponds to the VBM and each shaded orange region highlights the spin-channel band gap.

AFM_z-like state, in particular being ↑↓↑, as shown in Table 4.9. In other words, the energetically favored mechanism bringing to faced opposite spin patterns at one side of the central layer also works on the other side. Also in this case, the stacking geometry reveals its central role, in that for bulk stacking several tens of meV separate ↑↑↑ and ↑↑↓ from the ground state. On the other hand, they lay only $\simeq$12 and $\simeq$6 meV from the ground state. As far as the ground-state spin-polarized band structure is concerned, we do not expect any degeneracy for both stacking geometries, since no inversion symmetry operation can be identified. Indeed, the bulk stacking shows a semiconducting band structure for both spin channels with $E_{g,\uparrow} = 0.547$ eV and $E_{g,\downarrow} = 0.559$ eV (see Fig. 4.24(a)), whereas the A^3 stacking provides $E_{g,\uparrow} = 0.436$ eV and $E_{g,\downarrow} = 0.498$ eV (see Fig. 4.24(b)).

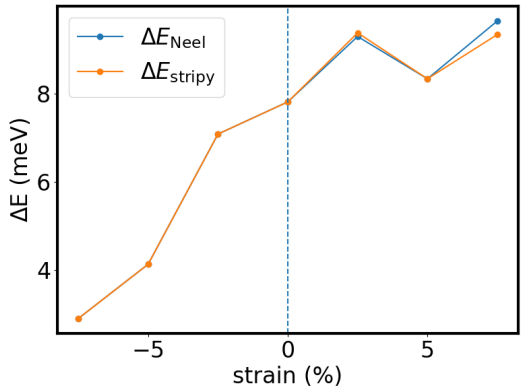

FIGURE 4.25: Relative stability of different magnetic states in Nb_3I_8-1L as a function of the strain. $\Delta E = E - E_{FM}$ is the energy difference between the energy of a given configuration and that of the FM state. Here, "Néel-1L" and "stripy-1L" configurations are considered.

4.3.5 Effects of strain on electronic and magnetic properties on multilayer Nb_3I_8

Once the ground states have been determined for Nb_3I_8-1L, -2L, and -3L, we have examined how strain engineering could tune their electronic and magnetic properties. In particular, we have considered an in-plane and biaxial strain $\epsilon = (a_{str} - a)/a$, where a is the unstrained lattice parameter and a_{str} is the strained lattice parameter, ranging from -7.5% to 7.5% in steps of 2.5%. Since the magnetism arises from the distances separating the magnetic atoms belonging to the lattice, we expected a crucial role of the strain in the magnetic properties, moving the system state within the magnetic phase diagram in an absolutely unpredictable way.

Let us start our analysis from Nb_3I_8-1L. We have monitored the energy differences between the FM, NM, and AFM_{xy} states on only one layer taken from the AFM_{xy} states of Nb_3I_8-2L in Fig. 4.22. In particular, the latter are AFM_{xy}-stripy-1L and AFM_{xy}-Néel-1L magnetic orderings. The FM state is the lowest-energy state regardless of the strain value, and the larger the compressive strain, the closer the different magnetic states. This is shown in Fig. 4.25, where the difference between the total energy of the AFM states and the FM state is reported as a function of the applied strain (NM state is excluded due to the too large energy difference). It is possible to distinguish a common behavior to each magnetic state: energy differences increase (decrease) with an increasing tensile (compressive) strain. This is a direct evidence of the strain engineering as a control knob to stabilize the magnetic phase during the deposition steps, since a sufficiently high tensile (compressive) strain enhances (reduces) the energy difference between NM and FM states.

The effect of strain is clearly visible also in the band structure, as shown in Figs. 4.26(a) and (b) for the band structures of Nb_3I_8-1L with $\epsilon = -7.5\%$ and ϵ =7.5%, respectively. As expected, in the strong tensile strain regime, the electronic bands exhibit a flattening deriving from the increasing of the in-plane interatomic distances. Instead, an unexpected effect of the strain on the band structure concerns the band gap variation: by tuning the strain from compressive to tensile, a decrease (increase) of the spin-up (spin-down) channel band gap is observed, as shown in Fig. 4.26(c). Such an opposite behavior for spin-up and spin-down channel may be ascribed to the number and nature of electronic bands in proximity of the energy gap region. As it will be further clarified in a while from the projection of the energy bands onto

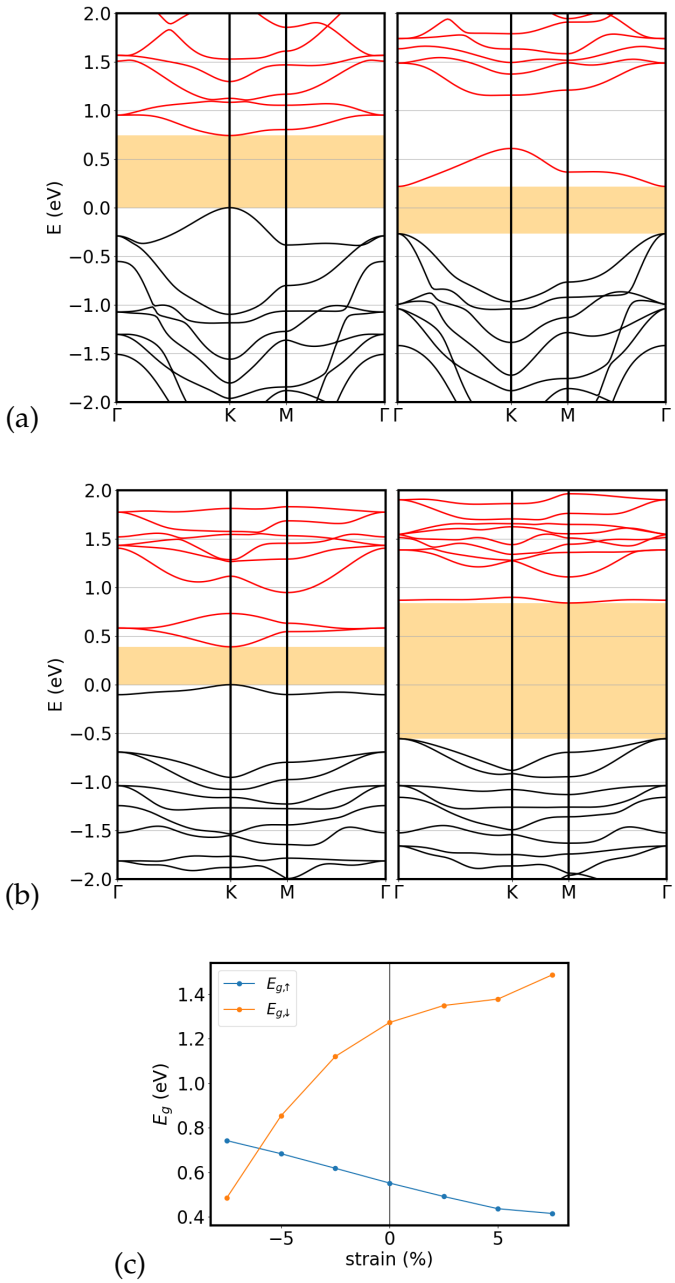

FIGURE 4.26: Electronic properties of strained Nb_3I_8-1L. Spin-up (left panels) and spin-down (right panels) band structure along the Γ-*K*-*M*-Γ path of Nb_3I_8-1L in the FM state under a (a) −7.5% and (b) 7.5% strain. Zero energy corresponds to the VBM and each shaded orange region highlights the spin-channel band gap. (c) Spin-up ($E_{g,\uparrow}$) and spin-down ($E_{g,\downarrow}$) energy gap of Nb_3I_8-1L in the FM state as a function of the strain.

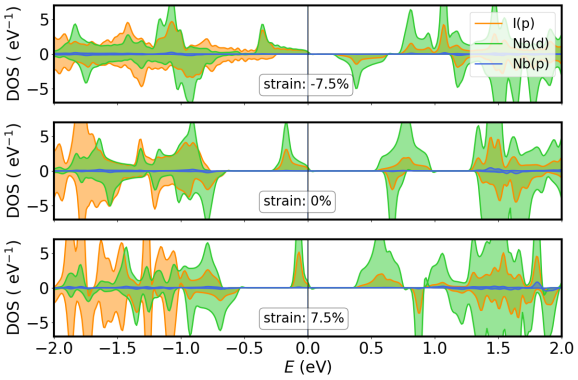

FIGURE 4.27: PDOS of Nb_3I_8-1L in the FM state Nb(d), Nb(p), and I(p) orbitals. The largest considered compressive (-7.5%) and tensile (7.5%) strains, together with the unstrained system are considered. Zero energy corresponds, for each system, to the VBM. Positive (negative) values of the PDOS correspond to spin-up (spin-down) bands.

atomic orbitals, the relative weight of Nb and I orbitals to those bands is differently influenced by the strain for the two spins, with a direct effect onto the energy gaps. We could expect that this intriguing peculiarity might be unveiled from absorption experiments, as an example.

An in-depth analysis also shows that upon increasing strain a decreasing of the ML thickness is observed, ranging from $\sim$ 4.57 Å for a -7.5% strain to $\sim$ 3.67 Å for a 7.5% strain, to be compared with 4.08 Å of the unstrained BL (that is indeed intermediate between the other two). In other words, tensile (compressive) strain tends to weaken (enhance) the interatomic interaction along the z direction.

In Fig. 4.27, we compare the PDOS plots at the strain values -7.5%, 0%, and 7.5%. As already observed in Figs. 4.17(b) and (c), the highest valence bands are mostly dominated by hybridized Nb(d) and I(p) orbitals, with the larger contribution coming from the former. Here, we notice that this feature is almost independent on the strain. However, by analyzing an energy window of $\sim$0.4 eV below the highest valence band, we have noticed that, on going from the largest compressive strain to the unstrained system to the largest tensile strain, the I(p) contribution to the total PDOS changes from 45% to 32% to 30%, respectively. Therefore, as a direct consequence on the electronic properties, the compressive strain significantly enhances the hybridization between Nb and I orbitals, whereas the opposite effect is observed in the case of tensile strain.

Moving to the MuL systems, it turns out that the strain does not alter the ground-state magnetic ordering. This can be observed in Figs. 4.28(a) and (b), where the energy differences of different magnetic orderings relative to the lowest-energy state of Nb_3I_8-2L and -3L, respectively, are reported, as a function of the applied strain and for both bulk and A^n stackings. There is only one case in which the strain affects the ground state: at -7.5% strain and below, Nb_3I_8-2L in the bulk stacking exhibits a PT to the NM state, since Nb magnetic moments monotonically vanish, as illustrated in Fig. 4.28(c). This does not hold for the A^2 stacking, providing further proof of the deposition steps importance for the expected magnetic state of the system.

Finally, as shown in the Figs. S2 and S3 of the Supplemental Material (SM) of our work [205], strain significantly affects the band structures of Nb_3I_8-2L and -3L, giving rise to non-trivial changes of spin-up and spin-down band gaps. Of course, the band flattening shows up also for this MuL systems, even though with a smaller amplitude if compared to the ML.

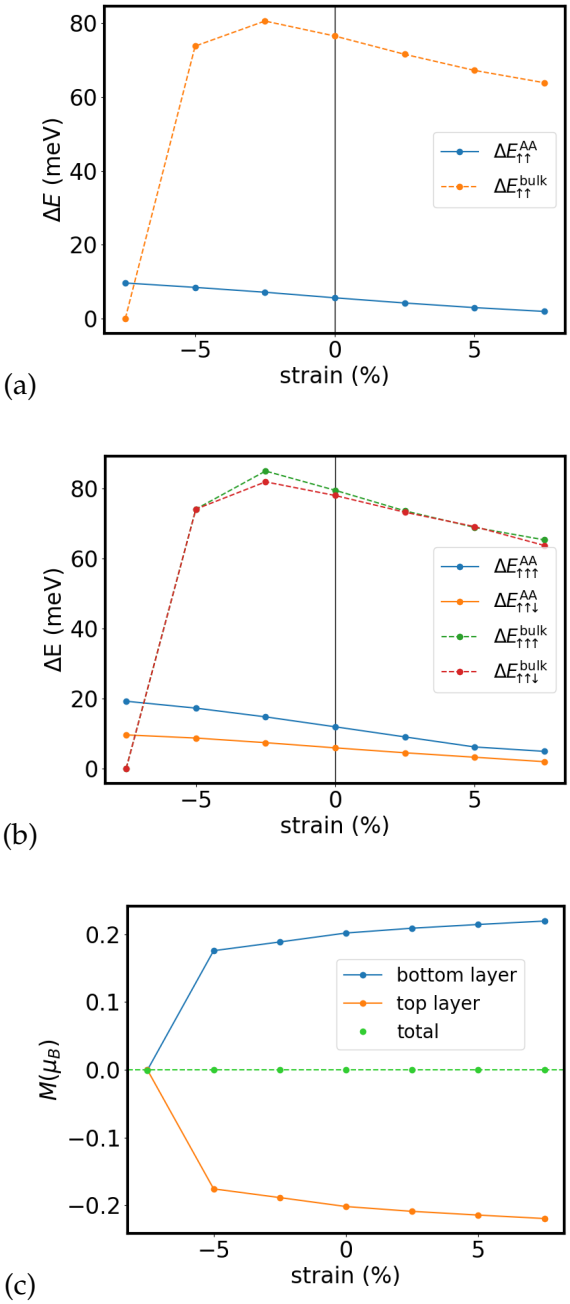

FIGURE 4.28: Strain effects on Nb_3I_8-2L and -3L ground states. Relative stability of the ↑↑ magnetic ordering in Nb_3I_8-2L (a) and -3L (b) for both A^n and bulk stacking as a function of the strain, referred to that of the lowest-energy ↑↓ and ↑↓↑ state, respectively. (c) Magnetization of Nb_3I_8-2L in the bulk stacking as a function of the applied strain in the lowest-energy ↑↓ state. The total magnetization is zero for all strains, the bottom and top layer contributions are shown.

Conclusions

"The opposite of a correct statement is a false statement.
But the opposite of a profound truth
may well be another profound truth."

Niels Henrik David Bohr

In this work, we investigated the properties of some of the most recent and intriguing 2D and vdW materials on which the condensed matter and quantum simulation communities are focused, that are TBG, twisted HeBL $MoS_2/NbSe_2$, ML and MuL Nb_3I_8. Using first-principles calculations carried out within the DFT framework, tight-binding approach, and MC simulations, we designed, simulated, and modeled platforms that can be used for the quantum simulation of correlated physics, such as superconductivity and quantum magnetism. We widely explored the countless DOFs characterizing the vdW systems, such as stacking, twist angle, magnetism, and strain, as control knobs to trigger novel phenomena and matter phases, finding out unexpected results that can be easily implemented in experiments.

We performed an in-depth analysis of the role of relaxation in electronic properties of TBG at the magic angle $\theta = 1.08^\circ$ and a few slightly larger angles, highlighting the effects of both the out-of-plane and in-plane atomic displacements. We demonstrated that the employed continuum model can be used to explore smaller angles, providing a minimal single-particle scheme for the quantum simulation of correlated phases as superconductivity and Mott insulating state. The next step is to improve the description of the long-range behavior of the electron-electron interactions in TBG, that have proven to be crucial to predict the correct twist angles realizing the experimentally observed strong correlation phenomena [379].

Our study on twisted HeBL $MoS_2/NbSe_2$ revealed some features making this platform as a probable candidate to explore the twist-angle-dependent Ising superconductivity induced by proximity effect by the ML $NbSe_2$. Using the vdW DOFs to tune the orbital hybridization amount around E_F is crucial for this purpose, being a feasible task for future experimental works due to the available deposition techniques and the tear-and-stack fabrication technique to control the twist angle. Indeed, today exfoliated flakes of $NbSe_2$ are twisted to realize Josephson junctions and superconducting quantum interference devices (SQUIDs), demonstrating a dependence on the twist angle [380]. Moreover, twisted TMDs as quantum simulation platforms still show remarkable results, as the recent observation of doping and bandwidth-controlled metal-insulator quantum PT for twisted WSe_2.

Finally, the investigation of ML and MuL Nb_3I_8 unveiled a novel vdW magnet with intriguing properties and applications, from the Curie temperature close to the room temperature of the ML form, to the layer-dependent magnetism and the layered AFM states, up to the strain-induced magnetic PTs. The use of the twist angle or other useful DOFs on the irregular kagome lattice of the magnetic Nb ions is strongly recommended for the quantum simulation of highly exotic correlated

phases, as observed for magnetic vdW materials as TaS_2, $TaSe_2$, and $RuCl_3$ [381–384]. As a further application of the magnetic kagome lattices, it has been recently demonstrated that AFM kagome structures can be used to enable efficient motion of domain walls by only tuning the frequency of the applied spin wave [385].

A natural progress of this work would be to validate these findings by experiments or by improving the theoretical tools. DFT could be replaced by the more accurate and computationally expensive GW approximation, as a first step to calculate the many-body effects characterizing the predicted correlated phases. Quantum MC simulations would better allow to reproduce the magnetic phase diagram arising from the interactions between the quantum spins compared to the classical case [386]. In general, the paradigm of the tuning-on-demand of the vdW systems based on their several DOFs produced results of utmost importance so far and, therefore, should be pursued also for future research with increasingly suitable theories and experimental techniques.

List of Figures

List of Tables

List of Abbreviations

2D	**T**wo-**d**imensional
AFM	**A**ntiferro**m**agnetic
ARPES	**A**ngle-**r**esolved **p**hoto**e**mission **s**pectroscopy
AVH	**A**nomalous **v**alley **H**all
BFGS	**B**royden-**F**letcher-**G**oldfarb-**S**hanno
BG	**B**ilayer **g**raphene
BKT	**B**erezinskii-**K**osterlitz-**T**houless
BL	**Bi**layer
BO	**B**orn-**O**ppenheimer
BZ	**B**rillouin **z**one
CI	**C**onfiguration **i**nteraction
CNP	**C**harge **n**eutrality **p**oint
CPU	**C**entral **p**rocessing **u**nit
DFPT	**D**ensity **f**unctional **p**erturbation **t**heory
DFT	**D**ensity **f**unctional **t**heory
DHK	**D**irac-**H**ohenberg-**K**ohn
DKS	**D**irac-**K**ohn-**S**ham
DM	**D**zyaloshinsky–**M**oriya
DOF	**D**egree **o**f **f**reedom
DOS	**D**ensity **o**f **s**tates
FDR	**F**luctuation-**d**issipation **r**elation
FD	**F**ermi-**D**irac
FET	**F**ield-**e**ffect **t**ransistor
FM	**F**erro**m**agnetic
FS	**F**ermi **s**urface
GGA	**G**eneralized-**g**radient **a**pproximation
HF	**H**artree-**F**ock
HK	**H**ohenberg-**K**ohn
HeBL	**He**tero**bi**layer
KS	**K**ohn-**S**ham
LDA	**L**ocal-**d**ensity **a**pproximation
LDOS	**L**ocal **d**ensity **o**f **s**tates
LR-cDFT	**L**inear-**r**esponse **c**onstrained **d**ensity **f**unctional **t**heory
LR	**L**inear-**r**esponse
LSDA	**L**ocal-**s**pin-**d**ensity **a**pproximation
MAE	**M**agnetic-**a**nisotropy **e**nergy
MBZ	**M**ini **B**rillouin **z**one
MC	**M**onte **C**arlo
MFT	**M**ean-**f**ield **t**heory
MG	**M**onolayer **g**raphene
ML	**M**ono**l**ayer
MP	**M**ethfessel-**P**axton
MP	**M**onkhorst-**P**ack

MWH	**M**ermin-**W**agner-**H**ohenberg
MuL	**Mu**ltil**l**ayer
NC	**N**orm-**c**onserving
NL-vdW	**N**on**l**ocal **v**an **d**er **W**aals
NM	**N**on**m**agnetic
PAW	**P**rojector **a**ugmented-**w**ave
PBE	**P**erdew-**B**urke-**E**rnzerhof
PDOS	**P**rojected **d**ensity **o**f **s**tates
PES	**P**otential **e**nergy **s**urface
PL	**P**hoto**l**uminescence
PP	**P**seudo**p**otential
PT	**P**hase **t**ransition
PW	**P**lane-**w**ave
QE	**Q**uantum-**E**SPRESSO
QSL	**Q**uantum **s**pin **l**iquid
QT	**Q**uantum **t**echnology
RGGA	**R**elativistic **g**eneralized-**g**radient **a**pproximation
RKKY	**R**udermann-**K**ittel-**K**asuya-**Y**osida
RLDA	**R**elativistic **l**ocal-**d**ensity **a**pproximation
RPA	**R**andom-**p**hase **a**pproximation
SIC	**S**elf-**i**nteraction **c**orrection
SIE	**S**elf-**i**nteraction **e**rror
SL	**S**emi**l**ocal
SOC	**S**pin-**o**rbit **c**oupling
SQUID	**S**uperconducting **qu**antum **i**nterference **d**evice
STM	**S**canning **t**unneling **m**icroscopy
TBG	**T**wisted **b**ilayer **g**raphene
TB	**T**ight-**b**inding
TF	**T**homas-**F**ermi
TL	**T**ri**l**ayer
TMD	**T**ransition **m**etal **d**ichalcogenide
US	**U**ltra**s**oft
VASP	**V**ienna **A**b initio **S**imulation **P**ackage
W90	**W**annier**90**
XCrySDen	**X**-Window **Cry**stalline **S**tructures and **Den**sities
XRD	**X**-**r**ay **d**iffraction
vdWHes	**v**an **d**er **W**aals **He**terostructure**s**
vdWHos	**v**an **d**er **W**aals **Ho**mostructure**s**
vdW	**v**an **d**er **W**aals

Physical Constants

Elementary charge	$e = 1.602\,176 \times 10^{-19}\,\mathrm{C}$
Electron mass	$m_e = 9.109\,382 \times 10^{-31}\,\mathrm{kg}$
Electron spin g-factor	$g_s = 2.002\,319$
Planck constant	$h = 4.135\,667\,696 \times 10^{-15}\,\mathrm{eV\ s}$
Reduced Planck constant	$\hbar = h/2\pi = 6.582\,119\,569 \times 10^{-16}\,\mathrm{eV\ s}$
Bohr magneton	$\mu_{\mathcal{B}} = e\hbar/2m_e = 5.788\,381\,801\,2(26) \times 10^{-5}\,\mathrm{eV\ T^{-1}}$
Bohr radius	$a_0 = \hbar^2/m_e e^2 = 5.291\,772\,109\,03(80) \times 10^{-11}\,\mathrm{m}$
Boltzmann constant	$k_B = 8.617\,333\,262\,145 \times 10^{-5}\,\mathrm{eV\ K^{-1}}$
Proton mass	$m_p = 1.672\,622 \times 10^{-27}\,\mathrm{kg}$
Rydberg energy	$Ry = e^2/2a_0 = 13.605\,692\,\mathrm{eV}$
Speed of light	$c = 299\,792\,458\,\mathrm{m\ s^{-1}}$
Hartree energy	$Ha = 2Ry = 27.211\,383\,\mathrm{eV}$

Bibliography

[1] K. S. Novoselov et al. “Electric Field Effect in Atomically Thin Carbon Films”. In: *Science* 306.5696 (2004), pp. 666–669.

[2] K. S. Novoselov et al. “Two-dimensional gas of massless Dirac fermions in graphene”. In: *Nature* 438.7065 (Nov. 2005), pp. 197–200.

[3] Matthew J. Allen, Vincent C. Tung, and Richard B. Kaner. “Honeycomb Carbon: A Review of Graphene”. In: *Chemical Reviews* 110.1 (Jan. 2010), pp. 132–145.

[4] George Wypych. *Graphene: Important Results and Applications*. ChemTec Publishing, 2019, p. 315.

[5] R. Eisenschitz and F. London. “Über das Verhältnis der van der Waalsschen Kräfte zu den homöopolaren Bindungskräften”. In: *Zeitschrift für Physik* 60.7 (July 1930), pp. 491–527.

[6] F. London. “Zur Theorie und Systematik der Molekularkräfte”. In: *Zeitschrift für Physik* 63.3 (Mar. 1930), pp. 245–279.

[7] F. London. “The general theory of molecular forces”. In: *Trans. Faraday Soc.* 33 (0 1937), 8b–26.

[8] Sten Haastrup et al. “The Computational 2D Materials Database: high-throughput modeling and discovery of atomically thin crystals”. In: *2D Materials* 5.4 (Sept. 2018), p. 042002.

[9] Lijie Ci et al. “Atomic layers of hybridized boron nitride and graphene domains”. In: *Nature Materials* 9.5 (May 2010), pp. 430–435.

[10] Qing Hua Wang et al. “Electronics and optoelectronics of two-dimensional transition metal dichalcogenides”. In: *Nature Nanotechnology* 7.11 (Nov. 2012), pp. 699–712.

[11] Michael Naguib et al. “Two-Dimensional Transition Metal Carbides”. In: *ACS Nano* 6.2 (Feb. 2012), pp. 1322–1331.

[12] C. C. Coleman, H. Goldwhite, and W. Tikkanen. “A Review of Intercalation in Heavy Metal Iodides”. In: *Chemistry of Materials* 10.10 (Oct. 1998), pp. 2794–2800.

[13] Bevin Huang et al. “Layer-dependent ferromagnetism in a van der Waals crystal down to the monolayer limit”. In: *Nature* 546.7657 (June 2017), pp. 270–273.

[14] Bum Jun Kim et al. “Structural and Electrical Properties of Nb3I8 Layered Crystal”. In: *Physica Status Solidi – Rapid Research Letters (RRL)* 13.3 (2019), p. 1800448.

[15] Seungbae Oh et al. “Large-area synthesis of van der Waals two-dimensional material Nb3I8 and its infrared detection applications”. In: *Journal of Alloys and Compounds* 831 (2020), p. 154877.

[16] Andrew J. Mannix et al. "Synthesis of borophenes: Anisotropic, two-dimensional boron polymorphs". In: *Science* 350.6267 (2015), pp. 1513–1516.

[17] Patrick Vogt et al. "Silicene: Compelling Experimental Evidence for Graphene-like Two-Dimensional Silicon". In: *Phys. Rev. Lett.* 108 (15 Apr. 2012), p. 155501.

[18] Elisabeth Bianco et al. "Stability and Exfoliation of Germanane: A Germanium Graphane Analogue". In: *ACS Nano* 7.5 (May 2013), pp. 4414–4421.

[19] Han Liu et al. "Phosphorene: An Unexplored 2D Semiconductor with a High Hole Mobility". In: *ACS Nano* 8.4 (Apr. 2014), pp. 4033–4041.

[20] F. Reis et al. "Bismuthene on a SiC substrate: A candidate for a high-temperature quantum spin Hall material". In: *Science* 357.6348 (2017), pp. 287–290.

[21] Jing-Yang You et al. "Two-dimensional Weyl half-semimetal and tunable quantum anomalous Hall effect". In: *Phys. Rev. B* 100 (6 Aug. 2019), p. 064408.

[22] Justin C. W. Song and Nathaniel M. Gabor. "Electron quantum metamaterials in van der Waals heterostructures". In: *Nature Nanotechnology* 13.11 (Nov. 2018), pp. 986–993.

[23] Stefan Wachter et al. "A microprocessor based on a two-dimensional semiconductor". In: *Nature Communications* 8.1 (Apr. 2017), p. 14948.

[24] Dhinesh Babu Velusamy et al. "Flexible transition metal dichalcogenide nanosheets for band-selective photodetection". In: *Nature Communications* 6.1 (Sept. 2015), p. 8063.

[25] Yiyang Gong et al. "High flex cycle testing of CVD monolayer WS 2 TFTs on thin flexible polyimide". In: *2D Materials* 3.2 (May 2016), p. 021008.

[26] Hamin Park et al. "Flexible and Transparent Thin-Film Transistors Based on Two-Dimensional Materials for Active-Matrix Display". In: *ACS Applied Materials & Interfaces* 12.4 (Jan. 2020), pp. 4749–4754.

[27] A. K. Geim and I. V. Grigorieva. "Van der Waals heterostructures". In: *Nature* 499.7459 (July 2013), pp. 419–425.

[28] Nguyen N. T. Nam and Mikito Koshino. "Lattice relaxation and energy band modulation in twisted bilayer graphene". In: *Phys. Rev. B* 96 (7 Aug. 2017), p. 075311.

[29] Yuan Cao et al. "Correlated insulator behaviour at half-filling in magic-angle graphene superlattices". In: *Nature* 556.7699 (Apr. 2018), pp. 80–84.

[30] Yuan Cao et al. "Unconventional superconductivity in magic-angle graphene superlattices". In: *Nature* 556.7699 (Apr. 2018), pp. 43–50.

[31] Procolo Lucignano et al. "Crucial role of atomic corrugation on the flat bands and energy gaps of twisted bilayer graphene at the magic angle $\theta \sim 1.08^\circ$". In: *Phys. Rev. B* 99 (19 May 2019), p. 195419.

[32] Kaihui Liu et al. "Evolution of interlayer coupling in twisted molybdenum disulfide bilayers". In: *Nature Communications* 5.1 (Sept. 2014), p. 4966.

[33] Boxiao Cao and Tianshu Li. "Interlayer Electronic Coupling in Arbitrarily Stacked MoS2 Bilayers Controlled by Interlayer S–S Interaction". In: *The Journal of Physical Chemistry C* 119.2 (Jan. 2015), pp. 1247–1252.

[34] Po-Chun Yeh et al. "Direct Measurement of the Tunable Electronic Structure of Bilayer MoS2 by Interlayer Twist". In: *Nano Letters* 16.2 (Feb. 2016), pp. 953–959.

[35] Ning Lu et al. "Twisted MX2/MoS2 heterobilayers: effect of van der Waals interaction on the electronic structure". In: *Nanoscale* 9 (48 2017), pp. 19131–19138.

[36] Riccardo Frisenda et al. "Recent progress in the assembly of nanodevices and van der Waals heterostructures by deterministic placement of 2D materials". In: *Chem. Soc. Rev.* 47 (1 2018), pp. 53–68.

[37] T. R. Albrecht et al. "Observation of tilt boundaries in graphite by scanning tunneling microscopy and associated multiple tip effects". In: *Applied Physics Letters* 52.5 (1988), pp. 362–364.

[38] H. Beyer, M. Müller, and T. Schimmel. "Monolayers of graphite rotated by a defined angle: hexagonal superstructures by STM". In: *Applied Physics A* 68.2 (Feb. 1999), pp. 163–166.

[39] Yang Gan, Wuyang Chu, and Lijie Qiao. "STM investigation on interaction between superstructure and grain boundary in graphite". In: *Surface Science* 539.1 (2003), pp. 120–128.

[40] J. Garbarz et al. "Dislocation networks in graphite: a scanning tunnelling microscopy study". In: *Philosophical Magazine A* 65.4 (1992), pp. 853–861.

[41] M. Kuwabara, D. R. Clarke, and D. A. Smith. "Anomalous superperiodicity in scanning tunneling microscope images of graphite". In: *Applied Physics Letters* 56.24 (1990), pp. 2396–2398.

[42] Chong Yang Liu, Hsiangpin Chang, and Allen J Bard. "Large scale hexagonal domainlike structures superimposed on the atomic corrugation of a graphite surface observed by scanning tunneling microscopy". In: *Langmuir* 7.6 (1991), pp. 1138–1142.

[43] J. Osing and I.V. Shvets. "Bulk defects in graphite observed with a scanning tunnelling microscope". In: *Surface Science* 417.1 (1998), pp. 145–150.

[44] Zhao Y. Rong and Pieter Kuiper. "Electronic effects in scanning tunneling microscopy: Moiré pattern on a graphite surface". In: *Phys. Rev. B* 48 (23 Dec. 1993), pp. 17427–17431.

[45] J. Xhie et al. "Giant and supergiant lattices on graphite". In: *Phys. Rev. B* 47 (23 June 1993), pp. 15835–15841.

[46] Rafi Bistritzer and Allan H. MacDonald. "Moiré bands in twisted double-layer graphene". In: *Proceedings of the National Academy of Sciences* 108.30 (2011), pp. 12233–12237.

[47] J. M. B. Lopes dos Santos, N. M. R. Peres, and A. H. Castro Neto. "Graphene Bilayer with a Twist: Electronic Structure". In: *Phys. Rev. Lett.* 99 (25 Dec. 2007), p. 256802.

[48] K. S. Novoselov et al. "Unconventional quantum Hall effect and Berry's phase of 2π in bilayer graphene". In: *Nature Physics* 2.3 (Mar. 2006), pp. 177–180.

[49] Edward McCann and Vladimir I. Fal'ko. "Landau-Level Degeneracy and Quantum Hall Effect in a Graphite Bilayer". In: *Phys. Rev. Lett.* 96 (8 Mar. 2006), p. 086805.

[50] J. M. B. Lopes dos Santos, N. M. R. Peres, and A. H. Castro Neto. "Continuum model of the twisted graphene bilayer". In: *Phys. Rev. B* 86 (15 Oct. 2012), p. 155449.

[51] G. Trambly de Laissardière, D. Mayou, and L. Magaud. "Numerical studies of confined states in rotated bilayers of graphene". In: *Phys. Rev. B* 86 (12 Sept. 2012), p. 125413.

[52] Y. Cao et al. "Superlattice-Induced Insulating States and Valley-Protected Orbits in Twisted Bilayer Graphene". In: *Phys. Rev. Lett.* 117 (11 Sept. 2016), p. 116804.

[53] Kyounghwan Kim et al. "Tunable moiré bands and strong correlations in small-twist-angle bilayer graphene". In: *Proceedings of the National Academy of Sciences* 114.13 (2017), pp. 3364–3369.

[54] Noah F. Q. Yuan and Liang Fu. "Model for the metal-insulator transition in graphene superlattices and beyond". In: *Phys. Rev. B* 98 (4 July 2018), p. 045103.

[55] Mikito Koshino et al. "Maximally Localized Wannier Orbitals and the Extended Hubbard Model for Twisted Bilayer Graphene". In: *Phys. Rev. X* 8 (3 Sept. 2018), p. 031087.

[56] Hoi Chun Po et al. "Origin of Mott Insulating Behavior and Superconductivity in Twisted Bilayer Graphene". In: *Phys. Rev. X* 8 (3 Sept. 2018), p. 031089.

[57] M. Angeli et al. "Emergent D_6 symmetry in fully relaxed magic-angle twisted bilayer graphene". In: *Phys. Rev. B* 98 (23 Dec. 2018), p. 235137.

[58] Pilkyung Moon and Mikito Koshino. "Optical absorption in twisted bilayer graphene". In: *Phys. Rev. B* 87 (20 May 2013), p. 205404.

[59] Alexander V. Kolobov and Junji Tominaga. *Two-Dimensional Transition-Metal Dichalcogenides*. Springer International Publishing, 2016, p. 538.

[60] Tianshu Li and Giulia Galli. "Electronic Properties of MoS2 Nanoparticles". In: *The Journal of Physical Chemistry C* 111.44 (Nov. 2007), pp. 16192–16196.

[61] S. Lebègue and O. Eriksson. "Electronic structure of two-dimensional crystals from ab initio theory". In: *Phys. Rev. B* 79 (11 Mar. 2009), p. 115409.

[62] Kin Fai Mak et al. "Atomically Thin MoS_2: A New Direct-Gap Semiconductor". In: *Phys. Rev. Lett.* 105 (13 Sept. 2010), p. 136805.

[63] Claudia Ruppert, Ozgur Burak Aslan, and Tony F. Heinz. "Optical Properties and Band Gap of Single- and Few-Layer MoTe2 Crystals". In: *Nano Letters* 14.11 (Nov. 2014), pp. 6231–6236.

[64] Di Xiao et al. "Coupled Spin and Valley Physics in Monolayers of MoS_2 and Other Group-VI Dichalcogenides". In: *Phys. Rev. Lett.* 108 (19 May 2012), p. 196802.

[65] Zhirui Gong et al. "Magnetoelectric effects and valley-controlled spin quantum gates in transition metal dichalcogenide bilayers". In: *Nature Communications* 4.1 (June 2013), p. 2053.

[66] Gui-Bin Liu et al. "Electronic structures and theoretical modelling of two-dimensional group-VIB transition metal dichalcogenides". In: *Chem. Soc. Rev.* 44 (9 2015), pp. 2643–2663.

[67] Hualing Zeng et al. "Valley polarization in MoS2 monolayers by optical pumping". In: *Nature Nanotechnology* 7.8 (Aug. 2012), pp. 490–493.

[68] C. R. Zhu et al. "Strain tuning of optical emission energy and polarization in monolayer and bilayer MoS_2". In: *Phys. Rev. B* 88 (12 Sept. 2013), p. 121301.

[69] G. Aivazian et al. "Magnetic control of valley pseudospin in monolayer WSe2". In: *Nature Physics* 11.2 (Feb. 2015), pp. 148–152.

[70] T. Smole ński et al. "Tuning Valley Polarization in a WSe_2 Monolayer with a Tiny Magnetic Field". In: *Phys. Rev. X* 6 (2 May 2016), p. 021024.

[71] Shun Feng et al. "Engineering Valley Polarization of Monolayer WS2: A Physical Doping Approach". In: *Small* 15.12 (2019), p. 1805503.

[72] K. F. Mak et al. "The valley Hall effect in MoS2 transistors". In: *Science* 344.6191 (2014), pp. 1489–1492.

[73] Nicolas Ubrig et al. "Microscopic Origin of the Valley Hall Effect in Transition Metal Dichalcogenides Revealed by Wavelength-Dependent Mapping". In: *Nano Letters* 17.9 (Sept. 2017), pp. 5719–5725.

[74] Wanxiang Feng et al. "Intrinsic spin Hall effect in monolayers of group-VI dichalcogenides: A first-principles study". In: *Phys. Rev. B* 86 (16 Oct. 2012), p. 165108.

[75] M. Tahir, A. Manchon, and U. Schwingenschlögl. "Photoinduced quantum spin and valley Hall effects, and orbital magnetization in monolayer MoS_2". In: *Phys. Rev. B* 90 (12 Sept. 2014), p. 125438.

[76] A. R. Klots et al. "Probing excitonic states in suspended two-dimensional semiconductors by photocurrent spectroscopy". In: *Scientific Reports* 4.1 (Oct. 2014), p. 6608.

[77] G. G. Macfarlane et al. "Exciton and phonon effects in the absorption spectra of germanium and silicon". In: *Journal of Physics and Chemistry of Solids* 8 (1959), pp. 388–392.

[78] Masaru Onga et al. "Exciton Hall effect in monolayer MoS2". In: *Nature Materials* 16.12 (Dec. 2017), pp. 1193–1197.

[79] A Taghizadeh and T G Pedersen. "Nonlinear excitonic spin Hall effect in monolayer transition metal dichalcogenides". In: *2D Materials* 7.1 (Oct. 2019), p. 015003.

[80] Etienne Lorchat et al. "Room-Temperature Valley Polarization and Coherence in Transition Metal Dichalcogenide–Graphene van der Waals Heterostructures". In: *ACS Photonics* 5.12 (Dec. 2018), pp. 5047–5054.

[81] Yi Wan et al. "Epitaxial Single-Layer MoS2 on GaN with Enhanced Valley Helicity". In: *Advanced Materials* 30.5 (2018), p. 1703888.

[82] Sanfeng Wu et al. "Electrical tuning of valley magnetic moment through symmetry control in bilayer MoS2". In: *Nature Physics* 9.3 (Mar. 2013), pp. 149–153.

[83] Pasqual Rivera et al. "Observation of long-lived interlayer excitons in monolayer MoSe2–WSe2 heterostructures". In: *Nature Communications* 6.1 (Feb. 2015), p. 6242.

[84] Sefaattin Tongay et al. "Tuning Interlayer Coupling in Large-Area Heterostructures with CVD-Grown MoS2 and WS2 Monolayers". In: *Nano Letters* 14.6 (June 2014), pp. 3185–3190.

[85] Ming-Hui Chiu et al. "Spectroscopic Signatures for Interlayer Coupling in MoS2–WSe2 van der Waals Stacking". In: *ACS Nano* 8.9 (Sept. 2014), pp. 9649–9656.

[86] Pramoda K. Nayak et al. "Probing Evolution of Twist-Angle-Dependent Interlayer Excitons in MoSe2/WSe2 van der Waals Heterostructures". In: *ACS Nano* 11.4 (Apr. 2017), pp. 4041–4050.

[87] J. A. Wilson, F. J. Di Salvo, and S. Mahajan. "Charge-density waves and superlattices in the metallic layered transition metal dichalcogenides". In: *Advances in Physics* 24.2 (1975), pp. 117–201.

[88] Christos D. Malliakas and Mercouri G. Kanatzidis. "Nb–Nb Interactions Define the Charge Density Wave Structure of 2H-NbSe2". In: *Journal of the American Chemical Society* 135.5 (Feb. 2013), pp. 1719–1722.

[89] E. Revolinsky, E.P. Lautenschlager, and C.H. Armitage. "Layer structure superconductor". In: *Solid State Communications* 1.3 (1963), pp. 59–61.

[90] E. Revolinsky, G.A. Spiering, and D.J. Beerntsen. "Superconductivity in the niobium-selenium system". In: *Journal of Physics and Chemistry of Solids* 26.6 (1965), pp. 1029–1034.

[91] C. M. Varma and A. L. Simons. "Strong-Coupling Theory of Charge-Density-Wave Transitions". In: *Phys. Rev. Lett.* 51 (2 July 1983), pp. 138–141.

[92] Th. Straub et al. "Charge-Density-Wave Mechanism in $2H-NbSe_2$: Photoemission Results". In: *Phys. Rev. Lett.* 82 (22 May 1999), pp. 4504–4507.

[93] T. Valla et al. "Quasiparticle Spectra, Charge-Density Waves, Superconductivity, and Electron-Phonon Coupling in $2H-NbSe_2$". In: *Phys. Rev. Lett.* 92 (8 Feb. 2004), p. 086401.

[94] D. W. Shen et al. "Primary Role of the Barely Occupied States in the Charge Density Wave Formation of $NbSe_2$". In: *Phys. Rev. Lett.* 101 (22 Nov. 2008), p. 226406.

[95] S. V. Borisenko et al. "Two Energy Gaps and Fermi-Surface "Arcs" in $NbSe_2$". In: *Phys. Rev. Lett.* 102 (16 Apr. 2009), p. 166402.

[96] F. Weber et al. "Extended Phonon Collapse and the Origin of the Charge-Density Wave in $2H-NbSe_2$". In: *Phys. Rev. Lett.* 107 (10 Sept. 2011), p. 107403.

[97] D. J. Rahn et al. "Gaps and kinks in the electronic structure of the superconductor $2H$-$NbSe_2$ from angle-resolved photoemission at 1 K". In: *Phys. Rev. B* 85 (22 June 2012), p. 224532.

[98] Anjan Soumyanarayanan et al. "Quantum phase transition from triangular to stripe charge order in NbSe2". In: *Proceedings of the National Academy of Sciences* 110.5 (2013), pp. 1623–1627.

[99] Johnpierre Paglione and Richard L. Greene. "High-temperature superconductivity in iron-based materials". In: *Nature Physics* 6.9 (Sept. 2010), pp. 645–658.

[100] Chandra Varma. "Mind the pseudogap". In: *Nature* 468.7321 (Nov. 2010), pp. 184–185.

[101] Matteo Calandra and Francesco Mauri. "Charge-Density Wave and Superconducting Dome in $TiSe_2$ from Electron-Phonon Interaction". In: *Phys. Rev. Lett.* 106 (19 May 2011), p. 196406.

[102] Maxime Leroux et al. "Strong anharmonicity induces quantum melting of charge density wave in $2H-NbSe_2$ under pressure". In: *Phys. Rev. B* 92 (14 Oct. 2015), p. 140303.

[103] Anshul Kogar et al. "Signatures of exciton condensation in a transition metal dichalcogenide". In: *Science* 358.6368 (2017), pp. 1314–1317.

[104] Chao Lian, Zulfikhar A. Ali, and Bryan M. Wong. "Charge density wave hampers exciton condensation in $1T-TiSe_2$". In: *Phys. Rev. B* 100 (20 Nov. 2019), p. 205423.

[105] B. Sipos et al. "From Mott state to superconductivity in 1T-TaS2". In: *Nature Materials* 7.12 (Dec. 2008), pp. 960–965.

[106] L. J. Li et al. "Influence of defects on charge–density–wave and superconductivity in 1T-TaS2 and 2H-TaS2 systems". In: *Physica C: Superconductivity* 492 (2013), pp. 64–67.

[107] K Rossnagel. "On the origin of charge-density waves in select layered transition-metal dichalcogenides". In: *Journal of Physics: Condensed Matter* 23.21 (May 2011), p. 213001.

[108] H. Suderow et al. "Pressure Induced Effects on the Fermi Surface of Superconducting $2H-NbSe_2$". In: *Phys. Rev. Lett.* 95 (11 Sept. 2005), p. 117006.

[109] V. G. Tissen et al. "Pressure dependence of superconducting critical temperature and upper critical field of $2H$-NbS_2". In: *Phys. Rev. B* 87 (13 Apr. 2013), p. 134502.

[110] Yijun Yu et al. "Gate-tunable phase transitions in thin flakes of 1T-TaS2". In: *Nature Nanotechnology* 10.3 (Mar. 2015), pp. 270–276.

[111] Xiaoxiang Xi et al. "Strongly enhanced charge-density-wave order in monolayer NbSe2". In: *Nature Nanotechnology* 10.9 (Sept. 2015), pp. 765–769.

[112] Miguel M. Ugeda et al. "Characterization of collective ground states in single-layer NbSe2". In: *Nature Physics* 12.1 (Jan. 2016), pp. 92–97.

[113] A. M. Clogston. "Upper Limit for the Critical Field in Hard Superconductors". In: *Phys. Rev. Lett.* 9 (6 Sept. 1962), pp. 266–267.

[114] B. S. Chandrasekhar. "A Note on the Maximum Critical Field of High-Field Superconductors". In: *Applied Physics Letters* 1.1 (1962), pp. 7–8.

[115] Yi-Ting Hsu et al. "Topological superconductivity in monolayer transition metal dichalcogenides". In: *Nature Communications* 8.1 (Apr. 2017), p. 14985.

[116] Xiaoxiang Xi et al. "Ising pairing in superconducting NbSe2 atomic layers". In: *Nature Physics* 12.2 (Feb. 2016), pp. 139–143.

[117] Chao-Sheng Lian, Chen Si, and Wenhui Duan. "Unveiling Charge-Density Wave, Superconductivity, and Their Competitive Nature in Two-Dimensional NbSe2". In: *Nano Letters* 18.5 (May 2018), pp. 2924–2929.

[118] Haicheng Lin et al. "Growth of atomically thick transition metal sulfide filmson graphene/6H-SiC(0001) by molecular beam epitaxy". In: *Nano Research* 11.9 (Sept. 2018), pp. 4722–4727.

[119] Raluca-Maria Stan et al. "Epitaxial single-layer NbS_2 on Au(111): Synthesis, structure, and electronic properties". In: *Phys. Rev. Materials* 3 (4 Apr. 2019), p. 044003.

[120] Yafang Yang et al. "Enhanced superconductivity upon weakening of charge density wave transport in $2H$-TaS_2 in the two-dimensional limit". In: *Phys. Rev. B* 98 (3 July 2018), p. 035203.

[121] Hyejin Ryu et al. "Persistent Charge-Density-Wave Order in Single-Layer TaSe2". In: *Nano Letters* 18.2 (Feb. 2018), pp. 689–694.

[122] Sanghyun Jo et al. "Electrostatically Induced Superconductivity at the Surface of WS2". In: *Nano Letters* 15.2 (Feb. 2015), pp. 1197–1202.

[123] Sanghyun Jo et al. “Mono- and Bilayer WS2 Light-Emitting Transistors”. In: *Nano Letters* 14.4 (Apr. 2014), pp. 2019–2025.

[124] Davide Costanzo et al. “Tunnelling spectroscopy of gate-induced superconductivity in MoS2”. In: *Nature Nanotechnology* 13.6 (June 2018), pp. 483–488.

[125] Daniel J. Trainer et al. “Proximity-Induced Superconductivity in Monolayer MoS2”. In: *ACS Nano* 14.3 (Mar. 2020), pp. 2718–2728.

[126] Patrick A. Lee, Naoto Nagaosa, and Xiao-Gang Wen. “Doping a Mott insulator: Physics of high-temperature superconductivity”. In: *Rev. Mod. Phys.* 78 (1 Jan. 2006), pp. 17–85.

[127] Alexei Kitaev. “Anyons in an exactly solved model and beyond”. In: *Annals of Physics* 321.1 (2006). January Special Issue, pp. 2–111.

[128] Lars Onsager. “Crystal Statistics. I. A Two-Dimensional Model with an Order-Disorder Transition”. In: *Phys. Rev.* 65 (3-4 Feb. 1944), pp. 117–149.

[129] V. L. Berezinsky. “Destruction of long range order in one-dimensional and two-dimensional systems having a continuous symmetry group. I. Classical systems”. In: *Sov. Phys. JETP* 32 (1971), pp. 493–500.

[130] J. M. Kosterlitz and D. J. Thouless. “Ordering, metastability and phase transitions in two-dimensional systems”. In: *Journal of Physics C: Solid State Physics* 6.7 (Apr. 1973), pp. 1181–1203.

[131] N. D. Mermin and H. Wagner. “Absence of Ferromagnetism or Antiferromagnetism in One- or Two-Dimensional Isotropic Heisenberg Models”. In: *Phys. Rev. Lett.* 17 (22 Nov. 1966), pp. 1133–1136.

[132] Liangzhi Kou et al. “Tunable Magnetism in Strained Graphene with Topological Line Defect”. In: *ACS Nano* 5.2 (Feb. 2011), pp. 1012–1017.

[133] H. Banerjee, P. Barone, and S. Picozzi. “Half-metallic ferromagnetism in layered CdOHCl induced by hole doping”. In: *2D Materials* 8.2 (Feb. 2021), p. 025027.

[134] Zewen Wu, Jin Yu, and Shengjun Yuan. “Strain-tunable magnetic and electronic properties of monolayer CrI3”. In: *Phys. Chem. Chem. Phys.* 21 (15 2019), pp. 7750–7755.

[135] A. V. Krasheninnikov et al. “Embedding Transition-Metal Atoms in Graphene: Structure, Bonding, and Magnetism”. In: *Phys. Rev. Lett.* 102 (12 Mar. 2009), p. 126807.

[136] Xiaodong Zhou et al. “Large magneto-optical effects in hole-doped blue phosphorene and gray arsenene”. In: *Nanoscale* 9 (44 2017), pp. 17405–17414.

[137] Shengwei Jiang et al. “Controlling magnetism in 2D CrI3 by electrostatic doping”. In: *Nature Nanotechnology* 13.7 (July 2018), pp. 549–553.

[138] Oleg V. Yazyev and Lothar Helm. “Defect-induced magnetism in graphene”. In: *Phys. Rev. B* 75 (12 Mar. 2007), p. 125408.

[139] J. Červenka, M. I. Katsnelson, and C. F. J. Flipse. “Room-temperature ferromagnetism in graphite driven by two-dimensional networks of point defects”. In: *Nature Physics* 5.11 (Nov. 2009), pp. 840–844.

[140] R. R. Nair et al. “Spin-half paramagnetism in graphene induced by point defects”. In: *Nature Physics* 8.3 (Mar. 2012), pp. 199–202.

[141] Cheng Gong et al. “Discovery of intrinsic ferromagnetism in two-dimensional van der Waals crystals”. In: *Nature* 546.7657 (June 2017), pp. 265–269.

[142] P. C. Hohenberg. "Existence of Long-Range Order in One and Two Dimensions". In: *Phys. Rev.* 158 (2 June 1967), pp. 383–386.

[143] J. L. Lado and J. Fernández-Rossier. "On the origin of magnetic anisotropy in two dimensional CrI 3". In: *2D Materials* 4.3 (June 2017), p. 035002.

[144] Katherine Bourzac. "Physicists have finally created a 2D magnet". In: *Nature* (June 2017).

[145] Kyle L. Seyler et al. "Valley Manipulation by Optically Tuning the Magnetic Proximity Effect in WSe2/CrI3 Heterostructures". In: *Nano Letters* 18.6 (2018). PMID: 29756784, pp. 3823–3828.

[146] Peiheng Jiang et al. "Spin Direction-Controlled Electronic Band Structure in Two-Dimensional Ferromagnetic CrI3". In: *Nano Letters* 18.6 (2018). PMID: 29783842, pp. 3844–3849.

[147] Fawei Zheng et al. "Tunable spin states in the two-dimensional magnet CrI3". In: *Nanoscale* 10 (29 2018), pp. 14298–14303.

[148] Lucas Webster and Jia-An Yan. "Strain-tunable magnetic anisotropy in monolayer $CrCl_3$, $CrBr_3$, and CrI_3". In: *Phys. Rev. B* 98 (14 Oct. 2018), p. 144411.

[149] Bevin Huang et al. "Electrical control of 2D magnetism in bilayer CrI3". In: *Nature Nanotechnology* 13.7 (July 2018), pp. 544–548.

[150] Tingxin Li et al. "Pressure-controlled interlayer magnetism in atomically thin CrI3". In: *Nature Materials* 18.12 (Dec. 2019), pp. 1303–1308.

[151] Tiancheng Song et al. "Switching 2D magnetic states via pressure tuning of layer stacking". In: *Nature Materials* 18.12 (Dec. 2019), pp. 1298–1302.

[152] Zhaowei Zhang et al. "Direct Photoluminescence Probing of Ferromagnetism in Monolayer Two-Dimensional CrBr3". In: *Nano Letters* 19.5 (May 2019), pp. 3138–3142.

[153] Xinghan Cai et al. "Atomically Thin CrCl3: An In-Plane Layered Antiferromagnetic Insulator". In: *Nano Letters* 19.6 (June 2019), pp. 3993–3998.

[154] Dahlia R. Klein et al. "Enhancement of interlayer exchange in an ultrathin two-dimensional magnet". In: *Nature Physics* 15.12 (Dec. 2019), pp. 1255–1260.

[155] Hyun Ho Kim et al. "Evolution of interlayer and intralayer magnetism in three atomically thin chromium trihalides". In: *Proceedings of the National Academy of Sciences* 116.23 (2019), pp. 11131–11136.

[156] Amilcar Bedoya-Pinto et al. *Intrinsic 2D-XY ferromagnetism in a van der Waals monolayer*. 2021.

[157] Junke Jiang et al. "Exploration of new ferromagnetic, semiconducting and biocompatible Nb3X8 (X = Cl, Br or I) monolayers with considerable visible and infrared light absorption". In: *Nanoscale* 9 (9 2017), pp. 2992–3001.

[158] Junyi Liu et al. "Exfoliating biocompatible ferromagnetic Cr-trihalide monolayers". In: *Phys. Chem. Chem. Phys.* 18 (13 2016), pp. 8777–8784.

[159] H. Bergmann and K. Hardt. "Analysis of dissolved Cr3+ and Cr6+ in water by APDC-MIBK extraction and atomic absorption spectrometry". In: *Fresenius' Zeitschrift für analytische Chemie* 297.5 (Jan. 1979), pp. 381–383.

[160] S. N. Magonov et al. "Scanning tunneling and atomic force microscopy study of layered transition metal halides Nb3X8 (X = Cl, Br, I)". In: *Journal of the American Chemical Society* 115.6 (Mar. 1993), pp. 2495–2503.

[161] Renju Zacharia, Hendrik Ulbricht, and Tobias Hertel. "Interlayer cohesive energy of graphite from thermal desorption of polyaromatic hydrocarbons". In: *Phys. Rev. B* 69 (15 Apr. 2004), p. 155406.

[162] Antonio Acín et al. "The quantum technologies roadmap: a European community view". In: *New Journal of Physics* 20.8 (Aug. 2018), p. 080201.

[163] Johnny Kung and Muriam Fancy. *A Quantum Revolution: Report on Global Policies for Quantum Technology*. https://cifar.ca/wp-content/uploads/2021/05/quantum-report-EN-11-accessible.pdf. 2021.

[164] Robert Loredo. *IBM Quantum: An Introduction*. https://www.epic-assoc.com/wp-content/uploads/2021/03/Robert-Loredo_IBM.pdf. 2021.

[165] Frank Arute et al. "Quantum supremacy using a programmable superconducting processor". In: *Nature* 574.7779 (Oct. 2019), pp. 505–510.

[166] Edwin Pednault et al. *Leveraging Secondary Storage to Simulate Deep 54-qubit Sycamore Circuits*. 2019.

[167] High-Level Steering Committee. *Quantum Technologies Flagship Final Report*. https://qt.eu//app/uploads/2018/04/170922_HLSC_Final_Report_online.pdf. 2017.

[168] Yuri Ivanovich Manin. *Vychislimoe i nevychislimoe (Computable and Noncomputable)*. Sov. Radio. pp. 13–15. Archived from the original on May 10, 2013. Retrieved March 4, 2013. 1980.

[169] Paul Benioff. "The computer as a physical system: A microscopic quantum mechanical Hamiltonian model of computers as represented by Turing machines". In: *Journal of Statistical Physics* 22.5 (May 1980), pp. 563–591.

[170] Richard P. Feynman. "Simulating physics with computers". In: *International Journal of Theoretical Physics* 21.6 (June 1982), pp. 467–488.

[171] David P. DiVincenzo. "The Physical Implementation of Quantum Computation". In: *Fortschritte der Physik* 48.9-11 (2000), pp. 771–783.

[172] Han-Sen Zhong et al. "Quantum computational advantage using photons". In: *Science* 370.6523 (2020), pp. 1460–1463.

[173] The LIGO Scientific Collaboration et al. "Advanced LIGO". In: *Classical and Quantum Gravity* 32.7 (Mar. 2015), p. 074001.

[174] F. Acernese et al. "Increasing the Astrophysical Reach of the Advanced Virgo Detector via the Application of Squeezed Vacuum States of Light". In: *Phys. Rev. Lett.* 123 (23 Dec. 2019), p. 231108.

[175] M. Tse et al. "Quantum-Enhanced Advanced LIGO Detectors in the Era of Gravitational-Wave Astronomy". In: *Phys. Rev. Lett.* 123 (23 Dec. 2019), p. 231107.

[176] Vittorio Giovannetti, Seth Lloyd, and Lorenzo Maccone. "Quantum-Enhanced Measurements: Beating the Standard Quantum Limit". In: *Science* 306.5700 (2004), pp. 1330–1336.

[177] Sisi Zhou et al. "Achieving the Heisenberg limit in quantum metrology using quantum error correction". In: *Nature Communications* 9.1 (Jan. 2018), p. 78.

[178] Markus Greiner et al. "Quantum phase transition from a superfluid to a Mott insulator in a gas of ultracold atoms". In: *Nature* 415.6867 (Jan. 2002), pp. 39–44.

[179] Tilman Esslinger. "Fermi-Hubbard Physics with Atoms in an Optical Lattice". In: *Annual Review of Condensed Matter Physics* 1.1 (2010), pp. 129–152.

[180] N. Y. Yao et al. "A quantum dipolar spin liquid". In: *Nature Physics* 14.4 (Apr. 2018), pp. 405–410.

[181] M. Hafezi et al. "Fractional quantum Hall effect in optical lattices". In: *Phys. Rev. A* 76 (2 Aug. 2007), p. 023613.

[182] Ehud Altman et al. "Quantum Simulators: Architectures and Opportunities". In: *PRX Quantum* 2 (1 Feb. 2021), p. 017003.

[183] C. Monroe et al. "Programmable quantum simulations of spin systems with trapped ions". In: *Rev. Mod. Phys.* 93 (2 Apr. 2021), p. 025001.

[184] Shannon Whitlock, Alexander W Glaetzle, and Peter Hannaford. "Simulating quantum spin models using Rydberg-excited atomic ensembles in magnetic microtrap arrays". In: *Journal of Physics B: Atomic, Molecular and Optical Physics* 50.7 (Mar. 2017), p. 074001.

[185] Samuel A. Wilkinson and Michael J. Hartmann. "Superconducting quantum many-body circuits for quantum simulation and computing". In: *Applied Physics Letters* 116.23 (2020), p. 230501.

[186] Xiaobo Lu, Ruixiang Fei, and Li Yang. "Curie temperature of emerging two-dimensional magnetic structures". In: *Phys. Rev. B* 100 (20 Nov. 2019), p. 205409.

[187] Thomas Olsen. "Theory and simulations of critical temperatures in CrI3 and other 2D materials: easy-axis magnetic order and easy-plane Kosterlitz-Thouless transitions". In: *MRS Communications* 9.4 (Dec. 2019), pp. 1142–1150.

[188] Xiaobo Lu et al. "Meron-like topological spin defects in monolayer CrCl3". In: *Nature Communications* 11.1 (Sept. 2020), p. 4724.

[189] Dante M. Kennes et al. "Moiré heterostructures as a condensed-matter quantum simulator". In: *Nature Physics* 17.2 (Feb. 2021), pp. 155–163.

[190] Liang Fu and C. L. Kane. "Superconducting Proximity Effect and Majorana Fermions at the Surface of a Topological Insulator". In: *Phys. Rev. Lett.* 100 (9 Mar. 2008), p. 096407.

[191] Roman M. Lutchyn, Jay D. Sau, and S. Das Sarma. "Majorana Fermions and a Topological Phase Transition in Semiconductor-Superconductor Heterostructures". In: *Phys. Rev. Lett.* 105 (7 Aug. 2010), p. 077001.

[192] Yuval Oreg, Gil Refael, and Felix von Oppen. "Helical Liquids and Majorana Bound States in Quantum Wires". In: *Phys. Rev. Lett.* 105 (17 Oct. 2010), p. 177002.

[193] D. Soriano, M. I. Katsnelson, and J. Fernández-Rossier. "Magnetic Two-Dimensional Chromium Trihalides: A Theoretical Perspective". In: *Nano Letters* 20.9 (Sept. 2020), pp. 6225–6234.

[194] Xiaobo Lu et al. "Superconductors, orbital magnets and correlated states in magic-angle bilayer graphene". In: *Nature* 574.7780 (Oct. 2019), pp. 653–657.

[195] Aaron L. Sharpe et al. "Emergent ferromagnetism near three-quarters filling in twisted bilayer graphene". In: *Science* 365.6453 (2019), pp. 605–608.

[196] Lede Xian et al. "Multiflat Bands and Strong Correlations in Twisted Bilayer Boron Nitride: Doping-Induced Correlated Insulator and Superconductor". In: *Nano Letters* 19.8 (Aug. 2019), pp. 4934–4940.

[197] Yohanes S. Gani, Hadar Steinberg, and Enrico Rossi. "Superconductivity in twisted graphene $NbSe_2$ heterostructures". In: *Phys. Rev. B* 99 (23 June 2019), p. 235404.

[198] Fengcheng Wu et al. "Hubbard Model Physics in Transition Metal Dichalcogenide Moiré Bands". In: *Phys. Rev. Lett.* 121 (2 July 2018), p. 026402.

[199] Yanhao Tang et al. "Simulation of Hubbard model physics in WSe2/WS2 moiré superlattices". In: *Nature* 579.7799 (Mar. 2020), pp. 353–358.

[200] Giovanni Cantele et al. "Structural relaxation and low-energy properties of twisted bilayer graphene". In: *Phys. Rev. Research* 2 (4 Oct. 2020), p. 043127.

[201] Humberto Terrones and Mauricio Terrones. "Bilayers of transition metal dichalcogenides: Different stackings and heterostructures". In: *Journal of Materials Research* 29.3 (2014), pp. 373–382.

[202] Seung Bae Son et al. "Ultraviolet Wavelength-Dependent Optoelectronic Properties in Two-Dimensional NbSe2–WSe2 van der Waals Heterojunction-Based Field-Effect Transistors". In: *ACS Applied Materials & Interfaces* 9.47 (Nov. 2017), pp. 41537–41545.

[203] Felice Conte, Domenico Ninno, and Giovanni Cantele. "Electronic properties and interlayer coupling of twisted $MoS_2/NbSe_2$ heterobilayers". In: *Phys. Rev. B* 99 (15 Apr. 2019), p. 155429.

[204] Felice Conte, Domenico Ninno, and Giovanni Cantele. "Layer-dependent electronic and magnetic properties of Nb_3I_8". In: *Phys. Rev. Research* 2 (3 July 2020), p. 033001.

[205] Felice Conte et al. *Strain-tunable electronic and magnetic properties of Nb_3I_8 multilayer*. 2021.

[206] Pedro Borlido et al. "Large-Scale Benchmark of Exchange–Correlation Functionals for the Determination of Electronic Band Gaps of Solids". In: *Journal of Chemical Theory and Computation* 15.9 (Sept. 2019), pp. 5069–5079.

[207] Chiara Ricca et al. "Self-consistent DFT + U + V study of oxygen vacancies in $SrTiO_3$". In: *Phys. Rev. Research* 2 (2 June 2020), p. 023313.

[208] Ruchika Mahajan et al. *Importance of intersite Hubbard interactions in β-MnO_2: A first-principles DFT+U+V study*. 2021.

[209] E. Schrödinger. "An Undulatory Theory of the Mechanics of Atoms and Molecules". In: *Phys. Rev.* 28 (6 Dec. 1926), pp. 1049–1070.

[210] Walter Ritz. "Über eine neue Methode zur Lösung gewisser Variationsprobleme der mathematischen Physik." In: 1909.135 (1909), pp. 1–61.

[211] V. Fock. "Näherungsmethode zur Lösung des quantenmechanischen Mehrkörperproblems". In: *Zeitschrift für Physik* 61.1 (Jan. 1930), pp. 126–148.

[212] Douglas Rayner Hartree and W. Hartree. "Self-consistent field, with exchange, for beryllium". In: *Proceedings of the Royal Society of London. Series A - Mathematical and Physical Sciences* 150.869 (1935), pp. 9–33.

[213] W. Pauli. "Über den Zusammenhang des Abschlusses der Elektronengruppen im Atom mit der Komplexstruktur der Spektren". In: *Zeitschrift für Physik* 31.1 (Feb. 1925), pp. 765–783.

[214] P. Hohenberg and W. Kohn. "Inhomogeneous Electron Gas". In: *Phys. Rev.* 136 (3B Nov. 1964), B864–B871.

[215] W. Kohn and L. J. Sham. "Self-Consistent Equations Including Exchange and Correlation Effects". In: *Phys. Rev.* 140 (4A Nov. 1965), A1133–A1138.

[216] L. D. Landau and E. M. Lifshitz. *Quantum Mechanics: Non-Relativistic Theory*. Teoreticheskaia fizika. Elsevier Science, 2013.

[217] A. Messiah. *Quantum Mechanics*. Quantum Mechanics v. 2. Elsevier Science, 1981.

[218] N. W. Ashcroft and N. D. Mermin. *Solid State Physics*. HRW international editions. Holt, Rinehart and Winston, 1976.

[219] M. Born and R. Oppenheimer. "Zur Quantentheorie der Molekeln". In: *Annalen der Physik* 389.20 (1927), pp. 457–484.

[220] P. O. Löwdin. "A classic review on electron correlation". In: *Adv. Chem. Phys* 2 (1959), p. 207.

[221] W. Kohn. "Nobel Lecture: Electronic structure of matter—wave functions and density functionals". In: *Rev. Mod. Phys.* 71 (5 Oct. 1999), pp. 1253–1266.

[222] L. H. Thomas. "The calculation of atomic fields". In: *Mathematical Proceedings of the Cambridge Philosophical Society* 23.5 (1927), pp. 542–548.

[223] Enrico Fermi. "Un metodo statistico per la determinazione di alcune priorieta dell'atome". In: *Rend. Accad. Naz. Lincei* 6.602-607 (1927), p. 32.

[224] D. R. Hartree. "The Wave Mechanics of an Atom with a Non-Coulomb Central Field. Part I. Theory and Methods". In: *Mathematical Proceedings of the Cambridge Philosophical Society* 24.1 (1928), pp. 89–110.

[225] D. R. Hartree. "The Wave Mechanics of an Atom with a Non-Coulomb Central Field. Part II. Some Results and Discussion". In: *Mathematical Proceedings of the Cambridge Philosophical Society* 24.1 (1928), pp. 111–132.

[226] D. R. Hartree. "The Wave Mechanics of an Atom with a non-Coulomb Central Field. Part III. Term Values and Intensities in Series in Optical Spectra". In: *Mathematical Proceedings of the Cambridge Philosophical Society* 24.3 (1928), pp. 426–437.

[227] W. Pauli. "Zur Quantenmechanik des magnetischen Elektrons". In: *Zeitschrift für Physik* 43.9 (Sept. 1927), pp. 601–623.

[228] J. Grotendorst and Forschungszentrum Jülich. *Computational Nanoscience: Do it Yourself!: Winter School, 14 - 22 February 2006, Forschungszentrum Jülich, Germany ; Lecture Notes*. NIC series. NIC, 2006.

[229] U. von Barth and L. Hedin. "A local exchange-correlation potential for the spin polarized case. i". In: *Journal of Physics C: Solid State Physics* 5.13 (July 1972), pp. 1629–1642.

[230] M. M. Pant and A. K. Rajagopal. "Theory of inhomogeneous magnetic electron gas". In: *Solid State Communications* 10.12 (1972), pp. 1157–1160.

[231] John P. Perdew et al. "Prescription for the design and selection of density functional approximations: More constraint satisfaction with fewer fits". In: *The Journal of Chemical Physics* 123.6 (2005), p. 062201.

[232] D. M. Ceperley and B. J. Alder. "Ground State of the Electron Gas by a Stochastic Method". In: *Phys. Rev. Lett.* 45 (7 Aug. 1980), pp. 566–569.

[233] D. Sholl and J.A. Steckel. *Density Functional Theory: A Practical Introduction*. Wiley, 2011.

[234] S. H. Vosko, L. Wilk, and M. Nusair. "Accurate spin-dependent electron liquid correlation energies for local spin density calculations: a critical analysis". In: *Canadian Journal of Physics* 58.8 (1980), pp. 1200–1211.

[235] John P. Perdew and Yue Wang. "Accurate and simple analytic representation of the electron-gas correlation energy". In: *Phys. Rev. B* 45 (23 June 1992), pp. 13244–13249.

[236] Julien Toulouse. *Review of approximations for the exchange-correlation energy in density-functional theory*. 2021.

[237] David C. Langreth and John P. Perdew. "Theory of nonuniform electronic systems. I. Analysis of the gradient approximation and a generalization that works". In: *Phys. Rev. B* 21 (12 June 1980), pp. 5469–5493.

[238] David C. Langreth and M. J. Mehl. "Beyond the local-density approximation in calculations of ground-state electronic properties". In: *Phys. Rev. B* 28 (4 Aug. 1983), pp. 1809–1834.

[239] C. D. Hu and David C. Langreth. "A Spin Dependent Version of the Langreth-Mehl Exchange-Correlation Functional". In: *Physica Scripta* 32.4 (Oct. 1985), pp. 391–396.

[240] John P. Perdew. "Accurate Density Functional for the Energy: Real-Space Cutoff of the Gradient Expansion for the Exchange Hole". In: *Phys. Rev. Lett.* 55 (16 Oct. 1985), pp. 1665–1668.

[241] John P. Perdew and Wang Yue. "Accurate and simple density functional for the electronic exchange energy: Generalized gradient approximation". In: *Phys. Rev. B* 33 (12 June 1986), pp. 8800–8802.

[242] John P. Perdew. "Density-functional approximation for the correlation energy of the inhomogeneous electron gas". In: *Phys. Rev. B* 33 (12 June 1986), pp. 8822–8824.

[243] A. D. Becke. "Density-functional exchange-energy approximation with correct asymptotic behavior". In: *Phys. Rev. A* 38 (6 Sept. 1988), pp. 3098–3100.

[244] John P. Perdew, Kieron Burke, and Matthias Ernzerhof. "Generalized Gradient Approximation Made Simple". In: *Phys. Rev. Lett.* 77 (18 Oct. 1996), pp. 3865–3868.

[245] Yingkai Zhang and Weitao Yang. "Comment on "Generalized Gradient Approximation Made Simple"". In: *Phys. Rev. Lett.* 80 (4 Jan. 1998), pp. 890–890.

[246] J. P. Perdew and Alex Zunger. "Self-interaction correction to density-functional approximations for many-electron systems". In: *Phys. Rev. B* 23 (10 May 1981), pp. 5048–5079.

[247] Yingkai Zhang and Weitao Yang. "A challenge for density functionals: Self-interaction error increases for systems with a noninteger number of electrons". In: *The Journal of Chemical Physics* 109.7 (1998), pp. 2604–2608.

[248] John P. Perdew and Mel Levy. "Physical Content of the Exact Kohn-Sham Orbital Energies: Band Gaps and Derivative Discontinuities". In: *Phys. Rev. Lett.* 51 (20 Nov. 1983), pp. 1884–1887.

[249] Jianmin Tao et al. "Climbing the Density Functional Ladder: Nonempirical Meta–Generalized Gradient Approximation Designed for Molecules and Solids". In: *Phys. Rev. Lett.* 91 (14 Sept. 2003), p. 146401.

[250] P. J. Stephens et al. "Ab Initio Calculation of Vibrational Absorption and Circular Dichroism Spectra Using Density Functional Force Fields". In: *The Journal of Physical Chemistry* 98.45 (Nov. 1994), pp. 11623–11627.

[251] Carlo Adamo, Gustavo E. Scuseria, and Vincenzo Barone. "Accurate excitation energies from time-dependent density functional theory: Assessing the PBE0 model". In: *The Journal of Chemical Physics* 111.7 (1999), pp. 2889–2899.

[252] Matthias Ernzerhof and Gustavo E. Scuseria. "Assessment of the Perdew–Burke–Ernzerhof exchange-correlation functional". In: *The Journal of Chemical Physics* 110.11 (1999), pp. 5029–5036.

[253] Jochen Heyd, Gustavo E. Scuseria, and Matthias Ernzerhof. "Hybrid functionals based on a screened Coulomb potential". In: *The Journal of Chemical Physics* 118.18 (2003), pp. 8207–8215.

[254] Vladimir I. Anisimov, Jan Zaanen, and Ole K. Andersen. "Band theory and Mott insulators: Hubbard U instead of Stoner I". In: *Phys. Rev. B* 44 (3 July 1991), pp. 943–954.

[255] V. I. Anisimov et al. "Density-functional theory and NiO photoemission spectra". In: *Phys. Rev. B* 48 (23 Dec. 1993), pp. 16929–16934.

[256] I. V. Solovyev, P. H. Dederichs, and V. I. Anisimov. "Corrected atomic limit in the local-density approximation and the electronic structure of d impurities in Rb". In: *Phys. Rev. B* 50 (23 Dec. 1994), pp. 16861–16871.

[257] Dong-Hwa Seo, Alexander Urban, and Gerbrand Ceder. "Calibrating transition-metal energy levels and oxygen bands in first-principles calculations: Accurate prediction of redox potentials and charge transfer in lithium transition-metal oxides". In: *Phys. Rev. B* 92 (11 Sept. 2015), p. 115118.

[258] Vladimir I Anisimov, F Aryasetiawan, and A I Lichtenstein. "First-principles calculations of the electronic structure and spectra of strongly correlated systems: theLDAUmethod". In: *Journal of Physics: Condensed Matter* 9.4 (Jan. 1997), pp. 767–808.

[259] Nicole E. Kirchner-Hall et al. "Extensive Benchmarking of DFT+U Calculations for Predicting Band Gaps". In: *Applied Sciences* 11.5 (2021).

[260] Vivaldo Leiria Campo Jr and Matteo Cococcioni. "Extended DFT UVmethod with on-site and inter-site electronic interactions". In: *Journal of Physics: Condensed Matter* 22.5 (Jan. 2010), p. 055602.

[261] Nicolas Tancogne-Dejean and Angel Rubio. "Parameter-free hybridlike functional based on an extended Hubbard model: DFT $+ U + V$". In: *Phys. Rev. B* 102 (15 Oct. 2020), p. 155117.

[262] Sang-Hoon Lee and Young-Woo Son. "First-principles approach with a pseudohybrid density functional for extended Hubbard interactions". In: *Phys. Rev. Research* 2 (4 Dec. 2020), p. 043410.

[263] J. Hubbard and Brian Hilton Flowers. "Electron correlations in narrow energy bands". In: *Proceedings of the Royal Society of London. Series A. Mathematical and Physical Sciences* 276.1365 (1963), pp. 238–257.

[264] Shiro Sakai. "Theoretical study of multi-orbital correlated electron systems with Hund's coupling". PhD dissertation. University of Tokyo, 2006.

[265] S. L. Dudarev et al. "Electron-energy-loss spectra and the structural stability of nickel oxide: An LSDA+U study". In: *Phys. Rev. B* 57 (3 Jan. 1998), pp. 1505–1509.

[266] Matteo Cococcioni and Stefano de Gironcoli. "Linear response approach to the calculation of the effective interaction parameters in the LDA + U method". In: *Phys. Rev. B* 71 (3 Jan. 2005), p. 035105.

[267] Stephen L. Adler. "Quantum Theory of the Dielectric Constant in Real Solids". In: *Phys. Rev.* 126 (2 Apr. 1962), pp. 413–420.

[268] Nathan Wiser. "Dielectric Constant with Local Field Effects Included". In: *Phys. Rev.* 129 (1 Jan. 1963), pp. 62–69.

[269] Iurii Timrov, Nicola Marzari, and Matteo Cococcioni. "Hubbard parameters from density-functional perturbation theory". In: *Phys. Rev. B* 98 (8 Aug. 2018), p. 085127.

[270] M. Dion et al. "Van der Waals Density Functional for General Geometries". In: *Phys. Rev. Lett.* 92 (24 June 2004), p. 246401.

[271] Axel D. Becke. "A new mixing of Hartree–Fock and local density-functional theories". In: *The Journal of Chemical Physics* 98.2 (1993), pp. 1372–1377.

[272] Axel D. Becke. "Density-functional thermochemistry. III. The role of exact exchange". In: *The Journal of Chemical Physics* 98.7 (1993), pp. 5648–5652.

[273] Oleg A. Vydrov and Troy Van Voorhis. "Nonlocal van der Waals Density Functional Made Simple". In: *Phys. Rev. Lett.* 103 (6 Aug. 2009), p. 063004.

[274] Oleg A. Vydrov and Troy Van Voorhis. "Nonlocal van der Waals density functional: The simpler the better". In: *The Journal of Chemical Physics* 133.24 (2010), p. 244103.

[275] Riccardo Sabatini, Tommaso Gorni, and Stefano de Gironcoli. "Nonlocal van der Waals density functional made simple and efficient". In: *Phys. Rev. B* 87 (4 Jan. 2013), p. 041108.

[276] Aleksandr V. Terentjev, Lucian A. Constantin, and J. M. Pitarke. "Dispersion-corrected PBEsol exchange-correlation functional". In: *Phys. Rev. B* 98 (21 Dec. 2018), p. 214108.

[277] Torbjörn Björkman. "van der Waals density functional for solids". In: *Phys. Rev. B* 86 (16 Oct. 2012), p. 165109.

[278] Haowei Peng and John P. Perdew. "Rehabilitation of the Perdew-Burke-Ernzerhof generalized gradient approximation for layered materials". In: *Phys. Rev. B* 95 (8 Feb. 2017), p. 081105.

[279] Kyuho Lee et al. "Higher-accuracy van der Waals density functional". In: *Phys. Rev. B* 82 (8 Aug. 2010), p. 081101.

[280] Narbe Mardirossian and Martin Head-Gordon. "B97X-V: A 10-parameter, range-separated hybrid, generalized gradient approximation density functional with nonlocal correlation, designed by a survival-of-the-fittest strategy". In: *Phys. Chem. Chem. Phys.* 16 (21 2014), pp. 9904–9924.

[281] Haowei Peng et al. "Versatile van der Waals Density Functional Based on a Meta-Generalized Gradient Approximation". In: *Phys. Rev. X* 6 (4 Oct. 2016), p. 041005.

[282] Jiřı Klimeš, David R Bowler, and Angelos Michaelides. "Chemical accuracy for the van der Waals density functional". In: *Journal of Physics: Condensed Matter* 22.2 (Dec. 2009), p. 022201.

[283] Oleksandr A. Loboda, Grygoriy A. Dolgonos, and A. Daniel Boese. "Towards hybrid density functional calculations of molecular crystals via fragment-based methods". In: *The Journal of Chemical Physics* 149.12 (2018), p. 124104.

[284] Peter Elliott and Kieron Burke. "Non-empirical derivation of the parameter in the B88 exchange functional". In: *Canadian Journal of Chemistry* 87.10 (2009), pp. 1485–1491.

[285] Ikutaro Hamada and Minoru Otani. "Comparative van der Waals density-functional study of graphene on metal surfaces". In: *Phys. Rev. B* 82 (15 Oct. 2010), p. 153412.

[286] Valentino R. Cooper. "Van der Waals density functional: An appropriate exchange functional". In: *Phys. Rev. B* 81 (16 Apr. 2010), p. 161104.

[287] Ivor Lon čari ć and Vito Despoja. "Benchmarking van der Waals functionals with noncontact RPA calculations on graphene-Ag(111)". In: *Phys. Rev. B* 90 (7 Aug. 2014), p. 075414.

[288] Jianmin Tao et al. "Modeling the physisorption of graphene on metals". In: *Phys. Rev. B* 97 (16 Apr. 2018), p. 165403.

[289] H.B. Mabiala-Poaty et al. "Structural and electronic properties of SnS2 stacked nanosheets: An ab-initio study". In: *Journal of Physics and Chemistry of Solids* 120 (2018), pp. 211–217.

[290] Fabian Schulz, Peter Liljeroth, and Ari Paavo Seitsonen. *Benchmarking van der Waals-treated DFT: The case of hexagonal boron nitride and graphene on Ir(111)*. 2019.

[291] F. Ortmann, F. Bechstedt, and W. G. Schmidt. "Semiempirical van der Waals correction to the density functional description of solids and molecular structures". In: *Phys. Rev. B* 73 (20 May 2006), p. 205101.

[292] Ikutaro Hamada. "van der Waals density functional made accurate". In: *Phys. Rev. B* 89 (12 Mar. 2014), p. 121103.

[293] Fabien Tran et al. "Nonlocal van der Waals functionals for solids: Choosing an appropriate one". In: *Phys. Rev. Materials* 3 (6 June 2019), p. 063602.

[294] A. D. Becke. "On the large-gradient behavior of the density functional exchange energy". In: *The Journal of Chemical Physics* 85.12 (1986), pp. 7184–7187.

[295] P. R. Antoniewicz and Leonard Kleinman. "Kohn-Sham exchange potential exact to first order in $\rho(\mathrm{K}\rightarrow)/\rho_0$". In: *Phys. Rev. B* 31 (10 May 1985), pp. 6779–6781.

[296] John P. Perdew et al. "Restoring the Density-Gradient Expansion for Exchange in Solids and Surfaces". In: *Phys. Rev. Lett.* 100 (13 Apr. 2008), p. 136406.

[297] Ji ří Klime š, David R. Bowler, and Angelos Michaelides. "Van der Waals density functionals applied to solids". In: *Phys. Rev. B* 83 (19 May 2011), p. 195131.

[298] Éamonn D. Murray, Kyuho Lee, and David C. Langreth. "Investigation of Exchange Energy Density Functional Accuracy for Interacting Molecules". In: *Journal of Chemical Theory and Computation* 5.10 (Oct. 2009), pp. 2754–2762.

[299] A. H. MacDonald and S. H. Vosko. "A relativistic density functional formalism". In: *Journal of Physics C: Solid State Physics* 12.15 (Aug. 1979), pp. 2977–2990.

[300] A. K. Rajagopal and J. Callaway. "Inhomogeneous Electron Gas". In: *Phys. Rev. B* 7 (5 Mar. 1973), pp. 1912–1919.

[301] E. Engel and R. M. Dreizler. "Relativistic density functional theory". In: *Density Functional Theory II: Relativistic and Time Dependent Extensions*. Ed. by R. F. Nalewajski. Berlin, Heidelberg: Springer Berlin Heidelberg, 1996, pp. 1–80.

[302] Andrea Dal Corso. "Projector augmented-wave method: Application to relativistic spin-density functional theory". In: *Phys. Rev. B* 82 (7 Aug. 2010), p. 075116.

[303] Julien Paquier. "Relativistic range-separated density functional theory". PhD dissertation. Sorbonne Université, 2020.

[304] Julien Paquier and Julien Toulouse. "Short-range correlation energy of the relativistic homogeneous electron gas". In: *International Journal of Quantum Chemistry* 121.16 (May 2021).

[305] Julien Toulouse. *Relativistic density-functional theory based on effective quantum electrodynamics*. 2021.

[306] E. Engel, S. Keller, and R. M. Dreizler. "Generalized gradient approximation for the relativistic exchange-only energy functional". In: *Phys. Rev. A* 53 (3 Mar. 1996), pp. 1367–1374.

[307] E. Engel, T. Auth, and R. M. Dreizler. "Relativistic spin-density-functional theory: Robust solution of single-particle equations for open-subshell atoms". In: *Phys. Rev. B* 64 (23 Nov. 2001), p. 235126.

[308] V. Theileis and H. Bross. "Relativistic modified augmented plane wave method and its application to the electronic structure of gold and platinum". In: *Phys. Rev. B* 62 (20 Nov. 2000), pp. 13338–13346.

[309] Andrea Dal Corso and Adriano Mosca Conte. "Spin-orbit coupling with ultrasoft pseudopotentials: Application to Au and Pt". In: *Phys. Rev. B* 71 (11 Mar. 2005), p. 115106.

[310] P. Giannozzi et al. "QUANTUM ESPRESSO: a modular and open-source software project for quantum simulations of materials". In: *Journal of Physics: Condensed Matter* 21.39 (Sept. 2009), p. 395502.

[311] P. Giannozzi et al. "Advanced capabilities for materials modelling with Quantum ESPRESSO". In: *Journal of Physics: Condensed Matter* 29.46 (Oct. 2017), p. 465901.

[312] P. Giannozzi et al. "Quantum ESPRESSO toward the exascale". In: *The Journal of Chemical Physics* 152.15 (2020), p. 154105.

[313] Felix Bloch. "Über die Quantenmechanik der Elektronen in Kristallgittern". In: *Zeitschrift für Physik* 52.7 (July 1929), pp. 555–600.

[314] E. Kaxiras and J. D. Joannopoulos. *Quantum Theory of Materials*. Cambridge University Press, 2019.

[315] D. R. Hamann, M. Schlüter, and C. Chiang. "Norm-Conserving Pseudopotentials". In: *Phys. Rev. Lett.* 43 (20 Nov. 1979), pp. 1494–1497.

[316] David Vanderbilt. "Soft self-consistent pseudopotentials in a generalized eigenvalue formalism". In: *Phys. Rev. B* 41 (11 Apr. 1990), pp. 7892–7895.

[317] P. E. Blöchl. "Projector augmented-wave method". In: *Phys. Rev. B* 50 (24 Dec. 1994), pp. 17953–17979.

[318] G. Kresse and D. Joubert. "From ultrasoft pseudopotentials to the projector augmented-wave method". In: *Phys. Rev. B* 59 (3 Jan. 1999), pp. 1758–1775.

[319] R. M. Martin, R. M. Martin, and Cambridge University Press. *Electronic Structure: Basic Theory and Practical Methods*. Cambridge University Press, 2004.

[320] Giovanni Pizzi et al. "Wannier90 as a community code: new features and applications". In: *Journal of Physics: Condensed Matter* 32.16 (Jan. 2020), p. 165902.

[321] Kurt Lejaeghere et al. "Reproducibility in density functional theory calculations of solids". In: *Science* 351.6280 (2016), aad3000.

[322] Gianluca Prandini et al. "Precision and efficiency in solid-state pseudopotential calculations". In: *npj Computational Materials* 4.1 (Dec. 2018), p. 72.

[323] Hendrik J. Monkhorst and James D. Pack. "Special points for Brillouin-zone integrations". In: *Phys. Rev. B* 13 (12 June 1976), pp. 5188–5192.

[324] A. Baldereschi. "Mean-Value Point in the Brillouin Zone". In: *Phys. Rev. B* 7 (12 June 1973), pp. 5212–5215.

[325] https://docs.quantumatk.com/manual/technicalnotes/occupation_methods.html.

[326] C. -L. Fu and K. -M. Ho. "First-principles calculation of the equilibrium ground-state properties of transition metals: Applications to Nb and Mo". In: *Phys. Rev. B* 28 (10 Nov. 1983), pp. 5480–5486.

[327] M. Methfessel and A. T. Paxton. "High-precision sampling for Brillouin-zone integration in metals". In: *Phys. Rev. B* 40 (6 Aug. 1989), pp. 3616–3621.

[328] H. Hellman. "Einführung in die Quantenchemie". In: *Leipzig: Franz Deuticke* (1937).

[329] R. P. Feynman. "Forces in Molecules". In: *Phys. Rev.* 56 (4 Aug. 1939), pp. 340–343.

[330] E. J. Mele. "Commensuration and interlayer coherence in twisted bilayer graphene". In: *Phys. Rev. B* 81 (16 Apr. 2010), p. 161405.

[331] Pilkyung Moon and Mikito Koshino. "Energy spectrum and quantum Hall effect in twisted bilayer graphene". In: *Phys. Rev. B* 85 (19 May 2012), p. 195458.

[332] W. Heisenberg. "Zur Theorie des Ferromagnetismus". In: *Zeitschrift für Physik* 49.9 (Sept. 1928), pp. 619–636.

[333] W. Heitler and F. London. "Wechselwirkung neutraler Atome und homöopolare Bindung nach der Quantenmechanik". In: *Zeitschrift für Physik* 44.6 (June 1927), pp. 455–472.

[334] W. Nolting and A. Ramakanth. *Quantum Theory of Magnetism*. Springer Berlin Heidelberg, 2009.

[335] R.K. Pathria. *Statistical Mechanics*. Elsevier Science, 2016.

[336] M. Gibertini et al. "Magnetic 2D materials and heterostructures". In: *Nature Nanotechnology* 14.5 (May 2019), pp. 408–419.

[337] I. Dzyaloshinsky. "A thermodynamic theory of "weak" ferromagnetism of antiferromagnetics". In: *Journal of Physics and Chemistry of Solids* 4.4 (1958), pp. 241–255.

[338] Tôru Moriya. "Anisotropic Superexchange Interaction and Weak Ferromagnetism". In: *Phys. Rev.* 120 (1 Oct. 1960), pp. 91–98.

[339] Jeffrey G. Rau, Eric Kin-Ho Lee, and Hae-Young Kee. "Generic Spin Model for the Honeycomb Iridates beyond the Kitaev Limit". In: *Phys. Rev. Lett.* 112 (7 Feb. 2014), p. 077204.

[340] Alexey Kartsev et al. "Biquadratic exchange interactions in two-dimensional magnets". In: *npj Computational Materials* 6.1 (Oct. 2020), p. 150.

[341] Changsong Xu et al. "Interplay between Kitaev interaction and single ion anisotropy in ferromagnetic CrI3 and CrGeTe3 monolayers". In: *npj Computational Materials* 4.1 (Nov. 2018), p. 57.

[342] Mei Ge et al. "Interface depended electronic and magnetic properties of vertical CrI3/WSe2 heterostructures". In: *RSC Adv.* 9 (26 2019), pp. 14766–14771.

[343] Kangying Wang et al. "Magnetic and electronic properties of Cr2Ge2Te6 monolayer by strain and electric-field engineering". In: *Applied Physics Letters* 114.9 (2019), p. 092405.

[344] Huei-Ru Fuh et al. "Newtype single-layer magnetic semiconductor in transition-metal dichalcogenides VX2 (X = S, Se and Te)". In: *Scientific Reports* 6.1 (Sept. 2016), p. 32625.

[345] Hongjun Xiang et al. "Magnetic properties and energy-mapping analysis". In: *Dalton Trans.* 42 (4 2013), pp. 823–853.

[346] Daniele Torelli and Thomas Olsen. "First principles Heisenberg models of 2D magnetic materials: the importance of quantum corrections to the exchange coupling". In: *Journal of Physics: Condensed Matter* 32.33 (May 2020), p. 335802.

[347] https://vampire.york.ac.uk.

[348] E. Vitali, M. Motta, and D.E. Galli. *Theory and Simulation of Random Phenomena: Mathematical Foundations and Physical Applications*. UNITEXT for Physics. Springer International Publishing, 2018.

[349] Francisco Guinea and Niels R. Walet. "Continuum models for twisted bilayer graphene: Effect of lattice deformation and hopping parameters". In: *Phys. Rev. B* 99 (20 May 2019), p. 205134.

[350] Fernando Gargiulo and Oleg V Yazyev. "Structural and electronic transformation in low-angle twisted bilayer graphene". In: *2D Materials* 5.1 (Nov. 2017), p. 015019.

[351] Shuyang Dai, Yang Xiang, and David J. Srolovitz. "Twisted Bilayer Graphene: Moiré with a Twist". In: *Nano Letters* 16.9 (Sept. 2016), pp. 5923–5927.

[352] Kuan Zhang and Ellad B. Tadmor. "Structural and electron diffraction scaling of twisted graphene bilayers". In: *Journal of the Mechanics and Physics of Solids* 112 (2018), pp. 225–238.

[353] Stephen Carr et al. "Relaxation and domain formation in incommensurate two-dimensional heterostructures". In: *Phys. Rev. B* 98 (22 Dec. 2018), p. 224102.

[354] G. Kresse and J. Furthmüller. "Efficient iterative schemes for ab initio total-energy calculations using a plane-wave basis set". In: *Phys. Rev. B* 54 (16 Oct. 1996), pp. 11169–11186.

[355] The scalar relativistic pseudopotential PAW_PBE C 08Apr2002 has been used for C atoms.

[356] Irina V. Lebedeva et al. "Comparison of performance of van der Waals-corrected exchange-correlation functionals for interlayer interaction in graphene and hexagonal boron nitride". In: *Computational Materials Science* 128 (2017), pp. 45–58.

[357] Youngjoon Choi et al. "Electronic correlations in twisted bilayer graphene near the magic angle". In: *Nature Physics* 15.11 (Nov. 2019), pp. 1174–1180.

[358] Alexander Kerelsky et al. "Maximized electron interactions at the magic angle in twisted bilayer graphene". In: *Nature* 572.7767 (Aug. 2019), pp. 95–100.

[359] Yonglong Xie et al. "Spectroscopic signatures of many-body correlations in magic-angle twisted bilayer graphene". In: *Nature* 572.7767 (Aug. 2019), pp. 101–105.

[360] Yuhang Jiang et al. "Charge order and broken rotational symmetry in magic-angle twisted bilayer graphene". In: *Nature* 573.7772 (Sept. 2019), pp. 91–95.

[361] Simone Lisi et al. "Observation of flat bands in twisted bilayer graphene". In: *Nature Physics* 17.2 (Feb. 2021), pp. 189–193.

[362] K. Ko śmider and J. Fernández-Rossier. "Electronic properties of the MoS_2-WS_2 heterojunction". In: *Phys. Rev. B* 87 (7 Feb. 2013), p. 075451.

[363] Ning Lu et al. "MoS2/MX2 heterobilayers: bandgap engineering via tensile strain or external electrical field". In: *Nanoscale* 6 (5 2014), pp. 2879–2886.

[364] Andrea Dal Corso. "Pseudopotentials periodic table: From H to Pu". In: *Computational Materials Science* 95 (2014), pp. 337–350.

[365] The scalar relativistic pseudopotentials Mo.pbe-spn-rrkjus_psl.0.2.UPF, S.pbe-n-rrkjus_psl.0.1.UPF, Nb.pbe-spn-rrkjus_psl.1.0.0.UPF, and Se.pbe-n-rrkjus_psl.0.2.UPF are used for Mo, S, Nb, and Se atoms, respectively.

[366] Kristian Berland and Per Hyldgaard. "Exchange functional that tests the robustness of the plasmon description of the van der Waals density functional". In: *Phys. Rev. B* 89 (3 Jan. 2014), p. 035412.

[367] Imam Abdul Rahman and Acep Purqon. "First Principles Study of Molybdenum Disulfide Electronic Structure". In: *Journal of Physics: Conference Series* 877 (July 2017), p. 012026.

[368] Rui He et al. "Interlayer breathing and shear modes in NbSe 2 atomic layers". In: *2D Materials* 3.3 (Aug. 2016), p. 031008.

[369] A Gul et al. "Theoretical and experimental investigation of conjugation of 1,6-hexanedithiol on MoS2". In: *Materials Research Express* 5.3 (Mar. 2018), p. 036415.

[370] Kristian Berland et al. "van der Waals forces in density functional theory: a review of the vdW-DF method". In: *Reports on Progress in Physics* 78.6 (May 2015), p. 066501.

[371] E. Khestanova et al. "Unusual Suppression of the Superconducting Energy Gap and Critical Temperature in Atomically Thin NbSe2". In: *Nano Letters* 18.4 (Apr. 2018), pp. 2623–2629.

[372] Anton Kokalj. "Computer graphics and graphical user interfaces as tools in simulations of matter at the atomic scale". In: *Computational Materials Science* 28.2 (2003). Proceedings of the Symposium on Software Development for Process and Materials Design, pp. 155–168.

[373] Bheema Lingam Chittari et al. "Carrier- and strain-tunable intrinsic magnetism in two-dimensional MAX_3 transition metal chalcogenides". In: *Phys. Rev. B* 101 (8 Feb. 2020), p. 085415.

[374] Bo Tai et al. "Two-dimensional CoSe structures: Intrinsic magnetism, strain-tunable anisotropic valleys, magnetic Weyl point, and antiferromagnetic metal state". In: *Phys. Rev. B* 102 (22 Dec. 2020), p. 224422.

[375] Xue-Juan Dong et al. "Strain-Induced Room-Temperature Ferromagnetic Semiconductors with Large Anomalous Hall Conductivity in Two-Dimensional $Cr_2Ge_2Se_6$". In: *Phys. Rev. Applied* 12 (1 July 2019), p. 014020.

[376] F. Hulliger. *Structural Chemistry of Layer-Type Phases*. Ed. by F. Lévy. Physics and Chemistry of Materials with A. Springer Netherlands, 1976, p. 392.

[377] The scalar relativistic pseudopotentials Nb.pbe-spn-kjpaw_psl.1.0.0.UPF and I.pbe-n-kjpaw_psl.1.0.0.UPF are used for Nb and I atoms, respectively.

[378] Rui Peng et al. "Intrinsic anomalous valley Hall effect in single-layer Nb_3I_8". In: *Phys. Rev. B* 102 (3 July 2020), p. 035412.

[379] Lennart Klebl et al. "Importance of long-ranged electron-electron interactions for the magnetic phase diagram of twisted bilayer graphene". In: *Phys. Rev. B* 103 (19 May 2021), p. 195127.

[380] Liam S. Farrar et al. "Superconducting Quantum Interference in Twisted van der Waals Heterostructures". In: *Nano Letters* 21.16 (2021). PMID: 34428907, pp. 6725–6731.

[381] K. T. Law and Patrick A. Lee. "1T-TaS2 as a quantum spin liquid". In: *Proceedings of the National Academy of Sciences* 114.27 (2017), pp. 6996–7000.

[382] Martin Klanjšek et al. "A high-temperature quantum spin liquid with polaron spins". In: *Nature Physics* 13.11 (Nov. 2017), pp. 1130–1134.

[383] Yi Chen et al. "Strong correlations and orbital texture in single-layer 1T-TaSe2". In: *Nature Physics* 16.2 (Feb. 2020), pp. 218–224.

[384] A. Banerjee et al. "Proximate Kitaev quantum spin liquid behaviour in a honeycomb magnet". In: *Nature Materials* 15.7 (July 2016), pp. 733–740.

[385] D. R. Rodrigues et al. "Spin-Wave Driven Bidirectional Domain Wall Motion in Kagome Antiferromagnets". In: *Phys. Rev. Lett.* 127 (15 Oct. 2021), p. 157203.

[386] Maxime Dupont and Nicolas Laflorencie. "Quantum magnetism on small-world networks". In: *Phys. Rev. B* 103 (17 May 2021), p. 174415.

Curriculum Vitae

Publications

1. **Felice Conte**, Ludovica Zullo, Domenico Ninno, and Giovanni Cantele
   Strain-tunable electronic and magnetic properties of Nb_3I_8 multilayer
   arXiv:2107.12836 (2021)

2. Giovanni Cantele, Dario Alfè, **Felice Conte**, Vittorio Cataudella, Domenico Ninno, and Procolo Lucignano
   Structural relaxation and low-energy properties of twisted bilayer graphene
   Physical Review Research 2, 043127 (2020)

3. **Felice Conte**, Domenico Ninno, and Giovanni Cantele
   Layer-dependent electronic and magnetic properties of Nb_3I_8
   Awarded as **Editors' Suggestion**
   Physical Review Research 2, 033001 (2020)

4. **Felice Conte**, Domenico Ninno, and Giovanni Cantele
   Electronic properties and interlayer coupling of twisted $MoS_2/NbSe_2$ heterobilayers
   Physical Review B 99, 155429 (2019)

Poster Presentations at Conferences/Schools

1. *Computational School on Electronic Excitations in Novel Materials Using the Yambo Code*
   International Centre for Theoretical Physics (ICTP), Trieste (TS), 2020.

2. *Carrier doping in two-dimensional layered materials: toward novel physical properties and electronic device applications*
   Centro Congressi Federico II, Napoli (NA), 2019.

Schools

1. *Computational School on Electronic Excitations in Novel Materials Using the Yambo Code*
   International Centre for Theoretical Physics (ICTP), Trieste (TS), 2020.

2. *The Capri Spring School on Transport in Nanostructures 2019*
   Centro Multimediale "Mario Cacace", Anacapri (NA), 2019.

Tutoring Experiences

1. *MaX School on Advanced Materials and Molecular Modelling with Quantum ESPRESSO*
   International Centre for Theoretical Physics (ICTP), Trieste (TS), 2021.

Supervised Theses

1. *Electronic and magnetic properties of twisted two- dimensional bilayers: insights from first principles*
   Master Degree in Physics, Ludovica Zullo, academic year 2019/2020.